



HAL
open science

Signal processing for high-capacity bandwidth efficient optical communications

Fadi Saibi

► **To cite this version:**

Fadi Saibi. Signal processing for high-capacity bandwidth efficient optical communications. domain_other. Télécom ParisTech, 2005. English. NNT: . pastel-00001045

HAL Id: pastel-00001045

<https://pastel.hal.science/pastel-00001045>

Submitted on 18 Feb 2005

HAL is a multi-disciplinary open access archive for the deposit and dissemination of scientific research documents, whether they are published or not. The documents may come from teaching and research institutions in France or abroad, or from public or private research centers.

L'archive ouverte pluridisciplinaire **HAL**, est destinée au dépôt et à la diffusion de documents scientifiques de niveau recherche, publiés ou non, émanant des établissements d'enseignement et de recherche français ou étrangers, des laboratoires publics ou privés.

THÈSE

présentée pour l'obtention du Diplôme de:

**Docteur de l'Ecole Nationale Supérieure des
Télécommunications**

Specialté: Communications et Electronique

Fadi SAIBI

TRAITEMENT DU SIGNAL
POUR LES COMMUNICATIONS OPTIQUES
À HAUTE EFFICACITÉ SPECTRALE

Soutenue le 10 janvier 2005 devant le jury composé de:

Président Prof. Jean-Claude Belfiore (ENST, France)

Rapporteurs Dr. Robert Jopson (Lucent Technologies, USA)
 Dr. Atul Srivastava (Bookham, USA)

Examineurs Dr. Kameran Azadet (Agere Systems, USA)
 Prof. Bernard Huyart (ENST, France)

Directeur Prof. Philippe Gallion (ENST, France)

PhD Thesis

presented in order to obtain the degree of:

**Docteur de l'Ecole Nationale Supérieure des
Télécommunications**

Specialty: Electronics and Communications

Fadi SAIBI

SIGNAL PROCESSING FOR HIGH-CAPACITY
BANDWIDTH EFFICIENT OPTICAL
COMMUNICATIONS

Defended on January 10, 2005 in front of the committee composed of:

Chairman	Prof. Jean-Claude Belfiore (ENST, France)
Referees	Dr. Robert Jopson (Lucent Technologies, USA) Dr. Atul Srivastava (Bookham, USA)
Examiners	Dr. Kameran Azadet (Agere Systems, USA) Prof. Bernard Huyart (ENST, France)
Advisor	Prof. Philippe Gallion (ENST, France)

© Copyright by Fadi SAIBI 2005
All Rights Reserved

Résumé

Les travaux de recherche présentés dans cette thèse s'intéressent à l'application de techniques de modulation et de traitement du signal numérique aux communications optiques. Ils se concentrent sur la conception d'un système de communication optique sur courte distance à 40Gb/s.

Pour une longueur d'onde optique donnée, l'accroissement du débit binaire s'obtient généralement en repoussant les limites technologiques afin d'augmenter la vitesse des modulations simples du type "on-off keying". Cette méthode ne satisfait cependant pas les exigences économiques des applications à haut débit sur courte distance. La combinaison du multiplexage de porteuses électriques et d'une modulation à plusieurs niveaux permet de réduire le support fréquentiel et la vitesse de modulation du signal porteur d'information. Des composants typiques des systèmes de transmission à 10Gb/s peuvent ainsi être utilisés pour transmettre 40Gb/s. La technologie de circuits CMOS est également exploitable pour l'intégration économe de fonctions de traitement du signal élaborées.

Les structures de traitement du signal adaptatives présentées permettent de réduire les exigences techniques dans la conception des fonctions analogiques. Elles permettent également de compenser les distorsions linéaires dues au canal de transmission et aux variations résultant d'une production industrielle.

Des modèles théoriques et numériques validés par l'expérimentation permettent l'analyse du système. Les résultats de simulations numériques montrent qu'un système de communication à 40Gb/s à bas coût et d'une portée dépassant 10km est possible. Nous présentons également un prototype utilisant un circuit intégré test en technologie CMOS réalisant les fonctions de modulation/demodulation pour le canal RF le plus difficile à implémenter, et transmettant des données dans une fibre monomode s'étendant sur plus de 30km.

Abstract

The research work presented in this dissertation deals with the application of modulation and digital signal processing techniques in the field of optical communications. It focuses on the design of a 40Gb/s short-reach optical transmission system.

For a given optical wavelength, capacity increase is generally achieved by pushing technological limits in order to augment the serial line rate of simple on-off keying modulations. This approach is not compatible with the economics of high-capacity short-reach applications. The use of sub-carrier multiplexing with multilevel signaling reduces bandwidth occupation and signaling rate. Components taken from existing 10Gb/s systems can thus be used to transmit 40Gb/s. At reduced signaling rates, CMOS circuit technology can be exploited to integrate elaborate signal processing functions.

The adaptive signal processing structures presented in this dissertation relax analog front-end design requirements and can compensate for linear impairments due to the channel as well as fabrication process variations.

The system is analyzed by deriving theoretical and numerical models agreeing with experimental validation. Simulation results show that a low-cost 40Gb/s system reaching beyond 10km is indeed feasible. We present a system prototype based on a CMOS test chip implementing modulation/demodulation functions for the highest-frequency and most challenging RF channel. This transmission system prototype operates over more than 30km of single mode fiber.

Acknowledgements

I wish to express my sincere appreciation to Agere Systems, Inc., Mark Pinto, Bryan Ackland and Kamran Azadet for having made the work presented in this dissertation possible. I am very thankful to Prof. Philippe Gallion for granting me the privilege of being one of his doctoral students. I am particularly grateful to my industrial mentor, Dr. Azadet, for his invaluable guidance, unlimited enthusiasm and friendship that have helped me develop, both professionally and personally, over the course of this research work.

This endeavor has its origin in an internship I performed from April to October 2000 at Lucent Technologies Bell Labs. I would like to express my appreciation to Helen Kim for her help at a key point in that internship. Thanks also go to Robert Jopson and Lynn Nelson for their kind answers to questions about PMD and other aspects of optical fiber modelling. Dr. Jopson deserves special recognition. As a member of the thesis defense committee and Referee, his review of the manuscript and many comments have lead to a clear improvement in the quality of the dissertation.

I learnt enormously from the discussions and lab seminars at Lucent Technologies and Agere Systems as well as from friends and colleagues. I wish to thank Andrew Blanksby, Chunbing Guo, Erich Harastsch, Chris Howland, Jenshan Lin, Leilei Song, Thomas Truman, Joseph Williams, Fuji Yang and Meng-Lin Yu for stimulating discussions on communications, coding, equalization, and VLSI architecture and implementation.

I would like to give special thanks to my friends and colleagues from the High Speed Communications VLSI Research Department who worked on the implementation of the CMOS QAM transceiver test chip: Kuang-Hu Huang, TP Liu, David Inglis and Eduard Säckinger. Dr. Säckinger conducted the test chip measurements and his exemplary rigor helped me greatly when I had to design the optical QAM transmission experiment.

Some of the results presented in this dissertation critically depend on the contribution of researchers at and around Agere Systems I had the pleasure to interact or closely collaborate

with. I wish to express my thanks to Jinghong Chen for his input on laser and receiver noise as well as laser clipping distortions, to Eva Peral for providing laser rate equation parameters and relative intensity noise data, and to Joe Othmer for our close collaboration in the design of the system simulation platform and stimulating discussions over the analysis of simulation results. I gratefully acknowledge the help Atul Srivastava provided by sharing his own experience in the design of multi-carrier QAM optical communication systems early in this research work. I am also grateful to Dr. Srivastava for accepting to be a Referee within my defense committee.

I had the great pleasure to collaborate with Martin Fischer on a PMD compensation project. His impressive mastery of the design of automated data acquisition systems has left me with an unforgettable impression. I wish to extend my thanks to Keisuke Kojima and Osamu Mizuhara also members of Swami Swaminathan's Advanced Photonics Research Department whom I had the delight to interact with and borrowed lab equipment from.

I thank Rose and Kamran Azadet, Volker Hilt, Xue Li, Andrea and Tom Truman, and Paulette and Joe Williams for their invaluable friendship and our sharing of great cultural, culinary and fun moments in and out of New Jersey and New York City.

Infinite gratitude goes to my mother for her total support in every one of my undertakings.

I finally thank the members of my defense committee for their appraisal of this work.

List of Abbreviations

A/D	Analog-to-digital
ADC	Analog-to-digital converter
ASE	Amplified spontaneous emission
BER	Bit error rate
CATV	Common-antenna television
CDR	Clock and data recovery
CMOS	Complementary Metal-Oxide-Semiconductor
CNLS	Coupled nonlinear Schrödinger (equation)
CSO	Composite second-order (distortion)
CTB	Composite triple beat (distortion)
CW	Continuous-wave (laser)
CWDM	Coarse wavelength division multiplex
D/A	Digital-to-analog
DAC	Digital-to-analog converter
DC	Direct current
DCF	Dispersion compensating fiber
DES	Dynamic eigenstate
DFB	Distributed feedback (laser)
DFE	Decision-feedback equalizer

DGD	Differential group delay
DML	Directly modulated laser
DOP	Degree of polarization
DSP	Digital signal processing (or processor)
EDFA	Erbium-doped fiber amplifier
ENST	Ecole Nationale Supérieure des Télécommunications
EO	Electro-optical
EOE	Electro-opto-electrical
FDM	Frequency division multiplex
FEC	Forward error correction
FFE	Feed-forward equalizer
FFT	Fast Fourier transform
FIR	Finite impulse response
GVD	Group velocity dispersion
HFC	Hybrid fiber-coax
HiBi	High birefringence (fiber)
HWP	Half-wave plate
IC	Integrated circuit
i.i.d.	Independent identically distributed
IIP2	Intermodulation intercept point of order 2
IIP3	Intermodulation intercept point of order 3
IMD2	Intermodulation distortion of order 2
IMD3	Intermodulation distortion of order 3
IM/DD	Intensity modulation / Direct detection
I/Q	In-phase / quadrature
ISI	Inter-symbol interference
LAN	Local area network

lcp	left circular polarization
LMS	Least mean square
MAN	Metropolitan area network
MLSE	Maximum likelihood sequence estimator
MSE	Mean square error
NRZ	Non-return-to-zero
OMI	Optical modulation index
NLC	Nonlinear canceller
NLS	Nonlinear Schrödinger (equation)
OFDM	Orthogonal frequency division multiplex
OOK	On-off keying
PAM-Q	Pulse amplitude modulation with Q levels
PAR	Peak-to-average ratio
PBS	Polarization beam splitter
PC	Polarization controller
PCD	Polarization-dependent chromatic dispersion
PDE	Partial differential equation
PDL	Polarization-dependent loss
PIR	Phase-to-intensity ratio
PMD	Polarization-mode dispersion
PMF	Polarization-maintaining fiber
POI	Parallel optical interface
PSP	Principal state of polarization
QAM-M	Quadrature amplitude modulation with M constellation points
QHQ	Quarter-half-quarter wave plates
QPSK	Quaternary phase shift keying
QWP	Quarter-wave plate

rcp	right circular polarization
RF	Radio Frequency
RIN	Relative intensity noise
ROSA	Receive optical sub-assembly
Rx	Receive
RZ	Return-to-zero
SCM	Sub-carrier multiplexing
SMF	Single-mode fiber
SNR	Signal-to-noise ratio
SOP	State of polarization
SPM	Self phase modulation
SSB	Single-sideband
TIA	Transimpedance amplifier
TOSA	Transmit optical sub-assembly
Tx	Transmit
VGA	Variable gain amplifier
VLSI	Very Large Scale Integration
WAN	Wide area network
WDM	Wavelength-division multiplex

Contents

Résumé	v
Abstract	vii
Acknowledgements	ix
List of Abbreviations	xi
1 Introduction	1
1.1 Motivation for the study	1
1.2 Research context	2
1.3 Overview of the thesis	3
2 Optical Fiber Modeling	7
2.1 Optical fibers	7
2.2 Mathematical models	10
2.3 Fiber models in the linear regime	21
2.4 Discussion	39
3 Bandwidth Efficient Modulation	41
3.1 Introduction	41
3.2 Sub-carrier multiplexing	44
3.3 Baseband digital signal processing	49
3.4 Discussion	67
4 Optical Channel: Features and Models	69
4.1 System and optical channel definition	69

4.2	Optical system electro-opto-electrical response	73
4.3	Channel impairments and noise	88
4.4	Dominant contributions	98
4.5	Directly modulated laser model and measurements	98
4.6	Simplified model and channel capacity	121
4.7	Conclusions	134
5	Application: a low-cost 40G Transceiver	135
5.1	Numerical simulation platform and performance analysis	135
5.2	Circuit design challenges and test chip	143
5.3	Conclusions	151
6	Conclusions and Suggestions for Future Work	153
6.1	Conclusions	153
6.2	Future work	155
A	Fiber Birefringence	157
A.1	Representation of lumped and infinitesimal birefringent elements	158
A.2	Spatial variations and birefringence vector	160
A.3	Frequency variations and polarization-mode dispersion vector	163
A.4	Dynamical polarization-mode dispersion equation	164
B	Fiber Electro-opto-electrical Response Calculations	169
B.1	Fiber response	169
B.2	Phase-to-intensity ratio and laser electro-optical response	170
C	Laser Noise Formulation with (N, E) Variables	175
C.1	Heuristics of the random evolution of E	175
C.2	Ito stochastic calculus for the determination of the carrier noise process	176
D	Fiber Dispersion in On-Off Keying Systems	177
D.1	Polarization-mode dispersion vector and pulse signal	178
D.2	Dispersion-induced power penalty in on-off keying optical systems	186
D.3	Fiber dispersion compensation solutions	189
D.4	Fixed-DGD optical PMD compensator	201

E	Version française réduite	241
E.1	Introduction	241
E.2	Modélisation des fibres optiques	243
E.3	Modulations à haute efficacité spectrale	249
E.4	Canal optique: caractéristiques et modèles	259
E.5	Application	274
E.6	Conclusions	280
	Bibliography	283

List of Tables

2.1	PMD-related probability density functions.	28
3.1	Peak-to-average ratio of different SCM schemes compared to NRZ.	46
3.2	Numerical values of SNR_{NRZ} and $\text{SNR}_{\text{QAM-16}}$ for different values of the BER.	47
3.3	16 QAM-16 SCM RF carrier frequency map.	48
3.4	System design “dimensions”.	68
5.1	Summary of system parameters.	136
5.2	System simulation platform and references to model descriptions.	139
5.3	System performance variations with fiber link length.	141
5.4	Summary of SNR requirements.	142
5.5	QAM transceiver test chip characteristics summary.	151
D.1	Values of the coefficients \mathcal{A} and \mathcal{B} in Eq. D.1 for a baseline BER of 10^{-9}	188
E.1	Vecteur PMD: densités de probabilité.	247
E.2	Résumé des paramètres de modulation choisis.	249
E.3	Résumé des caractéristiques de la puce de modulation/démodulation QAM.	277

List of Figures

1.1	Simple optical link.	1
1.2	Integrated transponder module	3
2.1	Loss and dispersion parameter of a standard single mode fiber.	8
2.2	Physical reference frame.	10
2.3	Polarization ellipse.	12
2.4	Poincaré sphere.	16
2.5	Jones and polarization-ellipse Poncaré sphere parameters.	17
2.6	Fiber transmission matrix.	23
2.7	Output SOP frequency dependence.	24
2.8	Principal States of Polarization.	27
2.9	Gaussian distribution for each component of the PMD vector $\vec{\tau}$	29
2.10	Maxwellian distribution for the DGD $ \vec{\tau} $	29
2.11	Soliton-amplitude distribution for each component of $\vec{\tau}'$	30
2.12	Illustration of higher-order PMD effects in fast-PSP pulse launch condition.	35
2.13	OOK NRZ signal with high level of PMD (all power in fast PSP).	37
2.14	OOK NRZ signal with high level of PMD (equal power in fast/slow PSP).	38
3.1	Comparison of the power spectra of NRZ and QAM-16 over 16 carriers	43
3.2	Subcarrier multiplexed system with receiver baudrate baseband DSP.	50
3.3	Inter-channel and image bands interference canceller.	56
3.4	Time-frequency equalization and cross-talk cancellation of channel k	59
3.5	LMS adaptive filtering block diagram.	61
3.6	Block diagram of the adaptive time-frequency equalization DSP.	63
3.7	Enhanced time-frequency equalizer performance with 6-bit A/D resolution.	64
3.8	Enhanced time-frequency equalizer performance with 10-bit A/D resolution.	65

3.9	Time-frequency equalizer compensation of RF front-end imperfections. . . .	66
4.1	Optoelectronic transmission chain overview.	70
4.2	Electro-optical conversion.	71
4.3	Laser diode direct modulation.	71
4.4	IM/DD optical transmission scheme.	73
4.5	System representation of an intensity modulating source with chirp.	74
4.6	Definition of the input signal m	75
4.7	Definition of the output signal m_{out}	75
4.8	EOE power transfer function: 10 km of fiber (1550 nm), unchirped source. . .	79
4.9	EOE power transfer function: 10 km of fiber (1550 nm), source with negative chirp.	81
4.10	EOE power transfer function: 10 km of fiber (1550 nm), semiconductor laser.	83
4.11	EOE response phase variations for 10 km of SMF at 1550 nm (DML case). . .	84
4.12	EOE response group delay variations for 10 km of fiber at 1550 nm (DML case).	85
4.13	SSB filtering: phase variations at 1550 nm.	87
4.14	Concatenation of laser and 10 km of fiber EOE response.	89
4.15	Concatenation of laser and 40 km of fiber EOE response.	89
4.16	Laser clipping.	92
4.17	Signal and noise model at the optical receiver.	96
4.18	Linearized laser electro-optical frequency response amplitude.	106
4.19	Laser damping time Γ^{-1} vs. bias current.	108
4.20	Laser oscillation and resonance frequencies vs. bias current.	108
4.21	Laser relaxation oscillations	109
4.22	Laser chirp when excited by a current step function.	109
4.23	Laser noisy behavior.	110
4.24	RIN power spectrum: theory vs. simulation.	110
4.25	RIN power spectrum: theory vs. measurements.	111
4.26	Intermodulation distortion of order 2.	112
4.27	Intermodulation distortion of order 3.	112
4.28	Setup for the measurement of intermodulation distortions.	114
4.29	Two-tone test result: example.	115
4.30	IIP2 at 50 mA above threshold.	115

4.31	IIP2 at 60 mA above threshold.	116
4.32	IIP2 at 70 mA above threshold.	116
4.33	IIP2 at 80 mA above threshold.	117
4.34	IIP2 at 90 mA above threshold.	117
4.35	IIP3 at 20 mA above threshold around f_6	118
4.36	IIP3 at 20 mA above threshold around f_9	119
4.37	IMD3 around 14 GHz at 30 mA and 50 mA above threshold.	120
4.38	Simplified channel model.	123
4.39	RIN at laser resonance vs. bias current.	124
4.40	Laser natural bandwidth.	125
4.41	Laser diode capacity vs. bias current.	126
4.42	Capacity vs. fiber length.	127
4.43	Probability of no clipping impulse vs. bias current.	128
4.44	Laser capacity vs. OMI with RIN and clipping noise.	129
4.45	Signal-to-RIN ratio distribution: flat input signal power spectral density.	130
4.46	Capacity-optimal “Water-filling” input signal power spectral density.	132
4.47	Capacity-optimal signal-to-RIN ratio distribution.	133
5.1	SNR variations with bias current.	138
5.2	SNR variations with total OMI.	138
5.3	Test chip block diagram.	144
5.4	Test chip die photo.	145
5.5	Test chip measurement setups.	146
5.6	Transmit electro-optical and receive opto-electrical interfaces.	147
5.7	Test chip transmitter electrical output power spectrum.	149
5.8	Measured QAM-16 constellations.	150
5.9	Bandwidth efficient modulation optical transponder concept.	152
D.1	Dispersion induced pulse spreading.	185
D.2	Receive path with analog FIR filter.	191
D.3	Analog FIR FFE micrograph.	192
D.4	Equalization of 10 Gb/s NRZ signal impaired by PMD.	193
D.5	Compensator based on PSP alignment.	196
D.6	First order compensator.	197

D.7	Variable DGD section.	198
D.8	Concatenation of PMD vectors.	198
D.9	Higher order compensator.	200
D.10	Block diagram of the experimental setup.	202
D.11	DOP calibration.	205
D.12	Spectral probe calibration.	207
D.13	Scan of the polarization controller.	209
D.14	QHQ polarization controller.	212
D.15	Convergence of the feedback loop.	215
D.16	Detailed block diagram of the experimental setup.	216
D.17	Typical compensator performance.	218
D.18	DOP scans.	220
D.19	Comparison of PC parameterization.	221
D.20	3-parameter compensator performance for 25 ps DGD.	223
D.21	3-parameter compensator performance for 50 ps DGD.	224
D.22	5-parameter compensator performance for 50 ps DGD.	225
D.23	Contribution of 1 st -order PMD to the system performance degradation. . .	230
D.24	Contribution of 2 nd -order PMD to the system performance degradation. . .	231
D.25	System performance measure.	232
D.26	Degree of polarization for different PC control parameter values.	233
D.27	Probed spectrum component for different PC control parameter values. . .	235
D.28	Optimal points comparison.	236
D.29	Probed spectrum component for different PC control parameter values. . .	238
D.30	Eye diagrams for maximized error signal.	240
E.1	Connection optique simple.	241
E.2	Matrice de transmission.	244
E.3	Dépendence en fréquence du SOP en sortie.	245
E.4	Etats principaux de polarisation.	246
E.5	Densité spectrale de puissance de NRZ et QAM-16 sur 16 porteuses.	250
E.6	Système de communication à sous-porteuses multiplexées.	251
E.7	Egalisation temps-fréquence et suppression d'interférence dans le canal k . .	254
E.8	Bloc DSP pour l'égalisation et la suppression d'interférences.	255

E.9	Bloc DSP pour l'adaptation temps-fréquence adaptative.	256
E.10	Performance de l'égaliseur temps-fréquence.	257
E.11	Chaîne de transmission optoélectronique: vue d'ensemble.	259
E.12	Méthode de transmission IM/DD.	260
E.13	Réponse linéaire de la chaîne laser modulé + 10 km de fibre.	261
E.14	Pincement laser.	263
E.15	Modèle de signal et bruit au niveau du récepteur optique.	264
E.16	Amplitude de la réponse en fréquence électro-optique linéarisée du laser. . .	266
E.17	Densité spectrale de puissance de RIN: théorie et simulation.	267
E.18	Densité spectrale de puissance de RIN: théorie et mesures.	267
E.19	Montage pour la mesure des distorsions d'intermodulation.	268
E.20	IIP2 à 50 mA au-dessus du seuil.	268
E.21	Modèle de canal simplifié.	269
E.22	Capacité en fonction de la longueur de fibre.	272
E.23	Capacité du laser en fonction de l'indice de modulation μ	273
E.24	Variations du rapport signal sur bruit avec le courant d'opération laser. . .	275
E.25	Variations du rapport signal sur bruit en fonction de l'indice de modulation.	275
E.26	Schéma de la puce test.	277
E.27	Microphotographie de la puce test.	278
E.28	Constellation QAM-16 mesurée.	279

Chapter 1

Introduction

1.1 Motivation for the study

Wireless and copper wireline communications have already greatly benefited from advances in digital signal processing (DSP). However optical communication is still widely based on simple on-off keying and the implementation of DSP techniques is very challenging at transmission rates in excess of 10 Gb/s. Higher speed such as 40 Gb/s require exotic and expensive optics and integrated circuit (IC) technologies. The research described in this dissertation is concerned with the use of modulation and DSP techniques in order to reduce the cost of optical transceivers and transponders with increased transmission capacity.

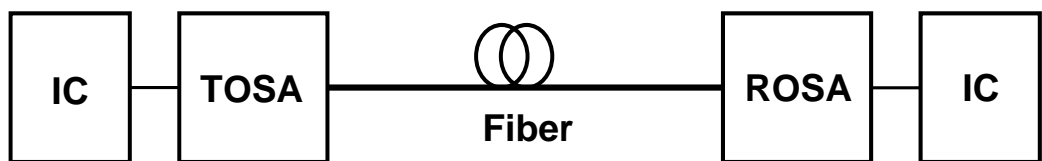


Figure 1.1: Simple optical link. IC: integrated circuits; TOSA: transmit optical sub-assembly; ROSA: receive optical sub-assembly.

A functional block diagram of the type of optical communication links this dissertation focuses on is represented in Fig. 1.1. The fiber link stretches over a few tens of kilometers

and uses a unique wavelength for the purpose of short-reach high speed communications at 40 Gb/s and beyond. This excludes from the realm of this work long-haul applications and metropolitan wavelength-division multiplexing (WDM). Short distances spare the necessity of optical amplifiers. The fiber strand considered is made of standard single-mode fiber. It has a widespread installed base and is believed to be more amenable than multi-mode fiber to transmission speed scaling beyond already achievable rates of 10 Gb/s.

In this context, system cost is dominated by the transponder module terminating the link (excluding fiber material and installation cost which is shared by any system). A typical structure for such a module is displayed in Fig. 1.2. Small form factor modules gather optical components and integrated circuits mounted on a printed circuit board within a single package providing standard electrical and optical input/output interfaces. Module cost is dominated by the cost of optical components. In essence, component bandwidth is the main cost driver: high bandwidth requirements demand exotic technologies, reduce production yield and call for enhanced packaging. Module power consumption is dominated by integrated circuits which pose a range of module design challenges in order to manage thermal dissipation. For speeds reaching tens of gigabit per second, the need for exotic integrated circuit technologies contributes both to cost (the material cost of a III/V compound wafer is more than ten times that of Si CMOS) and power consumption. CMOS technology has a significantly lower production cost than other technologies such as GaAs and InP when high production volumes are involved. Under this condition, mask cost, a fixed cost which is higher in the case of CMOS, is dominated by material and processing cost which is smaller for CMOS. Its cost advantage is even greater when the number of functions included on a single die increases, particularly for digital functions where high gate densities can be achieved.

1.2 Research context

This research work originates from an internship I performed from April to October 2000 within the High Speed Communications VLSI Research Department of Lucent Technologies Bell Labs in Holmdel, New Jersey. I later joined this department when it was being spun-off as part of Circuits and Systems Research Laboratory within the Lucent Microelectronics Division becoming Agere Systems, a newly independent company. At the time of the spin-off and when this research work was initiated, both optoelectronics and integrated-circuit

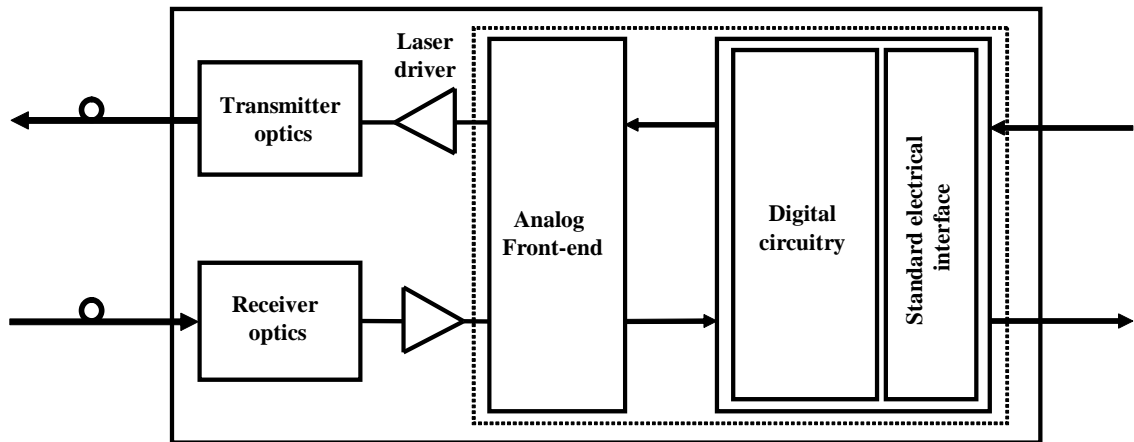


Figure 1.2: Integrated transponder module.

expertises were being leveraged to produce innovative opto-IC communication semiconductor solutions. This explains the multidisciplinary character of this research work carried out in an industrial context under the supervision of Prof. Gallion at ENST and the industrial mentorship of Dr. Azadet at Agere Systems. It greatly benefited from the interaction with renowned experts in the fields of opto-electronics, integrated-circuits design, signal processing and communications.

1.3 Overview of the thesis

Models for the transmission of optical signals in standard single mode fibers are presented in Chapter 2. Fiber-guided light can be described by a finite number of degrees of freedom (intensity, phase, state of polarization) that can all in principal be used to convey information over great distances. Most systems use light power as the conveyor of information. In systems that employ multiple wavelengths over distances of several hundred of kilometers, such as in wide area networks (WAN) and transoceanic networks, launch power is high and models need to include the fiber material nonlinear response. Yet for shorter distance applications, such backplane, data center communications, local area networks (LAN) and metropolitan area networks (MAN), the optical launch power is more modest and nonlinear products do not accumulate significant power in short distances. In these cases fiber

response can be assumed to be linear. A simple input/output linear model can be derived under this assumption describing the transmission of optical waveforms impaired by fiber dispersion. Illustration of the predictions of the models and their numerical implementation are presented in the case of the simple and widely used on-off keying (OOK) format.

Getting away from OOK, chapter 3 describes advantages and drawbacks of sub-carrier multiplexing (SCM) with multilevel signaling as a bandwidth efficient modulation scheme. The main motivation for using such a modulation lies in the lower signaling rate per radio-frequency (RF) carrier channel allowing the complex processing of multilevel signals with standard CMOS technology at low power consumption levels. Advanced digital signal processing (DSP) that was previously only the prerogative of wireless systems becomes accessible to optical communications. This brings a multitude of benefits ranging from the ability to effectively implement the promised bandwidth efficiency to easing circuit design constraints.

The definition of an optical link employing SCM for the transmission of 40 Gb/s is introduced in Chapter 4. The selection of link components based on their cost and widespread availability through volume industrial production is outlined before diving into the details of their operation. Sub-carrier multiplexing is sensitive to transmission link non-linear impairments. All impairment contributions are evaluated using realistic component characteristics. These contribution estimates motivate the precise modelling of the directly modulated laser (DML) source. These models are supported by experimental validation. In addition, a simplified information channel model is defined taking into account transmitter and receiver noise as well as laser clipping distortion. It provides the basis for the evaluation of the channel capacity and the investigation of its dependence on key parameters such as the laser bias current, the optical modulation index and the fiber length. The computed capacity and associated spectral efficiency offer a theoretical reference point for the implementation of a communication system based on such a channel.

Chapter 5 brings together models and concepts introduced in previous sections for the specification of a transmission system based on an integrated CMOS transceiver. A complete simulation platform was implemented to establish the feasibility of such a system and to provide a set of specifications for system implementation. These specifications are used to design a single-channel QAM transceiver test chip in 0.14- μm CMOS technology. The test chip proves that design challenges already encountered in wireless applications at lower frequencies can be overcome at frequencies approaching 14 GHz. Measurement results

for a single-channel transmission link are presented. The link is composed of the CMOS transceiver test chip connected through appropriate amplification stages to an optical link comprised of a DML, 30 km of fiber and a p-i-n photoreceiver.

Chapter 6 draws the conclusions of this research work and makes suggestions for future investigations. In an effort to provide a steady and coherent flow of information more detailed calculations as well as related developments are gathered in appendices at the end of this dissertation.

Chapter 2

Optical Fiber Modeling

This chapter provides a mathematical description of the input/output signal transmission behavior of single-mode optical fibers with an emphasis on dispersion due to the fiber birefringence. Fiber impairments are illustrated and discussed here in the context of on-off keying (OOK) optical transmission which is the most widely used optical modulation format.

Most complete and accurate fiber propagation models are based on partial differential equations describing the evolution of the optical field along the fiber length. Yet in a linear operation regime this description can be greatly simplified leading to a general form for the fiber 'black box' model that depends on a few basic quantities characterizing the different effects on transmitted optical signals.

These characteristic quantities could very well be defined in a more general framework. But in the case of optical fibers, additional modelling assumptions can be applied that lead to characteristic properties (specific numerical values or statistical distributions). These characteristic properties can be used as a basis for determining the actual magnitude of fiber dispersive effects on the signal integrity and devising mitigation strategies.

The fiber 'black box' model can be further simplified to provide efficient computational models for numerical simulation purposes.

2.1 Optical fibers

In an optical communication link an information-bearing electrical signal is converted into an optical signal that propagates through an optical fiber and is converted back into an

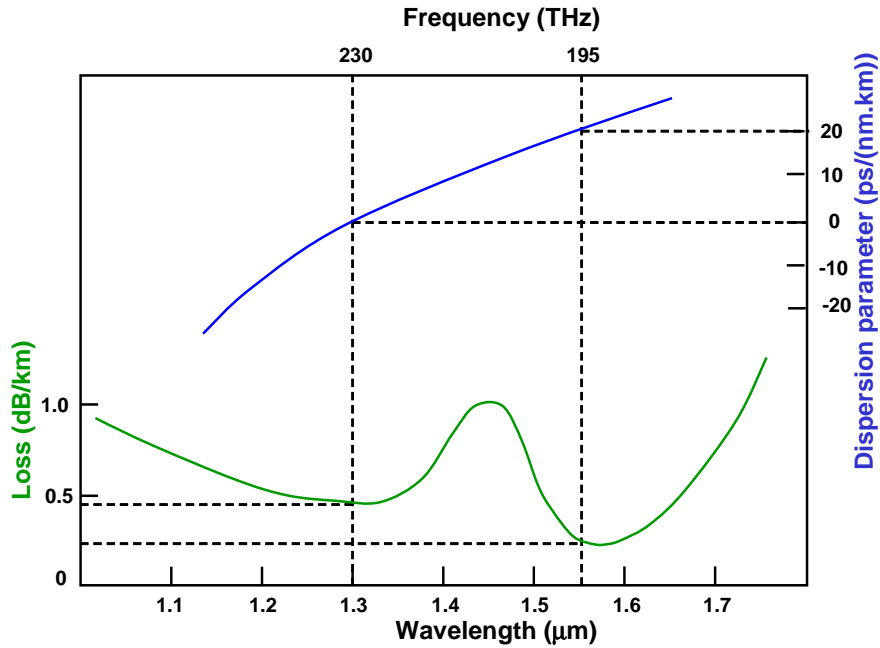


Figure 2.1: Loss and dispersion parameter of a standard single mode fiber.

electrical signal. In the case of single-mode fibers the optical signal can undergo a number of distortions due to the fiber material properties (doped silica) and geometry. A broad description of those effects as well as historical notes and typical values for commercially available fibers can be found in [Ref99].

1. Linear distortions

Attenuation

An optical signal gets attenuated as it propagates over a stretch of fiber. The attenuation curve of a typical silica-based fiber is shown in Fig. 2.1. Its shape exhibits three types of features related to different physical phenomena. Firstly it has an overall tendency to increase with decreasing (vacuum) wavelength below $1.3\ \mu\text{m}$ due to Rayleigh scattering. Secondly it shows absorption peaks due to the hydroxyl ion (OH^-) around $1.45\ \mu\text{m}$. And thirdly it has a tendency to increase above $1.6\ \mu\text{m}$ due to bending-induced loss and silica absorption. Silica-based fiber has two low-loss windows, one around the wavelength $1.3\ \mu\text{m}$ and one

around $1.55\ \mu\text{m}$, which are both used in optical communication. Common single-mode fibers have a loss of approximately $0.4\ \text{dB/km}$ at $1.3\ \mu\text{m}$ and $0.25\ \text{dB/km}$ at $1.55\ \mu\text{m}$.

Chromatic dispersion

Due to material and geometrical properties of glass fiber different wavelengths travel at different speeds. If chromatic distortion is high, optical pulses tend to broaden as they go down the fiber link. In digital optical communication systems, this can lead to inter-symbol interference and system performance degradation.

Polarization Mode Dispersion (PMD)

Despite its name the single-mode fiber generally allows for two polarization modes to propagate. These modes have different propagation properties when the fiber is not perfectly circularly symmetrical or is put under mechanical stress, their orientation is *a priori* unknown and can vary with time and wavelength. So light pulses generally incur broadening after transmission since they come out of the fiber as a superposition of two polarized pulses with different arrival times.

2. Nonlinear distortions

Stimulated scattering

This form of scattering occurs when an intense optical signal interacts with acoustic waves (Stimulated Brillouin Scattering) or with molecular modes of vibration (Stimulated Raman Scattering) within silica fiber.

Refractive index fluctuations

High optical power variations can locally modulate the material index. In turn, this index modulation alters the propagation of the optical signal itself (Self-Phase Modulation) or of other signals on other wavelength channels (Cross-Phase Modulation) in wavelength-division multiplex (WDM) systems. It can also result in the mixing of optical signals at two or three wavelengths (Four-Wave mixing) into one or more other wavelength channels.

The impact of these phenomena on the integrity of the signal of interest varies with operating parameters (wavelength, input power, fiber length, fiber manufacturing and environmental conditions, etc.). Differentiating different regimes of operation distinguishes the main contributors. It is of paramount importance in the derivation of an optical channel model that provides the best trade off between simplicity and accuracy.

In the following section we briefly review models for the description of the optical signal and its propagation in single-mode fibers.

2.2 Mathematical models

Light is the “messenger” that carries our signal through the fiber. Hence our description of the effects on the transmitted signal depends on our description of light. A “good” representation has to describe every phenomenon of interest and be simple. This is why the classical (i.e., non quantum-mechanical) theory of light will form the general framework for this representation here. If needed, quantum effects will be added by assuming that light is composed of photons following specific statistical distributions in space and time.

2.2.1 Guided light beam representation

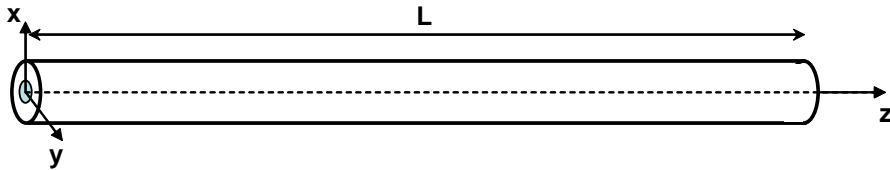


Figure 2.2: Physical reference frame.

Degrees of freedom Our main premise at this point is that the guided light wave can be represented by a two-dimensional complex vector at each point of space and time in a reference frame such as the one represented in Fig. 2.2

$$A(z, t)e^{i\omega_0 t} = \begin{pmatrix} A_x(z, t) \\ A_y(z, t) \end{pmatrix} e^{i\omega_0 t},$$

where ω_0 is the angular optical frequency of the modulated optical carrier and $A(z, t)$ the slowly varying part of the optical signal. This field is a solution of a wave equation stemming from the Maxwell equations in a dielectric medium, the electromagnetic response of that medium and its geometrical properties. It is useful to represent the propagation equations and their solutions in the Fourier domain

$$\tilde{A}(z, \omega) = \int A(z, t) e^{-i\omega t} dt,$$

where ω is the angular frequency relative to the optical carrier angular frequency ω_0 .

The Fourier representation allows an account of the number of degrees of freedom: the field can be viewed as a collection of complex functions in space indexed by a particular frequency. Each of these functions is completely determined by its value at one particular point (for instance $z = 0$, the input of the fiber). For each frequency we then have four degrees of freedom since each component can be specified by its real and imaginary parts or amplitude and phase (which depend on z and ω). The slowly varying part of the optical field can be written

$$\tilde{A}(z, \omega) = a(z, \omega) |s\rangle_{(z, \omega)} \quad (2.1)$$

where $|s\rangle = \begin{pmatrix} s_1 \\ s_2 \end{pmatrix}$ is a complex vector such that $\|s\|^2 = |s_1|^2 + |s_2|^2 = 1$

and $a(z, \omega)$ is the *complex amplitude* and $|s\rangle_{(z, \omega)}$ the *State of Polarization* (SOP) of the field at a certain frequency and at a certain point in space. The Dirac notation for two-dimensional complex vectors and their duals is used: $|s\rangle = \begin{pmatrix} s_1 \\ s_2 \end{pmatrix}$, $\langle s| = (s_1^*, s_2^*)$.

We can make a few comments at this point. The decomposition (2.1) is not unique since another valid one is $\tilde{A} = a'|s'\rangle$ with $a' = e^{i\theta} a$ and $|s'\rangle = e^{-i\theta} |s\rangle$, θ being an arbitrary function of z and ω , and this way we have accounted for every decomposition of that kind. The state of polarization of light refers to this family of unit complex vectors differing from each other by a multiplicative unit-modulus complex number. It can also be noted that complex amplitude and SOP bear different kinds of information: the first one gives the power and common phase of the field whereas the second one describes the relative power and relative phase of its two components once a physical reference frame has been chosen.

State of polarization representation In the following section we consider one particular frequency component ω of the field at one particular point in space z without necessarily referring to those quantities. We describe three representations for the SOP: the polarization ellipse representation, the Jones representation and the Poincaré sphere representation.

Polarization ellipse We imagine here that for an arbitrarily specified relative angular frequency, ω , the signal is composed of the single frequency component \tilde{A} at $\omega + \omega_0$. A complete expression of the field vector in the time domain can be written

$$\tilde{A}e^{i(\omega+\omega_0)t} = \begin{pmatrix} |\tilde{A}_x|e^{i\phi_x}, \\ |\tilde{A}_y|e^{i\phi_y} \end{pmatrix} e^{i(\omega+\omega_0)t},$$

which gives, if we project it on the subspace of real vectors

$$\text{Re}(\tilde{A}e^{i(\omega+\omega_0)t}) = \begin{pmatrix} |\tilde{A}_x| \cos((\omega + \omega_0)t + \phi_x) \\ |\tilde{A}_y| \cos((\omega + \omega_0)t + \phi_y) \end{pmatrix}.$$

If we graphically represent the time-parameterized curve thus generated in the x-y reference frame, we get an ellipse. If we normalize this vector so that $|A_x|^2 + |A_y|^2 = 1$ and change the time reference so that $\phi_x = 0$, we end up with a family of ellipses that graphically represent the states of polarization of the field vector. That family can be indexed by two independent real numbers $\alpha \in [0, \pi[$ and $\gamma \in [-\pi/4, +\pi/4]$ as shown in Fig. 2.3.

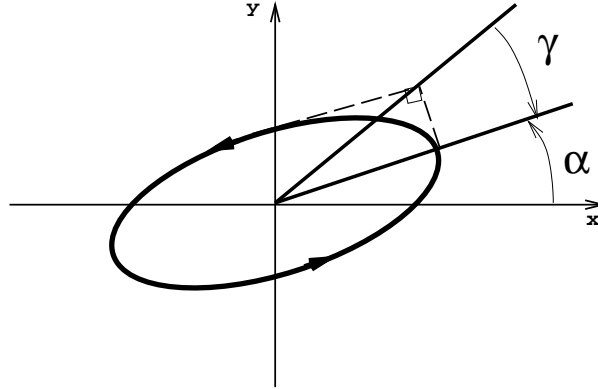


Figure 2.3: Polarization ellipse.

The names given to SOP's comes from this representation. If the ellipse is “degenerate” ($\gamma = 0$), the SOP is said to be *linear*. If, added to this, its axis is aligned with the x-axis ($\alpha = 0$), the state of polarization is said to be *horizontal* (H). If it is aligned with the y-axis ($\alpha = \pi/2$), it is said to be *vertical* (V). If the ellipse is a circle, the SOP can be a *right circular polarization* (rcp) if it rotates clockwise ($\gamma = \pi/4$), or a *left circular polarization*

(lcp) if it rotates counter-clockwise ($\gamma = -\pi/4$)¹.

Jones representation We have seen that the field vector can be written

$$\tilde{A} = \begin{pmatrix} |\tilde{A}_x|e^{i\phi_x} \\ |\tilde{A}_y|e^{i\phi_y} \end{pmatrix} = a|s\rangle \text{ with } \|s\|^2 = \langle s|s\rangle = 1,$$

which is equivalent to the relations

$$\begin{cases} a = \sqrt{|\tilde{A}_x|^2 + |\tilde{A}_y|^2} e^{i\phi} \\ |s\rangle = \begin{pmatrix} \cos(\theta/2)e^{i(\phi_x-\phi)} \\ \sin(\theta/2)e^{i(\phi_y-\phi)} \end{pmatrix} \end{cases} \text{ with } \begin{cases} \cos(\theta/2) = \frac{|\tilde{A}_x|}{\sqrt{|\tilde{A}_x|^2 + |\tilde{A}_y|^2}} \\ \sin(\theta/2) = \frac{|\tilde{A}_y|}{\sqrt{|\tilde{A}_x|^2 + |\tilde{A}_y|^2}} \end{cases}$$

where the phase ϕ is either arbitrarily chosen, or constrained by a propagation equation or any other relationship.

If we talk about the SOP of the field without relating the notion to a specific situation, this phase is arbitrary. Changing ϕ changes the Jones vector $|s\rangle$ but does not change the represented SOP. Thus, a more suitable way of representing SOP's is to use equivalence classes. On the set of Jones vectors $J = \{|s\rangle \in \mathbb{C}^2; \|s\|^2 = 1\}$ we define the equivalence relationship $|s_1\rangle \sim |s_2\rangle \iff \exists \phi \in \mathbb{R}, |s_1\rangle = e^{i\phi}|s_2\rangle$. The SOP of light can be defined as the corresponding equivalence class. Each class can be designated by one of its elements. We can add a constraint to the choice of the representative so that one and only one representative can be picked in each class (except possibly for a finite number of degenerate cases). This allows the representation SOP's with Jones vectors in an unambiguous way. For instance we can add the constraint that, assuming a particular orthonormal basis has been chosen in \mathbb{C}^2 (which can be related to a physical reference frame), *the* representative of each class is the element with a first component that is real. The corresponding parameterization of the SOP's is

$$\begin{pmatrix} \cos(\theta/2) \\ \sin(\theta/2)e^{i\Delta} \end{pmatrix} \text{ with } \theta \in [0, \pi] \text{ and } \Delta \in [0, 2\pi[. \quad (2.2)$$

A parameterization that “splits” the relative phase between the two components is often

¹The “right” and “left” denomination is arbitrary and has only a historical explanation. The contrary could have been chosen in order to agree with the vector product convention.

used

$$\begin{pmatrix} \cos(\theta/2)e^{-i\Delta/2} \\ \sin(\theta/2)e^{+i\Delta/2} \end{pmatrix} \text{ with } \theta \in [0, \pi] \text{ and } \Delta \in [0, 2\pi[. \quad (2.3)$$

If the constraint does not come from another physical equation, any choice is good as long as every subsequent statement is consistent with it. The parameters θ and Δ can be related to the polarization ellipse parameters. As a matter of fact it can be shown that each SOP can be represented by the pair (θ, Δ) or the pair (α, γ) and

$$\begin{pmatrix} \cos(\theta/2) \\ \sin(\theta/2)e^{i\Delta} \end{pmatrix} \sim \begin{pmatrix} \cos(\theta/2)e^{-i\Delta/2} \\ \sin(\theta/2)e^{+i\Delta/2} \end{pmatrix} \sim \begin{pmatrix} \cos(\alpha)\cos(\gamma) - i\sin(\alpha)\sin(\gamma) \\ \sin(\alpha)\cos(\gamma) + i\cos(\alpha)\sin(\gamma) \end{pmatrix}. \quad (2.4)$$

Poincaré sphere representation In the previous section we have seen that the states of polarization could be mathematically represented with equivalence classes over the set of Jones vectors. Though Jones vectors can be expressed in a specific basis that corresponds to a given physical reference frame, as mathematical objects they do not refer to any particular one. Consequently the same holds for the SOP's themselves. This very independence to any basis will lead us to the natural structure of the set of SOP's and a very powerful way to represent their evolution when passed through an optical system. This representation is not introduced here from more basic assumptions. Its structure and properties will simply be described.

The set of SOP's can be mapped onto a subset of the real space \mathbb{R}^3 . The dimensionality of this subset can already be derived from the fact that the set of SOP's is parameterized using two independent real parameters. More precisely let $\sigma_1 = \begin{pmatrix} 1 & 0 \\ 0 & -1 \end{pmatrix}$, $\sigma_2 = \begin{pmatrix} 0 & 1 \\ 1 & 0 \end{pmatrix}$ and $\sigma_3 = \begin{pmatrix} 0 & -i \\ i & 0 \end{pmatrix}$ be the Pauli matrices² which form an \mathbb{R} -basis of the space of the 2×2 traceless Hermitian matrices. Let $\vec{\sigma}$ be the following column

$$\vec{\sigma} = \begin{pmatrix} \sigma_1 \\ \sigma_2 \\ \sigma_3 \end{pmatrix}.$$

A map can be defined by picking for each SOP one of its Jones representatives and by

²In quantum mechanical problems, they are traditionally referred to as $\sigma_x = \sigma_2$, $\sigma_y = \sigma_3$ and $\sigma_z = \sigma_1$.

associating the following vector of \mathbb{R}^3

$$\vec{S} = \langle s | \vec{\sigma} | s \rangle = \begin{pmatrix} \langle s | \sigma_1 | s \rangle \\ \langle s | \sigma_2 | s \rangle \\ \langle s | \sigma_3 | s \rangle \end{pmatrix} = \begin{pmatrix} |s_1|^2 - |s_2|^2 \\ s_1^* s_2 + s_2^* s_1 \\ -i(s_1^* s_2 - s_2^* s_1) \end{pmatrix}. \quad (2.5)$$

The vector \vec{S} does not depend on the representative $|s\rangle$ that has been chosen but only on its equivalence class that is to say the SOP. This map is consequently well defined. It can be shown that this map is one-to-one from the set of SOP's to the unit radius sphere of \mathbb{R}^3 . In the present context this sphere is called the Poincaré sphere.

Through the map defined by (2.5) each parameterization of Jones vectors implies one for the sphere. The parameterizations (2.2) and (2.3) lead to the following for the Poincaré sphere

$$\vec{S}(\theta, \Delta) = \begin{pmatrix} \cos(\theta) \\ \sin(\theta) \cos(\Delta) \\ \sin(\theta) \sin(\Delta) \end{pmatrix} \quad \theta \in [0, \pi], \quad \Delta \in [0, 2\pi[. \quad (2.6)$$

We recognize here a standard spherical coordinate system relative to the first canonical basis vector (direction 1 in Fig. 2.4). The polarization ellipse parameterization expressed in (2.4) leads to a different description of the sphere

$$\vec{S}(\alpha, \gamma) = \begin{pmatrix} \cos(2\alpha) \cos(2\gamma) \\ \sin(2\alpha) \cos(2\gamma) \\ \sin(2\gamma) \end{pmatrix} \quad \alpha \in [0, \pi[, \quad \gamma \in [-\pi/4, +\pi/4]. \quad (2.7)$$

We recognize here an ‘‘azimuth-elevation’’ or ‘‘longitude-latitude’’ coordinate system relative to the third canonical basis vector (direction 3 in Fig. 2.4). 2α stands for the longitude and 2γ for the latitude. Fig. 2.4 shows correspondence between points on the sphere and polarization ellipses.

Fig. 2.5 shows the geometrical correspondence between (θ, Δ) and polarization-ellipse parameters (α, γ) . It is important to notice that axes 1, 2 and 3 are associated with a given physical reference frame x-y although the three-dimensional real space in which the sphere is embedded is not directly related to the physical space. Circles of constant γ gather the SOP's with same ellipticity but varying orientation of the ellipse longest principal axis. The semicircles of constant α gather the SOP's with same principal axis orientation but with

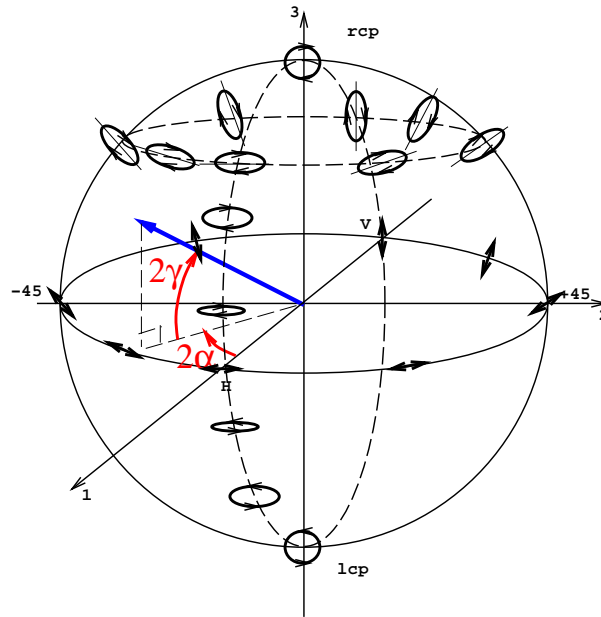


Figure 2.4: Poincaré sphere.

different ellipticities. The “northern hemisphere” is composed of the right SOP’s and the “southern hemisphere” the left SOP’s. The circles of constant θ gather the SOP’s with the same power distribution among their two components but with different relative phases. The semicircles of constant Δ are composed of the SOP’s with the same relative phase but with different power distribution among their x-y components.

2.2.2 Guided light beam propagation in single-mode fibers

There is an abundant literature deriving models for the propagation of the optical field along a single-mode fiber starting from the basic laws of electromagnetism and the response of the fiber material to the electromagnetic excitation (see for instance [Agr95b] and [Fra91]). They vary in the set of effects they intend to capture but they all result in the definition of a partial differential equation relating the variations of the optical field over the fiber length to the local value of the field and its time derivatives.

Nonlinear Schrödinger equation Given the geometrical structure of the fiber (cylindrical core and cladding having different dielectric properties), it can be shown (see [Agr95b]

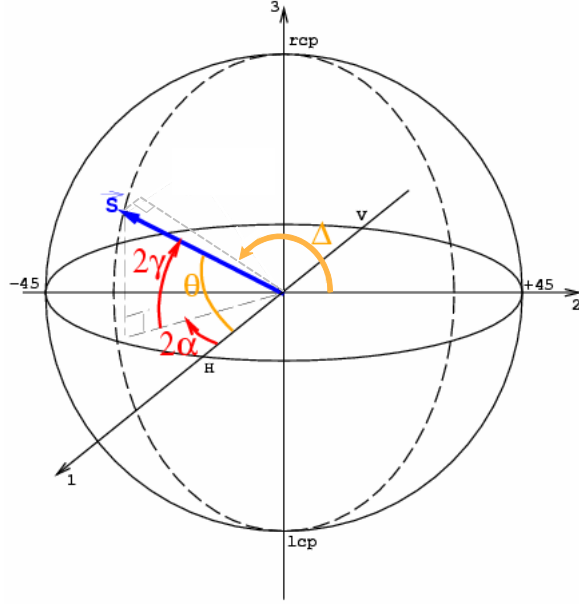


Figure 2.5: Relation between the Jones and polarization-ellipse coordinate systems on the Poincaré sphere.

for instance) that if the diameter of the core is small enough (less than $10 \mu\text{m}$ for the wavelengths used in optical communications) only one spatial mode can propagate at the angular optical wavelength, ω_0 , having wavelength in vacuum $\lambda_0 = \frac{2\pi c}{\omega_0}$. The electrical field takes the following variable-separated form

$$\mathbf{E}(\vec{r}, t) = \text{Re} \left(F(x, y) B(z, t) e^{i\beta_0 z} e^{-i\omega_0 t} \right),$$

where $F(x, y)$ describes the spatial distribution of the mode power in the x-y plane and $B(z, t)$ the z and temporal evolution of the slowly varying part of the field. F can be satisfyingly approximated by a Gaussian distribution. It is customary and convenient to normalize F such that $\iint |F(x, y)|^2 dx dy = 1$. Then $|B(z_0, t_0)|^2$ gives the optical power crossing the fiber section $z = z_0$ at the time $t = t_0$.

Once all this has been stated and kept in mind, it appears that B itself bears all the information about the optical field in the fiber. If it were a two-dimensional quantity it could be identified with the description of the field given in section (2.2.1). In fact, this can be done as will be made clearer in the next section. As shown in [Agr95b] and [Fra91] B

is a solution of the propagation equation called the *Nonlinear Schrödinger* (NLS) equation expressed here in the time domain

$$\frac{\partial B}{\partial z} + \beta_1 \frac{\partial B}{\partial t} + \frac{i}{2} \beta_2 \frac{\partial^2 B}{\partial t^2} + \frac{\alpha}{2} B = i\gamma |B|^2 B,$$

where α is the *attenuation coefficient* of the fiber and γ is the *nonlinearity coefficient* given by

$$\gamma = \frac{n_2 \omega_0}{c A_{\text{eff}}},$$

where $A_{\text{eff}} = \left(\iint |F(x, y)|^2 dx dy \right)^2 / \iint |F(x, y)|^4 dx dy$ is the *effective core area* and n_2 is the *nonlinear refractive index*. In optical fibers a typical value for n_2 is $3 \cdot 10^{-20} \text{ m}^2 \text{ W}^{-1}$ for wavelengths around $1.5 \mu\text{m}$. Typically $A_{\text{eff}} \approx 50 - 80 \mu\text{m}^2$ at $\lambda_0 \approx 1.5 \mu\text{m}$. The coefficients β_1 and β_2 , and their association with time derivatives of the corresponding order, stem from the truncation of the Taylor expansion of the *propagation coefficient* $\beta(\omega) \approx \beta_0 + \beta_1 \omega + \frac{1}{2} \beta_2 \omega^2$ in the frequency domain in the vicinity of the optical carrier frequency. Those latter coefficients are related to other customary quantities: the *group velocity* $v_g = 1/\beta_1$ and the *chromatic dispersion coefficient* $D = \frac{d\beta_1}{d\lambda} = -\frac{2\pi c}{\lambda_0^2} \beta_2$. As a matter of fact β_1 is the group delay experienced by a transmitted light pulse per unit length of fiber and the chromatic dispersion coefficient D quantifies the variations of this group delay per unit length with wavelength. $\beta_2 = \frac{d\beta_1}{d\omega}$ is another measure of chromatic dispersion and is called the *group velocity dispersion* (GVD) parameter. Typically $D \approx 17 \text{ ps}/(\text{nm} \cdot \text{km})$ at $\lambda_0 \approx 1.5 \mu\text{m}$ for a single-mode fiber (SMF) which means that a change in wavelength of 1 nm will change the group delay by 17 ps in a 1 km-long piece of fiber.

A better form for the NLS equation is obtained through the change of variable $T = t - \beta_1 z = t - z/v_g$ that describes the field in a reference frame moving along the fiber at the same speed v_g as a pulse

$$\frac{\partial B}{\partial z} + \frac{i}{2} \beta_2 \frac{\partial^2 B}{\partial T^2} + \frac{\alpha}{2} B = i\gamma |B|^2 B, \quad (2.8)$$

Numerical solutions for this nonlinear partial differential equation can be computed using the split-step Fourier method presented in [Agr95b].

Coupled non-linear Schrödinger equation If we now take into account fiber birefringence, the NLS equation can be modified in order to model this effect. The model

introduces the birefringence vector $\vec{\beta}$, a quantity that is defined along the fiber length and describes the action on the polarization of light of infinitesimal pieces of fiber at each point of the fiber span as explained in Appendix A. To include the effects of fiber distributed birefringence [Men89] makes the assumption that the birefringence vector variations takes the form $\vec{\beta}(z, \omega) = (2b + 2b'\omega)\vec{n}(z)$ where $2b$ is the birefringence strength at ω_0 , b' is the derivative of b with respect to ω at ω_0 and \vec{n} is a unit length vector following a diffusion process (random walk) parameterized by z . With these assumptions the field vector $B = \begin{pmatrix} B_x \\ B_y \end{pmatrix}$ evolution is governed by the *Coupled Nonlinear Schrödinger* (CNLS) equation

$$i\frac{\partial B}{\partial z} + \underbrace{b(\vec{n} \cdot \vec{\sigma})B + ib'(\vec{n} \cdot \vec{\sigma})\frac{\partial B}{\partial T}}_{\text{birefringence}} - \underbrace{\frac{1}{2}\beta_2\frac{\partial^2 B}{\partial T^2}}_{\text{chromatic dispersion}} + \underbrace{i\frac{\alpha}{2}B}_{\text{loss}} + \underbrace{\gamma\left(|B|^2B - \frac{1}{3}(B^\dagger\sigma_3B)\sigma_3B\right)}_{\text{nonlinear effects}} = 0,$$

where $B^\dagger = \begin{pmatrix} B_x^*, B_y^* \end{pmatrix}$ and as previously defined $T = t - \beta_1 z$.

We note the importance of the second birefringence term involving the quantity b' in accounting for polarization-dependent group delays as the presence of the $\partial/\partial T$ operator suggests. If the birefringence strength is not frequency dependent there is no polarization-related dispersion. In this case the action of the fiber is a simple state of polarization rotation and it does not have an impact on the transmission of optical signals encoded in the light beam complex amplitude.

Numerical solutions for this stochastic differential equation can be computed using the coarse-step method. This is basically the same as the split-step Fourier method for the NLS except for a pseudo-random scrambling of the SOP of the data after each step thus emulating the effect of an randomly oriented infinitesimal birefringent element.

Fiber operation regimes If we want to study the evolution of an input pulse of width T_0 and peak power P_0 , the NLS equation can be rewritten in a way that highlights every important phenomenon and naturally associates physical lengths to them. Let $\tau = T/T_0$ be the new time variable and $B(z, T) = \sqrt{P_0}e^{-\frac{\alpha}{2}z}u(z, \tau)$. u is now a quantity with no dimension and the NLS equation (2.8) is equivalent to

$$i\frac{\partial u}{\partial z} = \frac{\text{sgn}(\beta_2)}{2L_D}\frac{\partial^2 u}{\partial \tau^2} - \frac{e^{-\alpha z}}{L_{NL}}|u|^2,$$

where $\text{sgn}(\beta_2)$ is the sign of the GVD parameter β_2 , $L_D = T_0^2/|\beta_2|$ is the *dispersion length* and $L_{NL} = (\gamma P_0)^{-1}$ is the *nonlinearity length*. L_D and L_{NL} are the length scales over which the dispersive and nonlinear effects respectively become significant in the propagation of optical signals. If one of those two lengths is greater than the fiber strand length L the corresponding phenomenon does not accumulate significantly to play an important role on the evolution of the pulse.

A length scale L_{PMD} can also be associated with polarization-mode dispersion (PMD). Due to the stochastic nature of PMD L_{PMD} has to be inferred by other means than normalization of the CNLS. Since the main purpose of this section is the evaluation of the importance of nonlinear optical effects, we refer to Sec. 2.3.4 for a discussion on the length scale associated with polarization-mode dispersion. In cases where a linear approximation cannot be made [Men89], [WM96], [MMW97], [WMZ97] and [MMW97] define other length scales distinguishing a variety of operation regimes determined by the interaction of polarization-related effects and nonlinear effects.

If we consider an on-off keying (OOK) digital transmission at the wavelength $\lambda_0 \approx 1.55 \mu\text{m}$ and at a bit rate D_b through a standard SMF ($D = 17 \text{ ps}/(\text{nm} \cdot \text{km})$, $A_{\text{eff}} \approx 50 \mu\text{m}^2$, $\gamma \approx 2.10^{-3} \text{ m}^{-1} \cdot \text{W}^{-1}$), we then have

$$L_D \approx \frac{5000}{(D_b[\text{Gb/s}])^2} \text{ km},$$

$$L_{NL} \approx \frac{500}{P_o[\text{mW}]} \text{ km}.$$

In the case of a broadband point-to-point connection suitable for a LAN or a MAN we typically have fiber spans with length $L < 80 \text{ km}$. If we use $P_o \approx 4 \text{ mW}$ which is typical for such configurations we have $L_{NL} \approx 125 \text{ km}$. In this case we can assume that non-linear phenomena do not play an important role in the propagation of light pulses. In comparison a linear phenomenon such as chromatic dispersion cannot be neglected for communications at speeds in excess of 10 Gb/s since we have in this case L_D less than 50 km . We will consequently focus our attention on linear models in the next section.

2.3 Fiber models in the linear regime

2.3.1 Introduction

In this section we introduce the optical transmission matrix describing a fiber piece linear input/output behavior using the linearized version of the field propagation equation presented in the previous section. We emphasize its structure, thus highlighting some assumptions that form the basis for the derivation of the original propagation equation as well.

The parameter dependence of the transmission matrix allows us to define important quantities used for describing polarization-related dispersive effects on the transmission of optical signals: the PMD vector and the differential group delay (DGD).

Whereas the general form of the transmission matrix could be applied to a variety of optical systems the actual parameter dependence of the transmission matrix can be further modelled in the case of optical fibers. Successful stochastic and distributed models have been proposed, the theoretical predictions of which are validated by experimental results. We report the main results regarding the statistics of PMD highlighting basic parameters characterizing the strength of the phenomenon and commonly used by fiber and fiber cable manufacturers.

That knowledge does not allow the derivation of a simple form for the transmission matrix though and further approximations have to be made to arrive at simple expressions suitable for modelling the transmission of narrowband optical signals used for the transmission of digital data using an on-off keying modulation format. These simple expressions when applied in their domain of validity are very useful for the implementation of efficient numerical simulations allowing the effective exploration of fiber dispersive effects on optical signals with the design of optical communication systems or subsystems in mind.

2.3.2 Fiber transmission matrix

As a preliminary comment, note the use of different names (A in Sec. 2.2.1 and B in Sec. 2.2.2) to represent the optical field. This provides the opportunity to clarify differences in notations one can find in the literature depending on whether the subject matter is optical fiber propagation equations or input/output relationship. Up to this point the propagation equations were not formulated using the optical field A since it can lead to confusion when comparing to expressions in the literature. One convention is widely used for representing

the electrical field when dealing with field propagation equations in optical fibers

$$\mathbf{E}(\vec{r}, t) = \text{Re} \left(F(x, y) B(z, t) e^{i\beta_0 z} e^{-i\omega_0 t} \right),$$

where we note that the carrier phase term is $-\omega_0 t$ at $z = 0$. The definition of the Fourier transform \hat{B} of B is chosen accordingly and we have $\hat{B}(z, \omega) = \int B(z, t) e^{+i\omega t} dt$ and reversely $B(z, t) = \frac{1}{2\pi} \int \hat{B}(z, \omega) e^{-i\omega t} d\omega$. Another convention is used for representing the electrical field when using a system approach to optical fiber effects

$$\mathbf{E}(\vec{r}, t) = \text{Re} \left(G(x, y) A(z, t) e^{-i\beta_0 z} e^{+i\omega_0 t} \right),$$

where the carrier phase term is $+\omega_0 t$ at $z = 0$ and the Fourier transform \tilde{A} of A is defined as $\tilde{A}(z, \omega) = \int A(z, t) e^{-i\omega t} dt$ and $A(z, t) = \frac{1}{2\pi} \int \tilde{A}(z, \omega) e^{+i\omega t} d\omega$. In the remainder of this document the latter convention will be used. To reconcile the two representations we note that they represent the same physical electrical field and that we can switch from one to the other by complex conjugation: $A(z, t) = B^*(z, t)$ in the time domain and $\tilde{A}(z, \omega) = \hat{B}^*(z, \omega)$ in the frequency domain.

The linear propagation equation including chromatic and birefringence effects can be written the following way using the optical field A

$$\frac{\partial \tilde{A}}{\partial z} + i \frac{1}{2} \vec{\beta} \cdot \vec{\sigma} \tilde{A} + i \bar{\beta} \tilde{A} + \frac{\alpha}{2} \tilde{A} = 0,$$

where the propagation coefficient $\bar{\beta}(\omega) = \beta(\omega) - \beta_0$ can be expanded around the center frequency, $\bar{\beta}(\omega) \approx \beta_1 \omega + \frac{1}{2} \beta_2 \omega^2$ and $\vec{\beta}(z, \omega)$ is the birefringence vector.

We can condense this equation by writing $\tilde{C} = \tilde{A} e^{\frac{\alpha}{2} z} e^{i\bar{\beta}(\omega) z}$,

$$\frac{\partial \tilde{C}}{\partial z} + i \vec{\beta} \cdot \vec{\sigma} \tilde{C} = 0.$$

Since we have a linear ordinary differential equation in z for \tilde{C} with initial condition $\tilde{A}(0, \omega) = \tilde{A}_{\text{in}}(\omega)$ for each ω we can write

$$\tilde{C}(z, \omega) = U(z, \omega) \tilde{C}(0, \omega),$$

where U is a function of z and ω that takes its values in the space of the 2x2 complex

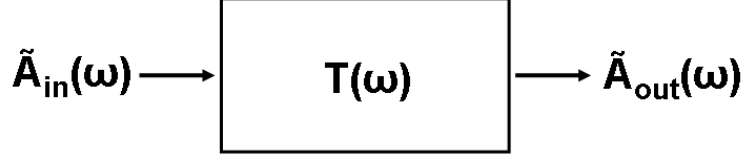


Figure 2.6: Fiber transmission matrix modelling the fiber input/output linear behavior.

matrices and satisfies

$$\begin{cases} U(0, \omega) = I_2 \\ \frac{\partial U}{\partial z} + i\frac{1}{2}\vec{\beta} \cdot \vec{\sigma} U = 0 \end{cases} \quad (2.9)$$

where I_2 is the 2x2 identity matrix. It directly stems from the fact that $\vec{\beta} \cdot \vec{\sigma}$ takes its values in the space of the 2x2 traceless Hermitian matrices that, for all z and ω , $U(z, \omega)$ is in $SU(2)$ as explained in Appendix A. The optical field A at any point in the fiber can be expressed as a function of the input

$$\tilde{A}(z, \omega) = e^{-\frac{\alpha}{2}z} e^{-i\vec{\beta}(\omega)z} U(z, \omega) \tilde{A}_{\text{in}}(\omega).$$

We consequently have a general expression for the *transmission matrix* T that relates the output of the fiber $\tilde{A}_{\text{out}}(\omega) = \tilde{A}(L, \omega)$ to its input $\tilde{A}_{\text{in}}(\omega) = \tilde{A}(0, \omega)$:

$$T(\omega) = e^{-\frac{\alpha}{2}L} e^{-i\vec{\beta}(\omega)L} U(L, \omega), \quad (2.10)$$

where L is the fiber length. From a system point of view the fiber is modelled as a black box with an optical input, an optical output and a linear relationship between those two quantities $\tilde{A}_{\text{out}}(\omega) = T(\omega)\tilde{A}_{\text{in}}(\omega)$ as illustrated in Fig. 2.6.

The transmission matrix T is the product of two terms:

$$T(\omega) = e^{-(\frac{\alpha}{2} + i\vec{\beta}(\omega))L} M(\omega), \quad (2.11)$$

where the first term, the common propagation term, is a complex function of ω and the second term $M(\omega) = U(L, \omega)$, the birefringence or Jones matrix, is a function of ω that takes its values in $SU(2)$. The transmission matrix T acts separately on the common complex amplitude and the SOP of the optical field. The common propagation term relates the

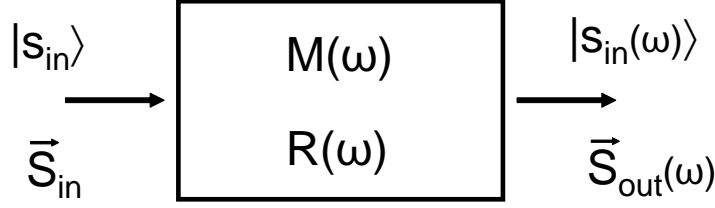


Figure 2.7: Illustration of the frequency dependence of the output SOP due to the frequency dependence of the input/output linear relationship.

input and output complex amplitudes and accounts for common group delay, chromatic dispersion and loss. The birefringence matrix M establishes the relationship between the input and the output SOP and accounts for a polarization-dependent group delay and chromatic dispersion. This can be further stated by writing $\tilde{A} = a|s\rangle$ as in Eq. 2.1 and expressing the input-output relationship for complex amplitude and SOP

$$a_{\text{out}} = e^{-(\frac{\alpha}{2} + i\tilde{\beta}(\omega))L} a_{\text{in}} \quad \text{and} \quad |s_{\text{out}}\rangle = M|s_{\text{in}}\rangle.$$

We have seen that the SOP can either be represented by a Jones vector or by a vector on the Poincaré sphere embedded in a three-dimensional real space called the Stokes space. As explained in Appendix A, the input-output SOP relationship can also be expressed in Stokes space

$$\vec{S}_{\text{out}}(\omega) = R(\omega)\vec{S}_{\text{in}},$$

where $R(\omega)$ is the rotation corresponding to the Jones matrix $M(\omega)$. It will be assumed in every case that the input optical field is completely polarized as can be produced by a laser source. The frequency dependence of M leads to a frequency dependent output SOP and depolarization of the light beam.

As noted earlier the action of the transmission matrix does not mix all the degrees of freedom. This comes from the fact that the local birefringence vector has only real components. A complex valued birefringence vector would mean that there exist in the system distributed sources of loss or gain that are sensitive to the light beam SOP. In real optical systems we can actually find sources of polarization-dependent loss (PDL) but they usually do not come from the fiber itself. Furthermore, they are generally generated by elements at the end the link (polarization beam splitters, optical amplifiers,...). So they can

be modelled by their own transmission matrix that could multiply the transmission matrix of the fiber to get a global model for the optical link.

The very general form for the transmission matrix shown in Eq. 2.11 could apply to the description of other linear optical systems. To really describe the fiber behavior we have to have an expression of the common propagation term and the Jones matrix as functions of the relative angular frequency ω :

- Common propagation term: The loss α is considered constant in the vicinity of the wavelength λ_0 of interest (see Sec. 2.1 for typical values) and the propagation coefficient can be approximated by $\bar{\beta}(\omega) \approx \beta_1\omega + \frac{1}{2}\beta_2\omega^2$ for the data rates considered in this document where β_1 and β_2 have been defined in Sec. 2.2.2.
- Birefringence matrix: In the case of an SMF, birefringence can be modelled as a white noise random process over the fiber length [FP91, SM00]. This turns Eq. 2.9 into a stochastic differential equation to be solved. The latter problem is not simple but further assumptions and approximations lead to expressions for the birefringence matrix that provide insight into the fiber polarization-dependent dispersion as well as numerical models for the implementation of efficient simulations.

2.3.3 Fiber PMD vector and Principal States of Polarization

The matrix $U(z, \omega)$ describes the birefringent behavior of a piece of fiber between 0 and z . The variable dependencies of U are completely summed up in two Stokes space vectors (see Appendix A): the local birefringence vector $\vec{\beta}$ we already encountered and the *PMD vector* $\vec{\tau}$.

The PMD vector is a notion of paramount importance in the study of the propagation of an optical signal in a birefringent medium. It is defined by the relationship

$$i\frac{\partial U}{\partial \omega}U^{-1} = \frac{1}{2}(\vec{\tau} \cdot \vec{\sigma}),$$

which is valid at every point z and frequency ω considered. As explained in [GK91], this definition of the PMD vector $\vec{\tau}$ corresponds to a Stokes space with an orientation given by the right-hand convention whereas the widely used PMD vector $\vec{\Omega}$ corresponds to the opposite orientation. We naturally define the *fiber output PMD vector* as $\vec{\tau}_{\text{out}}(\omega) = \vec{\tau}(L, \omega)$. Input-referred quantities are often useful and we define the *fiber input PMD vector*, $\vec{\tau}_{\text{in}} = R^{-1}\vec{\tau}_{\text{out}}$

(where $R(\omega)$ is the rotation matrix associated with $M(\omega) = U(L, \omega)$). The basic property of the PMD vector is that at any point in the fiber it relates the frequency derivative of the SOP to its value

$$\frac{\partial \vec{S}}{\partial \omega} = \vec{\tau} \times \vec{S}.$$

If the PMD vector is frequency independent this differential equation is readily solved and gives the evolution of the SOP with frequency. In this case it has a precession movement around the constant PMD vector when ω varies and the rate of rotation is given by the PMD vector length.

For each frequency ω there exists a pair of SOP's, the eigenstates of $M(\omega)$, that remain unchanged when transmitted through the optical fiber. There is also a pair of SOP's first pointed out by C. D. Poole and R. E. Wagner [PW86] that have interesting properties with regard to the the propagation of optical signals. We define them here from the PMD vector of the fiber $\vec{\tau}_{\text{out}}$

$$\vec{\tau}_{\text{out}} = \tau \vec{p} \quad \text{with} \quad \tau = |\vec{\tau}_{\text{out}}|,$$

where \vec{p} and $\vec{q} = -\vec{p}$ define two antipodal points on the Poincaré sphere, the (output) slow and fast *Principal States of Polarization* (PSP's). Their input-referred counterparts can also be defined, $\vec{p}_{\text{in}} = R^{-1}\vec{p}$ and $\vec{q}_{\text{in}} = R^{-1}\vec{q}$. The length of the fiber PMD vector $\tau = |\vec{\tau}_{\text{out}}| = |\vec{\tau}_{\text{in}}|$ is called the *Differential Group Delay* (DGD).

Considering The PSP values \vec{p}_0 and \vec{q}_0 at the center of the frequency band (frequency ω_0 ; relative frequency 0) and assuming that $\vec{S}_{\text{out}}(0)$ is equal to one of the PSP's we have

$$\frac{d\vec{S}_{\text{out}}}{d\omega}(0) = \vec{\tau}_{\text{out}}(0) \times \vec{S}_{\text{out}}(0) = \vec{0}.$$

That is to say the output SOP is constant to the first order in the vicinity of the center frequency if its value at the center of the frequency band is one of the PSP's. This property is a characteristic property of the PSP's. Since the input of the system is easier to control than its output (we can easily change the SOP of the polarized light beam at the input), it is of interest to express the property with input quantities

$$\frac{d\vec{S}_{\text{out}}}{d\omega}(0) = R(\vec{\tau}_{\text{in}}(0) \times \vec{S}_{\text{in}}),$$

and, for a nonvanishing PMD vector, we have that the output SOP, \vec{S}_{out} , is constant to the

first order at the center of the frequency band if and only if the input SOP, \vec{S}_{in} , is equal either to $\vec{p}_{\text{in}0}$ or to $\vec{q}_{\text{in}0}$, the value of the input PSP's at the center of the frequency band.

We now come to the central property of the PSP's when dealing with signal propagation in fibers (see Appendix D.1 for a proof). Let us imagine that we are sending a polarized light pulse into a fiber. We assume that its spectrum is centered at ω_0 . If we send it first with the SOP equal to $\vec{p}_{\text{in}0}$, its propagation time is $t_{\vec{p}}$ and it comes out of the fiber polarized around its value at ω_0 , that is to say \vec{p}_0 . If we now send the pulse with the SOP equal to $\vec{q}_{\text{in}0}$, its propagation time is $t_{\vec{q}}$ and it comes out of the fiber polarized around \vec{q}_0 . The fact that $t_{\vec{p}} > t_{\vec{q}}$ justifies the names slow and fast PSP. Furthermore the difference of propagation times $t_{\vec{p}} - t_{\vec{q}}$ is equal to τ , the DGD as illustrated in Fig. 2.8.

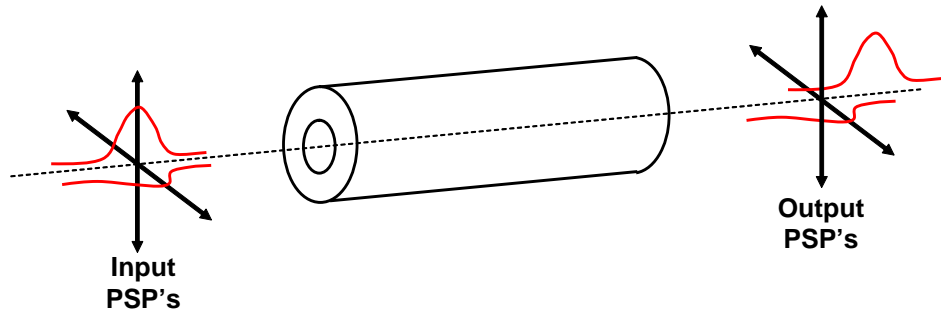


Figure 2.8: Principal States of Polarization.

This last property ultimately shows the importance of the notion of PMD vector when describing polarization-related effects on the transmission of optical signals through fibers. The DGD provides a measure of the impact of PMD in digital optical communication systems when compared to the symbol period.

2.3.4 Fiber Polarization-Mode Dispersion statistics

Modelling fiber birefringence as a random phenomenon accumulating over the fiber length leads to numerous fundamental results. Statistical properties related to PMD have been extensively studied both theoretically and experimentally [FP91, FJNK99, FNK00, NJKF00, JNK99]. This section summarizes the main results about the statistics of the PMD vector.

The basis of the theoretical derivation of the statistics of the PMD vector is the dynam-

X	$p_X(x)$	$E(X)$	$E(X^2)$
τ_i	$\frac{2}{\pi\bar{\tau}} e^{-\frac{1}{\pi}(\frac{2x}{\bar{\tau}})^2}$, Gaussian	0	$\frac{\pi}{8}\bar{\tau}^2 = \sigma^2$
$\tau = \vec{\tau} $	$\frac{8}{\pi^2\bar{\tau}} (\frac{2x}{\bar{\tau}})^2 e^{-\frac{1}{\pi}(\frac{2x}{\bar{\tau}})^2} \mathbf{1}_{x \geq 0}$, Maxwellian	$\bar{\tau}$	$\frac{3\pi}{8}\bar{\tau}^2 = 3\sigma^2$
τ'_i	$\frac{4}{\pi\bar{\tau}^2} \text{sech}(\frac{4x}{\bar{\tau}^2})$, soliton amplitude	0	$(\frac{\pi}{8})^2\bar{\tau}^4 = \sigma^4$
$ \vec{\tau}' $	$\frac{8}{\pi\bar{\tau}^2} \frac{4x}{\bar{\tau}^2} \tanh(\frac{4x}{\bar{\tau}^2}) \text{sech}(\frac{4x}{\bar{\tau}^2}) \mathbf{1}_{x \geq 0}$	$\frac{2G\bar{\tau}^2}{\pi}$ $G \approx 0.915965$	$3(\frac{\pi}{8})^2\bar{\tau}^4 = 3\sigma^4$
$\tau' = \frac{d}{d\omega} \vec{\tau} $	$\frac{2}{\bar{\tau}^2} \text{sech}^2(\frac{4x}{\bar{\tau}^2})$, soliton intensity	0	$\frac{1}{3}(\frac{\pi}{8})^2\bar{\tau}^4 = \frac{\sigma^4}{3}$

Table 2.1: Probability distributions of PMD-related quantities derived, validated in simulations and experiments in Ref. [FP91, FJNK99, FNK00].

ical PMD equation (see Appendix A) $\frac{\partial \vec{\tau}}{\partial z} = \frac{\partial \vec{\beta}}{\partial \omega} + \vec{\beta} \times \vec{\tau}$ that relates the local birefringence vector $\vec{\beta}$ to the PMD vector $\vec{\tau}$ along with a simple stochastic model for the evolution of the local birefringence vector $\vec{\beta}$ over the fiber length with a linear dependence with frequency. Although slightly different models have been proposed for the birefringence random process [FP91, SM00, WMZ97] they all lead to the same basic conclusion for fibers of realistic length. A complete analysis of this stochastic differential equation shows that the components of the PMD vector are independent Gaussian random variables as illustrated in Fig. 2.9, which implies a Maxwellian distribution for the DGD (Fig. 2.10). The frequency derivatives of the PMD vector are also of interest. If we write $\vec{\tau} = \tau \vec{p}$ we have $\vec{\tau}' = \tau' \vec{p} + \tau \vec{p}'$. The term τ' is called *Polarization-dependent Chromatic Dispersion (PCD)* which is consistent with the fact that this is a polarization dependent variation of the group delay experienced by optical pulses. \vec{p}' is the *rotation rate vector of the PSP's*. The components of $\vec{\tau}'$ have a soliton-amplitude probability distribution as shown in Fig. 2.11.

The probability distributions presented in table 2.1 are scaled by one common parameter, the *mean DGD* $\bar{\tau} = E(\tau)$. In the literature the term mean PMD seems to interchangeably designate the DGD rms value and the DGD mean value. These two values are almost equal (the ratio of the first to the second is $\sqrt{\frac{3\pi}{8}} \approx 1.08$). These two quantities can both serve as the basis for discussing the magnitude of the PMD phenomenon.

The fundamental result about the mean PMD coefficient states that, for a given type of fiber (resulting from a given manufacturing process and put under given field conditions),

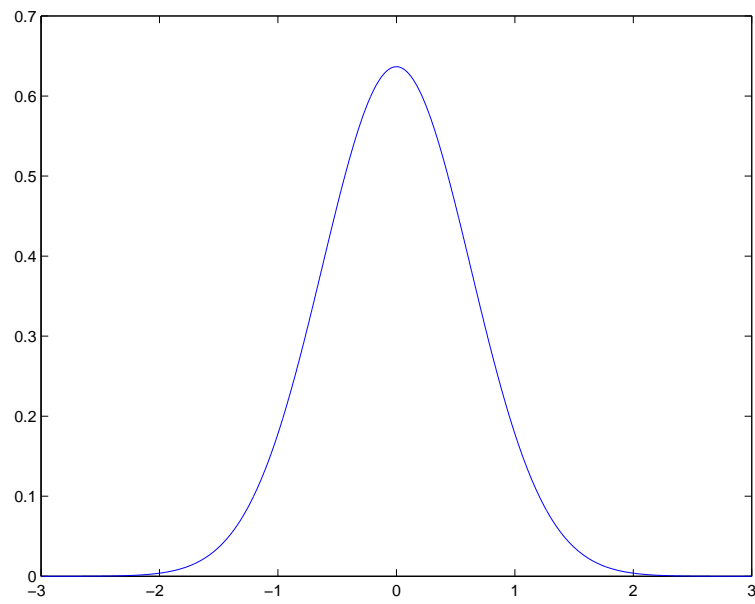


Figure 2.9: Gaussian distribution for each component of the PMD vector $\vec{\tau}$.

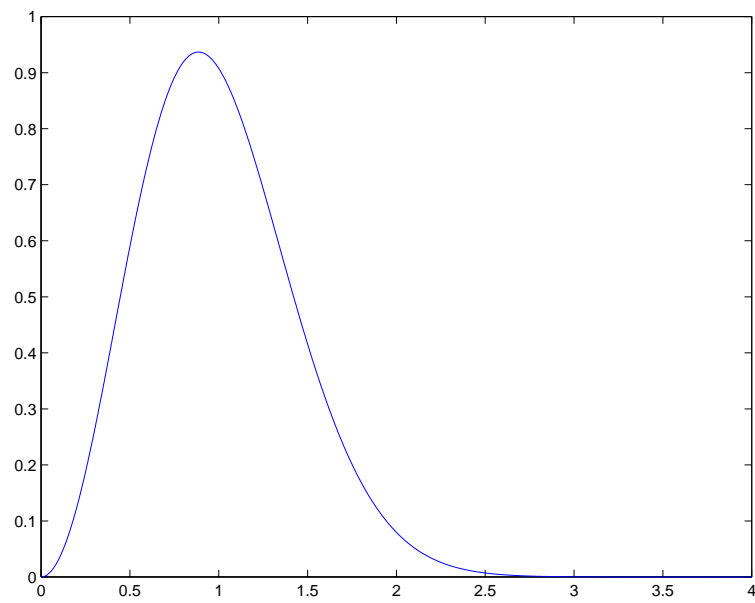


Figure 2.10: Maxwellian distribution for the DGD $|\vec{\tau}|$

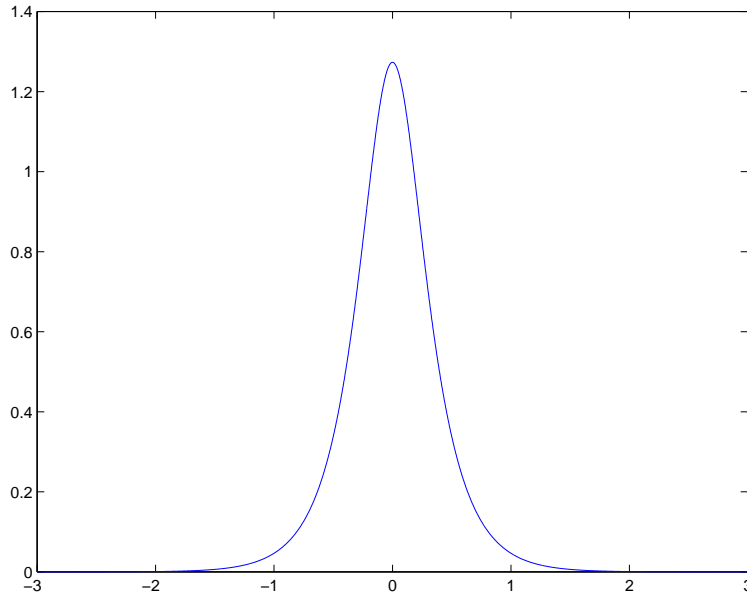


Figure 2.11: Soliton-amplitude distribution for each component of $\vec{\tau}'$

it is proportional to the square-root of the fiber length:

$$\sqrt{E(\vec{\tau}'^2)} = D_{pmd}\sqrt{L}$$

and the coefficient D_{pmd} expressed in $\text{ps}/\sqrt{\text{km}}$ alone summarizes the PMD behavior of a homogenous population of fibers or of a given fiber over time under stationary conditions. In 2000, companies were announcing new fibers with a PMD coefficient under $0.1 \text{ ps}/\sqrt{\text{km}}$. But several studies reported that the majority of the installed SMF fibers in metropolitan networks exhibit a PMD coefficient around $1 \text{ ps}/\sqrt{\text{km}}$. The PMD coefficient of some “pathological” fibers can even lie beyond $5 \text{ ps}/\sqrt{\text{km}}$ [Nel01, PDK97].

It is commonly assumed that field operating conditions are stationary for fibers and that the processes that describe the time evolution of the PMD vector are ergodic. Under these assumptions, the statistical results presented here can serve the computation of outage probabilities, the probability of DGD exceeding a fixed limit defining good system operating conditions, the probability that system performance penalty due to PMD exceeds a given level [Shi00], etc.

For input pulses of width T_0 the characteristic fiber length over which PMD accumulates

significantly is

$$L_{PMD} = \frac{T_0^2}{(D_{pmd})^2}.$$

This can be compared to the chromatic dispersion typical length: $L_D = T_0^2/|\beta_2|$.

2.3.5 A simple transmission matrix for fibers with PMD

In this section, simple models for the transmission matrix of an SMF,

$$T(\omega) = e^{-(\frac{\alpha}{2} + i\bar{\beta}(\omega))L} M(\omega),$$

and more specifically for the Jones matrix, M , are presented.

From a signal transmission standpoint, the transmission matrix frequency dependence is of most interest. As explained in Appendix A, it is consequently natural to derive its form from the PMD vector through the relationship

$$i \frac{dM}{d\omega} = \frac{1}{2} (\vec{\tau} \cdot \vec{\sigma}) M. \quad (2.12)$$

Eq. 2.12 does not in general allow itself to be integrated into an elementary function if the variations of $\vec{\tau}$ are complex. In the case of a randomly birefringent SMF used for the transmission of a bandpass signal at a given optical carrier wavelength, the model can be simplified by considering only the vicinity of the central frequency having a width on the order of the narrowband signal bandwidth of interest. Under these conditions the PMD vector is assumed to be well approximated by a truncation of its Taylor expansion around the carrier frequency ($\omega = 0$). The literature designates as an order- $(m+1)$ model, a Jones matrix model resulting from the truncation of the PMD vector Taylor expansion in ω up to the m^{th} order. In the remainder of this section, the subscript 0 will designate the value at $\omega = 0$ of frequency-dependent quantities.

Order 1. In this case the PMD vector is assumed to be approximated by a constant over the frequency band: $\vec{\tau} \approx \vec{\tau}_0$. The differential equation (2.12) can then easily be solved:

$$M(\omega) = e^{-i\omega\vec{\tau}_0 \cdot \frac{\vec{\sigma}}{2}} = P_1 \begin{pmatrix} e^{-i\frac{\tau_0}{2}\omega} & 0 \\ 0 & e^{+i\frac{\tau_0}{2}\omega} \end{pmatrix} P_2,$$

where $\tau_0 = |\vec{\tau}_0|$ is the DGD. P_1 and P_2 are two frequency independent $SU(2)$ matrices relating the laboratory reference frames at the input and output of the fiber to the position the PSP's orthonormal basis. The statistics of the DGD τ_0 is that of a Maxwellian variable determined by the PMD coefficient and the fiber length as explained in Sec. 2.3.4.

The example of a HiBi (also called polarization-maintaining) fiber given at the end of Appendix A leads to the same expression for the Jones matrix. The difference in the two models lies in the properties of the PMD vector. In the case of a HiBi fiber the PMD vector is non-random, determined and fixed by clear fiber geometrical or physical design properties and scales linearly with the fiber length.

Order 2. We now use the following approximation of the PMD vector over the frequency band: $\vec{\tau} \approx \vec{\tau}_0 + \vec{\tau}'_0 \omega$. We distinguish several quantities coming from the PMD vector and its first derivative at the center of the frequency band

$$\begin{aligned}\vec{\tau}_0 &= \tau_0 \vec{p}_0, \\ \vec{\tau}'_0 &= \tau'_0 \vec{p}_0 + \tau_0 \vec{p}'_0,\end{aligned}$$

where prime designates derivation relative to ω , τ is the Differential Group Delay (DGD) and \vec{p} is the slow PSP. The derivatives of the latter quantities are τ' the *polarization-dependent chromatic dispersion* (PCD) coefficient and \vec{p}' the *PSP rotation rate vector*.

The integration of the differential equation is not as easy this time. [FV01] proposes a consistent approximation in this case and reviews other popular “order-2” models for the Jones matrix M . In particular the following has been proposed in [KNGJ00, FBPC00]

$$M = P_1 Q D Q^{-1} P_2,$$

where P_1 and P_2 are frequency independent $SU(2)$ matrices and

$$\begin{aligned}Q(\omega) &= e^{-ik\omega\sigma_3} = \begin{pmatrix} \cos(k\omega) & -\sin(k\omega) \\ \sin(k\omega) & \cos(k\omega) \end{pmatrix} \quad \text{with} \quad k = \frac{1}{4} |\vec{p}'_0|, \\ D(\omega) &= e^{-i\frac{\phi(\omega)}{2}\sigma_1} = \begin{pmatrix} e^{-i\frac{\phi(\omega)}{2}} & 0 \\ 0 & e^{i\frac{\phi(\omega)}{2}} \end{pmatrix} \quad \text{with} \quad \phi(\omega) = \tau_0\omega + \frac{1}{2}\tau'_0\omega^2.\end{aligned}$$

Some predictions of the models In most digital optical communication systems information is encoded in light pulses. They are referred to as on-off keying (OOK) intensity modulation/direct detection (IM/DD) systems. Consequently the transmission quality depends on the fact that those pulses remain undistorted after propagation. Generally speaking, fiber dispersion and PMD result in pulse broadening and inter-symbol interference (ISI) which translates into digital eye closure and an increased bit error rate for a given launch power. Depending on the fiber PMD characteristics and the optical signal bandwidth the electrical eye diagram undergoes different types of degradation.

The light signal $A_{\text{in}}(t) = a_{\text{in}}(t)|s_{\text{in}}\rangle$ is sent through the fiber link and becomes $A_{\text{out}}(t) = a_{\text{out}}(t)|s_{\text{out}}\rangle$ at the output. Without any loss of generality, it is assumed that the laboratory input and output reference frames are aligned with the PSP's at the center of the frequency band ($P_1 = P_2 = I_2$). Loss (α) and common group delay (β_1) are not taken into account in this discussion since neither of them translates into an alteration of the signal shape. The former introduces an amplitude scaling and the latter a fixed propagation delay. Consequently, in this section all figures representing signal waveforms make use of $T = t - \beta_1 z$ ($T = t$ at the fiber input and $T = t - \beta_1 L$ at the fiber output) as the time variable and the same vertical power scale for input and output pulses (actual output power can be obtained by applying an $e^{-\alpha L}$ factor).

Order-1 model effects At the output, the optical signal is given by $\tilde{A}_{\text{out}} = e^{-i\beta_1 L \omega} \tilde{a}_{\text{out}} M |s_{\text{in}}\rangle$ with $\tilde{a}_{\text{out}} = e^{-i(\bar{\beta} - \beta_1 \omega)L} \tilde{a}_{\text{in}}$ and $M(\omega) = \begin{pmatrix} e^{-i\frac{\tau_0}{2}\omega} & 0 \\ 0 & e^{+i\frac{\tau_0}{2}\omega} \end{pmatrix}$.

If we write $|s_{\text{in}}\rangle = \begin{pmatrix} \cos(\theta/2) \\ \sin(\theta/2)e^{i\Delta} \end{pmatrix}$ then $A_{\text{out}}(t) = \begin{pmatrix} a_{\text{out}}(T - \tau_0/2) \cos(\theta/2) \\ a_{\text{out}}(T + \tau_0/2) \sin(\theta/2)e^{i\Delta} \end{pmatrix}$. The electrical signal $m(t)$ generated by an ideal photoconverter can be written

$$m(t) \propto \gamma s(t) + (1 - \gamma)s(t - \tau_0),$$

where $\gamma = \sin^2(\theta/2) = (1 - \vec{S}_{\text{in}} \cdot \vec{q})/2$ quantifies the position of the input SOP relative to the fiber fast PSP and $s(t) = |a_{\text{out}}(T - \tau_0/2)|^2$ with $T = t - \beta_1 L$.

If the input SOP is not aligned with one of the PSP's (γ different from 0 and 1), the output signal is the superposition of two replicae of the same signal shifted in time by an amount equal to the DGD. The optical signal is the combination of its projected components on the signal space associated with each PSP. These components travel through the fiber

at different speeds and arrive at the fiber output separated by a delay equal to the DGD. In particular if the input SOP is aligned with one of the input PSP's, pulse distortions resulting from PMD are minimized

This result suggests that the signal can be equalized at the output of the transmission system using well known simple inter-symbol interference (ISI) reduction technique. Depending on the values of r and the DGD the system undergoes different levels of eye closure. With changes in the fiber environment (temperature, vibrations related to human activity,...) r and τ incur unpredictable variations suggesting that equalization techniques need be adaptive.

Order-2 model effects This time $\tilde{A}_{\text{out}} = e^{-i\beta_1 L \omega} \tilde{a}_{\text{out}} M |s_{\text{in}}\rangle$ with $\tilde{a}_{\text{out}} = e^{-i(\bar{\beta} - \beta_1 \omega)L} \tilde{a}_{\text{in}}$, $M = QDQ^{-1}$ and the matrices Q and D are as described on page 32.

Using results presented in [FBPC00] and making the additional assumption that $k \ll \tau_0$ we can get insight in some effects predicted by this “order-2” model for the Jones matrix in the case where the input SOP is aligned with one of the PSP's (fast input PSP here for instance). The “order-1” model was predicting that PMD would not create any signal distortion in this configuration. But in the present case the received electrical signal $m(t)$ can be written

$$m(t) \propto |a_{\text{out}}^+(T^+)|^2 + 16k^2 |\dot{a}_{\text{out}}^-(T^-) - \dot{a}_{\text{out}}^+(T^+)|^2,$$

where $T^+ = T + \tau_0/2$ and $T^- = T - \tau_0/2$. The dot notation represents a time derivative of the corresponding function of time. a_{out}^+ and a_{out}^- denote two forms of the output complex amplitude after having undergone the effect of total GVD $\beta_2 L$ augmented by $\tau_0'/2$ and reduced by $\tau_0'/2$ respectively (explaining the denomination polarization-dependent chromatic dispersion). If we had assumed a launch on the slow PSP the result would be identical except for the swapping of the + and - symbols in the above expression. The first term is the result of the propagation of the pulse according to the fast PSP mode. The second term is the expression of the power that leaked from the fast PSP to the slow one because of their coupling. The presence of the signal time derivatives in the expression of the latter suggests that leakage is bigger at high frequencies or at the edges of a pulse in the time domain as illustrated in Fig. 2.12.

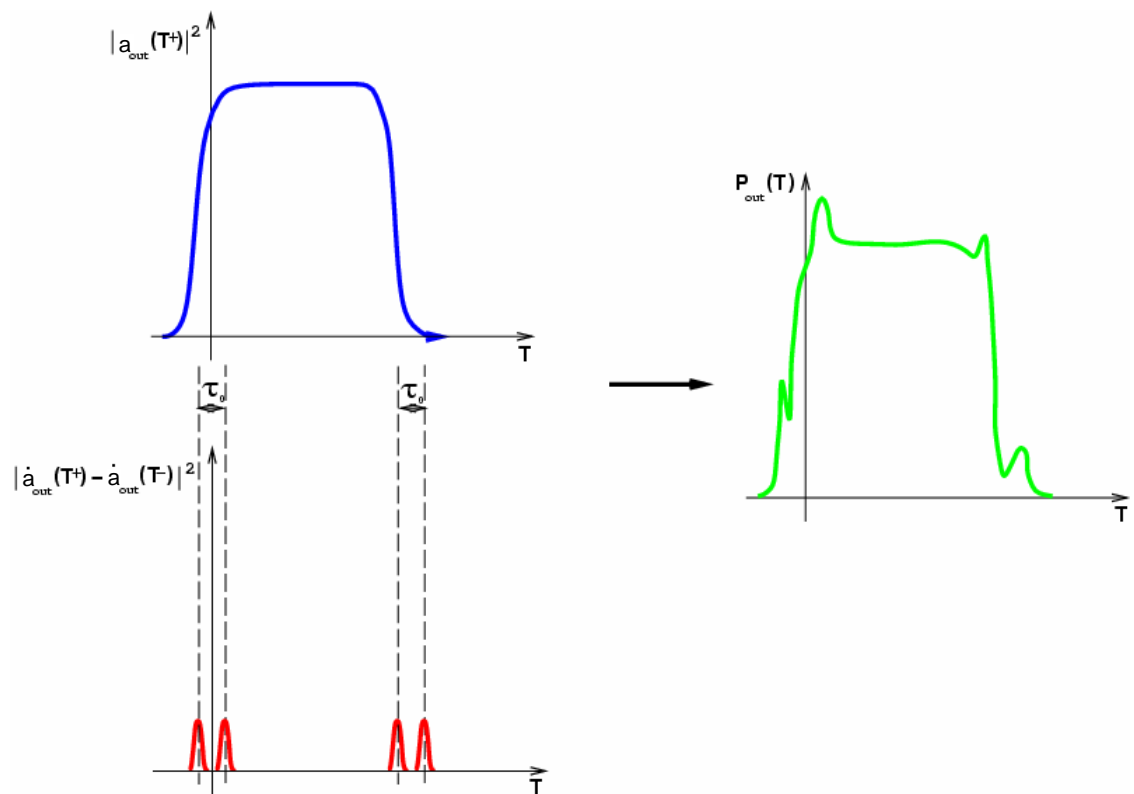


Figure 2.12: Illustration of higher-order PMD effects in fast-PSP pulse launch condition.

2.3.6 Numerical implementation of a simple fiber transmission matrix

Several photonic simulation software packages include a model for an SMF fiber. They seem to be exclusively based on a numerical solution of the CNLS equation by the split-step Fourier method and a pseudo-random scrambling of the SOP of the light beam after each step. Those numerical models form the basis for the simulation of the propagation of optical signals even in non-linear regimes. Each simulation step requires going into the Fourier domain (computation of an FFT of the discretized signal), applying Fourier domain incremental operators as determined by the linear part of the propagation equation, and going back into the time domain (computation of an inverse-FFT) to compute the incremental contribution of fiber nonlinearities determined by the nonlinear part of the propagation equation.

In the linear regime, the simplified input-output models described in the previous section should be preferred. They are not based on the numerical integration of a partial differential equation (PDE) but on an approximation of the transfer matrix of the system. Optical fiber transmission computation steps are as follows:

1. Compute the FFT on the appropriately discretized version of the optical field, A_{in} , at the fiber input,
2. Apply the transfer matrix at each discrete frequency value,
3. Compute the inverse-FFT of the result to get the discretized version of the optical field, A_{out} , at the fiber output.

For a 10 Gb/s input signal, simulation time is on the order of a few minutes when the numerical integration of the CNLS equation requires more than an hour and depends on the simulated fiber length.

But there is another advantage in the system input-output approach. In the numerical solution of the stochastic PDE, the random phenomenon is simulated by the scrambling of the SOP of light through pseudo-random numbers generation. It is not possible to set the DGD value and PSP's that the system will finally exhibit when the simulation ends. In the transfer matrix model we know the statistics of quantities such as the DGD and we can choose their value according to their statistical distribution before launching a simulation by using known methods for the numerical generation of random variables. It is also easy to set the input polarization to explore worst case scenarii.

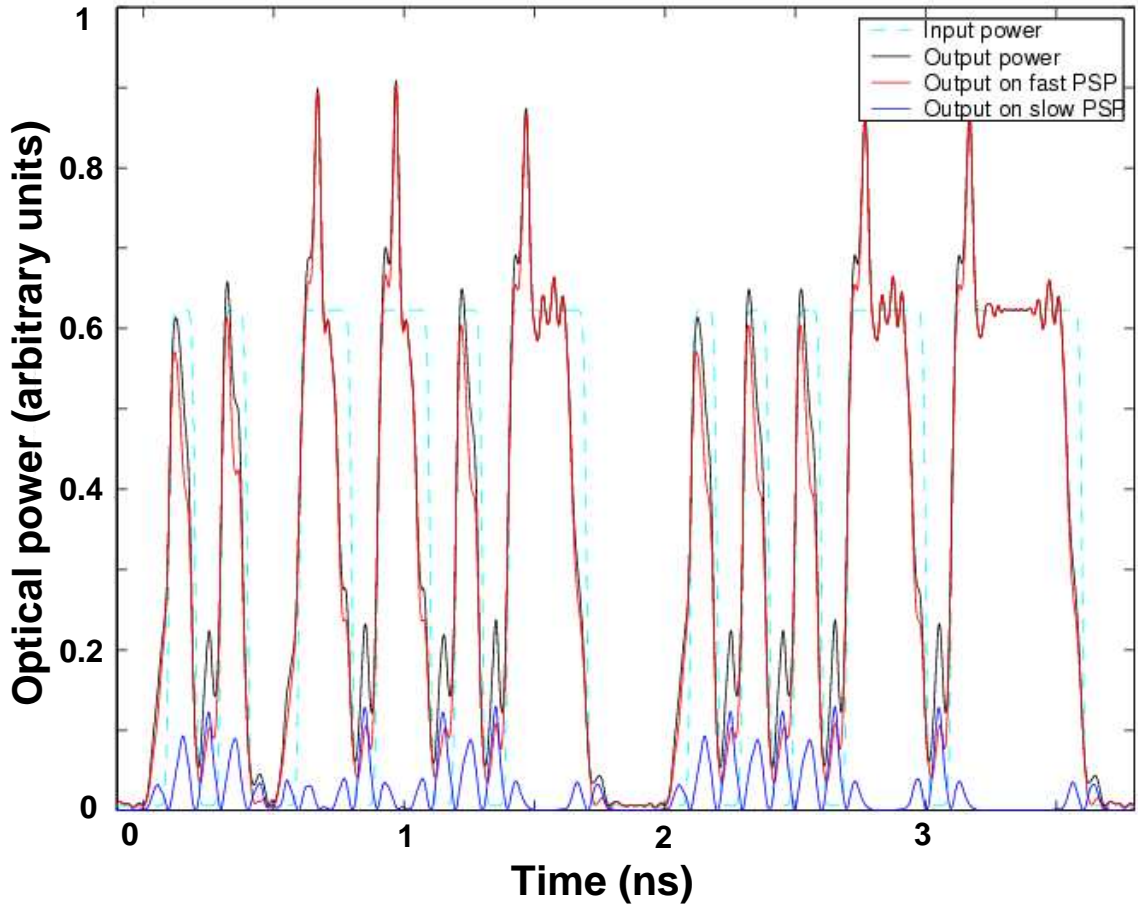


Figure 2.13: Optical signal waveforms for an NRZ modulation signal when the input SOP is aligned with the input fast PSP. $D_b = 1/T_0 = 10 \text{ Gb} \cdot \text{s}^{-1}$, $\tau/T_0 = 0.6$, $q_w/T_0 = 0.75$ and $\tau'/T_0^2 = 1$. The input waveform is represented in light blue dashed line, output optical power on the fast PSP in red, output optical power on the slow PSP in blue and total output power in black.

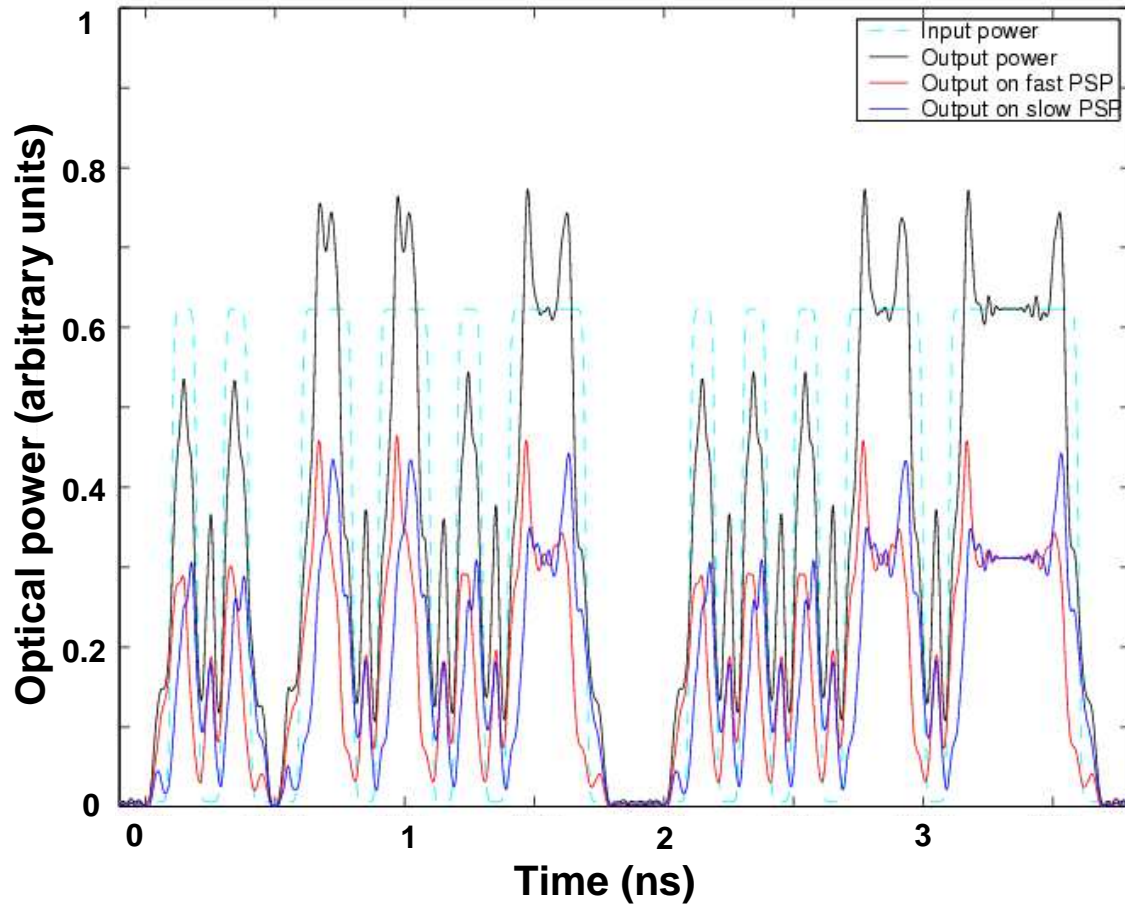


Figure 2.14: Optical signal waveforms for an NRZ modulation signal when the input SOP is such that equal power is launched in each PSP. $D_b = 1/T_0 = 10 \text{ Gb} \cdot \text{s}^{-1}$, $\tau/T_0 = 0.6$, $q_w/T_0 = 0.75$ and $\tau'/T_0^2 = 1$. The input waveform is represented in light blue dashed line, output optical power on the fast PSP in red, output optical power on the slow PSP in blue and total output power in black.

In the results we present we also took great care in the modelling of other optical elements. We chose to model a laboratory setup based on the external modulation scheme using a continuous-wave laser model and a balanced (no chirp) LiNbO₃-based external modulator. All diagrams show the optical signal power that would be measured by a high bandwidth photoreceiver (no receiver filtering applied). The length L of the link has been chosen equal to 80 km, the GVD $\beta_2 = -16 \text{ ps}^2\text{km}^{-1}$, the DGD $\tau_0 = 60 \text{ ps}$ which is a probable value if the mean DGD is equal to 20 ps since $\mathbb{P}(|\bar{\tau}| > 3\bar{\tau}) \approx 4.2 \cdot 10^{-5}$. If the ergodic assumption holds true over a year time period (which can be criticized), that is to say ensemble averages can be taken as time averages over a year, this value would be exceeded for approximately 22 min per year. This value of 20 ps would correspond to a “pathological” fiber with $D_{\text{pmd}} \approx 2.2 \text{ ps}/\sqrt{\text{km}}$. The bit rate has been set to a value of $D_b = 1/T_0 = 10 \text{ Gb/s}$ and the OOK format is NRZ. Using the order-2 model presented in Sec. 2.3.5 we chose dramatically high values, $0.75T_0$ and T_0^2 , for the parameters $q_w = 4k$ and τ' in this example to highlight patterns appearing when a high level of order-2 PMD is present. In Fig. 2.13 we chose to send the entire optical power on the fast PSP of the link. The input optical power is represented with a light-blue dotted line, the total output power is in black. We separated the contribution coming out of each PSP mode: from the fast PSP in red and from the slow PSP in blue. If there were no coupling between the two modes no power should come out of the slow PSP mode. Furthermore some of the features of the waveform, such as the location of the power leakage on the edges of the “ones”, are qualitatively the same as shown on Fig. 2.12. Figure 2.14 displays the result of a simulation where equal signal power was sent on each PSP. The shift in time of the signal coming out of each polarization mode is visible. Those results were compared to the waveforms obtained using a commercial photonic-simulation software and good qualitative agreement was found.

2.4 Discussion

This chapter presented models for single mode fibers in the linear optical regime emphasizing on the description of linear dispersive effects: chromatic dispersion and polarization mode dispersion. While they both induce light pulse broadening they are quite different in nature. While their effects increase in a similar fashion with signal bandwidth the former is deterministic and dependent upon the operating wavelength and the other stochastic with

wide fiber link and time variations. Appendix D delves into the impact of fiber dispersion on OOK optical communication systems and presents electronic and optical signal processing techniques for dispersion compensation.

The present study focuses on electrical modulation schemes other than OOK in the case of short fiber links. The effects on transmitted signals will have to be revisited in the context of new modulations. Whenever the linear optical regime assumption holds, the models introduced in this chapter will be used as well as its computationally efficient numerical implementation.

Chapter 3

Bandwidth Efficient Modulation

This chapter presents sub-carrier multiplexing (SCM) modulation in the electrical domain as a bandwidth efficient modulation with numerous advantages over OOK in the design and actual implementation of a high-speed communication system where bandwidth comes at a premium and optical power is not a limiting factor.

The signaling rate in SCM can be lowered to a level where current cost-effective mixed-signal and digital circuit technology can operate and be effectively implemented (analog-to-digital conversion being a critical functional sub-block). Novel digital signal processing techniques are presented that make possible the loosening of design specifications in areas where the implementation of SCM at high frequencies presents serious challenges (frequency offset, I/Q gain and phase mismatch, baseband and RF filtering).

3.1 Introduction

Numerous wireless and copper wireline communication systems have benefited from advances in digital signal processing (DSP). However optical communication is still widely based on simple on-off keying that makes the use of DSP techniques very challenging at rates in excess of 10 Gb/s. These speeds often require exotic technologies. Bandwidth-efficient modulation formats make possible the use of standard technologies by reducing the required electrical signal bandwidth and dealing with digital symbols at a lower rate. This makes possible the use of advanced DSP bringing numerous benefits in terms of reliability, flexibility and system implementation.

3.1.1 Multilevel signaling and intensity modulation

The basic trade-off that takes place when choosing a modulation format for digital communications is explained in [BB99]:

(...) the choice of a digital modulation scheme aims at the best trade-off among error probability, bandwidth efficiency, power efficiency, and complexity.

In particular, increasing the modulation set size trades power efficiency for bandwidth efficiency if power per transmitted bit can be increased without adverse effects. The complexity metric is somewhat more difficult to evaluate but directly impacts system implementation cost.

For high speed short distance communication where cost is critical, bandwidth comes at a big premium since it is directly tied to the limits of the basic technology being used, be it for electrical (CMOS, GaAs semiconductor technologies) or optical components (directly modulated lasers, LiNbO₃ modulators).

Advances have been made in the field of bandwidth efficient optical modulation aiming at mitigating the effect of optical impairments which scale with bandwidth and at increasing operating distance with fewer signal regeneration sections in long-haul applications [WE03]. Reduction of system cost in long-haul systems when using such optical modulations offsets the additional complexity and cost of the optical transmitter and receiver. For short distance applications (backplane, LAN, MAN), cost of the transceiver is dominant. This is why the simplicity of intensity modulation and direct detection makes it still a very attractive solution in that space. Bandwidth efficiency can still be achieved in the electrical domain in that case by the use of multilevel signaling instead of on-off keying. Signal processing is further facilitated by partitioning the available bandwidth into independent sub-channels transporting synchronized digital symbols in parallel at a manageable signaling rate.

3.1.2 Overview

Fig. 3.1 shows the comparative bandwidth occupation of NRZ and QAM-16 over 16 carriers both achieving data transmission at 40 Gb/s. In the multi-carrier modulation format carriers have been pushed very close to each other in order to fit in a 14 GHz bandwidth determined from the capabilities of low-cost available optical components. The latter modulation format is often referred to as *subcarrier multiplexing* (SCM) the advantages and drawbacks of which are presented in a first section.

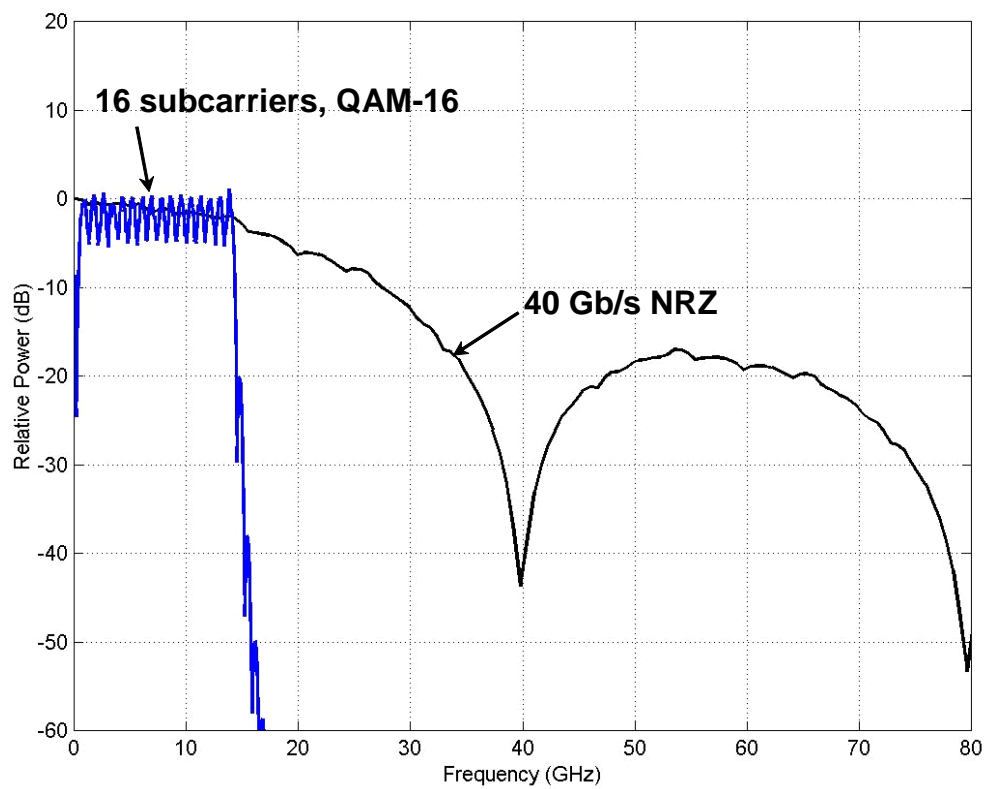


Figure 3.1: Comparison of the power spectra of NRZ and QAM-16 over 16 carriers for a 40 Gb/s throughput.

One of the main limitations of multi-carrier modulation in achieving high spectral efficiency comes from the spacing of microwave channels. Bringing them close to each other causes linear crosstalk between channels which results in bit error rate (BER) degradation when using conventional detection schemes. Nonetheless new DSP techniques and architectures of reasonable complexity presented in a second section are capable of cancelling most detrimental effects as well as greatly relax constraints put on the RF circuit implementation of the modulator/demodulator.

3.2 Sub-carrier multiplexing

Digital subcarrier multiplexing consists of multiplexing independently modulated frequency carriers. Each frequency carrier is modulated by digital symbols taken from a finite set of complex numbers.

3.2.1 Advantages and drawbacks

Advantages and drawbacks of SCM compared to plain NRZ OOK are reviewed hereafter. The SCM signal is supposed to be composed of K carriers each modulated with the same symbol set \mathcal{C} composed of $M = 2^h$ symbols.

- **Spectral efficiency**

Since cost and technology limit the available bandwidth, this is the most important modulation “dimension” to improve. For a given baseband pulse shape the signal power spectrum width scales linearly with $1/\log_2(M)$. The bigger the signal set the better the spectral efficiency. If a brick-wall Nyquist pulse shape is assumed, for pulse amplitude modulation with Q levels (PAM- Q) bandwidth efficiency is proportional to $2 \log_2(Q)$ and for QAM- M it is proportional to $\log_2(M)$.

- **Signaling rate**

In the case of NRZ OOK, the signaling rate (symbol rate) is equal to the source bit rate $R_S = R_b$. In the case of SCM with K carriers and a symbol set of size M the symbol rate becomes

$$R_S = \frac{R_b}{K \log_2(M)}. \quad (3.1)$$

It appears that increasing the number of carriers K is an efficient way to reduce the signaling rate.

- **Scalability**

In the case of SCM all K channels can be loaded independently making traffic segmentation and upgrading easier when the link is put in the context of a bigger transport or multi-service network.

- **Peak-to-average ratio**

The peak to average ratio of a signal $s(t)$ is defined as the ratio of the absolute peak value it can take to its root-mean-square value when these quantities are defined. More precisely, in the context of digital communications $s(t)$ is a cyclostationary signal of period T with zero mean and the peak to average ratio of s is given by

$$\text{PAR} = \sqrt{\frac{\max(|s|^2)}{\langle |s|^2 \rangle}},$$

where \max denotes the maximum and $\langle \bullet \rangle$ the average over all signal parameters including time.

The NRZ signal can be written

$$s(t) = \sum_n s_n p(t - nT_b),$$

where $p(t)$ is the baseband pulse shaping filter, (s_n) is a sequence of independent identically distributed (i.i.d.) symbols taken from $\mathcal{C} = \{-1, +1\}$ with equiprobable symbol values. Its PAR is equal to 1. The QAM-M SCM signal can be written

$$s(t) = \sum_n p(t - nT_S) \sum_{k=0}^{K-1} (a_{n,k} \cos(\omega_k t + \phi_k) - b_{n,k} \sin(\omega_k t + \phi_k)),$$

where T_S is the symbol period, $p(t)$ is the baseband pulse shaping filter, $(s_{n,k})_n = (a_{n,k} + ib_{n,k})_n$ are K i.i.d sequences of i.i.d symbols taken from the set $\mathcal{C} = \{a + ib; a, b \in \{-(Q-1), \dots, -1, +1, \dots, +(Q-1)\}\}$ formed of $M = Q^2$ symbols and the terms ϕ_k are undetermined phases. The peak-to-average energy ratio PAR^2 of the QAM-M SCM system is given by

$$\text{PAR}^2 = 2K3 \frac{\sqrt{M} - 1}{\sqrt{M} + 1}.$$

The factor K comes from the incoherent addition of the K carriers, 2 comes from

Modulation	PAR
NRZ	1
4 QAM-4	2.8
16 QAM-4	5.7
16 QAM-16	7.6
16 QAM-M ($M \gg 1$)	9.9

Table 3.1: Peak-to-average ratio of different SCM schemes compared to NRZ.

the two dimensions of the signal set, and $3\frac{\sqrt{M}-1}{\sqrt{M+1}}$ is the peak-to-average energy ratio of one dimension of the QAM-M symbol set. The number of carriers appears to be the main contributor in the increase of the peak-to-average ratio. In comparison the contribution to the PAR coming from the signal set size saturates for large M to reach a value of $\sqrt{3}$ from a minimum value of 1 when $M=4$.

Table 3.1 shows the peak-to-average ratio for different SCM configurations (number of carriers, constellation size) compared to that of simple OOK NRZ. Later chapters will show that system component technologies (e.g., semiconductor technology maximum voltage level, laser clipping) and basic operation can put hard constraints on the signal peak ($\max(|s|^2)$ term) whereas the system performance when only Gaussian noise is assumed to be present is determined by the signal mean square ($\langle |s|^2 \rangle$ term). So it is of very practical importance to keep this number as low as possible.

- **Signal-to-noise ratio**

In this dissertation the signal to noise ratio (SNR) is defined as the ratio of the signal variance to the noise variance before the system decision stage. The probability of bit error for NRZ is given by

$$p = \frac{1}{2} \operatorname{erfc} \left(\sqrt{\frac{\operatorname{SNR}_{\text{NRZ}}}{2}} \right), \quad (3.2)$$

where erfc is the complementary error function and $\operatorname{SNR}_{\text{NRZ}}$ denotes the signal-to-noise ratio of the NRZ signal. For adequate bit to symbol mapping and small probability of symbol error the probability of bit error for QAM-M for large M is given

BER	SNR _{NRZ} (dB)	SNR _{QAM-16} (dB)
10 ⁻³	9.8	17.6
10 ⁻⁴	11.4	19.0
10 ⁻⁵	12.6	20.1
10 ⁻⁶	13.5	20.9
10 ⁻⁷	14.3	21.6
10 ⁻⁸	15.0	22.3
10 ⁻⁹	15.6	22.8
10 ⁻¹⁰	16.1	23.3
10 ⁻¹¹	16.5	23.7
10 ⁻¹²	16.9	24.1
10 ⁻¹³	17.3	24.5
10 ⁻¹⁴	17.7	24.8
10 ⁻¹⁵	18.0	25.1

Table 3.2: Numerical values of SNR_{NRZ} and SNR_{QAM-16} for different values of the BER.

by

$$p \approx 2 \operatorname{erfc} \left(\sqrt{\frac{3}{M-1} \frac{\operatorname{SNR}_{\text{QAM-M}}}{2}} \right). \quad (3.3)$$

Values of SNR_{NRZ} given by Eq. 3.2 and SNR_{QAM-16} given by a slightly better approximation than Eq. 3.3 obtained by replacing the asymptotic factor 2 for large M by a factor 3/2 when $M = 16$ are listed in Table 3.2 for some commonly used BER values.

Assuming constant noise power spectral density in the QAM- M over K carriers scheme, the SNR per channel SNR_{QAM-M} is equal to the SCM signal signal-to-noise ratio, SNR_{SCM}. For a given target probability of error, the required SNR increases with the number of symbols in the symbol set. This translates into increased required signal power for fixed noise power. Yet since the system bandwidth is smaller when M increases the bandwidth in which noise is integrated is smaller. This means that for a given signal power level, the SCM system experiences a $\log_2(M)$ signal-to-noise ratio enhancement factor despite the $3/(M-1)$ degradation factor.

Similarly, channel impairments other than noise have a bigger impact on an SCM system performance than NRZ but in general their magnitude diminishes significantly with a reduced system bandwidth. In addition some bandwidth efficiency can be traded for relaxed

SNR requirements by using well known forward-error correction techniques [AHS⁺02].

3.2.2 Modulation parameters

Squeezing 40 Gb/s (with 7% overhead for forward-error correction) in less than 14 GHz is the target we set. This requires a modulation with bandwidth efficiency equal to 2.9 bit/s/Hz. The smallest (to minimize the SNR requirements) QAM symbol set permitting this is QAM-16. The number of radio-frequency (RF) carriers needs to be high enough to bring the signaling rate in the vicinity of 500 MHz. The choice of 16 carriers defines a signaling rate of 666 MHz. With these parameters the signal peak-to-average ratio is 7.6.

Channel	Frequency (GHz)
F_1	0.83
F_2	1.67
F_3	2.5
F_4	3.33
F_5	4.17
F_6	5.0
F_7	5.83
F_8	6.67
F_9	7.5
F_{10}	8.33
F_{11}	9.17
F_{12}	10.0
F_{13}	10.83
F_{14}	11.67
F_{15}	12.50
F_{16}	13.33

Table 3.3: 16 QAM-16 SCM RF carrier frequency map.

Implementation issues as discussed in Chapter 5 and early high-level simulations brought the focus on the regular carrier frequency map presented in table 3.3 where carriers are regularly spaced at multiples of 833 MHz. This brings the carrier channels fairly close to each other thus aiming at the ideal bandwidth efficiency provided by the modulation. Yet this leads to inter-channel cross-talk when taking into account realistic pulse shaping filter implementations.

3.3 Baseband digital signal processing: a novel time-frequency equalizer and cross-talk canceller

The use of subcarrier multiplexing and multilevel signaling lowers maximum signal frequency and digital signaling rate. This makes possible the use of cost-effective, reliable and power-efficient CMOS technology for data recovery and processing. Yet, even though already proven for wireless applications, additional analog front-end design challenges exist in the present case for individual channel bandwidths in excess of 500 MHz. These challenges can be worked around by designing a modulation/demodulation system that forms an orthogonal frequency division multiplex (OFDM) as presented in a first section. But this comes at the cost of reduced bandwidth efficiency or additional constraints in terms of carrier channel placement. A second section shows that digital signal processing structures can spare the necessity for OFDM and can compensate for inter-channel cross-talk when channels are brought close to each other to minimize overall bandwidth occupation with relaxed pulse shaping and baseband bandwidth tightness requirements. A third and fourth section present how this can be generalized in an adaptive scheme that performs inter-symbol interference equalization, inter-channel cross-talk cancellation, and makes the overall system robust to circuit implementation and fabrication variations.

3.3.1 Introductory developments

Fig. 3.2 shows a complete view of the subcarrier multiplexed transmission system including a baseband digital signal processing stage in the receiver. It is composed of K carrier channels at angular frequencies $0 < \omega_0 < \omega_1 < \dots < \omega_{K-1}$. K streams of symbols $(s_{n,0})_n$, $(s_{n,1})_n$, \dots , $(s_{n,K-1})_n$ with common symbol period T form the input to the transmitter. Each symbol is a random variable with values in a fixed constellation composed of a finite number of points in the complex plane. The real and imaginary part of all symbols of all K streams are assumed to be independent and identically distributed. The variance (energy) of each symbol is assumed to be σ_s^2 . Each channel transmission path is composed of the same real pulse-shaping filter $p(t)$ and a mixer performing the modulation of each baseband waveform with the corresponding carrier. The K passband waveforms are added together

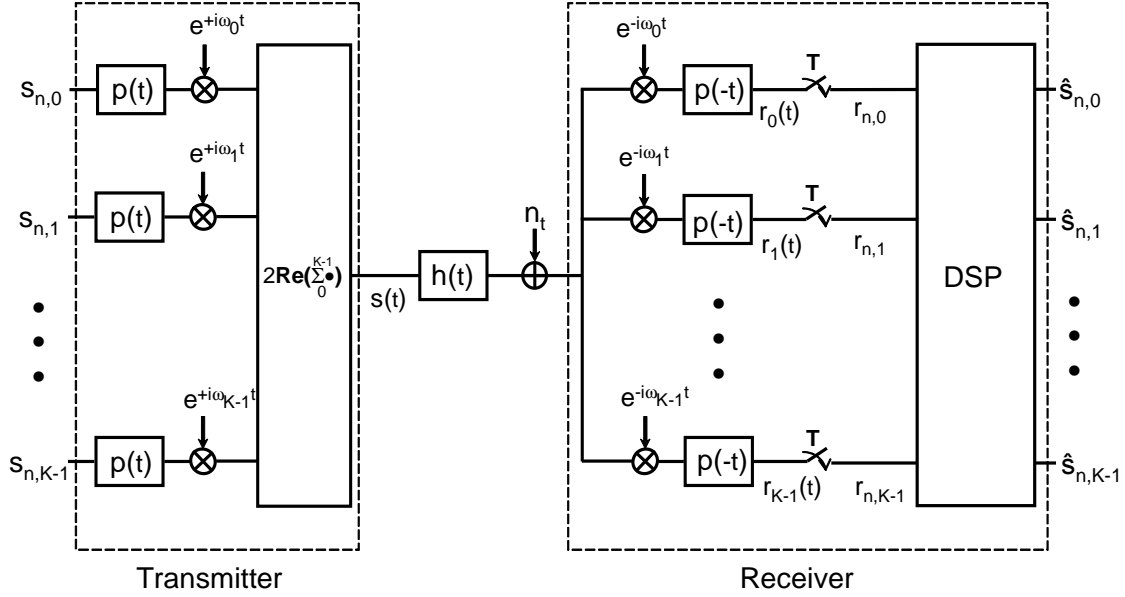


Figure 3.2: Subcarrier multiplexed system with receiver baudrate baseband DSP.

to form the transmitter output waveform $s(t)$,

$$s(t) = \sum_{k=0}^{K-1} \left[\left(\sum_n s_{n,k} p(t-nT) \right) e^{+i\omega_k t} + \left(\sum_n s_{n,k}^* p(t-nT) \right) e^{-i\omega_k t} \right], \quad (3.4)$$

where we are ignoring phase misalignment between the carriers in order to simplify this discussion.

The physical channel is modelled here by a linear relationship described by the channel impulse response $h(t)$ with additive noise n_t . In order to highlight system design characteristics independent from the channel it will be assumed that the channel is perfect (h is the Dirac distribution and n is 0) in the following development except when expressly mentioned.

The transmitted waveform is passed through K demodulation paths comprising a receiver filter matched to the transmitter pulse-shaping filter to produce the K demodulated received waveforms. With the index l varying from 0 to $K-1$, we have for the received

signals:

$$r_l(t) = \int s(u) e^{-i\omega_l u} p(-(t-u)) du$$

Assuming the sampling phase in each demodulation path is perfect, we get the following expression for the received sequences of samples at the output of each of the K demodulation paths. For l between 0 and $K-1$ the received sample at sampling instant mT $r_{m,l} = r_l(mT)$ is given by

$$r_{m,l} = \sum_n \left[\sum_{k=0}^{K-1} s_{n,k} a_{lk}((m-n)T) e^{-i(\omega_l - \omega_k)nT} + \sum_{k=0}^{K-1} s_{n,k}^* b_{lk}((m-n)T) e^{-i(\omega_l + \omega_k)nT} \right] \quad (3.5)$$

where:

$$\begin{cases} a_{lk}(t) = \int p(v) p(v-t) e^{-i(\omega_l - \omega_k)v} dv = \int \tilde{p}(\omega) \tilde{p}(\omega - (\omega_l - \omega_k)) e^{-i\omega t \frac{d\omega}{2\pi}} e^{-i(\omega_l - \omega_k)t} \\ b_{lk}(t) = \int p(v) p(v-t) e^{-i(\omega_l + \omega_k)v} dv = \int \tilde{p}(\omega) \tilde{p}(\omega - (\omega_l + \omega_k)) e^{-i\omega t \frac{d\omega}{2\pi}} e^{-i(\omega_l + \omega_k)t} \end{cases} \quad (3.6)$$

and \tilde{p} is the Fourier transform of p .

We note that these expressions are obtained in conditions where there is no frequency offset and no phase misalignment at the sampling stage. In practice these parameters would be identified and tracked by clock and data recovery functions in the receiver, the discussion of which is outside the scope of the present matter.

Ideally the received samples $r_{m,l}$ in the l^{th} channel should be equal to the input symbols on that same channel $s_{m,l}$. We can see from Eq. 3.5 that some interference terms are present in general. These interferences fall into three different categories:

- They could be coming from other demodulated channels than the l^{th} channel when terms $a_{lk}(0)$ with $k \neq l$ are non-zero. We are then talking about *inter-channel crosstalk*.
- They could be due to the demodulation process itself in the form of image bands when the terms $b_{lk}(0)$ are non-zero. We are then talking about *image bands interference*.
- They could be coming from other time slots when terms a_{lk} and b_{lk} are non-zero at time instants other than 0. We are then talking about *inter-symbol interference (ISI)*.

Fig. 3.2 shows that the system receiver can also include a digital signal processing (DSP) block operating at the symbol rate $1/T$ and manipulate the sequences of received

samples from all K channels to derive K sequences of decision variables $\hat{s}_{n,k}$ that form the final estimates of the transmitted symbols $s_{n,k}$ to be passed through an appropriate decision device (in-phase and quadrature multilevel slicers for QAM-M constellations for instance).

The following sections will explore some of the system design rules that remove or minimize these interferences thus improving data transmission reliability even without the presence of a DSP stage ($\hat{s}_{n,k} = r_{n,k}$). It will be shown that specific digital signal processing structures can be implemented to greatly relax these rules by cancelling the effects of inter-channel cross-talk and image bands interference as well as ISI.

3.3.2 Inter-channel cross-talk and OFDM systems

It is assumed here that the impulse response of the shaping filter is such that inter-symbol interference vanishes, focusing our attention on inter-channel interference. That is to say we have for all l and k in $0, \dots, K-1$,

$$\begin{cases} a_{lk}((m-n)T) = 0 & \text{for } m \neq n. \\ b_{lk}((m-n)T) = 0 & \text{for } m \neq n. \end{cases}$$

In this case we have a simpler expression for the received sample in channel l at discrete time mT ,

$$r_{m,l} = \sum_{k=0}^{K-1} s_{m,k} \alpha_{lk} e^{-i(\omega_l - \omega_k)mT} + \sum_{k=0}^{K-1} s_{m,k}^* \beta_{lk} e^{-i(\omega_l + \omega_k)mT} \quad (3.7)$$

where we have:

$$\begin{cases} \alpha_{lk} = a_{lk}(0) = \int p^2(v) e^{-i(\omega_l - \omega_k)v} dv = \int \tilde{p}(\omega) \tilde{p}(\omega - (\omega_l - \omega_k)) e^{-i\omega t} \frac{d\omega}{2\pi} \\ \beta_{lk} = b_{lk}(0) = \int p^2(v) e^{-i(\omega_l + \omega_k)v} dv = \int \tilde{p}(\omega) \tilde{p}(\omega - (\omega_l + \omega_k)) e^{-i\omega t} \frac{d\omega}{2\pi} \end{cases} \quad (3.8)$$

Orthogonal frequency division multiplexing Once the pulse shaping function p is fixed, the constraint that the system be free from inter-channel interference turns into a constraint on the carrier frequencies $\omega_0, \omega_1, \dots, \omega_{K-1}$.

A first example is given by a square pulse shape (NRZ transmit filter; integrate-and-

dump receive filter) of duration T ,

$$p(t) = \begin{cases} 1/T & \text{if } -T/2 \leq t \leq +T/2, \\ 0 & \text{elsewhere.} \end{cases}$$

and we have for l and k in $0, \dots, K-1$,

$$\begin{cases} \alpha_{lk} = \text{sinc} \left((\omega_l - \omega_k) \frac{T}{2\pi} \right) \\ \beta_{lk} = \text{sinc} \left((\omega_l + \omega_k) \frac{T}{2\pi} \right) \end{cases}$$

where $\text{sinc}(x) = \sin(\pi x)/(\pi x)$ is the sinus-cardinal function. A necessary and sufficient condition for all terms to vanish except $\alpha_{00} = \alpha_{11} = \dots = \alpha_{K-1, K-1} = 1$ is for the difference of any two distinct carrier frequencies to be an integer multiple of $2\pi/T$ and for each carrier frequency to be a integer multiple of π/T . This can be summarized by saying that the carrier frequencies occupy positions on a regular grid defined by the frequencies that are all either even multiples of π/T or odd multiples of π/T . Such a system is said to be an *orthogonal frequency division multiplexing* (OFDM) system.

The square pulse shape of duration equal to the symbol rate defines an SCM system that is free of inter-channel interference on top of being free of ISI. Beyond the argument about the ideality of such a waveform it can be shown that the multiplexing of several carriers modulated using such a pulse shaping filter results in a quite dramatic reduction of the horizontal eye opening in a given channel. The system is consequently very sensitive to inherent timing jitter and sampling time misalignments in real communication systems thus greatly reducing the transmission reliability.

Another known pulse shaping function that, when combined with its matched receive filter, provides an ISI free transmission has a square-root raised-cosine spectrum $\tilde{p}(\omega) = \sqrt{\tilde{c}(\omega)}$ with

$$\tilde{c}(\omega) = \begin{cases} T & \text{for } 0 \leq |\omega| \leq (1 - \alpha)\pi/T \\ \frac{T}{2} \left(1 - \sin \left(\frac{T}{2\alpha} \left(|\omega| - \frac{\pi}{T} \right) \right) \right) & \text{for } (1 - \alpha)\pi/T \leq |\omega| \leq (1 + \alpha)\pi/T \\ 0 & \text{for } |\omega| \geq (1 + \alpha)\pi/T \end{cases}$$

where T is the symbol period and $\alpha \in [0, 1]$ is the filter *excess bandwidth* which indicates the amount of bandwidth occupied by this filter in excess of the minimum possible for

a transmission at symbol rate $1/T$ given by the Nyquist frequency $\omega_{\text{Nyquist}} = \pi/T$. The expression of the interference coefficients in terms of the pulse shaping filter spectrum given in Eq. 3.6 gives us sufficient conditions on the carrier frequencies $0 < \omega_0 < \dots < \omega_{K-1}$. Actually choosing these frequencies such that $\omega_0 > (1 + \alpha)\pi/T$ and they are all distant to each other by more than $2(1 + \alpha)\pi/T$ (non-overlapping carrier-centered passband spectra) brings the inter-channel and image bands interference terms to 0. In this case again the frequency division multiplexing system is OFDM again.

This type of pulse-shaping and FDM is widely used in wireless applications. In practice the pulse shaping filter is realized in the discrete time domain using an over-sampling of 2 to 8 times the symbol rate (fractional spacing of $T/8$ to $T/2$). The digital-to-analog (D/A) converter is followed by an analog filter to remove the image bands due to the discrete filtering process. Trade-offs between oversampling rate and continuous time filter selectivity are possible for such an implementation: $T/4$ to $T/8$ fractional spacing in combination with a simple RC filter or $T/2$ fractional spacing with more selective continuous-time filters are acceptable. For the FDM system described in this dissertation, with a symbol rate close to 650 Mbaud operating frequencies are in general more than two orders of magnitude higher than in wireless applications. The implementation of even a $T/2$ fractionally spaced filter would require processing of 1.3 GS/s and the design of selective analog RF filters. Implementation of the pulse shaping filter becomes extremely challenging, putting very stringent requirements on the continuous timer filter analog implementation.

OFDM conditions put further constraints on the system implementation by either imposing a precise spacing of the carrier frequencies, posing implementation challenges, or pushing them away from each other thus reducing the achievable spectral efficiency.

Inter-channel interference DSP cancellation Still assuming that the transmission system is free from ISI, we note that since the discrete received samples in a given channel are linear combinations of symbols in this channel as well as symbols in other channels it could be possible to “invert” the linear system in order to recover interference-free symbols.

When considering the $K \times 1$ complex vector of received samples at time mT we have the following linear expression as a function of the input symbols and their complex conjugates:

$$R_m = \theta_m^{-1} (A\theta_m S_m + B\theta_m^{-1} S_m^*) \quad (3.9)$$

where:

$$\begin{aligned}
 R_m &= \begin{pmatrix} r_{m,0} \\ \vdots \\ r_{m,K-1} \end{pmatrix} \\
 \theta_m &= \begin{pmatrix} e^{i\omega_0 mT} & 0 & \dots & 0 \\ 0 & \ddots & \ddots & \vdots \\ \vdots & \ddots & \ddots & 0 \\ 0 & \dots & 0 & e^{i\omega_{K-1} mT} \end{pmatrix} \\
 S_m &= \begin{pmatrix} s_{m,0} \\ \vdots \\ s_{m,K-1} \end{pmatrix} \\
 S_m^* &= \begin{pmatrix} s_{m,0}^* \\ \vdots \\ s_{m,K-1}^* \end{pmatrix} \\
 A &= (\alpha_{lk})_{0 \leq l, k \leq K-1} \\
 B &= (\beta_{lk})_{0 \leq l, k \leq K-1}
 \end{aligned}$$

It can be shown that A is a Hermitian positive definite $K \times K$ matrix. It is in particular invertible.

The following linear expression in the received samples and their complex conjugates can be naturally formed to create the vector \hat{S}_m of the K symbols at the instant m at the receiver output

$$\hat{S}_m = \theta_m^{-1} (\Lambda \theta_m R_m + \Gamma (\theta_m R_m)^*), \quad (3.10)$$

where the $*$ symbol indicates that we are taking the complex conjugate of the components of a vector and Λ and Γ are $K \times K$ complex matrices called here *inter-channel interference cancellation matrix* and *image bands interference cancellation matrix* respectively. This leads to the following expression for the receiver output symbol vector \hat{S}_m as a function of the transmitter input symbol vector S_m :

$$\hat{S}_m = \theta_m^{-1} (\Lambda A + \Gamma B^*) \theta_m S_m + \theta_m^{-1} (\Lambda B + \Gamma A^*) \theta_m^{-1} S_m^*. \quad (3.11)$$

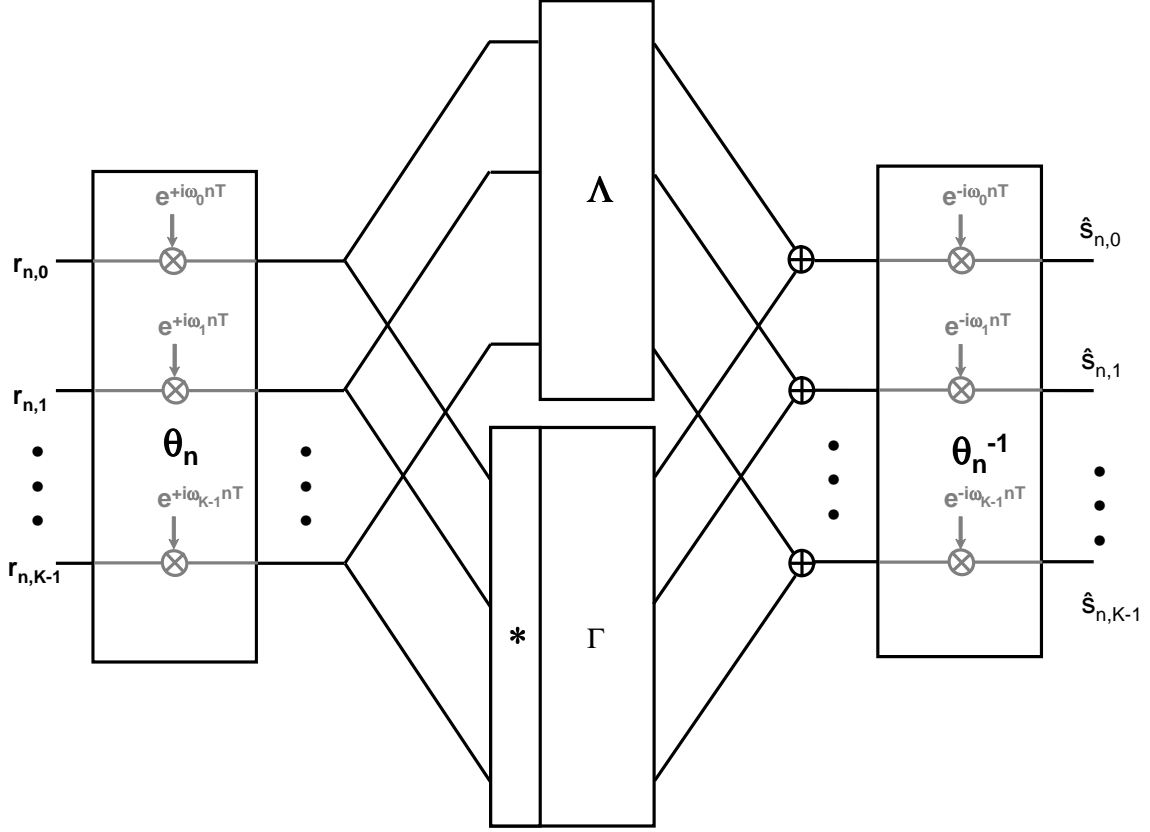


Figure 3.3: Inter-channel and image bands interference canceller.

This last expression yields a necessary and sufficient condition on Λ and Γ for perfect interference cancellation

$$\begin{cases} \Lambda A + \Gamma B^* = I_K \\ \Lambda B + \Gamma A^* = 0_K \end{cases} \quad (3.12)$$

where I_K is the $K \times K$ identity matrix and 0_K is the $K \times K$ null matrix. The $2K \times 2K$ matrix

$$C = \begin{pmatrix} A & B \\ B^* & A^* \end{pmatrix}$$

is Hermitian and positive definite, and thus invertible. Consequently, matrices Λ and Γ verifying 3.12 indeed exist.

Fig. 3.3 represents the DSP architecture described by Eq. 3.10 where each output of the blocks Λ and Γ is a complex linear combination of its inputs. It is interesting to place the DSP structure represented in Fig. 3.3 in the context of Fig. 3.2. This structure seems to mirror in the discrete time domain the part of the system that is in the continuous time domain. Intuitively the block θ_n undoes in the discrete time domain the effect of the receive mixers whereas the block θ_n^{-1} undoes the effect of the transmitter mixers. The cross-talk cancellation blocks reverse in the discrete time domain the effects of the chain of linear components between the transmit and the receive mixer stages effectively performing cross-talk cancellation between frequency channels.

3.3.3 Inter-symbol interference

For a system that is not free of ISI the expression of the $K \times 1$ vector of received samples at discrete time mT becomes (to be compared to Eq. 3.9 for the ISI-free case)

$$R_m = \sum_n [\theta_m^{-1} (A_{m-n}\theta_n S_n + B_{m-n}(\theta_n S_n)^*)] \quad (3.13)$$

where this time

$$A_q = (e^{i\omega_l qT} a_{lk}(qT))_{0 \leq l, k \leq K-1} = \left(\int p(v) e^{+i\omega_k v} p(v - qT) e^{-i\omega_l (v - qT)} dv \right)_{l, k},$$

$$B_q = (e^{i\omega_l qT} b_{lk}(qT))_{0 \leq l, k \leq K-1} = \left(\int p(v) e^{-i\omega_k v} p(v - qT) e^{-i\omega_l (v - qT)} dv \right)_{l, k},$$

with $a_{lk}(t)$ and $b_{lk}(t)$ are given by Eq. 3.6. With the reasonable assumption that the system has finite memory, there is a positive integer N such that, for $q < 0$ or $q \geq N$, $A_q = B_q = 0_K$.

DSP equalization In order to simplify this presentation of ISI cancellation we assume that image band interferences are negligible knowing that the results of this section can be generalized without fundamental difficulty. In this case, the expression of the vector of received samples from all K channels at discrete time mT is

$$R_m = \theta_m^{-1} (A_0 \theta_m S_m + A_1 \theta_{m-1} S_{m-1} + \cdots + A_{N-1} \theta_{m-N+1} S_{m-N+1}).$$

Now considering the receive sample vector of dimensions $KP \times 1$, \mathbf{R}_m , formed by the concatenation of the vectors of K receive samples at P different discrete time instants $mT, (m-1)T, \dots, (m-P+1)T$, we get a condensed expression for these KP samples

$$\mathbf{R}_m = \boldsymbol{\theta}_m^{-1} \mathbf{A} \boldsymbol{\Omega}_m \boldsymbol{\Sigma}_m, \quad (3.14)$$

where we have the complex matrices and their dimensions

$$\begin{aligned} \boldsymbol{\theta}_m &= \begin{pmatrix} \theta_m & & \\ \mathbf{0} & \ddots & \mathbf{0} \\ & & \theta_{m-P+1} \end{pmatrix} : PK \times PK, \\ \mathbf{A} &= \begin{pmatrix} A_0 & A_1 & \cdots & A_{N-1} & 0 & \cdots & 0 \\ 0 & A_0 & A_1 & \cdots & A_{N-1} & \ddots & \vdots \\ \vdots & \ddots & \ddots & \ddots & & \ddots & 0 \\ 0 & \cdots & 0 & A_0 & A_1 & \cdots & A_{N-1} \end{pmatrix} : PK \times (N+P-1)K, \\ \boldsymbol{\Omega}_m &= \begin{pmatrix} \theta_m & & \\ \mathbf{0} & \ddots & \mathbf{0} \\ & & \theta_{m-N-P+2} \end{pmatrix} : (N+P-1)K \times (N+P-1)K, \\ \boldsymbol{\Sigma}_m &= \begin{pmatrix} S_m \\ \vdots \\ S_{m-N-P+2} \end{pmatrix} : (N+P-1)K \times 1. \end{aligned}$$

In order to cancel ISI in the presence of inter-channel interference using a linear feed-forward (FFE) DSP architecture with FFE equalizer of length P , we form the vector of K output symbols at discrete time mT thanks to a linear combination of the KP received samples at P different time instants $mT, (m-1)T, \dots, (m-P+1)T$ in the K channels

$$\hat{S}_m = \theta_m^{-1} \boldsymbol{\Lambda} \boldsymbol{\theta}_m \mathbf{R}_m, \quad (3.15)$$

which gives the receiver output symbols as a function of the input symbols

$$\hat{S}_m = \theta_m^{-1} \boldsymbol{\Lambda} \mathbf{A} \boldsymbol{\Omega}_m \boldsymbol{\Sigma}_m, \quad (3.16)$$

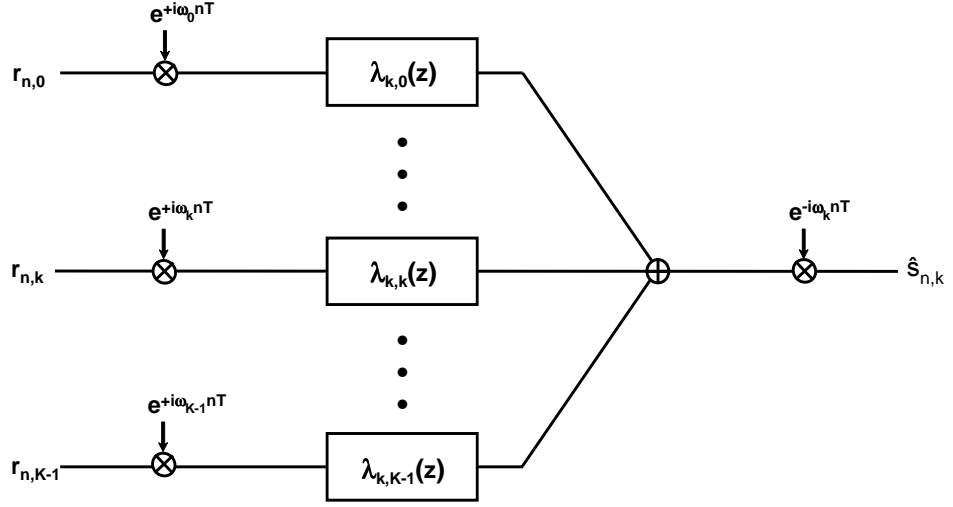


Figure 3.4: Time-frequency equalization and cross-talk cancellation of channel k .

where $\mathbf{\Lambda}$ is now a $K \times PK$ complex matrix meant to perform ISI (as well as inter-channel interference) cancellation. It has the following time-related structure:

$$\mathbf{\Lambda} = \begin{pmatrix} \Lambda_0 & \Lambda_1 & \cdots & \Lambda_{P-1} \end{pmatrix}.$$

The DSP architecture corresponding to Eq. 3.15 is shown in Fig. 3.4 representing the finite-impulse response (FIR) filtering operations performed on the “rotated” complex received samples to get the receiver output symbols. The digital FIR filter z -transforms are all of length at most P given by

$$\Lambda(z) = \Lambda_0 + \Lambda_1 z^{-1} + \cdots + \Lambda_{P-1} z^{-(P-1)} = \begin{pmatrix} \lambda_{0,0}(z) & \cdots & \lambda_{0,K-1}(z) \\ \vdots & & \vdots \\ \lambda_{K-1,0}(z) & \cdots & \lambda_{K-1,K-1}(z) \end{pmatrix}. \quad (3.17)$$

The diagonal filters $\lambda_{k,k}(z)$ can be interpreted as time-slot ISI cancellers in each frequency channel and the non-diagonal filters $\lambda_{k,l}(z)$ for $k \neq l$ can be interpreted as frequency-channel cross-talk cancellers. This is why we can qualify this DSP technique as time-frequency equalization and cross-talk cancellation.

Mean-square error criterion To determine the coefficients of the matrix \mathbf{A} that performs interference cancellation, a matrix inversion argument is not necessarily possible or of practical interest. The use of a mean-square error performance criterion turns the problem of reliable transmission and equalization into a well formulated mathematical optimization problem that also permits simple, effective and robust implementation. This quadratic optimization problem identifies a good solution to the problem and allows the derivation of practical algorithms for the identification of the optimal cancellation matrix \mathbf{A}^{opt} . Recognizing that the sequence of input symbol vectors is a stationary random sequence and that the sequence of receiver output vectors has the same property assuming time invariance of the channel, the average quadratic error is a deterministic time-independent constant

$$\mathcal{E}^2 = \mathbb{E}(|\hat{S}_m - S_m|^2) = \mathbb{E}(\|E_m\|^2) = \text{Tr}(\mathbb{E}(\theta_m E_m (\theta_m E_m)^H)), \quad (3.18)$$

where Tr is the trace matrix operator, \cdot^H is the conjugate-transpose operator and the error vector E_m at discrete time mT is given by

$$E_m = \hat{S}_m - S_m = \theta_m^{-1} (\mathbf{A}\mathbf{A} - \mathbf{\Delta}) \mathbf{\Omega}_m \mathbf{\Sigma}_m,$$

where $\mathbf{\Delta}$ is the $K \times (N + P - 1)K$ matrix $\begin{pmatrix} I_K & 0_K & \dots & 0_K \end{pmatrix}$. Given the fact that the sequences of input symbols on all K channels are i.i.d we have $\mathbb{E}(\mathbf{\Sigma}_m \mathbf{\Sigma}_m^H) = \sigma_s^2 I_{(N+P-1)K}$ where σ_s^2 is the variance of the input symbol random variables. This provides the following expression for the mean square-error:

$$\mathcal{E}^2 = \sigma_s^2 \text{Tr}((\mathbf{A}\mathbf{A} - \mathbf{\Delta})(\mathbf{A}\mathbf{A} - \mathbf{\Delta})^H). \quad (3.19)$$

This becomes

$$\mathcal{E}^2 = \sigma_s^2 (K - \text{Tr}(\mathbf{\Psi}^H \mathbf{\Phi}^{-1} \mathbf{\Psi}) + \text{Tr}((\mathbf{\Phi}^{-1} \mathbf{\Psi} - \mathbf{\Lambda}^H)^H \mathbf{\Phi} (\mathbf{\Phi}^{-1} \mathbf{\Psi} - \mathbf{\Lambda}^H))), \quad (3.20)$$

if we assume that the Hermitian matrix $\mathbf{\Phi}$ is positive definite where definitions and dimensions of $\mathbf{\Phi}$ and $\mathbf{\Psi}$ are as follows:

$$\begin{aligned} \mathbf{\Phi} &= \mathbf{A}\mathbf{A}^H & : PK \times PK, \\ \mathbf{\Psi} &= \mathbf{A}\mathbf{\Delta}^H & : PK \times K. \end{aligned}$$

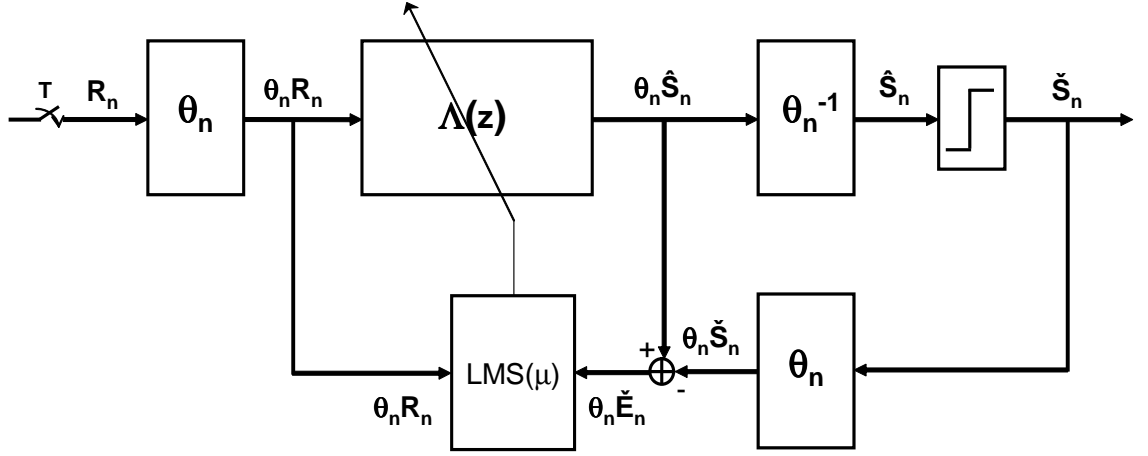


Figure 3.5: Block diagram of the implementation of the LMS algorithm of step μ for the adaptation of the coefficients of the inter-channel interference and ISI cancellation DSP.

Eq. 3.20 indicates that the mean-square error (MSE) is uniquely minimized by the following optimal matrix $\mathbf{\Lambda}$,

$$\mathbf{\Lambda}^{\text{opt}} = \mathbf{\Psi}^H \mathbf{\Phi}^{-1} = \mathbf{\Delta} \mathbf{A}^\sharp, \tag{3.21}$$

where \mathbf{A}^\sharp is the pseudo-inverse of \mathbf{A} .

Stochastic gradient algorithm In practice ensemble averages or their precise estimates cannot be computed at high communication speeds and the stochastic gradient or LMS algorithm is used instead. It consists in updating the equalization filter coefficients following the gradient respective to these coefficients of the instantaneous square error as it appears in the argument of the ensemble average producing the mean square error. In the present case the square error at time nT is

$$e_n^2 = \|\hat{S}_n - S_n\|^2 = \|\theta_n E_n\|^2,$$

with $\mathcal{E}^2 = \mathbb{E}(e_n^2)$ and where

$$E_n = \hat{S}_n - S_n = \theta_n^{-1} (\mathbf{\Lambda} \mathbf{A} - \mathbf{\Delta}) \mathbf{\Omega}_n \mathbf{\Sigma}_n.$$

This gives the following condensed expression for the gradient relative to the filter coefficients which is a $PK \times K$ complex matrix. The matrix coefficient in row k and column l is given by $\left(\frac{\partial}{\partial x_{k,l}} + i \frac{\partial}{\partial y_{k,l}} \right) e_n^2$ where $\lambda_{k,l} = x_{k,l} + iy_{k,l}$ is the coefficient of $\mathbf{\Lambda}$ in row k and column l :

$$\nabla(e_n^2)(\mathbf{\Lambda}) = 2(\mathbf{\Lambda} \mathbf{A} - \mathbf{\Delta}) \mathbf{\Omega}_n \mathbf{\Sigma}_n (\mathbf{\theta}_n \mathbf{R}_n)^H = 2\theta_n E_n (\mathbf{\theta}_n \mathbf{R}_n)^H. \quad (3.22)$$

In practice the sequence of input symbols (S_n) is not directly known at the receiver and the sequence of recovered data symbols at the output of the decision device (\check{S}_n) is used instead to form the sequence of error vectors (\check{E}_n) = ($\hat{S}_n - \check{S}_n$). Fig. 3.5 shows a block diagram of the implementation of the LMS algorithm for the adaptation of the cancellation filter $\Lambda(z) = \Lambda_0 + \Lambda_1 z^{-1} + \dots + \Lambda_{P-1} z^{-(P-1)}$. Using a step coefficient $\mu \geq 0$ that guarantees a stable as well as fast convergence the coefficient adaptation operation to get the filter coefficient values at time $(n+1)T$ from the values at time nT is

$$\mathbf{\Lambda}_{n+1} = \mathbf{\Lambda}_n - \mu \theta_n \check{E}_n (\mathbf{\theta}_n \mathbf{R}_n)^H. \quad (3.23)$$

It can be observed that this update algorithm can be expressed for each row thus setting the update method for individual channel equalization structures such as the one shown for channel k in Fig. 3.4. It can be noted that the equalization of channel k only depends on the error in that channel. This result has been obtained by using the overall square error for all K channels which is the sum of the square errors in each channel. The result would be identical if the algorithm were to be developed from the minimization of the individual channel square errors independently.

3.3.4 Adaptive baseband DSP equalization and cross-talk cancellation

When considering the presence of ISI, inter-channel and image band interferences the approaches taken in the two previous sections can be combined and generalized to give the adaptive DSP architecture shown in Fig. 3.6 for the time-frequency equalizer and cross-talk canceller. A generalized stochastic gradient algorithm is used for the adaption of the

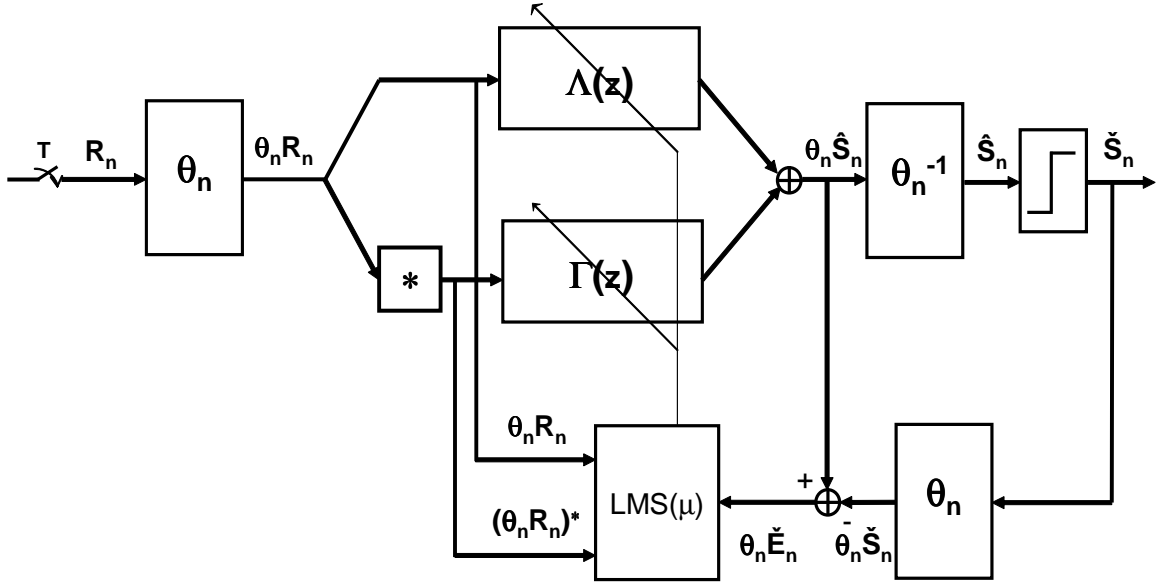


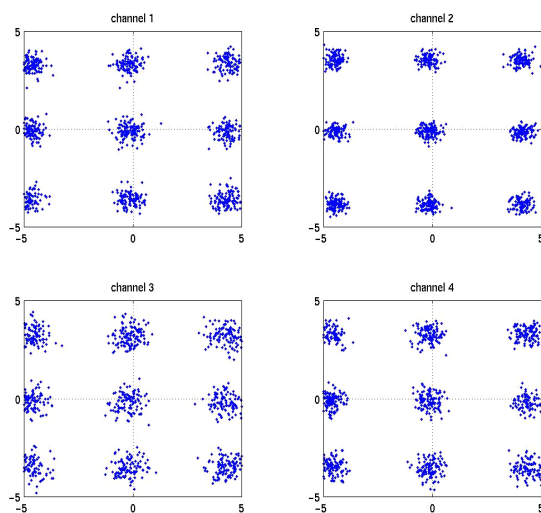
Figure 3.6: Block diagram of the adaptive time-frequency equalization DSP.

coefficients of $\Lambda(z)$ and $\Gamma(z)$:

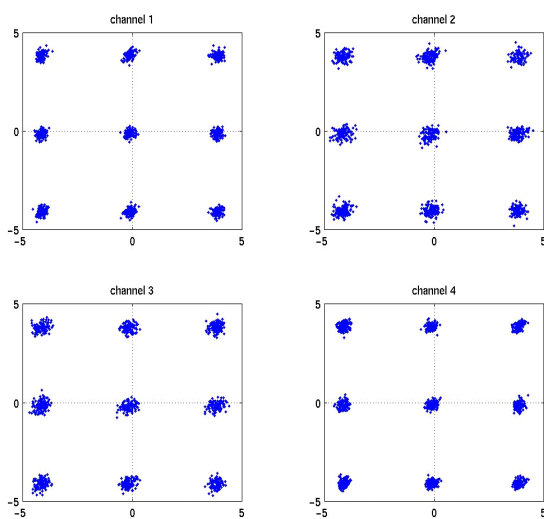
$$\begin{aligned}\Lambda_{n+1} &= \Lambda_n - \mu \theta_n \check{E}_n (\theta_n \mathbf{R}_n)^H \\ \Gamma_{n+1} &= \Gamma_n - \mu \theta_n \check{E}_n ((\theta_n \mathbf{R}_n)^*)^H.\end{aligned}$$

This mean square error analysis can be carried out in the presence of a non-ideal channel response and in the presence of noise from the channel and the quantization stage at the input of the DSP. This complicates the algebra further without modifying the basic results presented here.

Figures 3.7 to 3.9 show that performance can be greatly improved when using the DSP architecture shown in Fig. 3.6 compared to the one shown in Fig. 3.5. In this illustrative case a QAM-9 symbol constellation has been chosen and symbols are transmitted over 4 carriers with transmit and receive filter shapes that do not make the system free of inter-symbol and inter-channel interference. The enhanced architecture brings a 7dB improvement in

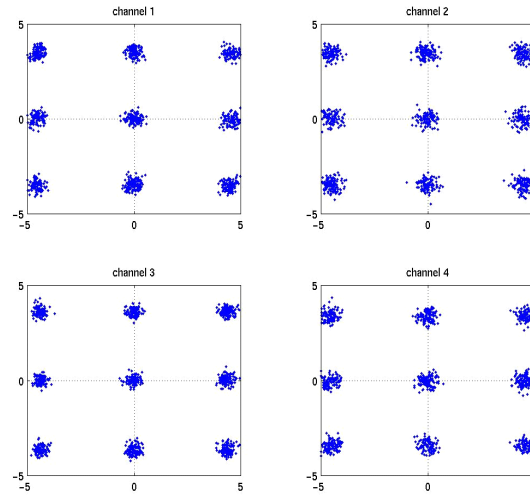


(a)

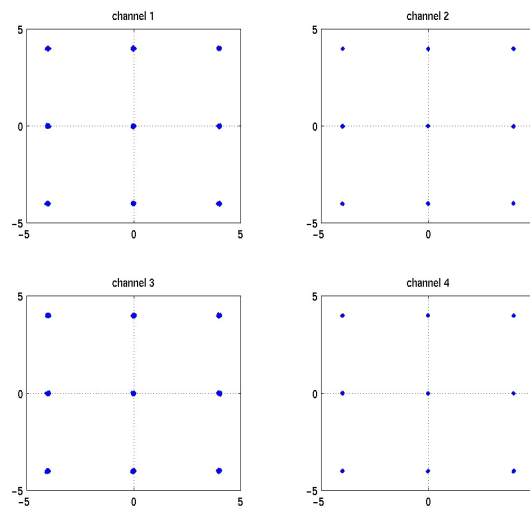


(b)

Figure 3.7: QAM-9 constellations over 4 carriers at multiples of the symbol rate $1/T$. The transmit shaping filter is third-order Butterworth with $F_c = 1.2/T$. The receive filter is fifth-order Butterworth with $F_c = 0.9/T$. A/D conversion is performed with 6-bit precision. Equalization and cross-talk cancellation with a tap length P equal to 8. (a) DSP structure of Fig. 3.5. (b) DSP structure of Fig. 3.6.

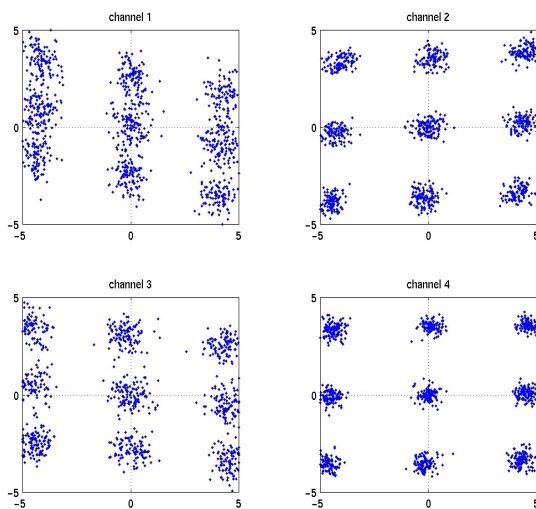


(a)

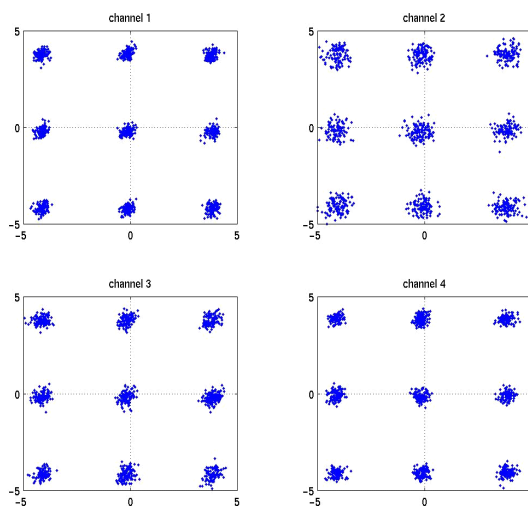


(b)

Figure 3.8: QAM-9 constellations over 4 carriers at multiples of the symbol rate $1/T$. The transmit shaping filter is third-order Butterworth with $F_c = 1.2/T$. The receive filter is fifth-order Butterworth with $F_c = 0.9/T$. A/D conversion is performed with 10-bit precision. Equalization and cross-talk cancellation with a tap length P equal to 8. (a) DSP structure of Fig. 3.5. (b) DSP structure of Fig. 3.6.



(a)



(b)

Figure 3.9: QAM-9 constellations over 4 carriers at multiples of the symbol rate $1/T$. The transmit shaping filter is third-order Butterworth with $F_c = 1.2/T$. The receive filter is fifth-order Butterworth with $F_c = 0.9/T$. A/D conversion is performed with 6-bit precision. A $\pm 15^\circ$ I/Q phase mismatch and a ± 3 dB I/Q gain mismatch are introduced. Equalization and cross-talk cancellation with a tap length P equal to 8. (a) DSP structure of Fig. 3.5. (b) DSP structure of Fig. 3.6.

the worst channel for the time-averaged square error with 6-bit A/D conversion as shown in Fig. 3.7. The improvement becomes 27dB if 10-bit A/D conversion is used as depicted in Fig. 3.8. Fig. 3.9 illustrates increased robustness to mixer implementation imperfections.

The addition of a matrix of filters operating on the complex conjugate of the received samples was initially motivated by the cancellation of image bands after demodulation. Yet as illustrated by the previous example it brings additional benefits that can be interpreted as the ability to cancel interferences not only within and between complex channels but also between in-phase and quadrature components per channel. This corrects cross-talk due to I/Q phase mismatch in the implementation of mixers (also known as image rejection non-ideality) or in the implementation of the local oscillator phase shifters, small channel frequency offsets between modulation and demodulation, carrier phase offsets between the transmitter and the receiver. In particular such an architecture is expected to support and ease carrier frequency and phase recovery and tracking.

3.4 Discussion

In a system where power efficiency could potentially be reduced in order to gain bandwidth efficiency sub-carrier multiplexing with multilevel signaling can be used for that purpose. Its advantages can be practically exploited and implementation hurdles can be overcome thanks to flexible DSP. Depending on the precise subcarrier-multiplexed system to be designed trade-offs can be performed between the analog front-end design specifications (shaping and receive filters, carrier frequencies placement, phase shifters and mixers) and the DSP architecture complexity. If the carriers are close to each other because bandwidth is at a premium and design constraints on the pulse shaping filter need to be relaxed for technological reasons a fair amount of inter-channel cross-talk occurs even between non-adjacent channels. If bandwidth efficiency is slightly reduced and greater effort is spent on filter design if the technology allows then inter-channel cross-talk could be only significant for adjacent channels. In this case, referring to Fig. 3.4, only FIR filters $\gamma_{k,k-1}$ and $\gamma_{k,k+1}$ would have to be implemented in order to cancel inter-channel cross-talk in a given middle channel k .

Table 3.4 summarizes constraints on the implementation of the sub-carrier multiplexed system shown in Fig. 3.2. Constraints apply in order to reach the targeted system performance. They can be relaxed thanks to the implementation of specific DSP features in the

System implementation	Impairments	System performance parameter	DSP complexity
Pulse shaping and receiver filter design	ISI	Symbol rate	Number of FIR filter taps
	Inter-channel interference	Bandwidth efficiency	Number of inter-channel cancellation filters
	Image bands interference Degraded SNR	Bandwidth efficiency Constellation size, transmit power	“Conjugate” cancellation filters DSP adaptation for square error minimization
Carrier positions	Inter-channel and image-band interference	Bandwidth efficiency	Number of inter-channel cancellation filters and number of FIR filter taps
Mixers design and carrier generation	I/Q components orthogonality	Maximum carrier frequency	Direct and “conjugate” architecture
Carrier frequency and phase recovery	Frequency and phase offsets for symbol recovery	Maximum carrier frequency	Direct and “conjugate” architecture

Table 3.4: System design “dimensions”: Limitations in the implementation of system elements (column 1) generate impairments (column 2) that can be alleviated by giving away system performance (column 3) or by increasing DSP complexity (column 4) instead.

receiver. In practice the system of Fig. 3.2 may require the instantiation of a per-channel passband RF filter and gain amplifier before going into the associated mixer. The characteristics of these elements have been conceptually aggregated with the characteristics of the receiver baseband filter in order to simplify this presentation.

For the high capacity SCM systems of interest, it is not obvious whether reliable transmission of information is possible given the targeted throughput, available bandwidth and technology even when accounting for the benefits brought by the presented DSP structures. Processing has to be possible at the targeted signaling speed which depends on the number of symbols in the constellation and the number of carrier channels. The signal to noise ratio at the receiver has to be high enough despite constraints on the transmit signal power. This ultimately depends on the channel distortion and noise characteristics.

Chapter 4

Optical Channel: Features and Models

This chapter defines the optical link this dissertation focuses on. It is formed of optoelectronic components selected according to their commercial availability and low cost.

After a review of the optical system definition the notion of *electro-opto-electrical* (EOE) response of the an optical link is introduced. This serves as a basis for the determination of linear impairments experienced by a transmitted *sub-carrier multiplexed* (SCM) electrical signal composed of multiple radio-frequency (RF) carrier channels as introduced in Sec. 3.2. Besides linear distortions, the magnitude of non-linear distortions and noise is evaluated.

The *directly modulated laser* (DML) is identified as being the most critical link element (non-linear distortions and noise) in the chain motivating a detailed study of its dynamic and noise behavior. This investigation is based on theoretical models supported by noise experimental data as well as selected linearity measurements.

The last section of this chapter introduces a simplified information channel model which provides limits on the information capacity of such a system and compares practical bandwidth efficiency targets to theoretical results.

4.1 System and optical channel definition

Fig. 4.1 presents a high-level view of the bandwidth efficient optical communication chain. It is composed of a transmit digital section, a transmit RF front-end, an electro-optical (EO) converter (optical transmitter), an optical transmission medium, an opto-electrical



Figure 4.1: Optoelectronic transmission chain overview.

(OE) converter (photoreceiver), a receiver RF front-end and a digital section.

The optical channel which is the focus of the present chapter is defined here to include:

- The physical transmission medium which is standard single mode fiber,
- the optical transmitter and receiver,
- the RF analog circuit sections including RF amplifiers and filters.

4.1.1 Optical transmitter

Fig. 4.2 shows the two main procedures for conversion of an electrical signal into an optical signal. Fig. 4.2(a) presents the external modulation scheme: a continuous-wave (CW) laser produces a steady optical wave that is input into an external device that responds to electrical stimulation by changing optical wave parameters. The simplest schemes change the optical output power and are based on an interferometric Mach-Zehnder modulator or an electro-absorption modulator. Other external modulator configurations allow for the modulation of other optical wave characteristics for the purpose of information transmission at the price of additional optical transmitter complexity and cost. Fig. 4.2(b) presents the direct modulation scheme: the optical output power of a semiconductor laser is modulated by directly applying an electrical input current signal.

For complexity and related cost reasons the usage of a commercially available semiconductor distributed feedback (DFB) directly modulated laser (DML) operating at 1310 nm was chosen. These lasers have been already widely used in subcarrier multiplexing fiber systems for the transmission of analog and digital video signals. They are able to meet the very stringent linearity and noise requirements of these systems keeping in mind though that modulation frequencies are almost two orders of magnitude bigger in the present system.

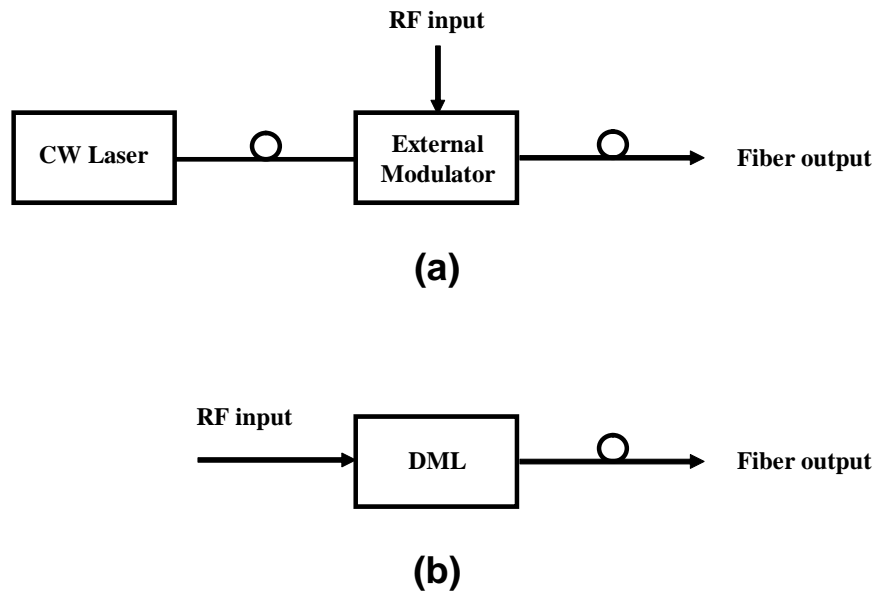


Figure 4.2: Electro-optical conversion: (a) external modulation, (b) direct modulation.

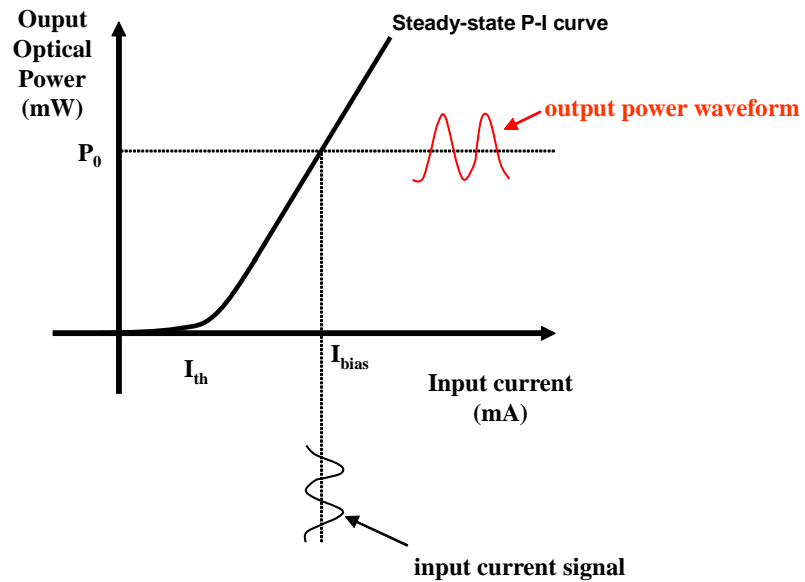


Figure 4.3: Laser diode direct modulation.

A laser diode emits coherent light when biased above threshold. Directly modulated lasers are inherently nonlinear devices but operating conditions (bias current, input signal level) can be found where the response is sufficiently linear as illustrated in Fig. 4.3. The efficiency of the electro-optical conversion above threshold is characterized by the laser *external efficiency* η_{ext} expressed in W/A. The ratio of the standard deviation of the input RF signal to the the bias above threshold is called the (rms) *optical modulation index* (OMI).

Laser efficiency, linearity and bandwidth can be impaired by aging and temperature conditions. This is why a cooled packaged commercial DFB DML integrating temperature monitoring and control circuitry was chosen even though uncooled DMLs are significantly less costly and power hungry devices.

4.1.2 Photo-receiver

A photodiode is used for performing opto-electrical conversion in a very linear fashion. The conversion efficiency is characterized by the photodiode *responsivity* R_{resp} expressed in A/W. The photodiode itself has a finite response time that compounds with the effect of passive and active circuit networks and limit the photoreceiver bandwidth.

A photoreceiver comprising a high-speed p-i-n planar photodiode with a $50\ \Omega$ matched output impedance over its bandwidth in excess of 14 GHz was chosen. If receiver noise (mainly thermal noise here) limits the system performance other photoreceiver designs composed of a photodiode followed by a transimpedance amplifier can be used to improve the link gain and reduce receiver noise power.

4.1.3 Electrical amplification stages

Wideband RF amplification stages are required to bring signals to the desired level and compensate for a less than unity link electrical power gain given by

$$G_{\text{link}} = (\eta_{\text{ext}} R_{\text{resp}} e^{-\alpha_l L})^2 \frac{R_{\text{out}}}{R_{\text{in}}},$$

where η_{ext} is the laser external efficiency, R_{resp} is the photodiode responsivity, α_l is fiber loss per unit length, L is fiber length, R_{out} is the photodiode load resistor and R_{in} is the laser module input resistance.

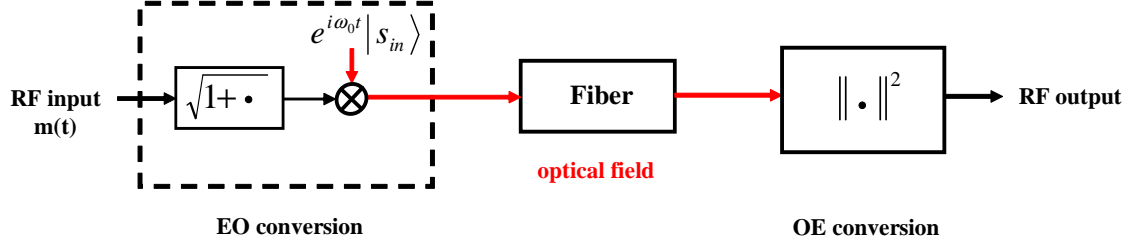


Figure 4.4: Intensity modulation with direct detection (IM/DD) optical transmission scheme.

4.2 Optical system electro-opto-electrical response

4.2.1 Introduction

Fig. 4.4 presents a simplified view of the intensity modulation with direct detection (IM/DD) optical transmission scheme. It is apparent that even in a linear fiber operation regime linear effects other than optical signal amplitude scaling and time delay will translate into nonlinear transformations of the input RF signal into the output RF signal.

Nonetheless linearization of the input/output RF signal relationship can yield insight into some important signal impairments. This is what is done in the following sections.

4.2.2 Framework and definitions

We consider a coherent light source producing an intensity and phase modulated optical carrier (Directly Modulated Laser, continuous-wave laser followed by a Mach-Zehnder or electro-absorption modulator). The optical field produced by the system can be represented by the following complex two-dimensional waveform:

$$e(t) = \sqrt{P_0} \sqrt{1 + m(t)} e^{i\phi(t)} |s_{in}\rangle,$$

where P_0 is the emitted optical power and $|s_{in}\rangle$ is the State of Polarization (SoP) of the coherent light beam. The total optical field at the source (carrier angular frequency ω_0) output is given by $e(t)e^{i\omega_0 t}$. The waveform sent over the fiber link is $m(t)$ ($\|m\|_\infty \leq 1$). This scheme is referred to as IM/DD (Intensity Modulation/Direct Detection). That is to say the meaningful signal that we want to receive in a remote place is born by the optical

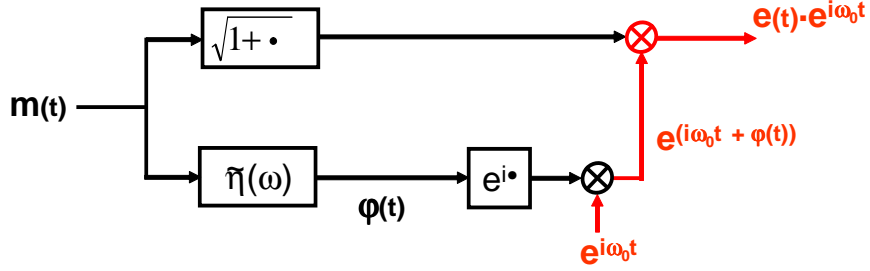


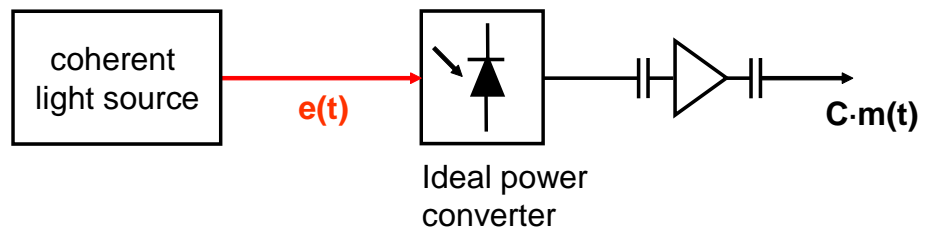
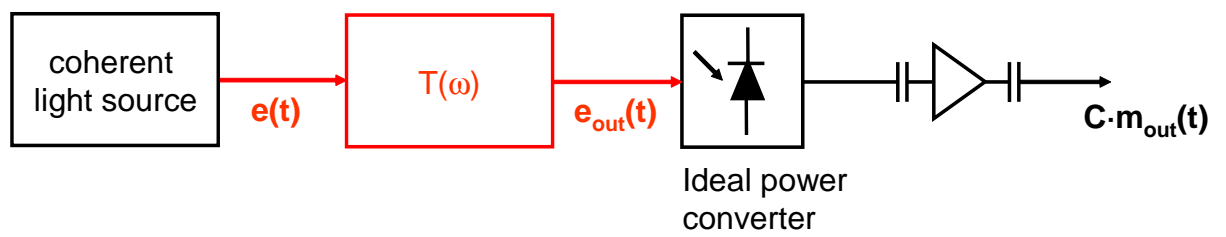
Figure 4.5: System representation of an intensity modulating source with chirp.

power of the light beam that we launch into the optical fiber. This power signal is then detected with a photoreceiver (e.g., PIN diode followed by the necessary preamplification and amplification stages). A system representation of the optical intensity-modulation source is shown in Fig. 4.5. A perfect IM source would not induce any phase modulation. The latter occurs in practice and it is assumed that the phase variations depend on the input signal in a linear fashion.

To define the EOE (electro-opto-electrical) response of the linear optical system we proceed as follows. We define our input electrical signal according to figure 4.6. That is we imagine we can detect the optical power right after the source with an ideal power converter. Once the DC component has been blocked we get a signal proportional to our message signal. It is assumed that this ideal detector is such that the proportionality coefficient C is unity.

We then consider the same ideal photoreceiver but placed at the output of the optical chain of elements as shown in figure 4.7. The signal that comes out is the system output signal m_{out} that should be as close to the input signal $m(t)$ as possible .

The goal of the present section is to relate m_{out} and m under some specific assumptions. Namely it is assumed that $m(t) = \bar{m}s(t)$ where s is an arbitrarily fixed function in the right functional space (included in $L^\infty \cap L^2$, i.e., s is bounded and has finite energy) so that all quantities are well defined, and is such that $\|s\|_\infty = 1$. \bar{m} is real and can be made arbitrarily small. The limit when \bar{m} tends towards 0 should give us the linear EOE small-signal response of the optical system.

Figure 4.6: Definition of the input signal m .Figure 4.7: Definition of the output signal m_{out} .

4.2.3 Fiber linearized response

We assume that the optical system is described by a frequency response matrix $T(\omega)$ such that

$$T(\omega) = H(\omega)M(\omega),$$

where $H(\omega)$ is the common propagation frequency response, $M(\omega)$ is an $SU(2)$ matrix (M is two-dimensional, unitary and $\det(M) = 1$) that describes the birefringent behavior of the optical system, and ω is the angular frequency relative to the optical carrier angular frequency.

In the case of a non-birefringent system ($M = I_2$ the two-dimensional identity matrix) the related EOE frequency response is the same as what is stated in [PMY98] and is derived in Appendix B:

$$H_f(\omega) = H_e(\omega) + 2iH_o(\omega)\tilde{\eta}(\omega)$$

where $H_e(\omega) = \frac{H(\omega)+H^*(-\omega)}{2}$ is the conjugate symmetric part of $H(\omega)$ and $H_o(\omega) = \frac{H(\omega)-H^*(-\omega)}{2}$ is the conjugate antisymmetric part of $H(\omega)$. $\tilde{\eta}(\omega)$ is called *phase to intensity ratio* and gives the linear relationship between intensity and phase modulation. It is important to notice that this is actually the conjugate anti-symmetric part of the fiber optical response that is responsible for the frequency to intensity modulation conversion phenomenon.

Assuming that the optical system has first-order PMD with a Differential Group Delay τ the birefringence (Jones) matrix is given by

$$M(\omega) = e^{-i\omega\frac{\tau}{2}}|p\rangle\langle p| + e^{+i\omega\frac{\tau}{2}}|q\rangle\langle q|,$$

where $|p\rangle$ and $|q\rangle$ are the slow and fast Principal State of Polarization (PSP) of the system respectively. If we let $\gamma = |\langle q|s_{in}\rangle|^2$ be the proportion of the optical power that is launched on the fast PSP, the EOE frequency response is given by

$$H_f(\omega) = \left(H_e(\omega) + 2iH_o(\omega)\tilde{\eta}(\omega) \right) \left((1-\gamma)e^{-i\omega\frac{\tau}{2}} + \gamma e^{+i\omega\frac{\tau}{2}} \right).$$

In the following section several cases are presented based on different optical source and optical transmission medium configurations.

4.2.4 Cascade of linearized electro-optical systems

If we are now interested in the small-signal EOE response of the entire link from the source input to the receiver output including other elements than the purely passive optical system the notion of EOE response can easily be adapted to the case of devices with one optical port and one electrical port¹. The optical signal going in or coming from the optical port just has to be converted to an electrical one using the ideal photoreceiver defined in Sec. 4.2.2. The concatenation (multiplication) of those responses provides the response of the entire link.

4.2.5 Application examples

Non birefringent dispersive fiber We assume here that the optical system is a piece of single-mode fiber of length L that does not exhibit any Polarization-Mode Dispersion (PMD) behavior. Thus M is the identity matrix and the input State of Polarization (SOP) does not have any kind of influence. The optical frequency response of the fiber is assumed to be such as:

$$H(\omega, L) = e^{-i(\beta_1\omega + \frac{1}{2}\beta_2\omega^2)L}$$

where only the first two relevant terms in the Taylor expansion of the common propagation term $\beta(\omega)$ around the optical carrier frequency have been kept. The inverse of β_1 is the group velocity and β_2 is called the Group Velocity Dispersion (GVD) coefficient (both values are taken here at the optical carrier wavelength). Loss is not taken into account in the following discussion as it can be introduced in a straightforward manner without modifying the conclusions of this discussion. The conjugate symmetric and antisymmetric parts are thus:

$$\begin{cases} H_e(\omega, L) &= e^{-i\beta_1 L\omega} \cos(\theta(\omega, L)) \\ H_o(\omega, L) &= e^{-i\beta_1 L\omega} i \sin(\theta(\omega, L)) \end{cases} \quad \text{with} \quad \boxed{\theta(\omega, L) = -\frac{1}{2}\beta_2 L\omega^2}$$

which gives the following expression for the small-signal EOE response of the fiber

$$\boxed{H_f(\omega, L) = \left(\cos(\theta(\omega, L)) - 2\sin(\theta(\omega, L))\tilde{\eta}(\omega) \right) e^{-i\beta_1 L\omega}}$$

¹But it is no more a unit-free quantity in general. Its units are specified by the nature of the physical quantities supporting the signals at the different ports.

It can be readily noticed that if $\beta_2 = 0$ (at 1310nm for standard SMF for instance), the response is just that of a pure delay and the transmission is then perfect. Hereafter this coefficient is assumed to be non-zero.

In the following sections different models are introduced for the phase to intensity ratio and the impact of source chirping on the received signal power spectrum is discussed.

Balanced Mach-Zehnder modulator In the case of an ideally balanced MZM, $\tilde{\eta} = 0$ which gives:

$$H_f(\omega, L) = \cos(\theta(\omega, L))e^{-i\beta_1 L\omega}$$

There is no phase distortion induced by the fiber transmission and the power transfer function is

$$|H_f(\omega, L)|^2 = \cos^2(\theta(\omega, L)).$$

The power transfer function is represented in figure 4.8. This function has a set of zeros defined by

$$|H_f(\omega, L)|^2 = 0 \quad \Leftrightarrow \quad \exists n \in \mathbb{Z}, \quad \omega^2 = -\frac{(2n+1)\pi}{\beta_2 L}.$$

The zeros values are proportional to $1/\sqrt{L}$. Which means that the position of the notches created in the signal spectrum by the optical transmission will be divided by two when the fiber length is multiplied by four.

Numerical example We consider a 10 km piece of SMF at a wavelength of 1550 nm ($\beta_2 = -20 \text{ ps}^2/\text{km}$). The first zero occurs at a frequency $f_1 \approx 20 \text{ GHz}$.

Electro-absorption modulator We assume a simple transient chirp model in the case of an electro-absorption modulator where the instantaneous angular frequency relative to the unmodulated carrier frequency is given by

$$\frac{d\phi}{dt} = \frac{\alpha}{2} \frac{1}{P} \frac{dP}{dt},$$

where α is the modulator *chirp coefficient*, and $P(t) = P_0(1+m(t))$ is the modulated optical power. We consequently have $\tilde{\eta}(\omega) = \frac{\alpha}{2}$ (since $m \ll 1$) which yields the link EOE frequency

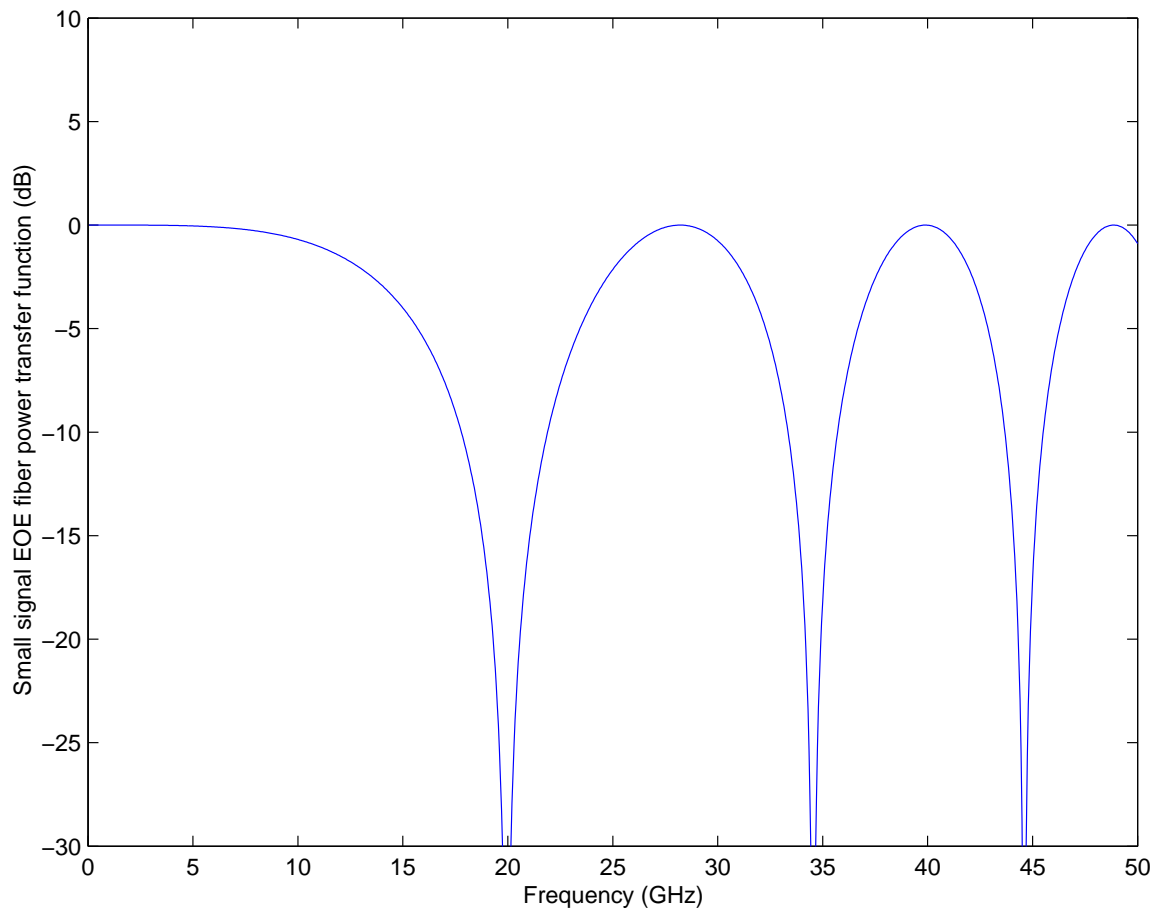


Figure 4.8: EOE power transfer function for 10 km of dispersive fiber when an unchirped source is used at 1550 nm.

response:

$$H_f(\omega, L) = \left(\cos(\theta(\omega, L)) - \alpha \sin(\theta(\omega, L)) \right) e^{-i\beta_1 L \omega}$$

There is no phase distortion and

$$|H_f(\omega, L)|^2 = \left(\cos(\theta(\omega, L)) - \alpha \sin(\theta(\omega, L)) \right)^2.$$

This function has a set of zeros defined by

$$|H_f(\omega, L)|^2 = 0 \quad \Leftrightarrow \quad \exists n \in \mathbb{Z}, \quad \omega^2 = -\frac{2}{\beta_2 L} (\arctan(1/\alpha) + n\pi).$$

This time again zeros positions scale with $1/\sqrt{L}$. Measurements of this power transfer function and its zeros for a known fiber link is a technique used for the precise measurement of an external modulator chirp coefficient.

Numerical example We consider a 10 km piece of SMF at a wavelength of 1550 nm ($\beta_2 = -20 \text{ ps}^2/\text{km}$). The first zero occurs at a frequency $f_1 \approx 26 \text{ GHz}$.

The power transfer function is represented in figure 4.9 in the case of a 50km span of SMF at 1550nm with a chirp coefficient of -2 .

Semiconductor laser The derivation from the laser rate equations of an approximate expression for the phase to intensity ratio is presented in Appendix B:

$$\tilde{\eta}(\omega) = \frac{\alpha}{2} \left(1 + \frac{\kappa P_0}{i\omega} \right).$$

In the context of laser sources α is called the *linewidth broadening factor* and always has a positive value². The first term corresponds to transient chirp (similar to what is produced by an electro-absorption modulator) and the second term is called adiabatic chirp. κP_0 is thus a frequency that characterizes the relative strength of those two effects depending on the input signal frequency content. In this simplified model κ is a real constant but it is actually complex and frequency dependent in general [PMY98]. The link EOE response

²With the convention we have chosen.

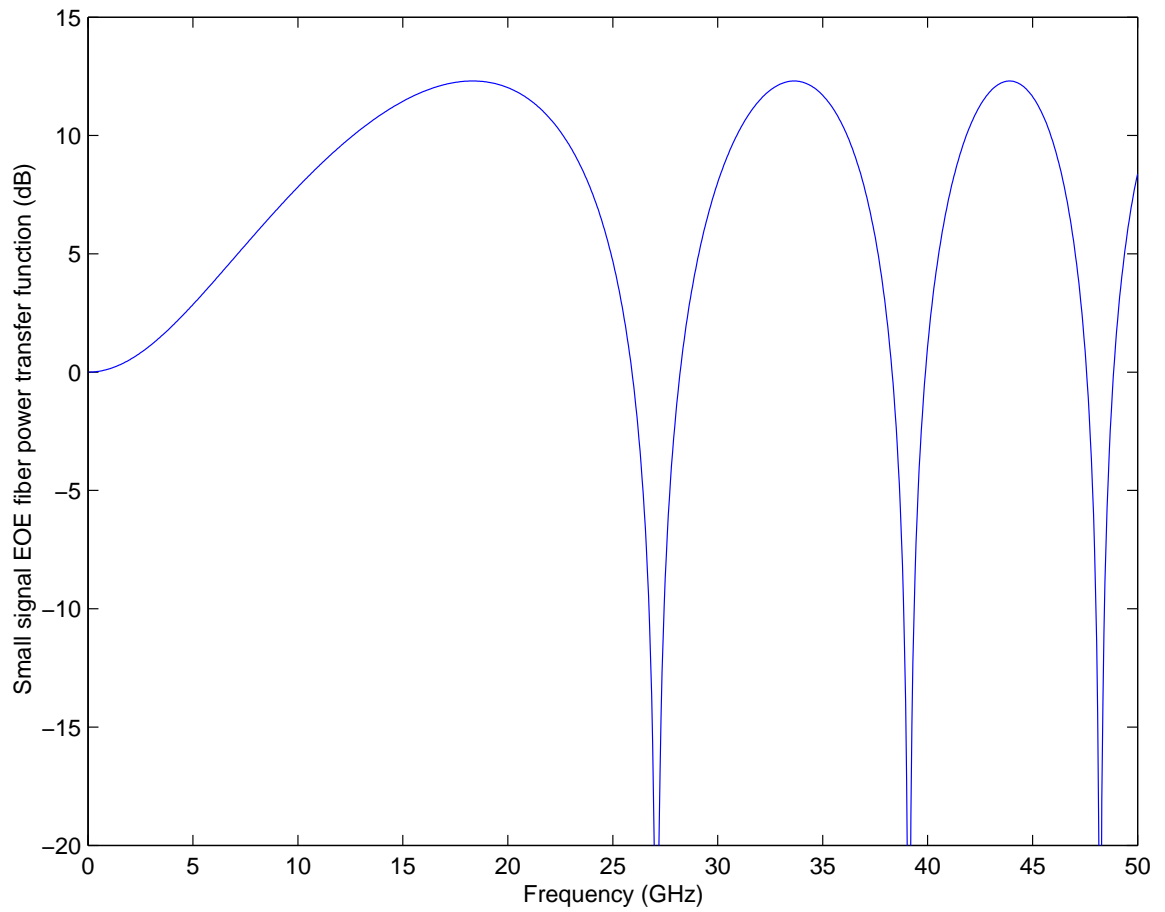


Figure 4.9: EOE power transfer function for 10 km of dispersive fiber when an source with a negative chirp coefficient is used at 1550 nm.

now becomes:

$$H_f(\omega, L) = \left(\cos(\theta(\omega, L)) - \alpha \sin(\theta(\omega, L)) + i\alpha \frac{\kappa P_0}{\omega} \sin(\theta(\omega, L)) \right) e^{-i\beta_1 L \omega}$$

It is composed of three terms. The first one describes an effect purely related to chromatic dispersion, the second one results from the interplay of chromatic dispersion and transient chirp and the last one is due to the interaction of chromatic dispersion and adiabatic chirp. The transmitted signal experiences phase distortions this time. The power transfer function is now:

$$|H_f(\omega, L)|^2 = \left(\cos(\theta(\omega, L)) - \alpha \sin(\theta(\omega, L)) \right)^2 + \alpha^2 \frac{(\kappa P_0)^2}{\omega^2} \sin^2(\theta(\omega, L))$$

In general this transfer function does not have zeros. But dips occur at points close to the zeros of the transfer function one would get ignoring adiabatic chirp. The last term becomes smaller at higher frequencies and dip values become closer and closer to zero (transient chirp domination). This is illustrated in Fig. 4.10 for a laser with a linewidth enhancement factor of 2. The phase and group delay variations are shown in Fig. 4.11 and 4.12 (The constant group delay $\beta_1 L$ has been subtracted in this figure).

Dispersive fiber with first-order PMD The results obtained in the case of a simply dispersive fiber get modified the same way in every case in the presence of first-order Polarization-Mode Dispersion (PMD). The link is assumed to have a Differential Group Delay (DGD) τ and that the input SoP $|s_{in}\rangle$ is such that the proportion of the optical power sent on the fast PSP is γ . In every case the frequency response is multiplied by the frequency dependent coefficient $(1 - \gamma)e^{-i\omega\frac{\tau}{2}} + \gamma e^{+i\omega\frac{\tau}{2}}$ and the power transfer functions by $1 - 4\gamma(1 - \gamma) \sin^2(\omega\tau/2)$. Interestingly source chirping does not interact with first order PMD.

Unchirped intensity modulation In this case the link frequency response is

$$H_f(\omega, L) = \cos(\theta(\omega, L)) \left((1 - \gamma)e^{-i\omega\frac{\tau}{2}} + \gamma e^{+i\omega\frac{\tau}{2}} \right) e^{-i\beta_1 L \omega},$$

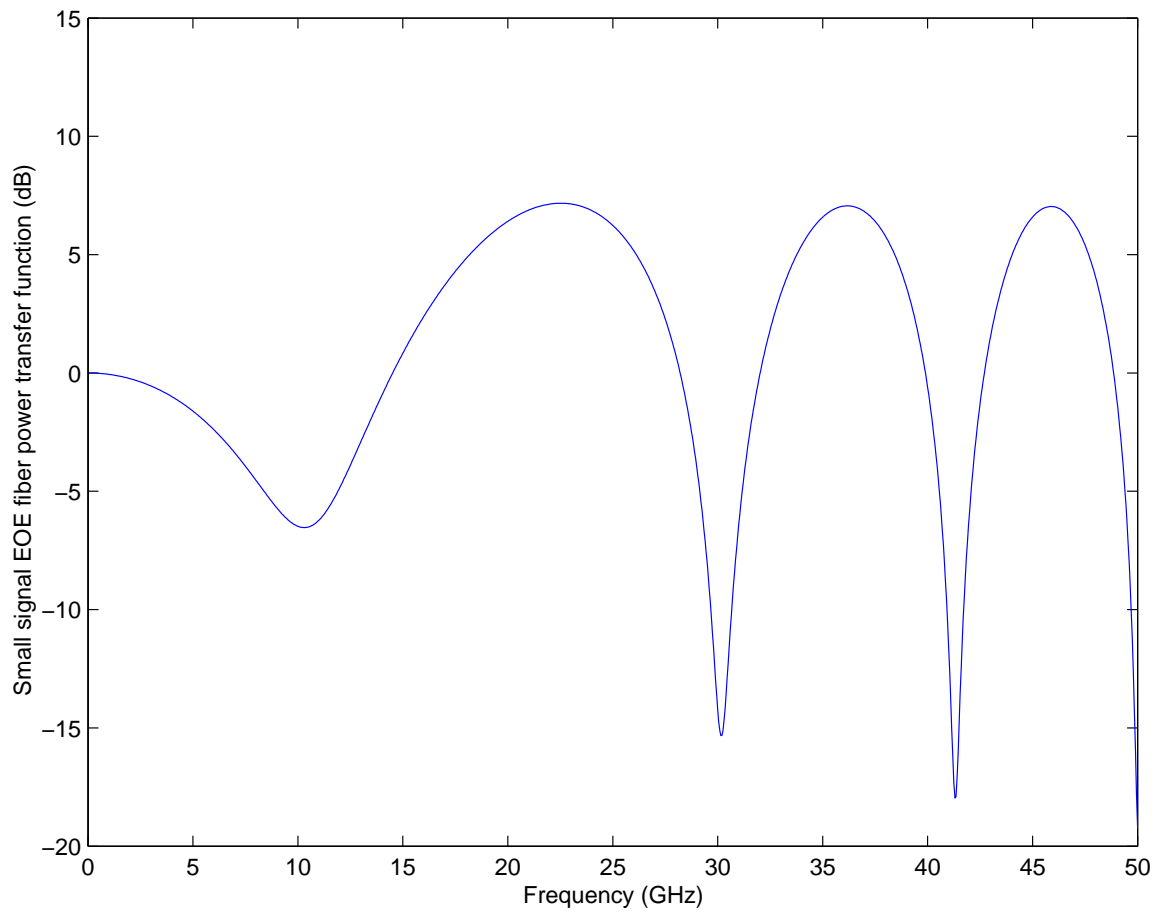


Figure 4.10: EOE power transfer function for 10 km of dispersive fiber when a semiconductor laser is used at 1550 nm.

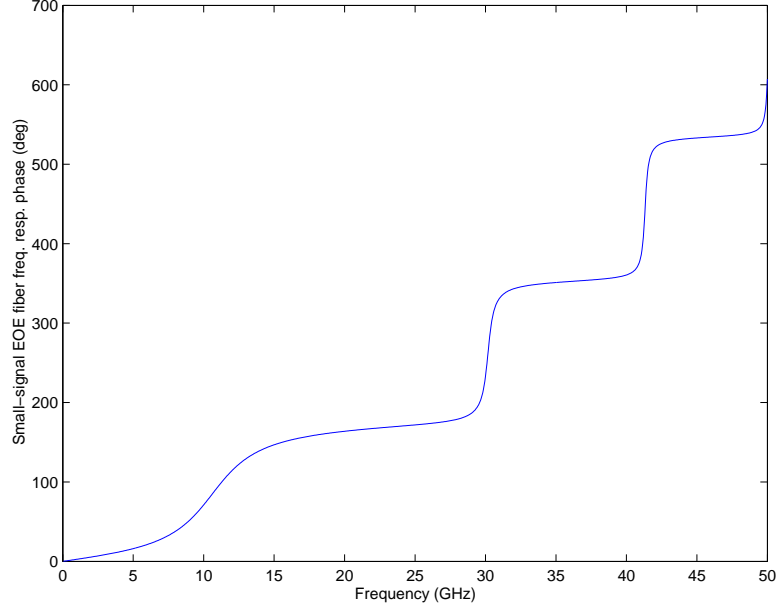


Figure 4.11: EOE response phase variations for 10 km of SMF at 1550 nm when a semiconductor laser is used.

and the power transfer function

$$|H_f(\omega, L)|^2 = \cos^2(\theta(\omega, L)) \left(1 - 4\gamma(1 - \gamma) \sin^2(\omega\tau/2)\right).$$

Transient chirp In the case of a source with transient chirp

$$H_f(\omega, L) = \left(\cos(\theta(\omega, L)) - \alpha \sin(\theta(\omega, L))\right) \left((1 - \gamma)e^{-i\omega\frac{\tau}{2}} + \gamma e^{+i\omega\frac{\tau}{2}}\right) e^{-i\beta_1 L\omega},$$

and

$$|H_f(\omega, L)|^2 = \left(\cos(\theta(\omega, L)) - \alpha \sin(\theta(\omega, L))\right)^2 \left(1 - 4\gamma(1 - \gamma) \sin^2(\omega\tau/2)\right).$$

Laser chirp When using a semiconductor laser we have

$$H_f(\omega, L) = \left(\cos(\theta(\omega, L)) - \alpha \sin(\theta(\omega, L)) + i\alpha \frac{\kappa P_0}{\omega} \sin(\theta(\omega, L))\right) \left((1 - \gamma)e^{-i\omega\frac{\tau}{2}} + \gamma e^{+i\omega\frac{\tau}{2}}\right) e^{-i\beta_1 L\omega},$$

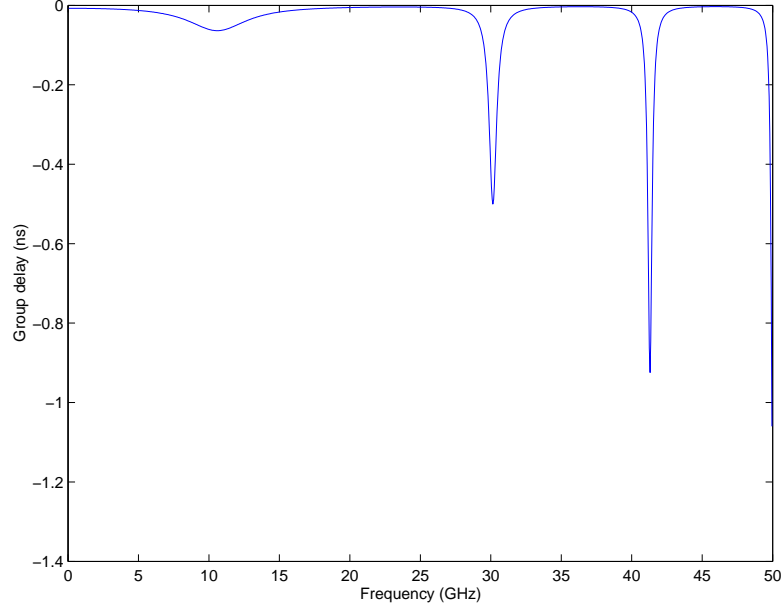


Figure 4.12: EOE response group delay variations for 10 km of fiber at 1550 nm when a semiconductor laser is used.

and

$$|H_f(\omega, L)|^2 = \left(\left(\cos(\theta(\omega, L)) - \alpha \sin(\theta(\omega, L)) \right)^2 + \alpha^2 \frac{(\kappa P_0)^2}{\omega^2} \sin^2(\theta(\omega, L)) \right) \left(1 - 4\gamma(1-\gamma) \sin^2(\omega\tau/2) \right).$$

An extension: fiber and single-sideband filter In this paragraph we still consider that the optical system is composed of a span of single-mode fiber of length L that does not exhibit any PMD behavior. Yet this time an optical filter that brings to zero one sideband of the optical spectrum is added. In practice this can be done by using a specific waveguide-based modulator structure right after a CW light source or by putting an appropriately designed optical filter before or even after the fiber span. In this case the following idealized optical frequency response of the system is assumed:

$$H(\omega, L) = e^{-i(\beta_1\omega + \frac{1}{2}\beta_2\omega^2)L} \left(\frac{1}{2} \mathbf{1}_{\omega=0} + \mathbf{1}_{\omega>0} \right),$$

where $\mathbf{1}$ is the characteristic function of the set described by its subscript (it is one if its subscript is true and zero otherwise). The second part of the expression is our model for an

ideal single-sideband (SSB) filter. Thus the conjugate symmetric and antisymmetric parts of the small-signal EOE response are now:

$$\begin{cases} H_e(\omega, L) &= \frac{1}{2} e^{i \operatorname{sign}(\omega) \theta(\omega, L)} e^{-i \beta_1 L \omega} \\ H_o(\omega, L) &= \frac{1}{2} \operatorname{sign}(\omega) e^{i \operatorname{sign}(\omega) \theta(\omega, L)} e^{-i \beta_1 L \omega} \end{cases} \quad \text{with } \theta(\omega, L) = -\frac{1}{2} \beta_2 L \omega^2,$$

which gives the following expression for the small-signal EOE response of the fiber

$$H_f(\omega, L) = \frac{1}{2} \left(1 + 2i \operatorname{sign}(\omega) \tilde{\eta}(\omega) \right) e^{i \operatorname{sign}(\omega) \theta(\omega, L)} e^{-i \beta_1 L \omega}$$

This expression does not look at all like what one gets for a double-sideband signal. A close look at the terms generating the output signal page 170 gives an interesting insight in the cause of such a fact. It appears that the photodetector generates an electrical signal output the spectrum of which is composed of the superposition of the positive and negative frequency components appearing in the optical signal. When the optical signal is double-sideband the consequence is an interference-like pattern between the negative and positive frequency components that gives rise to zeros in the instance of a dispersive link with no chirp and amplitude variations in general. When the optical signal is single-sideband the same process generates a double-sideband electrical signal but now only one sideband is used to generate positive and negative frequency components in the output signal spectrum. Consequently no interference pattern is present this time. Yet phase distortions experienced by the optical signal now show up in the electrical signal. In the following paragraphs those facts are highlighted considering different types of optical sources.

Unchirped intensity modulation In this case the EOE frequency response reduces to

$$H_f(\omega, L) = \frac{1}{2} e^{i \operatorname{sign}(\omega) \theta(\omega, L)} e^{-i \beta_1 L \omega}$$

and the optical link acts like an all-pass filter. If we do not take into account the linear phase term due to the propagation delay $\beta_1 L$, the residual phase is

$$\psi(\omega) = \operatorname{sign}(\omega) \theta(\omega, L) = -\operatorname{sign}(\omega) \frac{1}{2} \beta_2 L \omega^2,$$

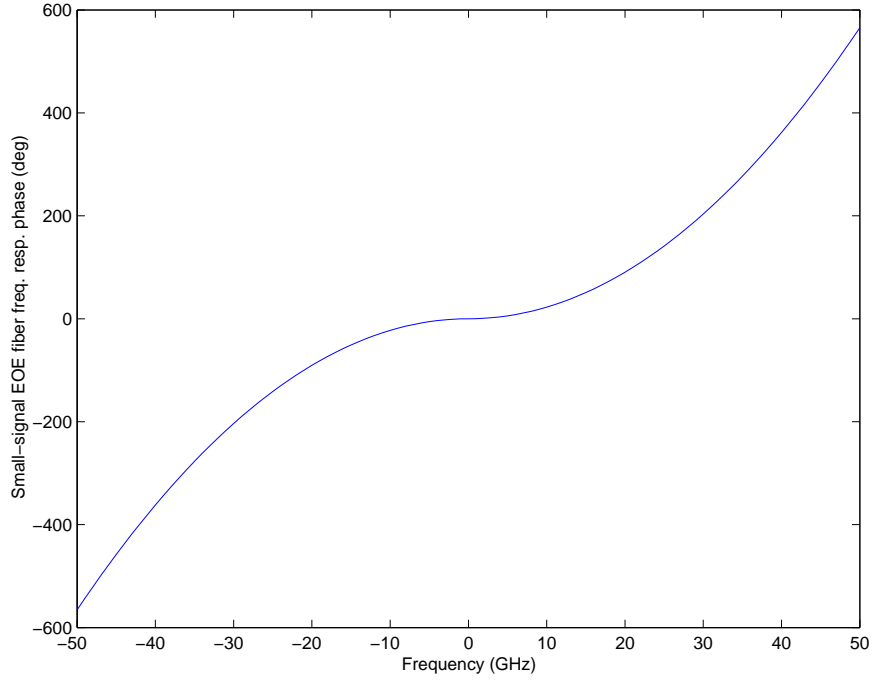


Figure 4.13: EOE response phase variations in the case of SSB filtering and 10 km of SMF at 1550 nm.

displayed in Fig. 4.13 and the residual group delay is given by

$$\tau(\omega) = -\frac{d\psi}{d\omega} = \beta_2 L |\omega|.$$

Transient chirp When using a source with pure transient chirp the EOE frequency response becomes

$$H_f(\omega, L) = \frac{1}{2}(1 + i \operatorname{sign}(\omega)\alpha)e^{i \operatorname{sign}(\omega)\theta(\omega, L)} e^{-i\beta_1 L\omega}$$

This is an all-pass filter again. This time the expression includes a multiplicative term that induces a phase jump going from negative to positive frequencies. The case when the optical system used is reduced to the SSB filter alone gives an interesting result. The EOE

frequency response is then

$$H_f(\omega, L) = \frac{1}{2}(1 + i \operatorname{sign}(\omega)\alpha)e^{-i\beta_1 L\omega},$$

and the output signal is a linear combination of the input signal and its Hilbert transform.

Laser chirp The EOE frequency response now becomes

$$H_f(\omega, L) = \frac{1}{2}(1 + \operatorname{sign}(\omega)\alpha \frac{\kappa P_0}{\omega} + i \operatorname{sign}(\omega)\alpha)e^{-i\beta_1 L\omega}.$$

The filter is no more all-pass. This expression is now singular in the vicinity of 0. (This artifact would disappear with a more realistic SSB filter model. What is here a sign function would appear in reality as a smooth and odd function that goes to 0 in the vicinity of the 0 frequency faster than ω .)

4.3 Channel impairments and noise

4.3.1 Linear impairments

As seen in the previous section the linearized response of the chain formed by the directly modulated laser, a piece of dispersive fiber and a photoreceiver provides insight in the impairments experienced by the transmitted signal.

The directly modulated laser transmission wavelength is specified within 20 nm of the nominal value equal to 1310 nm the standard SMF zero-dispersion wavelength. In this range the group velocity dispersion varies between $+2 \text{ ps}^2/\text{km}$ and $-2 \text{ ps}^2/\text{km}$. Fig. 4.14 and Fig. 4.15 show the linearized frequency response of a 10-km and a 40-km fiber link respectively. These results are obtained by multiplying (concatenating) the laser EO linearized response presented in Appendix B with the fiber link EOE response. These filtering effects impact the signal to noise ratio at the end of the link by changing the signal power frequency distribution. This contribution has to be taken into account together with noise enhancement and non-linear effects in order to determine the net effect on SNR.

First-order PMD translates into translates into the interference of the carrier signals with themselves in each channel. Since the signaling rate is approximately twenty times smaller than in OOK systems where the effects of PMD are apparent the impact is expected to be very limited and readily compensated for thanks to linear baseband signal processing.

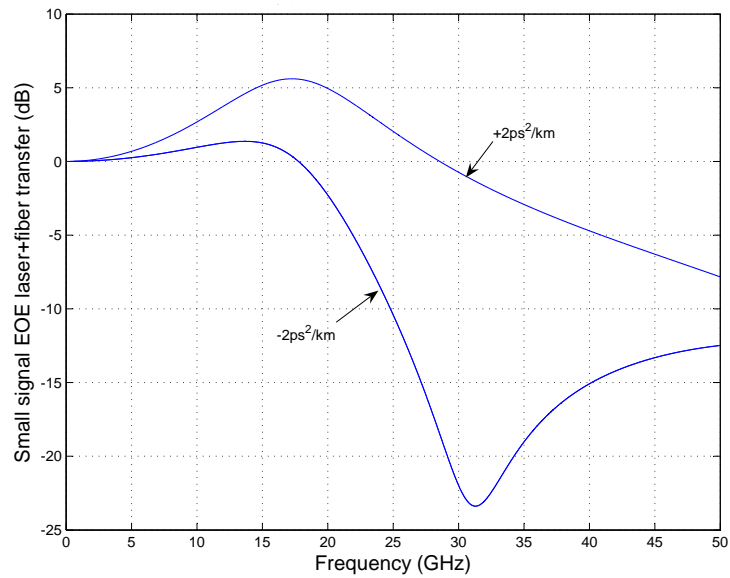


Figure 4.14: Linearized response of the laser and fiber (ideal photodiode) for a laser bias set to 50 mA above threshold and a fiber with group velocity dispersion values of $+2 \text{ ps}^2/\text{km}$ and $-2 \text{ ps}^2/\text{km}$ and length 10 km.

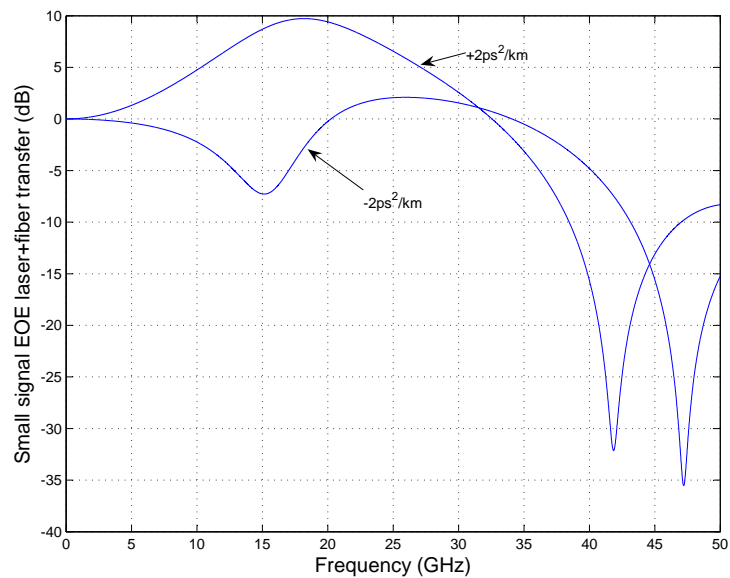


Figure 4.15: Linearized response of the laser and fiber (ideal photodiode) for a laser bias set to 50 mA above threshold and a fiber with group velocity dispersion values of $+2 \text{ ps}^2/\text{km}$ and $-2 \text{ ps}^2/\text{km}$ and length 40 km.

4.3.2 Non-linear impairments

This section presents the different sources of transmission non-linearity the optical subcarrier multiplexed system of interest is subjected to. These nonlinearities have a direct impact on the communication system performance and have extensively been studied in the field of hybrid fiber coax (HFC) and common-antenna television (CATV) [PD97, PDMF91, PD93]. They are reviewed in turn and characteristic numerical values for associated distortion measures are computed in an effort to separate significant from negligible impairments in the system under study.

Sub-carrier multiplexed system nonlinearity measures If the system nonlinear response can be approximated by a power series $x + ax^2 + bx^3 + \dots$ a signal composed of multiple frequency carriers will incur distortions that can be categorized according to the order (or degree) of the system response monomes at the source of these distortions. In CATV applications ([PD97] the dominant distortions result from the terms of order 2 and 3. For simplicity, the input signal is assumed to be

$$s(t) = \sum_{j=1}^K m \cos(2\pi f_j t + \phi_j),$$

where all the carriers have the same time independent amplitude and randomly distributed time independent relative phases. In this case quadratic distortions result from the mixing of duets of frequency carriers and cubic distortions from the mixing of triplets. If the carriers form a regularly spaced grid which is the case in practice some of these mixing components fall outside the carrier grid and others fall in the vicinity of signal carriers. Only the latter distortion components have detrimental effects on a subcarrier multiplexed transmission system as others can be filtered out.

The effect of second and third-order nonlinearities in subcarrier multiplexed systems is characterized thanks to two measures: the *composite second-order* distortion (CSO) and the *composite triple beat* distortion (CTB). The CSO and CTB can be defined in each individual channel d by forming the ratio of the second-order signal distortion component

to the considered carrier channel power:

$$\begin{aligned} \text{CSO}_{\text{dB}}(d) &= 10 \log_{10} \left(N_{\text{CSO}}(d) (am)^2 \right), \\ \text{CTB}_{\text{dB}}(d) &= 10 \log_{10} \left(N_{\text{CTB}}(d) \left(\frac{3}{2} bm^2 \right)^2 \right), \end{aligned}$$

where a , b and m are as defined on page 90, and $N_{\text{CSO}}(d)$ is the second-order product count in channel d , that is to say the number of duets of carriers for which the mixing component appears in the vicinity of channel d , and $N_{\text{CTB}}(d)$ is the third-order product count, the number of carrier triplets for which the mixing component falls in the vicinity of channel d . A number independent from the channel d considered is usually computed or measured based on a approximation or a bound for $N_{\text{CSO}}(d)$ and $N_{\text{CTB}}(d)$ that does not depend on d . In later sections the following inequalities are used:

$$\begin{aligned} N_{\text{CSO}}(d) &\leq K - 1, \\ N_{\text{CTB}}(d) &\leq \frac{3}{8} K^2 - \frac{1}{2} K. \end{aligned}$$

The following practical procedure is used to measure the aggregate of these (as well as higher-order) nonlinear distortions: one channel is selected and turned off while all the other channels are operating, and the signal power in the turned-off channel is measured.

Directly modulated laser non-linear response and clipping Fig. 4.16 illustrates the phenomenon laser clipping. If adiabatic modulation can be assumed the output power to input current relationship is quasi linear for currents above the laser threshold. If there are current incursions below the threshold current this part of the signal is clipped in the output power waveform. In the case of lightwave subcarrier multiplexing as can be found in hybrid fiber-coax (HFC) systems a high number of QAM modulated carriers is used and the input signal can be modelled as Gaussian random process and clipping as an impulse noise source [Lam00, CW97]. The corresponding signal to noise ratio in that case is only dependent upon the total input signal standard deviation.

This model has some obvious limitations when using input signals with a low channel count (in the tens) and high frequencies. It was shown on page 45 that the peak to average ratio of a signal consisting in QAM-16 on 16 carriers is close to 7.6 and the signal peak is

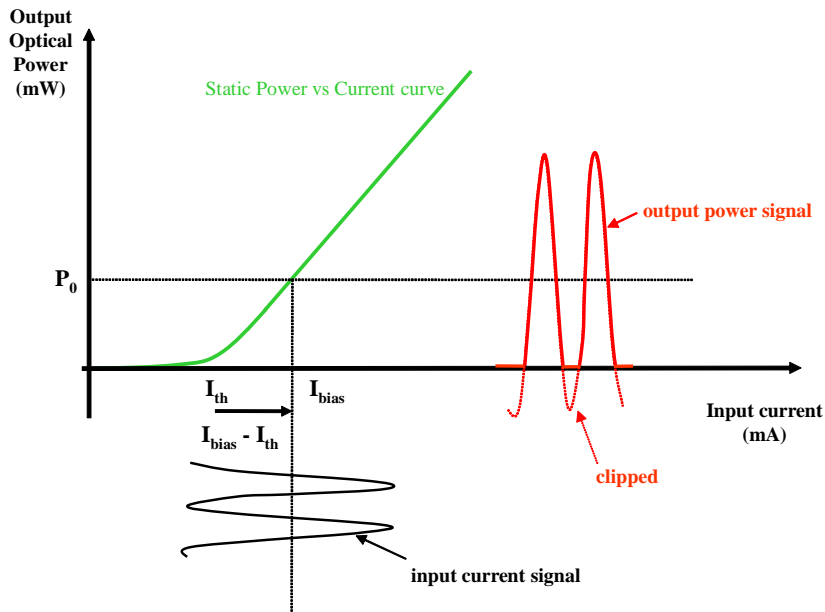


Figure 4.16: Signal clipping non-linear distortion when the input current signal peak value exceeds the bias current above threshold value.

obviously finite. This means that if the input signal standard deviation (or rms OMI) is lower than 13% signal clipping does not occur. Furthermore frequencies used are not far smaller than the laser characteristic relaxation frequency the laser dynamics cannot be reduced to its adiabatic behavior. The laser response in the frequency range considered is complex and could prove to be not as linear as expected when making a steady state assumption. A detailed model of the laser dynamics is needed. Yet the simplifying assumptions of a clipping impulse noise determined by the laser adiabatic modulation as the main source of laser modulation nonlinearity together with a limited bandwidth determined by the laser linearized response will form the basis for the information channel model introduced in Sec. 4.6 and the evaluation of channel capacity.

Effects of laser chirp and fiber dispersion Chirp is the variation of optical carrier wavelength with output power that exists in most optical transmitters and in directly modulated lasers in particular. Since chromatic dispersion is a variation of the group delay experienced by a transmitted signal the combination of chirp and chromatic dispersion

turns the modulation of wavelength due to modulated power variations into additional power modulation. The dependence of this unwanted additional modulation on the original modulating signal is nonlinear.

Using relationships presented in [PD97, PD93] and adapted to take into account adiabatic as well as transient chirp the CSO in any channel is bounded by

$$\text{CSO}_{\text{dB}} \leq 10 \log_{10} \left((K-1) \left(\gamma^2 + \left(\frac{\alpha \omega_M}{2} \right)^2 \right) m^2 \omega_M^2 \left((\beta_2 L)^2 + \frac{1}{12} (\bar{\tau}'_0)^2 \right) \right), \quad (4.1)$$

and the CTB in any channel is bounded by

$$\text{CTB}_{\text{dB}} \leq 10 \log_{10} \left((3K^2/8 - K/2) (m|\beta_2|L\omega_M)^4 \left(\frac{3}{4} \left(\gamma^2 + \left(\frac{\alpha \omega_M}{2} \right)^2 \right) + \frac{1}{48} \omega_M^2 \right) \right), \quad (4.2)$$

where K is the number of multiplexed RF channels, γ and α are the directly modulated laser adiabatic chirp coefficient and linewidth broadening factor respectively both defined in Appendix B page 173, ω_M is an upper bound for the carrier frequencies, m is the optical modulation depth per channel equal to $\sqrt{2/K}$ OMI, β_2 is the group velocity dispersion at the modulated optical carrier frequency ω_0 , $\bar{\tau}'_0$ is value of the derivative of the fiber PMD vector at the optical carrier frequency ω_0 and L is the fiber length.

The following numerical values are all chosen in excess of actual values in order to estimate a numerical upper bound for the CSO due to the interplay between chirp and fiber dispersion: $K = 16$, $\gamma/2\pi = 8$ GHz, $\alpha = 4$, $\omega_M/2\pi = 14$ GHz, $m = 10\%$ corresponding to an OMI of about 30% with $K = 16$, $|\beta_2| = 2$ ps²/km, $L = 2$ km. For a fiber with a PMD coefficient D_{pmd} the average value for $(\tau'_0)^2/L^2$ is $\frac{1}{3} D_{\text{pmd}}^4$ according to Sec. 2.3.4. If a value of 1 ps/ $\sqrt{\text{km}}$ is assumed for D_{pmd} the average PMD effect can be neglected in comparison with chromatic dispersion effects. With these numerical values an approximate upper bound for the CSO due to chirp and dispersion is

$$\text{CSO}_{\text{dB}} \approx -32 \text{ dB}$$

and

$$\text{CTB}_{\text{dB}} \approx -71 \text{ dB}.$$

Effects of chromatic dispersion and self-phase modulation Self-phase modulation (SPM) is the variation of optical phase induced by changes in the fiber nonlinear index

(see Sec. 2.2.2) with variations of the modulated signal power. Combined with chromatic dispersion present in a dispersive medium such as fiber the induced phase modulation creates additional power modulation that depends on the original power signal in a nonlinear fashion.

Using relationships presented in [PD97, PDMF91] and adapted to take into account adiabatic as well as transient chirp the CSO in any channel is bounded by

$$\text{CSO}_{\text{dB}} \leq 20 \log_{10} \left(\sqrt{K-1} \frac{1}{2} m |\beta_2| \omega_M^2 a_0 P_0 L_{\text{eff}}^2 \right), \quad (4.3)$$

and the CTB in any channel is bounded by

$$\text{CTB}_{\text{dB}} \leq 10 \log_{10} \left(\sqrt{3K^2/8 - K/2} \frac{1}{2} (m |\beta_2| \omega_M^2 a_0 P_0 L)^2 \frac{1}{\alpha_l^2} \right), \quad (4.4)$$

where K is the number of multiplexed RF channels, m is the optical modulation depth per channel equal to $\sqrt{2/K} \text{OMI}$, β_2 is the group velocity dispersion at the modulated optical carrier frequency ω_0 , ω_M is an upper bound to the carrier frequencies, $a_0 = \frac{2\pi n_2}{\lambda_0 A_{\text{eff}}}$ where n_2 is the nonlinear refractive index, λ_0 is the optical carrier wavelength in vacuum, A_{eff} is the effective core area, P_0 is the average optical power at the transmitter output and $L_{\text{eff}}^2 = \frac{1}{\alpha_l} (L - (1 - e^{-\alpha_l L})/\alpha_l)$ with α_l the fiber loss per unit distance and L the fiber length.

Using the numerical values $n_2 = 3 \cdot 10^{-20} \text{ m}^2 \cdot \text{W}^{-1}$, $A_{\text{eff}} = 50 \mu\text{m}^2$, $\lambda_0 \approx 1310 \text{ nm}$, $P_0 = 10 \text{ mW}$, $L = 10 \text{ km}$, $\omega_M/2\pi = 14 \text{ GHz}$, $|\beta_2| = 2 \text{ ps}^2/\text{km}$, $m = 0.1$ we get estimates for the CSO and CTB due to the interplay of SPM and chromatic dispersion:

$$\text{CSO}_{\text{dB}} \approx -80 \text{ dB}$$

and

$$\text{CTB}_{\text{dB}} \approx -148 \text{ dB}.$$

Analog front-end linearity High-speed semiconductor circuits designs are based on transistors which are a fundamentally nonlinear devices. A great amount of techniques exists to implement linear systems using such nonlinear components. For the present system acceptable levels of nonlinearity for the planned signal levels need to be specified as part of a noise and nonlinearity budget allocation.

4.3.3 Semiconductor laser noise

Light produced by a semiconductor laser even though still very pure is noisy by nature due to fundamental phenomena such as spontaneous emission and electrical carriers fluctuations. Laser light can be described by a monochromatic wave bearing amplitude and phase random fluctuations.

Relative intensity noise Relative intensity noise (RIN) designates random fluctuations in the laser output intensity ([AD93] p.261). The characterization of such a noise is critical in IM/DD systems where information is encoded in optical intensity waveforms. Since the optical transmitter can be considered source of signal and noise simultaneously the associated signal to noise ratio is independent of the transmission distance and attenuation. This is why RIN produces a noise floor limiting optical communication systems ultimate performance. As a matter of fact for a given target capacity if this noise level is too high reliable communication might simply be impossible given other physical constraints limiting the maximum signal power level.

A typical RIN (double sided) power spectral density level for the laser used in this system under average operating conditions is

$$\text{RIN}_{\text{laser}} = -145 \text{ dB} \cdot \text{Hz}^{-1}.$$

For a bandwidth of 14 GHz and an OMI of 10% (which is a realistic lower bound for actual modulation index values) the signal to intensity noise ratio is close to 21 dB

Phase noise Even though light phase is not used to carry information in an IM/DD system phase noise cannot be overlooked. In particular phase-modulation to intensity-modulation conversion mechanisms such as dispersion turn phase noise into intensity noise. Since the intensity and phase noise sources are correlated in a laser transmitter the conversion of phase fluctuations to intensity fluctuations can have non-trivial consequences on the signal to noise ratio as demonstrated in [MPY00].

4.3.4 Reflection-induced relative intensity noise

Assuming that reflection induced noise is due to two discontinuities in the fiber link, a rough estimate of the reflection-induced relative intensity noise can be computed thanks to the

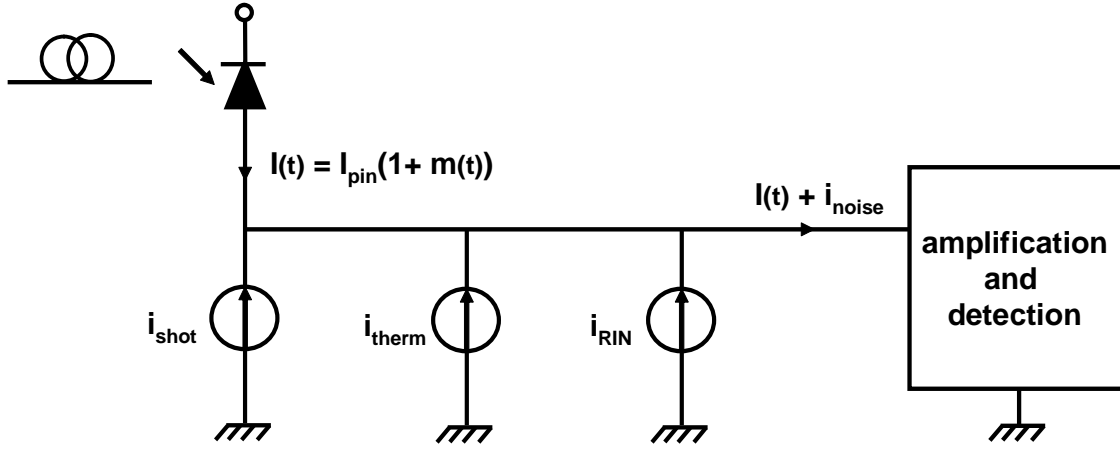


Figure 4.17: Signal and noise model at the optical receiver.

expression provided in [DS91] for cases where the transmitter is a directly modulated DFB laser:

$$\text{RIN}_{\text{refl}} = 10 \log_{10} \left(4\sqrt{2\pi} \frac{R_1 R_2}{\sqrt{K} m \sqrt{\gamma^2 + \left(\frac{\alpha\omega_M}{2}\right)^2}} \right).$$

Using standard requirements for optical connectors used in digital optical transmission we choose $R_1 = R_2 = -30$ dB. Other parameter values being chosen as in Sec. 4.3.2 we get the following estimate for the reflection-induced RIN level:

$$\text{RIN}_{\text{refl}} = -159 \text{ dB} \cdot \text{Hz}^{-1}.$$

It is noteworthy that as opposed to nonlinear impairments presented in previous sections the detrimental effects of reflections are reduced by a highly chirped laser source.

4.3.5 Photo-receiver and amplification stages noise contributions

Fig. 4.17 describes a model for an optical communication system referring the signal and noise to the output of an ideal noiseless photodiode with responsivity R_{resp} converting the average received optical power P_0 into a current $I_{\text{pin}} = R_{\text{resp}} P_0$. Noise contributions appear as stochastic current sources producing white noise in the receiver noise bandwidth BW_N . They model the current noise contributions associated with shot noise, receiver

thermal noise and optical relative intensity noise. Assuming a simple high-speed receiver design where the photodiode current is converted into a voltage thanks to a $50\ \Omega$ impedance followed by low noise voltage amplification stages, we have the following expression for the variance of each noise contribution:

$$\begin{aligned}\sigma_{\text{therm}}^2 &= \frac{4k_B T_0}{R} F \cdot \text{BW}_N \\ \sigma_{\text{shot}}^2 &= 2q I_{\text{pin}} \cdot \text{BW}_N \\ \sigma_{\text{RIN}}^2 &= \text{RIN} I_{\text{pin}}^2 \cdot \text{BW}_N,\end{aligned}$$

where $k_B = 1.38 \cdot 10^{-23}\ \text{J} \cdot \text{K}^{-1}$ is Boltzmann's constant, T_0 is the operating temperature assumed to be 293 K, R is the load resistor assumed to be $50\ \Omega$, F is the noise figure of subsequent electrical amplification stages, $q = 1.6 \cdot 10^{-19}\ \text{C}$ is the electron charge, I_{pin} is the average photocurrent at the photodiode output, RIN is the single-sided relative intensity noise power spectral density assumed to be constant. The optical modulation index (OMI) being the standard deviation of the signal $m(t)$ the signal to noise ratio is

$$\text{SNR} = \frac{\text{OMI}^2 I_{\text{pin}}^2}{\text{BW}_N \left(4 \frac{k_B T_0}{R} F + 2q I_{\text{pin}} + \text{RIN} I_{\text{pin}}^2 \right)}.$$

If the optical transmitter of choice is a directly modulated laser with external efficiency η_{ext} the average received photocurrent is

$$I_{\text{pin}} = R_{\text{resp}} e^{-\alpha_l L} \eta_{\text{ext}} (I_b - I_{\text{th}}),$$

where the loss of a fiber link of length L is accounted for thanks to the fiber loss coefficient α_l , $I_b - I_{\text{th}}$ is the laser bias current above threshold and η_{ext} is the laser external efficiency.

For a very short link such that $e^{\alpha_l L} \approx 1$, a photodiode with responsivity $R_{\text{resp}} = 0.7\ \text{A} \cdot \text{W}^{-1}$, a laser with $\eta_{\text{ext}} = 0.15\ \text{W} \cdot \text{A}^{-1}$ biased at 50 mA above laser threshold, a temperature T_0 of 293 K, a noise figure F of 3 dB, a RIN of $-140\ \text{dB} \cdot \text{Hz}^{-1}$ for that bias and a noise bandwidth of approximately 14 GHz numerical values for noise current rms

contributions are:

$$\begin{aligned}\sigma_{\text{therm}} &\approx 3 \mu\text{A} \\ \sigma_{\text{shot}} &\approx 5 \mu\text{A} \\ \sigma_{\text{RIN}} &\approx 60 \mu\text{A}.\end{aligned}$$

When expressed in dB_A thermal noise stays constant with increasing fiber length L , shot noise decreases linearly with L and RIN noise decreases twice as fast as shot noise. The signal level decreases similarly to the RIN noise level with L meaning that at short distance RIN is dominant while at higher distances receiver thermal noise and ends up becoming the greatest contributor. In general the best noise level/received optical power trade-off is obtained when shot noise is dominant.

4.4 Dominant contributions

In the light of the previous numerical evaluations it appears that:

- Thorough characterization of the laser dynamics and noise behavior is critical,
- Receiver noise needs to be taken into account but channel noise is dominated by laser relative intensity noise at short distances,
- Optical signal propagation in fibers need only be described under the linear assumption as is done in Sec. 2.3.

The first two points are addressed in the following section. The third point allows us in particular to use the fiber models developed in Sec. 2.3.2 for the design of link simulation and performance evaluation tools presented in Sec. 5.1.2.

4.5 Directly modulated laser model and measurements

Given the highlighted importance of the DML dynamic and noise behavior in the transmission chain operation the present section delves into a detailed model for a commercially available cooled DFB DML, its numerical implementation as well as its experimental validation.

4.5.1 Laser rate equation and parameters

Rate equations with (N, P, ϕ) variables The dynamic behavior of a semiconductor laser can be modelled by a system of nonlinear ordinary differential equations ruling the evolution of the laser state variables namely the *electron number* N and the *photon number* P . Such variables are usually defined as dimensionless variables. But for practical purposes it is convenient to define normalized versions of these bearing dimension.

The set of normalized³ rate equations ruling the dynamics of semiconductor laser of interest is as follows:

$$\begin{cases} \frac{dN}{dt} = i_L - G(N, P)P - R_{\text{rec}}(N) \\ \frac{dP}{dt} = (G(N, P) - \alpha_L)P + R_{\text{sp}}(N) \end{cases}$$

where i_L is the injected current in mA, G is the laser gain, α_L is the loss coefficient which includes mirror and inside cavity material loss, R_{sp} is the rate of creation of photons due to spontaneous emission and R_{rec} the rate of “destruction” of electrons through different electron-hole recombination processes. The gain coefficient can be expressed as

$$G(N, P) = \frac{G_0}{1 + \varepsilon P} \ln\left(\frac{N}{N_T}\right),$$

where ε is the *gain compression factor* and N_T is the *carrier number at transparency*. The carrier recombination rate takes the form

$$R_{\text{rec}}(N) = AN + BN^2 + CN^3,$$

where A is the *nonradiative recombination* coefficient, B is the *radiative recombination* coefficient and C is the *Auger coefficient* [AD93]. The net effect of spontaneous emission on the rate equations is given by the R_{sp} factor related to the carrier number through the relationship

$$R_{\text{sp}}(N) = \beta_{\text{sp}}N^2,$$

where β_{sp} is the *spontaneous emission factor*.

Since the time scale unit is 1 ns and the injected current is expressed in mA and does not appear in the equations divided by the electron charge, carrier and photon numbers

³This is why quantities such as the electron charge, the volume of the gain region and the laser mode confinement factor do not appear here.

are expressed in pC. This choice of units translates into the following units for the rate equation parameters:

$$\begin{aligned}
 G_0 & : \text{ ns}^{-1} \\
 \varepsilon & : \text{ pC}^{-1} \\
 N_T & : \text{ pC} \\
 A & : \text{ ns}^{-1} \\
 B & : \text{ ns}^{-1} \cdot \text{ pC}^{-1} \\
 C & : \text{ ns}^{-1} \cdot \text{ pC}^{-2} \\
 \alpha_L & : \text{ ns}^{-1} \\
 \beta_{\text{sp}} & : \text{ ns}^{-1} \cdot \text{ pC}^{-1},
 \end{aligned}$$

and the output optical power expressed in mW is then given by $P_{\text{out}} = KP$ where K depends on the emission efficiency of the laser. For the laser we consider here, $K = 50.3 \text{ mW} \cdot \text{ pC}^{-1}$ and corresponds to an output power of 6 mW when a constant bias current of 40 mA above the laser threshold flows into the device.

If not only the power but also the phase of the optical field coming out of the laser is of interest, a third state variable ϕ has to be taken into account. Its own evolution equation has to be added to the set of rate equations and is as follows:

$$\frac{d\phi}{dt} = \frac{\alpha}{2}(G_0(N) - \alpha_L),$$

where α is the *linewidth broadening factor*⁴ and has a value comprised between 2.5 and 4, and $G_0(N) = G_0 \ln(N/N_T)$ is the *unsaturated gain*.

Rate equations with (N,E) variables Another set of variables can be used to describe the laser internal state, namely the carrier number N and a complex phasor E describing the internal optical field. $|E|^2$ is scaled such that it is equal to P . And as pointed out in [Hen86] and [AD93], P is indeed only a conveniently scaled measure of the optical intensity proportional to $|E|^2$. In the context of a semiclassical laser theory this point is important when discussing laser intensity noise since, though optical intensity and the (rigorously defined) photon number may be scaled to have the same ensemble average⁵,

⁴Sometimes called *linewidth enhancement factor*.

⁵Hence we did not need to make any distinction between those two quantities before when talking about the deterministic evolution of this average. We keep the letter P to designate this intensity-related "photon number" in the following paragraphs.

they have different probability distributions [Hen86]. The laser rate equations can also be formulated as follows:

$$\begin{cases} \frac{dN}{dt} &= i_L - G(N, |E|^2)|E|^2 - R_{rec}(N) \\ \frac{dE}{dt} &= \frac{1}{2} \left(\tilde{G}(N, |E|^2) - \alpha_L \right) E \end{cases}$$

where $\tilde{G}(N, P) - \alpha_L = (G(N, P) - \alpha_L) + i\alpha(G_0(N) - \alpha_L)$. The optical field phasor at the output of the laser is given by $E_{out}(t) = \sqrt{K}E(t)$.

As will be shown this formulation can provide advantages in terms of its numerical implementation of the model in cases of interests here.

4.5.2 Laser noise model

Spontaneous emission and carrier recombination noise sources A fully quantum mechanical description of the physical system (active material+electromagnetic field modes inside the cavity), which would rely on the use of observable variables defined on the system Hilbert space, would allow one to derive the statistics of the results of measures of physical quantities such as the laser output power. A simpler semiclassical theory ("quantum mechanical" gain material coupled to a "classical" electromagnetic field) can accurately describe the system. Yet the random nature of the observations has to be taken into account and imported from quantum theory considerations (spontaneous emission can only be predicted in this framework) as explained in [Hen86]. This is done by adding *a posteriori* defined random processes turning the rate equations into stochastic differential equations. This can be done by adding Langevin forces for the evolution of each variable of the system $F_N(t)$, $F_P(t)$ and $F_\phi(t)$. We prefer here to use the stochastic differential equations theory notations⁶

$$\begin{cases} dN_t &= (i_L(t) - G(N_t, P_t)P_t - R_{rec}(N_t)) dt + dN_t^{sp} \\ dP_t &= ((G(N_t, P_t) - \alpha_L) P_t + R_{sp}(N_t)) dt + dP_t^{sp} \\ d\phi_t &= \frac{\alpha}{2} (G_0(N_t) - \alpha_L) dt + d\phi_t^{sp} \end{cases}$$

where N^{sp} , P^{sp} and ϕ^{sp} are Brownian motions (the superscript ^{sp} is used here to designate the random walk stochastic processes) i.e., continuous-time white Gaussian noise processes.

⁶Time t appears as a subscript for each stochastic process.

The underlying markoffian assumption is valid in the case of semiconductor lasers as explained in [Hen86]. Those random processes result from the randomness of the carrier recombination and spontaneous emission mechanisms and their diffusion coefficients are given by⁷ [Hen83, AD93]

$$\begin{aligned}
2D_{PP} &= 2R_{\text{sp}}(N)P \\
2D_{NN} &= 2(R_{\text{sp}}(N)P + R_{\text{rec}}(N)) \\
2D_{PN} &= -2R_{\text{sp}}(N)P \\
2D_{\phi\phi} &= \frac{R_{\text{sp}}(N)}{2P} \\
2D_{\phi P} &= 0 \\
2D_{\phi N} &= 0.
\end{aligned}$$

It appears that photon number and carrier number noise sources have an intuitive structure. The carrier number noise source is actually composed of two independent ones and one of them is fully anti-correlated to the photon number noise source. This accounts for the spontaneous emission process where carrier number drops one unit (electron-hole recombination) when photon number increases by one. The other part of the carrier number noise source accounts for fluctuations stemming from other electron-hole recombination mechanisms. When operating above threshold laser noise is spontaneous emission dominated and the second term in the expression of $2D_{NN}$ can be neglected. We hence drop this term from now on.

Formulation with (N,E) variables As derived in Appendix C, the stochastic rate equations for the carrier number and optical field phasor are

$$\begin{cases} dN_t &= (i_L(t) - G(N_t, |E_t|^2)|E_t|^2 - R_{\text{rec}}(N_t)) dt - (E_t^* dE_t^{\text{sp}} + E_t dE_t^{\text{sp}*}) \\ dE_t &= \frac{1}{2} (\tilde{G}(N_t, |E_t|^2) - \alpha_L) E_t dt + dE_t^{\text{sp}} \end{cases}$$

where E^{sp} is a Brownian motion in the complex plane representing the spontaneous emission noise contribution between time 0 and time t . Infinitesimal increments of its real and

⁷Those expressions hold for unit free variables. A unit and scaling factor has to multiply the second term of the second coefficient otherwise.

imaginary part form a Gaussian vector with covariance matrix

$$\begin{pmatrix} \frac{1}{2}R_{\text{sp}}(N_t)dt & 0 \\ 0 & \frac{1}{2}R_{\text{sp}}(N_t)dt \end{pmatrix}.$$

Or equivalently the diffusion coefficients are $\frac{1}{2}R_{\text{sp}}(N_t)$, $\frac{1}{2}R_{\text{sp}}(N_t)$ and 0.

4.5.3 Numerical implementation

A numerical solver for the stochastic rate equations of the laser has been implemented. It is based on the widely used Runge-Kutta algorithm of order four for solving ordinary differential equations. The basic random processes were simulated using the Box-Muller algorithm for generating pseudo-random Gaussian variables scaled in order to get appropriate diffusion coefficients. For each simulation step, the laser internal state increment is computed using four intermediate Runge-Kutta steps for deterministic contributions and a simple Euler step for noise contributions.

Different considerations have to be made in order to determine which set of laser state parameters should be used in the numerical implementation of the model. Though the two sets of stochastic differential equations are theoretically equivalent with the assumptions that were made they are not from a computational efficiency standpoint. If the choice of the format of the output data is free (optical power and phase or real and imaginary part of the field) the fact that one should outperform the other is not so clear. At each integration step one floating point multiplication and one floating point division are needed in order to compute the diffusion coefficients of the random processes in the (N, P, ϕ) representation. This compares with four floating point multiplications for the computation of the random process sample associated with N in the (N, E) representation. Yet the “deterministic” part of the increments need three more multiplications in the (N, E) representation than in the (N, P, ϕ) one. Furthermore the power $|E|^2$ has to be computed which requires two costly multiplications whereas this quantity is directly available in the other representation. Nevertheless one last point needs to be made in the present case. The numerical implementation of the fiber model presented in Chap. 2 add a specific constraint. The optical fiber model implemented does not only require the specification of the optical power produced by the transmitter but it has to get a complete optical field description (complex amplitude and state of polarization) as an input. The extra computation of $\sqrt{P}e^{i\phi}$ is expected to add

significant computation time. This is why the (N, E) representation has been used in this case.

4.5.4 First numerical results

Linearized rate equations A theoretical study of the small signal response of the laser and of the Relative Intensity Noise (RIN) power spectrum is of great interest in the prospect of validating the implementation of the model. For a given steady bias current I_b the system falls into a stable equilibrium state, its steady state (N_0, P_0) , which is determined by setting time derivatives to zero in the rate equations,

$$\begin{cases} P_0 &= \frac{1}{\alpha_L}(I_b - R_{\text{rec}}(N_0) + R_{\text{sp}}(N_0)) \\ 0 &= (G(N_0, P_0) - \alpha_L)P_0 + R_{\text{sp}}(N_0) \end{cases}$$

The rate equations can then be linearized in the vicinity of this steady state, $N(t) = N_0 + n(t)$ and $P(t) = P_0 + p(t)$ for a small input signal $I(t) = I_b + i_s(t)$:

$$\begin{cases} \frac{dn}{dt} &= -\Gamma_N n - C_{NP}p + i_s(t) \\ \frac{dp}{dt} &= -\Gamma_P p + C_{PN}n \end{cases}$$

where damping constants and cross terms are given by

$$\begin{aligned} \Gamma_N &= G_N P_0 + R_{\text{rec}}^N \\ \Gamma_P &= \alpha_L - G - G_P P_0 \\ C_{NP} &= G + G_P P_0 \\ C_{PN} &= G_N P_0 + R_{\text{sp}}^N. \end{aligned}$$

The parameters appearing in the previous equations can be computed from the steady state point:

$$\begin{aligned} G &= G(N_0, P_0) \\ G_N &= \frac{\partial G}{\partial N}(N_0, P_0) \\ G_P &= \frac{\partial G}{\partial P}(N_0, P_0) \end{aligned}$$

$$\begin{aligned}
R_{sp} &= R_{sp}(N_0) \\
R_{sp}^N &= \frac{dR_{sp}}{dN}(N_0) \\
R_{rec}^N &= \frac{dR_{rec}}{dN}(N_0).
\end{aligned}$$

The free motion of this linear system is obtained when setting $i_s(t)$ to 0 and looking for a solution of the form e^{st} . It is characterized by its *damping coefficient* $\Gamma = (\Gamma_N + \Gamma_P)/2$ and *free oscillation frequency* $\omega_{\text{free}} = 2\pi f_{\text{free}} = \sqrt{C_{PN}C_{NP} - \Gamma^2}$. When $i_s(t)$ is non-zero we get the system frequency response

$$\begin{cases} \tilde{n}(\omega) &= \frac{i\omega + \Gamma_P}{-\omega^2 + 2\Gamma i\omega + \omega_r^2 + 2\Gamma^2} \tilde{i}_s(\omega) \\ \tilde{p}(\omega) &= \frac{C_{PN}}{-\omega^2 + 2\Gamma i\omega + \omega_r^2 + 2\Gamma^2} \tilde{i}_s(\omega) \end{cases}$$

where the Fourier transform of a function f is defined by $\tilde{f}(\omega) = \int f(t)e^{-i\omega t} dt$. Maximizing the magnitude of the denominator of the ratio $\frac{\tilde{p}}{\tilde{i}_s}$ we get the *resonance frequency* of the system $\omega_r = 2\pi f_r = \sqrt{C_{PN}C_{NP} - 2\Gamma^2} = \sqrt{\omega_{\text{free}}^2 - \Gamma^2}$. The frequency response is shown in Fig. 4.18 for different bias currents. For the range of bias currents of practical interest the free oscillation and resonance frequencies are pretty close as shown in Fig. 4.20.

Theoretical noise spectra and steady-state parameters When operating the laser with a constant bias current spontaneous emission leads to intensity and phase fluctuations of the emitted optical field. Computing the windowed Fourier transforms over $[0, T]$ of quantities appearing in the linearized stochastic rate equations leads to the following relationship:

$$\tilde{p}^T(\omega) = \frac{(i\omega + \Gamma_N)\tilde{F}_P^T(\omega) + C_{PN}\tilde{F}_N^T(\omega)}{-\omega^2 + 2\Gamma i\omega + \omega_r^2 + 2\Gamma^2},$$

where for a function f defined over $[0, +\infty)$, $\tilde{f}^T(\omega) = \int_0^T f(t)e^{-i\omega t} dt$, $\tilde{F}_P^T(\omega) = \int_0^T e^{-i\omega t} dP_t^{\text{sp}}$ and $\tilde{F}_N^T(\omega) = \int_0^T e^{-i\omega t} dN_t^{\text{sp}}$. The RIN power spectrum is obtained using the following formula for the power spectral density function of the random process p , $S_{pp}(\omega) = \lim_{T \rightarrow +\infty} \frac{1}{T} E(|\tilde{p}^T(\omega)|^2)$. With the assumption made page 102 the RIN double-sided power

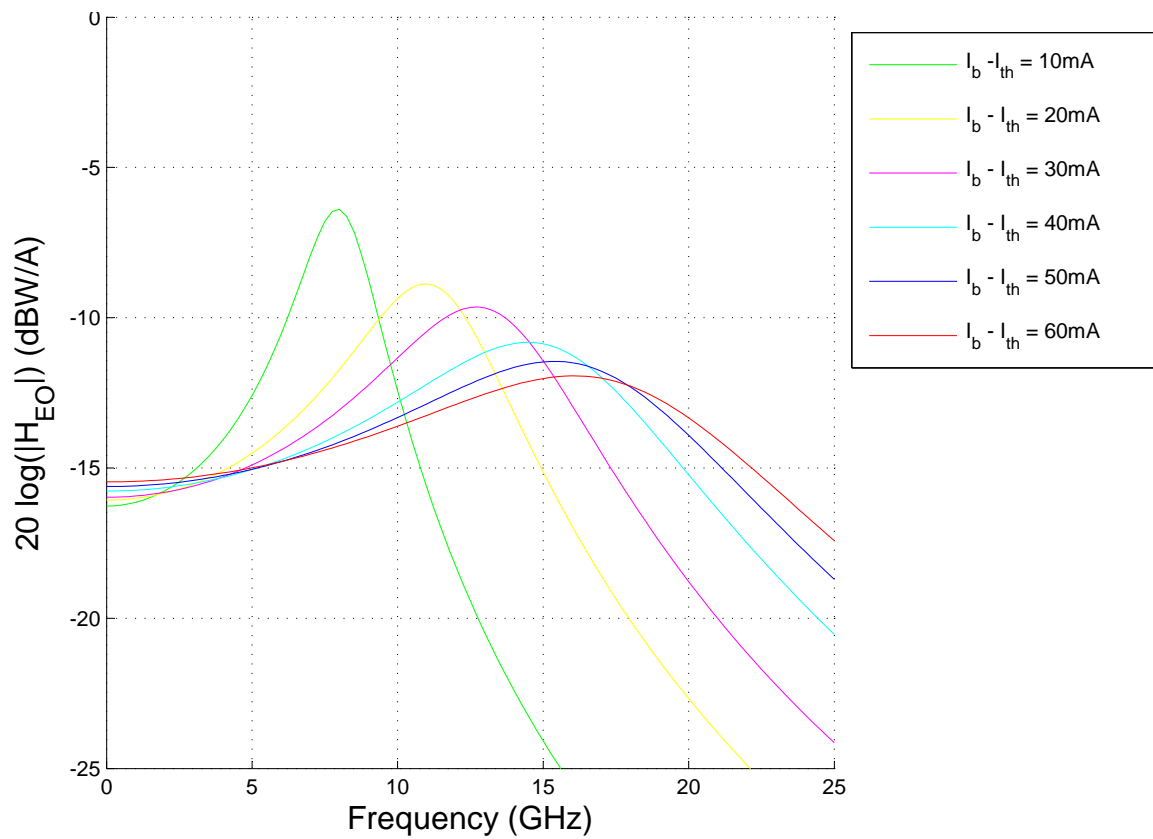


Figure 4.18: Linearized electro-optical frequency response amplitude at a bias current of 5, 10, 20, 30, 40, 50 and 60 mA above threshold.

spectrum is given by

$$\text{RIN}(\omega) = \frac{1}{P_0^2} S_{\text{pp}}(\omega) = \frac{2R_{\text{sp}}}{P_0} \frac{\omega^2 + (R_{\text{rec}}^N - R_{\text{sp}}^N)^2}{(\omega^2 - \omega_r^2)^2 + 4(\omega_r^2 + \Gamma^2)\Gamma^2}.$$

The spectrum depends on several parameters. Numerical resolution of the steady state equations yields values for P_0 and N_0 for a given bias current I_b . It is then possible to compute the values of the different sets of parameters. First G , G_N , R_{sp}^N and R_{rec}^N , then Γ_N , Γ_P , C_{PN} and C_{NP} , and finally Γ , ω_{free} and ω_r .

The laser threshold is the point where the laser starts lasing when increasing its bias current. The carrier number at threshold N_{th} is defined by the relationship $G_0(N_{\text{th}}) = \alpha_L$ and the threshold current is given by $I_{\text{th}} = R_{\text{rec}}(N_{\text{th}})$. From the numerical values of the laser rate equation parameters shown on page 100 we get $N_{\text{th}} \approx 13.03$ pC and $I_{\text{th}} \approx 17.9$ mA. Above threshold for the range of bias current of practical interest (absolute bias current below 90 mA) a number of approximations of the previous parameters can be stated. Firstly, N_0 stays close to the threshold value N_{th} by a few percent and $P_0 \approx (I_b - I_{\text{th}})/\alpha_L$. Secondly, the oscillation and resonance frequencies change approximately as the square-root of $I_b - I_{\text{th}}$:

$$f_{\text{free}} \approx f_r \approx \frac{1}{2\pi} \sqrt{\frac{G_0(I_b - I_{\text{th}})}{N_{\text{th}}}}.$$

The evolution of those quantities with the bias current is shown in Fig. 4.19 and Fig. 4.20.

Simulation results and validation The numerical models for the stochastic rate equations were implemented in C code. Examples of simulations of the laser dynamic behavior are displayed in Fig. 4.21 and Fig. 4.22. The validation of the numerical implementation of the noise sources was done by comparing the simulated RIN power spectral density to the theoretical one for different bias currents as shown in Fig. 4.24. Figure 4.25 shows a comparison of theoretical and experimental RIN spectra.

4.5.5 Two-tone test measurements

Goals Relative intensity noise measurements provided an indication of the accuracy of the laser model being used. This section presents further experimental and simulation results exploring the effects of the directly modulated laser dynamics on a microwave multi-carrier transmission system.

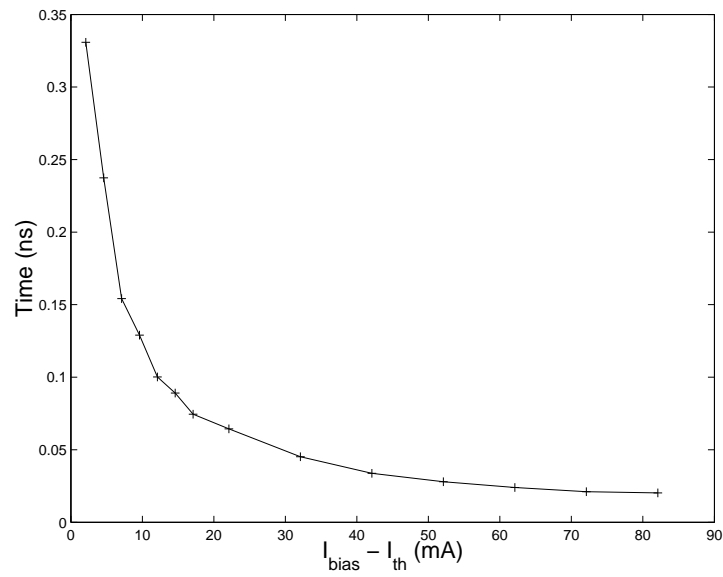


Figure 4.19: Laser damping time Γ^{-1} vs. bias current.

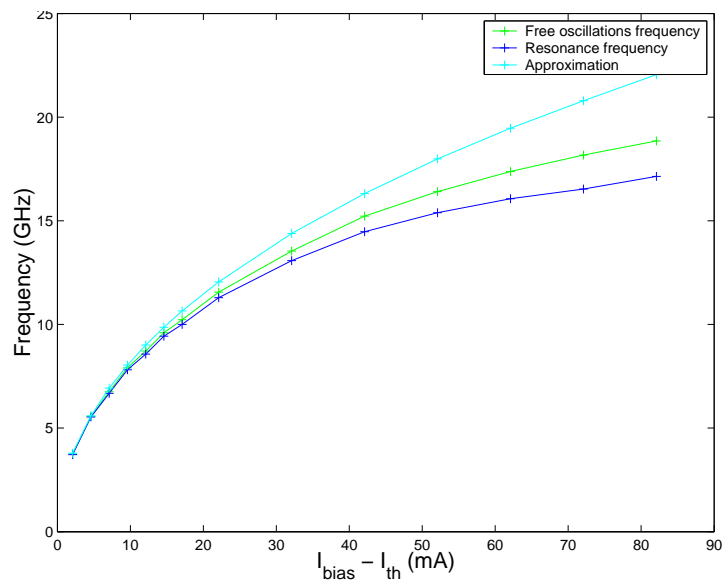


Figure 4.20: Laser oscillation and resonance frequencies vs. bias current.

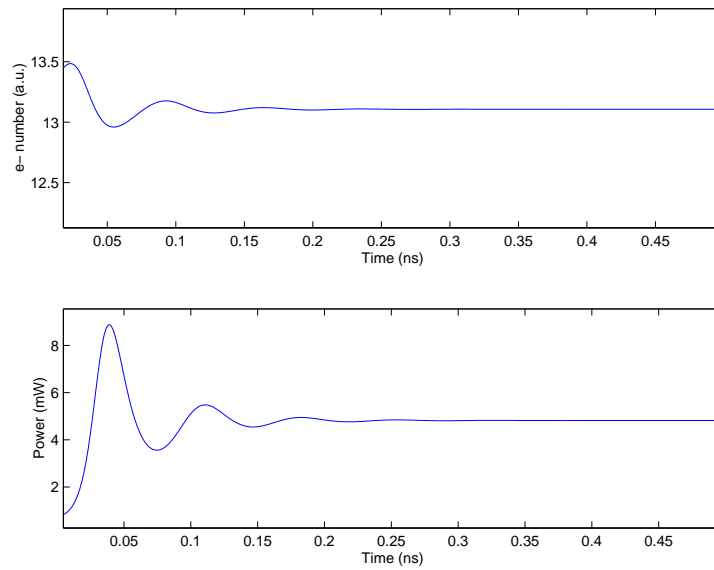


Figure 4.21: Laser relaxation oscillations (spontaneous emission noise turned off) for $I_b - I_{th}$ jumping from 10 to 30 mA.

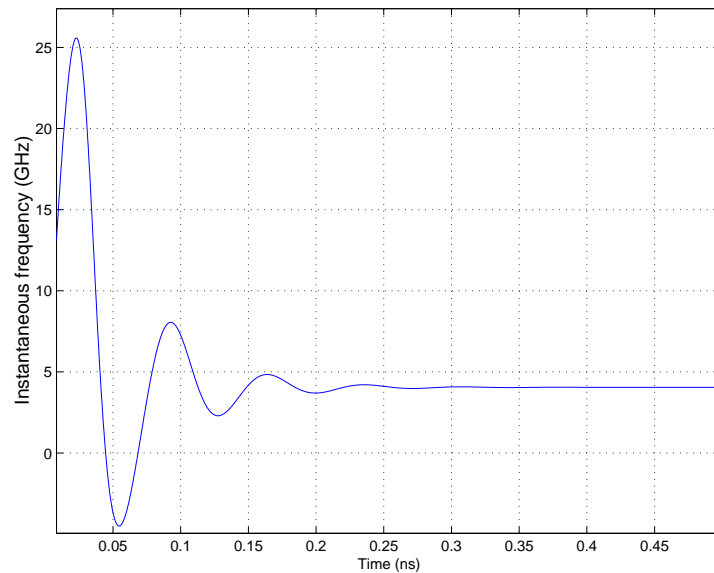


Figure 4.22: Laser chirp when excited by a current step function.

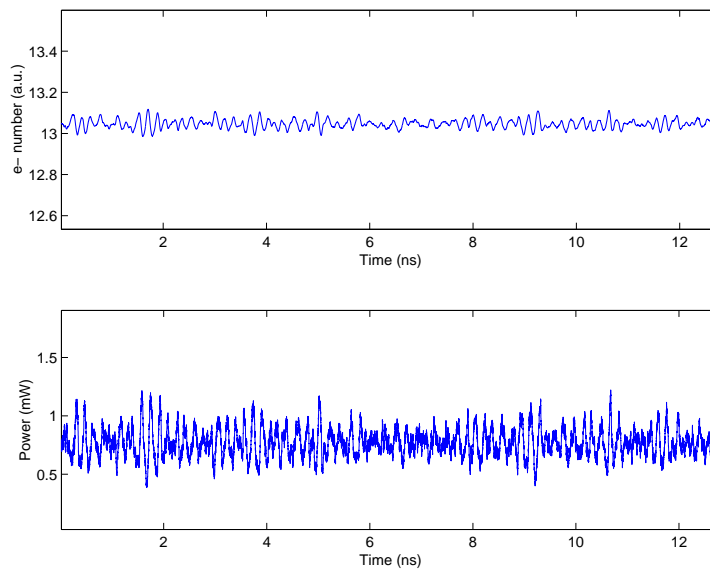


Figure 4.23: Laser noisy behavior (steady input current of 5 mA above threshold). Electron number (arbitrary units) and output power shown.

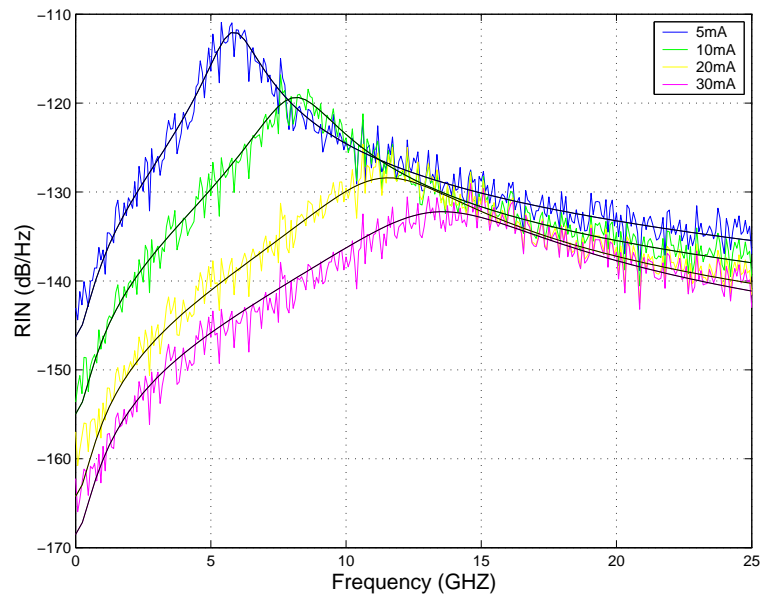


Figure 4.24: Comparison of RIN spectra from theory (black) and simulation (colored) for different bias currents.

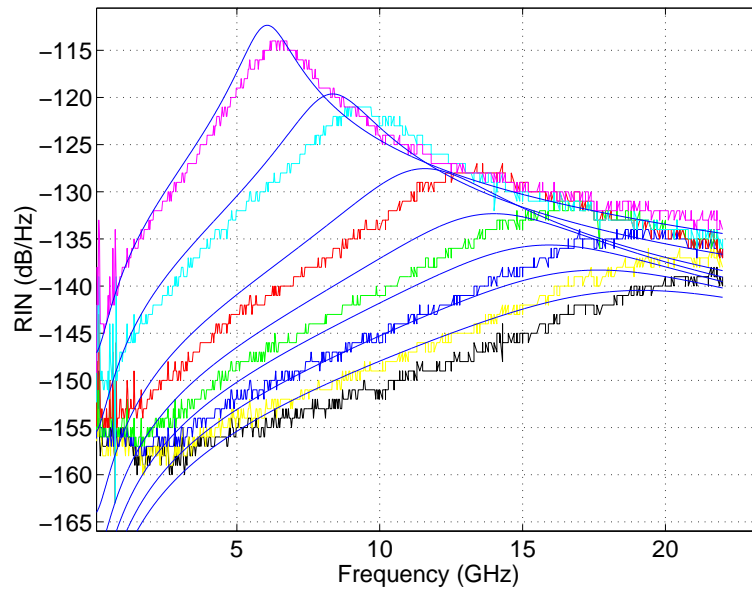


Figure 4.25: Comparison of theoretical and measured RIN spectra for bias currents of 5, 10, 20, 30, 40, 50 and 60mA above threshold.

An extensive test would require assembling a complete system using discrete RF components as is done to experimentally determine CSO and CTB levels for CATV systems [WCW00]. These systems operate at maximum frequencies approximately a hundred times smaller than the 14 GHz maximum frequency of the present system. Such a test in our case is mainly limited by the availability of off-the-shelf RF components operating over multiple octaves in the gigahertz range. The present experimental results confined themselves to gathering evidence with a limited number of two-tone tests with carrier tones extracted from the complete system frequency map. This provides elements of comparison with simulation results for:

- The level on nonlinear distortions under typical laser operation.
- The variation of such distortions with the laser bias current.

Comparison of experimental and simulation experiments should lead to agreeing qualitative results. Matching of quantitative results is only expected to be up to the experimental uncertainties and laser fabrication variations since the rate equations of a typical laser diode have been used and measurements on packaged representatives have been made for

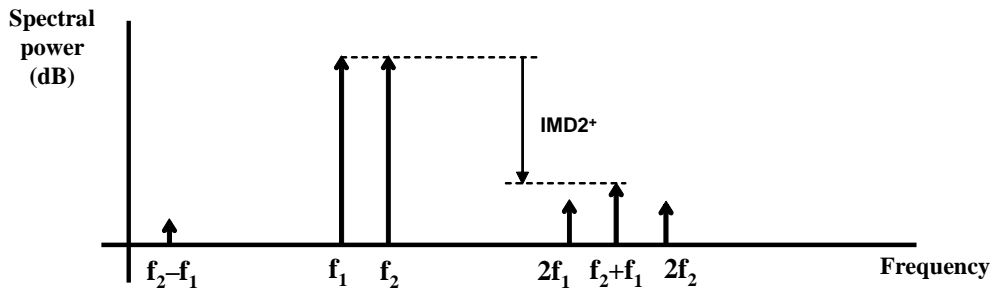


Figure 4.26: Intermodulation distortion of order 2.

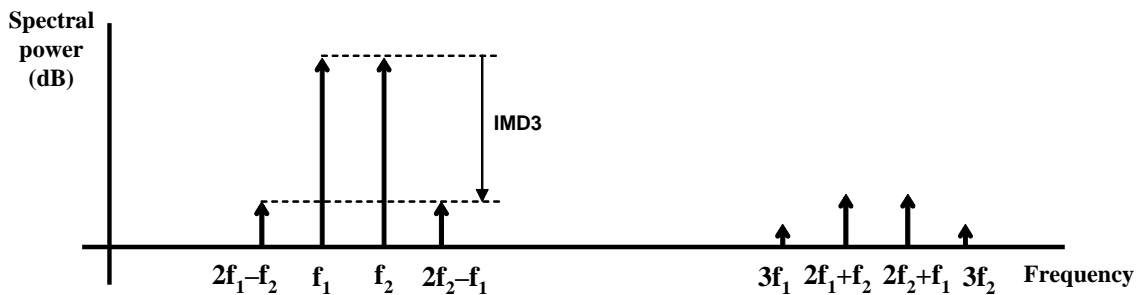


Figure 4.27: Intermodulation distortion of order 3.

the same laser design. The main purpose is to get further confidence that the laser numerical model provides a good typical description of real laser operation before its inclusion into a system simulation platform.

Two-tone tests consist in stimulating of the system input with couples of tones at predefined probing frequencies and measuring of characteristic distortion quantities at the output of the system that would not be present if the system were purely linear. Roughly speaking the system response could be approximated by a power series valid for input signals with limited peak values. Quadratic terms lead to distortions of order-2, cubic terms distortions of order-3, etc. The measurable quantities of interest are depicted in Fig. 4.26 and 4.27 in the case of order-2 and order-3 distortions.

As shown in Fig. 4.26 tones at given frequencies f_1 and f_2 at the system input will be accompanied by order-2 distortions at the system output consisting in the presence of

tones at frequencies $f_1 + f_2$ and $|f_1 - f_2|$ resulting from the intermixing of the input tones. Measuring the power of the tones at $2f_1$ and $2f_2$ is not of practical interest since they could in practice be present at the input of the system due to existence of harmonics in the RF source. The ratio of the power level of these additional tones to the power level of the corresponding input tones is called *intermodulation distortion of order 2* (IMD2). If the system had no memory and had a flat frequency response the two additional tones would have the same power level as the development of $(\cos(2\pi f_1 t) + \cos(2\pi f_2 t))^2$ shows. This is obviously not the case here since the linear response itself is not flat in the frequency range of interest even exhibiting a resonant behavior. In the measurements presented in this section power levels for the intermodulation component at frequency $f_1 + f_2$ were measured. In Fig. 4.26 the corresponding intermodulation distortion is noted IMD2^+ .

Fig. 4.27 shows that the same tones will appear at the output of a system containing cubic nonlinearity together with tones at frequencies $2f_1 + f_2$, $2f_2 + f_1$, $2f_1 - f_2$ and $2f_2 - f_1$. Similarly the ratio of the power level of these additional tones to the power level of the reference tones at the output of the system is called *intermodulation distortion of order 3* (IMD3). In the presented IMD3 measurements we were only interested in pairs of tones located close to a given frequency ($f_1 = f - \Delta f$ and $f_2 = f + \Delta f$ with $\Delta f = 10$ MHz) in the system frequency map and observing the amount of spurious energy folding back in the vicinity of that same system frequency at frequencies $2f_1 - f_2 = f - 3\Delta f$ and $2f_2 - f_1 = f + 3\Delta f$.

Experimental setup Fig. 4.28 shows the two-tone test setup. It is composed of two waveform generators providing tones of equal power at the two frequencies of interest, a power combiner (4 to 8 GHz range of operation), a DC block, a packaged version of the directly modulated laser biased with a current I_{bias} and connected to a reference optoelectrical converter (12 GHz 3-dB bandwidth) through its integrated pigtail fiber bearing a standard fiber connector. For each measurement setting (tone frequencies, common power level of the tones, laser bias current) observations were made at the setup points A and B thanks to a spectrum analyzer with appropriate range and bandwidth adjustments. The figure does not show the control for the laser internal cooling system. The same piece of equipment was used to control laser bias, and temperature accessible through an integrated laser die temperature probe. In all the measurements presented the laser temperature was kept constant and close to 20°C.

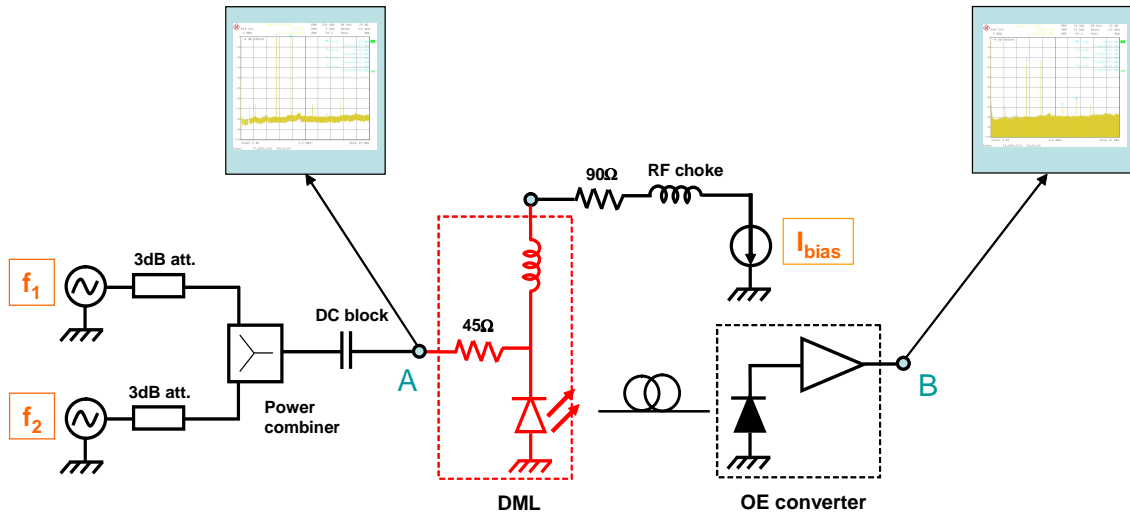


Figure 4.28: Setup for the measurement of intermodulation distortions.

Given the operation bandwidth of the available discrete components (combinations of tones possible at system frequencies between $f_5 = 4.17$ GHz and $f_{11} = 9.17$ GHz). $f_5 = 4.17$ GHz and $f_7 = 5.83$ GHz were the chosen system frequencies for our IMD2 measurements. IMD3 measurements have been made in the vicinity of $f_6 = 5$ GHz and $f_9 = 7.5$ GHz.

Measurement and simulation results Each of the figures from Fig. 4.30 to Fig. 4.34 shows a set of measurements for varying power levels of the input tones for a given couple of frequencies ($f_5 = 4.17$ GHz and $f_7 = 5.83$ GHz were chosen within the frequency map for these tests) and a fixed laser bias current. The abscissa of the displayed points is the power level expressed in dBm ($10 \log_{10}(\text{mW})$) of the two input tones in a given measurement. The ordinate of points in blue color is the power level expressed in dBm of the input tones at the system output (at frequencies f_5 and f_7). The ordinate of points in red color is the power level expressed in dBm of the intermodulation tone at the frequency $f_5 + f_7 = f_{12} = 10$ GHz) present at the output of the system. Using log scales two-tone points (in blue color) stand on a line with slope 1. For small input levels the intermodulation points (in red color) should stand on a line of slope 2 characterizing the quadratic nature of the nonlinearity being measured. Each picture represents the least-mean square fit of a line of slope 1 (blue

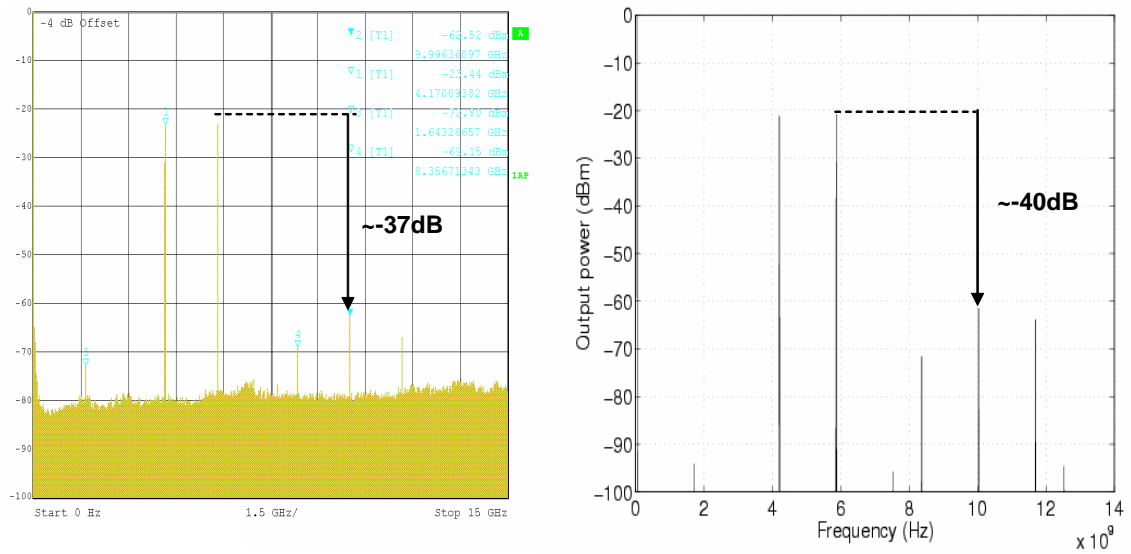


Figure 4.29: Example of two-tone test result for tones of input power -5 dBm each at frequencies $f_5 = 4.17$ GHz and $f_7 = 5.83$ GHz and laser bias $I_b = 60$ mA above threshold. Measurement (left) and simulation (right).

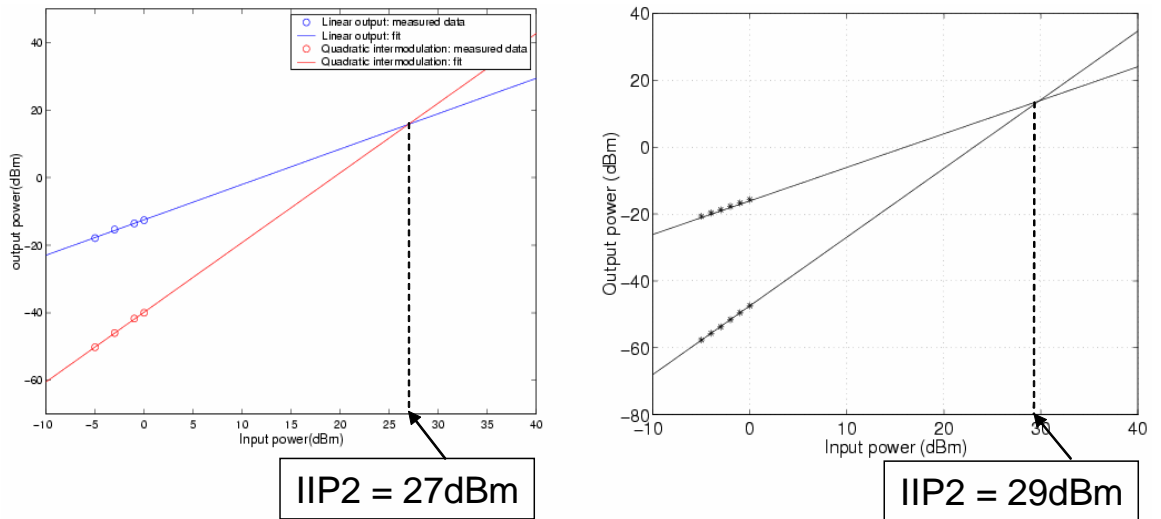


Figure 4.30: Input-referred intercept point of order 2 (IIP2) for two tones at frequencies $f_5 = 4.17$ GHz and $f_7 = 5.83$ GHz and laser bias $I_b = 50$ mA above threshold. Measurements (left) and simulations (right).

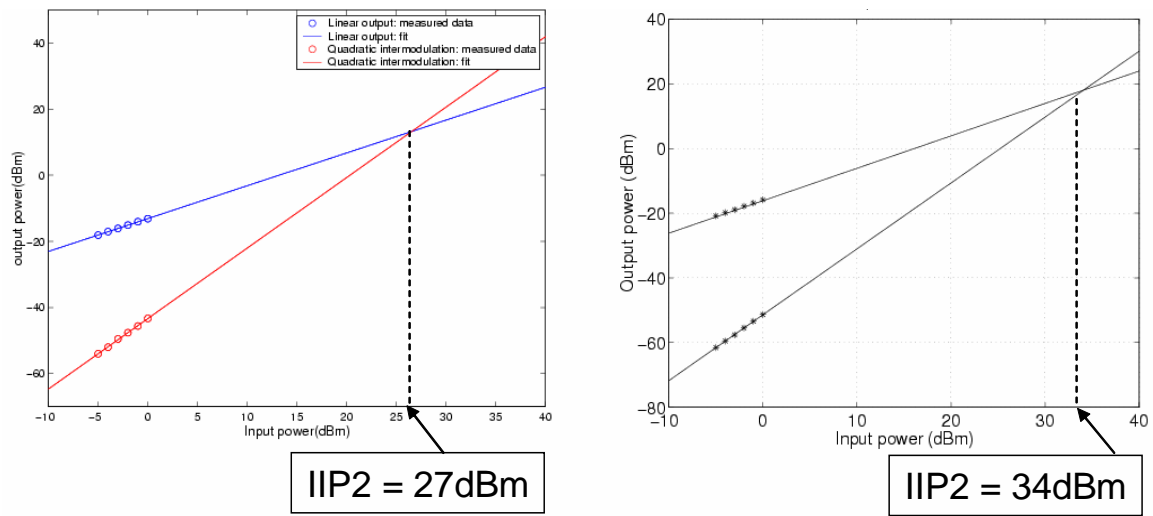


Figure 4.31: Input-referred intercept point of order 2 (IIP2) for two tones at frequencies $f_5 = 4.17$ GHz and $f_7 = 5.83$ GHz and laser bias $I_b = 60$ mA above threshold. Measurements (left) and simulations (right).

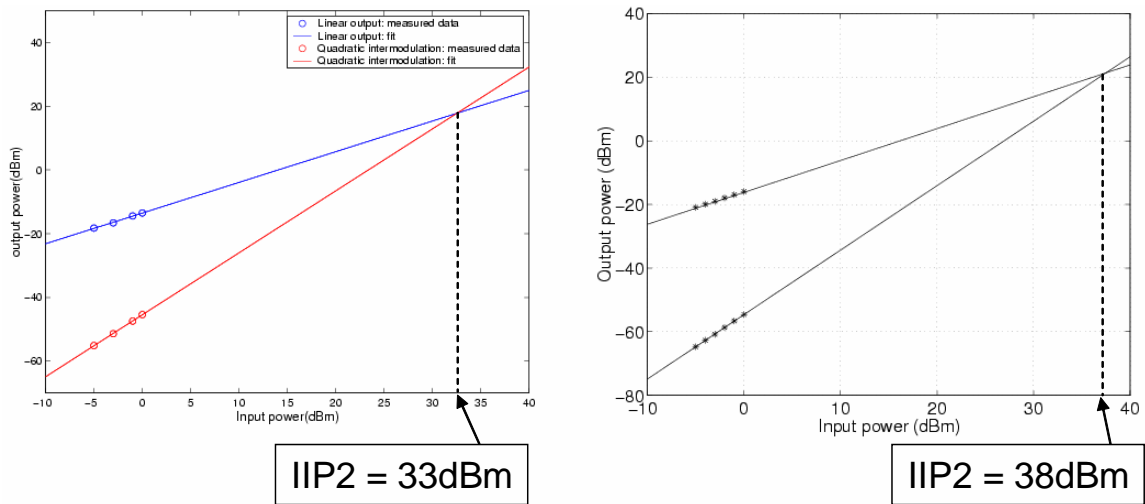


Figure 4.32: Input-referred intercept point of order 2 (IIP2) for two tones at frequencies $f_5 = 4.17$ GHz and $f_7 = 5.83$ GHz and laser bias $I_b = 70$ mA above threshold. Measurements (left) and simulations (right).

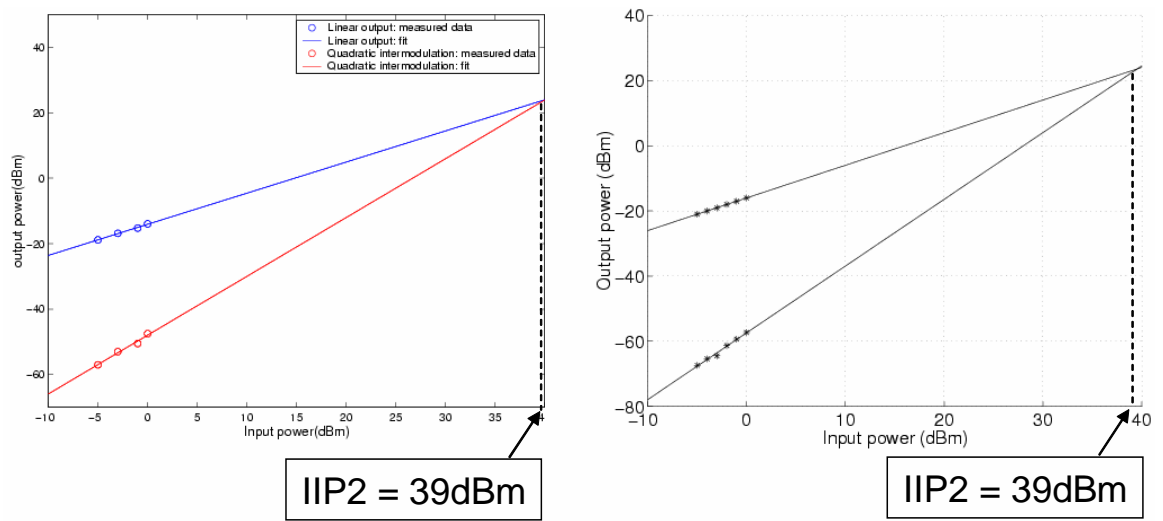


Figure 4.33: Input-referred intercept point of order 2 (IIP2) for two tones at frequencies $f_5 = 4.17$ GHz and $f_7 = 5.83$ GHz and laser bias $I_b = 80$ mA above threshold. Measurements (left) and simulations (right).

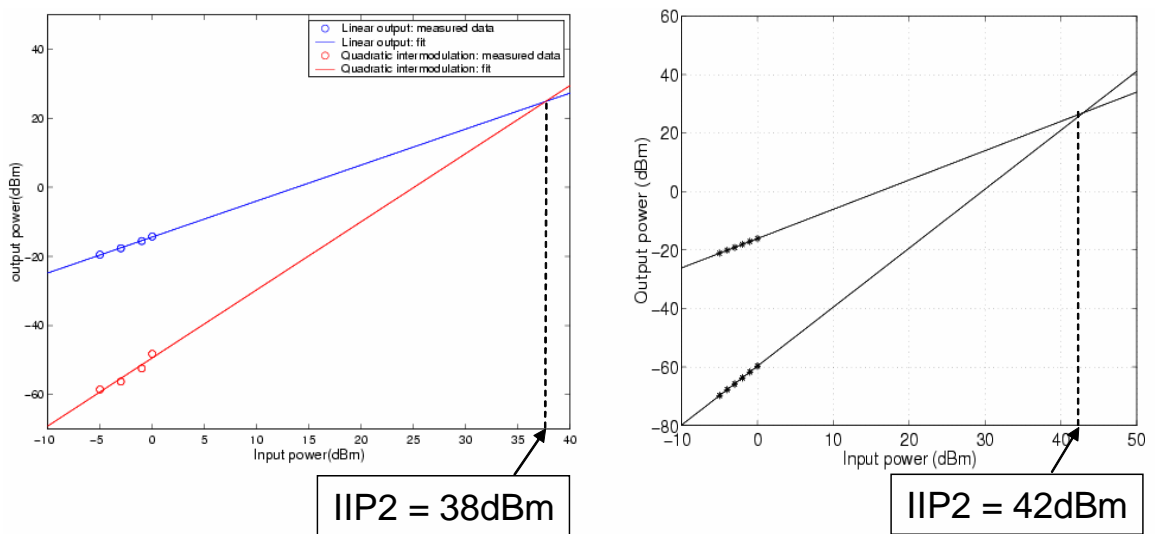


Figure 4.34: Input-referred intercept point of order 2 (IIP2) for two tones at frequencies $f_5 = 4.17$ GHz and $f_7 = 5.83$ GHz and laser bias $I_b = 90$ mA above threshold. Measurements (left) and simulations (right).

line) for the measured two-tone points and the least mean square fit of a line of slope 2 (red line) for the measured intermodulation points. If the nonlinearity were purely quadratic intermodulation points at higher two-tone input power levels should also remain on the line of slope 2. In general and in our case points depart from this line at higher power levels. This line is still used as an extrapolation of the order-2 nonlinear behavior at higher power levels. In particular a quantity characterizing the strength of the order-2 nonlinearity can be derived. This quantity is the *input-referred intercept point of order 2* (IIP2) which is the two-tone power level at the system input that would have the system generate an intermodulation tone at the system output of power equal to the two-tone output power if the nonlinearity were purely of order 2.

These measurement show a decrease in the strength of the order 2 laser nonlinearity for an increasing biasing current in the practical range of operation of the laser. This behavior is confirmed by simulation results. In general measured and simulated IIP2 results agree within a few dBs which seems satisfactory considering the uncertainty on the measurement points which translates into a greater uncertainty on the IIP2. Measured and simulated intermodulation levels are in good agreement and an example of a direct comparison is shown in Fig. 4.29.

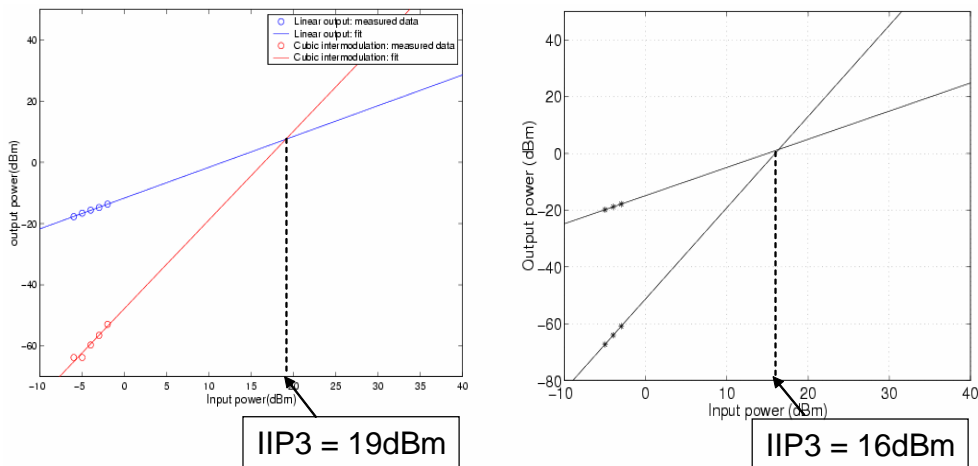


Figure 4.35: Input-referred intercept point of order 3 (IIP3) for two tones at frequencies $f_6 - 10$ MHz = 4.99 GHz and $f_6 + 10$ MHz = 5.01 GHz and laser bias $I_b = 20$ mA above threshold. Measurements (left) and simulations (right).

Figures 4.35 and 4.36 show examples of IMD3 measurements in the vicinity of $f_6 =$

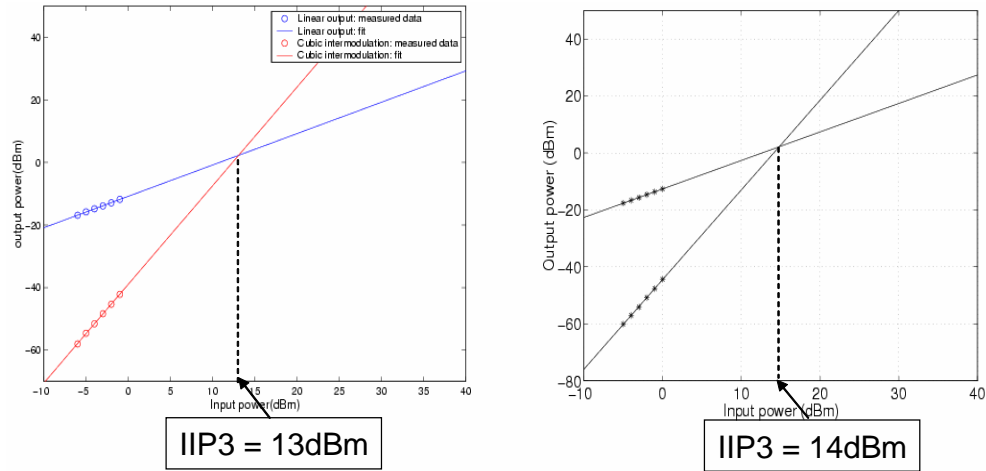


Figure 4.36: Input-referred intercept point of order 3 (IIP3) for two tones at frequencies $f_9 - 10 \text{ MHz} = 7.49 \text{ GHz}$ and $f_6 + 10 \text{ MHz} = 7.51 \text{ GHz}$ and laser bias $I_b = 20 \text{ mA}$ above threshold. Measurements (left) and simulations (right).

5 GHz and $f_9 = 7.5 \text{ GHz}$. The definition of measurement points is the same as in the case of IMD2 except for the output intermodulation tones under consideration being now in the close vicinity of the two reference tones separated by 20 MHz around the frequency of interest. The *input-referred intercept point of order 3* (IIP3) can similarly be defined.

Measurements and simulation are in agreement again. Increased laser bias current leads to a weaker nonlinearity of order 3 in the range of bias currents considered here. This last point is also apparent in the direct observation of the intermodulation tones shown in Fig. 4.37 measured in the vicinity of a higher frequency for illustration purpose.

Conclusions The two-tone tests carried out showed a decrease in laser order-2 and order-3 nonlinearities with increasing laser bias currents in the range of practical interest (20 to 90 mA above threshold) under controlled laser temperature conditions. This observation was confirmed by laser simulations carried out using the model presented in Sec. 4.5. Measurements and simulation were showing good qualitative agreement and reasonable quantitative agreement thus increasing the confidence in the laser model before its integration into a complete system simulation platform.

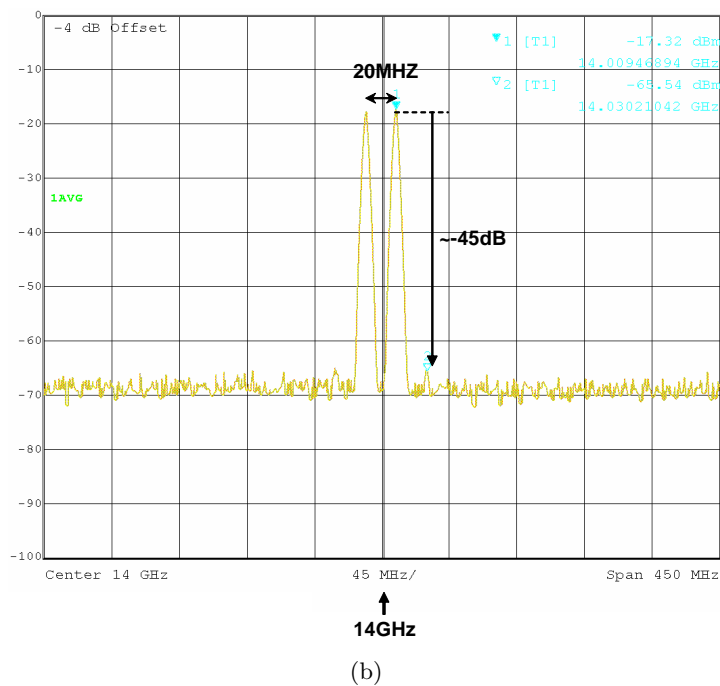
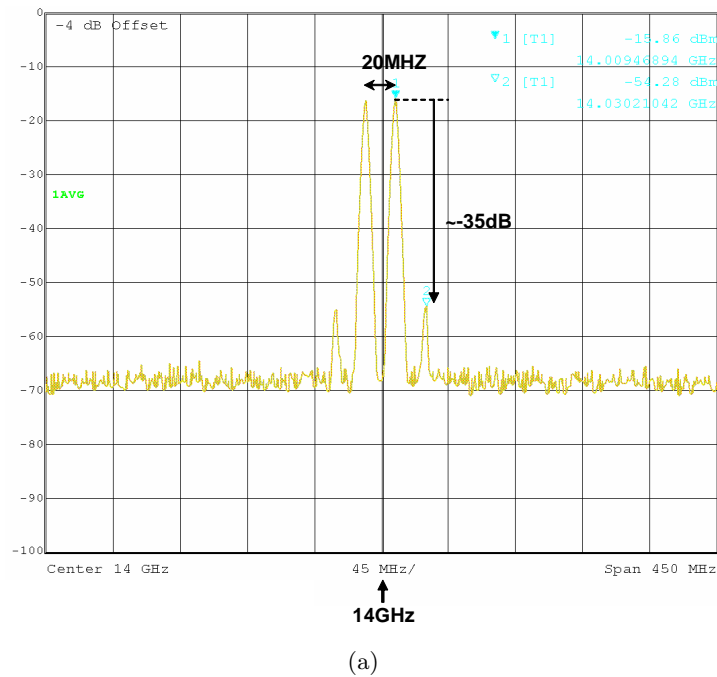


Figure 4.37: Example of a two-tone test result showing intermodulation products of order 3 for tones at frequencies 13.99 GHz and 14.01 GHz and laser bias: (a) $I_b = 30$ mA above threshold; (b) $I_b = 50$ mA above threshold.

4.6 Simplified model and channel capacity

4.6.1 Introduction

Previous sections introduced the characteristics, impairments and noise of the channel defined in Sec. 4.1. Preliminary estimates indicate that uncoded SCM QAM modulation should allow the transmission 40 Gb/s in 14 GHz bandwidth through this channel. The precise models defined in this dissertation allows the creation of a numerical simulation environment for the purpose of confirming or disproving the feasibility of the system.

However information theory provides ways to define bounds on the maximum achievable data rates with vanishing error rates. They set important reference points to which the design target can be compared. The study of this information channel is complicated by the existence of nonlinearities introduced by the laser diode electro-optical conversion process and fiber transmission. Capacity evaluation models have been proposed for modulation schemes that bear laser clipping [FH95] or avoid it altogether [YK02].

This section presents a simplified channel model along the lines of [FH95]. It is used to determine the capacity of the channel of interest. It illustrates its dependence on laser bias current, optical modulation index (OMI) and fiber length. The linearized laser model detailed in Sec. 4.5 makes possible the evaluation of the ultimate capacity of the laser diode channel in a quasi-linear regime thanks to the noise spectrum “water-filling” procedure.

4.6.2 Information channel model

The simple channel model used to determine the information channel capacity is outlined in Fig. 4.38:

- The signal X is a random process modelling the DML input current signal filtered by the laser linearized electro-optical response and converted by the photoreceiver. The process average is

$$E(X) = I_{\text{pin}} = I_0 \gamma(L),$$

where $I_0 = R_{\text{resp}} \eta_{\text{ext}} (I_b - I_{\text{th}})$ is the average photodiode current when no fiber is present which depends upon the photodiode responsivity R_{resp} , the laser external efficiency η_{ext} and the laser bias current above threshold $I_b - I_{\text{th}}$ (see Sec. 4.1 and Sec. 4.3), and $\gamma(L) = 10^{-\frac{\alpha_{\text{dB}}}{10} L}$ is the fiber loss factor function of the fiber length L and the fiber loss coefficient α_{dB} equal to 0.4 dB/km at a wavelength of 1310 nm. The

process variance is

$$\sigma_X^2 = \mu^2 I_{\text{pin}}^2,$$

where μ designates the OMI.

In CATV systems the number of carrier channels exceeds 100 and as mentioned in [FH95]:

The modulating current is assumed to be Gaussian. This is a safe assumption because a large number of channels are involved.

Even though the number of channels is more limited (16 has been chosen) the Gaussian assumption is still made in the present model.

- The noise Z is a Gaussian process with zero mean representing the channel noise contributions (laser RIN, thermal and shot noise in the receiver). Its variance is

$$\sigma_Z^2 = B \left(\frac{4k_B T_0}{R} F + 2q I_{\text{pin}} + \text{RIN} I_{\text{pin}}^2 \right),$$

where I_{pin} depends on the fiber length L through the coefficient $\gamma(L)$, the noise bandwidth is identified with the system bandwidth B and other quantities involved are defined on page 97. Typical numerical values are provided on page 98 in the case of a short fiber link.

- The main source of non-linear distortions is assumed to be laser clipping depicted in Fig. 4.16. This distortion can be modelled by an additive impulse-like noise that brings the signal to 0 at the time of negative excursions. This impulse-like noise can be modelled by a Poisson process with average rate of impulses per second r [Maz92, FH95],

$$r = \frac{B}{\sqrt{3}} e^{-\frac{1}{2\mu^2}},$$

where the bandwidth occupied by the input signal is identified with the system bandwidth B and μ is the OMI. If T is the signalling period $B \approx K/T$ where K is the number of carrier channels. The probability of having at least one clipping event in a symbol period is given by

$$P_{\text{clip}} = 1 - e^{-rT} = 1 - e^{-\frac{K}{\sqrt{3}} e^{-\frac{1}{2\mu^2}}}.$$

To take into account the effect of clipping noise on information transmission it is assumed that whenever a clipping event occurs within a symbol period this creates an symbol erasure that the receiver is aware of (photocurrent comes close to 0). This is represented in Fig. 4.38 and defines the received signal Y ,

$$Y = \begin{cases} W & \text{if } \theta = 0 \\ e & \text{if } \theta = 1 \end{cases}$$

where $W = X + Z$, e is the erasure symbol and θ is Bernoulli random variable independent from X and Z such that

$$\mathbb{P}(\theta = 1) = P_{\text{clip}}.$$

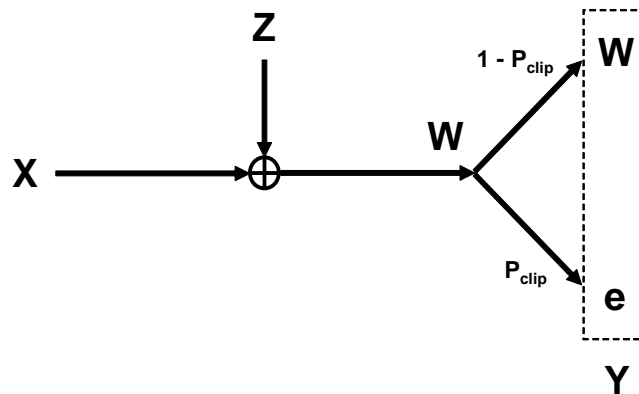


Figure 4.38: Simplified channel model outline.

This simple model is believed to provide a good basis for the derivation of the channel capacity and the investigation of its variations with some key system parameters. Yet it does not take into account:

- Aspects of the laser non-linear behavior (other than clipping) that translate into channel mixing noise,
- Laser detuning from the zero-dispersion wavelength and associated linear and nonlinear effects on signal and RIN.

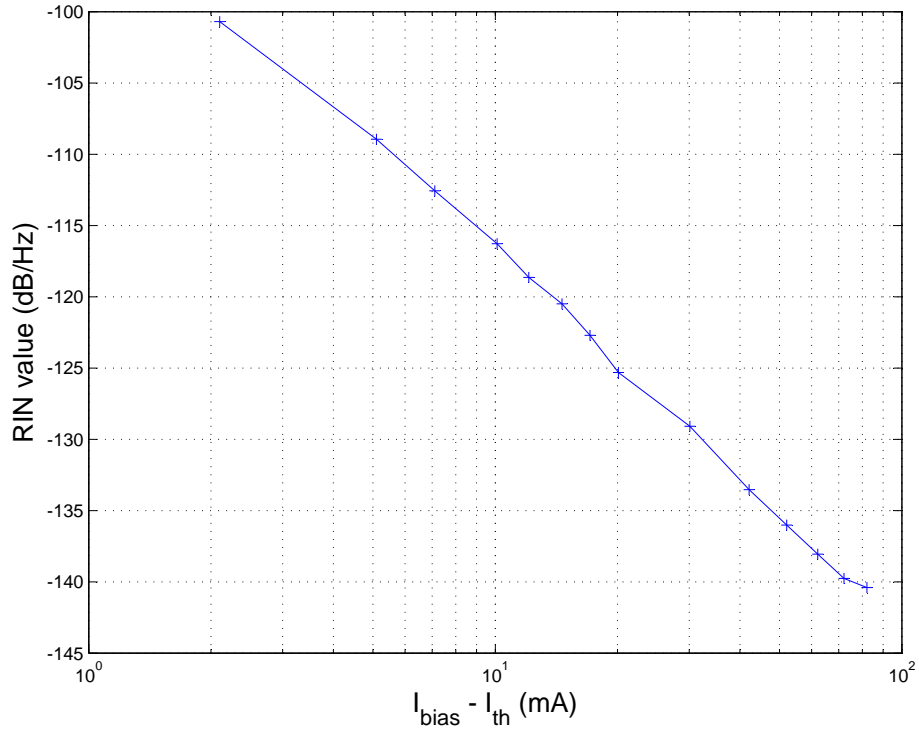


Figure 4.39: Value of the RIN single-sided power spectral density at laser resonance vs. laser bias current above threshold.

The following sections present channel capacity dependencies under the linear assumption. These results are then adapted to take into account the effects of laser clipping.

4.6.3 Linear assumption

If we can neglect clipping noise, $Y = W$ and the channel capacity is given by [CT91]

$$C = B \log_2 \left(1 + \frac{\sigma_X^2}{\sigma_Z^2} \right).$$

Laser bias current dependence For short fiber lengths RIN is the dominant noise contributor. The power spectral density of RIN is frequency dependent as shown in Fig. 4.24. We find a capacity lower bound by taking the single-sided RIN power spectral density value

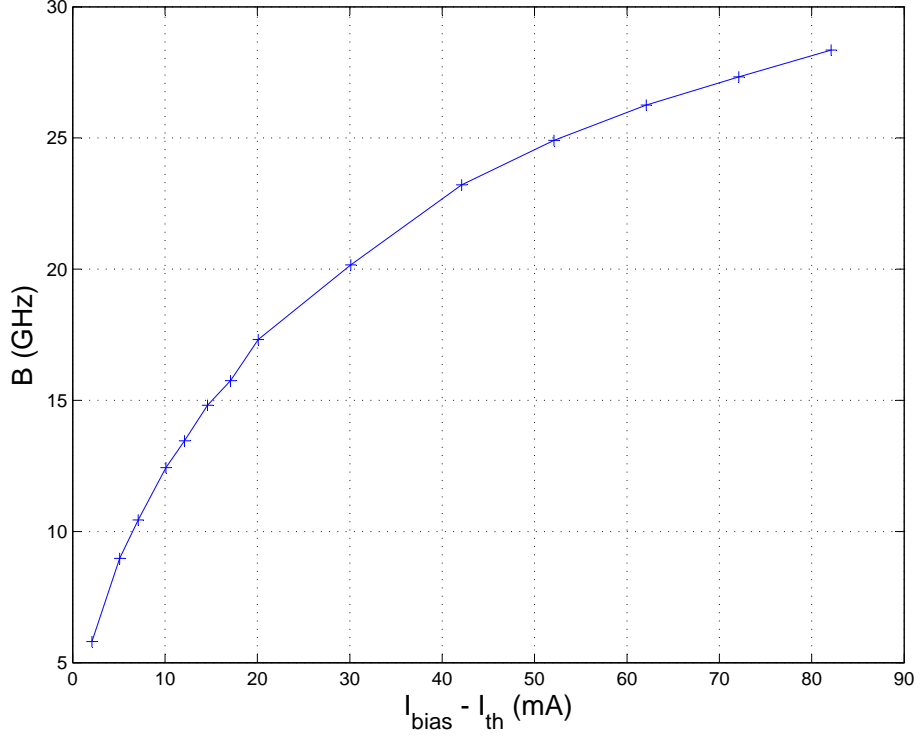


Figure 4.40: Laser 3-dB bandwidth.

at laser resonance

$$\begin{aligned} \text{RIN} &= \frac{4R_{\text{sp}}}{P_0} \frac{\omega_r^2 + \Gamma_N^2}{4(\omega_r^2 + \Gamma^2)\Gamma^2} \\ &\approx \frac{4R_{\text{sp}}}{P_0^3(G_N - G_P)^2}, \end{aligned}$$

where all used quantities are defined in Sec. 4.5. Above threshold and for values of P_0 such that εP_0 remains small compared to 1, this gives $\text{RIN} \propto (I_b - I_{\text{th}})^{-3}$ since the carrier number, N , remains approximately equal to N_{th} . Fig. 4.39 plotting the RIN value at laser resonance at different bias current values shows that this is a satisfying dependence approximation.

The laser available bandwidth B is defined to be equal to the laser 3-dB bandwidth,

$$B_{3\text{dB}} = \frac{\omega_r}{2\pi} \left(1 + \sqrt{2 + 4 \left(1 + \left(\frac{\Gamma}{\omega_r} \right)^2 \right) \left(\frac{\Gamma}{\omega_r} \right)^2} \right)^{1/2}.$$

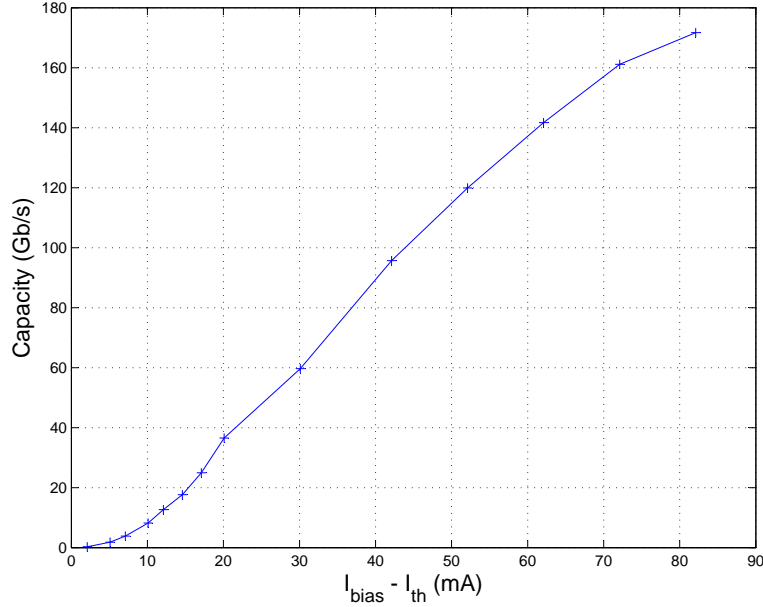


Figure 4.41: Laser diode capacity vs. bias current for an OMI of 13% and a signal spectral width B equal to the laser 3-dB bandwidth.

Its variations with the laser bias current are shown in Fig. 4.40. These variations can be approximated by $B \propto (I_b - I_{\text{th}})^{1/2}$.

Fig. 4.41 shows the variations of the capacity with bias current for short fiber lengths, $\mu = 0.13$ and assuming a signal bandwidth equal to the laser 3-dB bandwidth. This value of 13% for the OMI corresponds to the limit where an SCM QAM-16 signal over 16 channels starts getting clipped (the signal is actually bounded despite the Gaussian variable model).

In the remainder of this section, the signal bandwidth is fixed to $B = 14$ GHz in order to match the characteristics of the system this dissertation focuses on. The laser 3-dB bandwidth exceeds this value for a bias current greater than 15 mA above threshold. It is well above 14 GHz for a bias current exceeding 30 mA. For a value of the bias current of 50 mA above threshold the value of RIN at resonance is approximately -140 dB/Hz. In this case the capacity is 97 Gb/s and the bandwidth efficiency is close to 6.9 b/s/Hz. This is approximately twice the 2.9 b/s/Hz bandwidth efficiency of the SCM modulation used in this work and presented in Sec. 3.2.

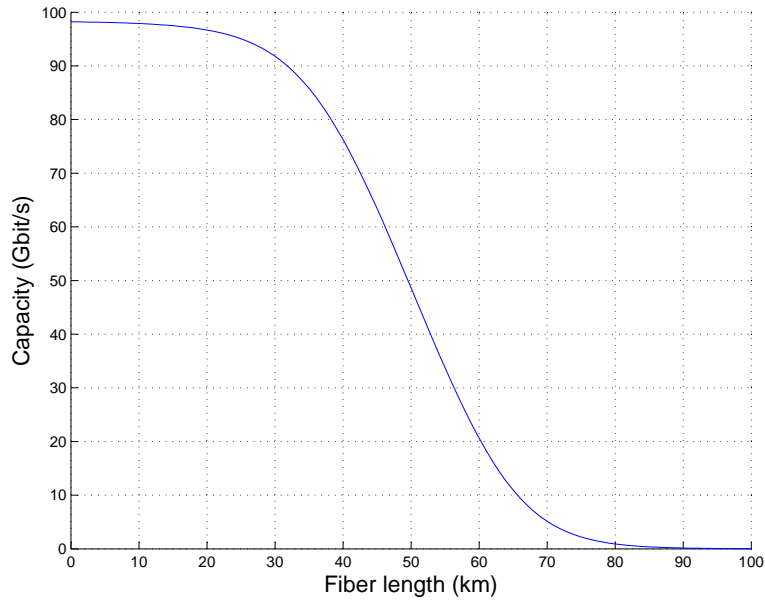


Figure 4.42: System capacity at the fiber zero-dispersion point with RIN and receiver thermal and shot noise vs. fiber length. $\mu = 0.13$; B chosen equal to 14 GHz; $I_b - I_{th} = 50$ mA; $T_0 = 293$ K.

Receiver noise and fiber loss Fiber loss affects signal, RIN noise and shot noise absolute levels leading to variations of the signal-to-noise ratio with fiber length. The correlated variations of the capacity C are shown in Fig. 4.42 in the case of 13% OMI, a signal bandwidth of 14 GHz and a bias current of 50 mA above threshold and a thermal noise temperature of 293 K.

4.6.4 Effect of laser clipping

When the linear assumption is not valid and clipping cannot be neglected the clipping erasure channel model introduced in Sec. 4.6.2 gives the following expression for the channel

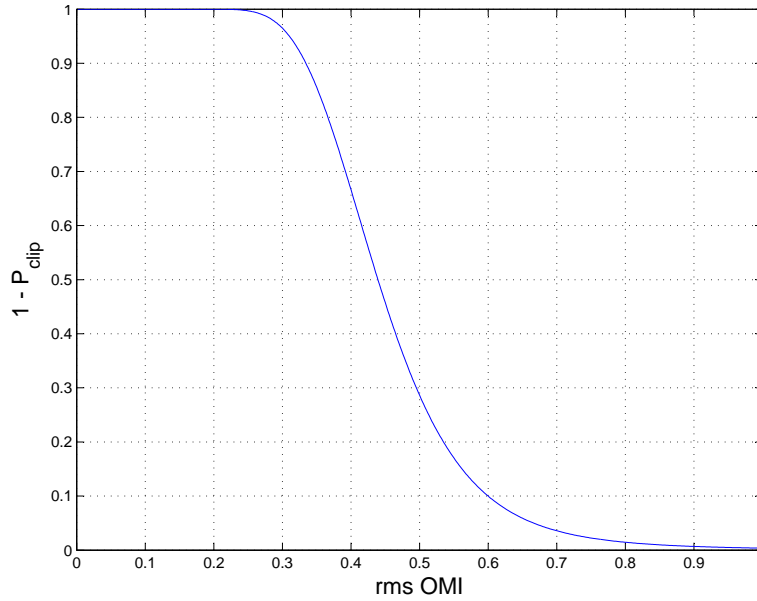


Figure 4.43: Probability of absence of laser clipping impulse in a data signaling period for 16 carrier channels vs. rms OMI μ .

capacity⁸ c :

$$\begin{aligned} c &= (1 - P_{\text{clip}})C \\ &= B e^{-\frac{\kappa}{\sqrt{3}}} e^{-\frac{1}{2\mu^2}} \log_2 \left(1 + \frac{\mu^2 I_{\text{pin}}^2}{\sigma_Z^2} \right). \end{aligned}$$

The probability that no clipping event occurs in a given symbol period is shown in Fig. 4.43 as a function of the OMI for a 16-channel SCM modulation. The variations of the channel capacity c and the linear channel bound C with the OMI μ are shown in Fig. 4.44. While C is not bounded, and can be arbitrarily large for large μ , c is. An optimal OMI setting can be found that trades off signal-to-RIN ratio and non-linear clipping distortions. In the illustrated case which corresponds to the SCM modulation of interest the information channel model sets the optimal OMI to 30%. It is also apparent that for an OMI of 13% the linear assumption is very good (P_{clip} is a very flat function of μ in the vicinity of 0) and remains so until the optimal OMI is reached. The capacity degrades rapidly for higher OMI

⁸Obtained using the definition of the mutual information $I(X, Y)$ and entropy chain rules for $H(Y, \theta)$ and $H(Y, \theta|X)$.

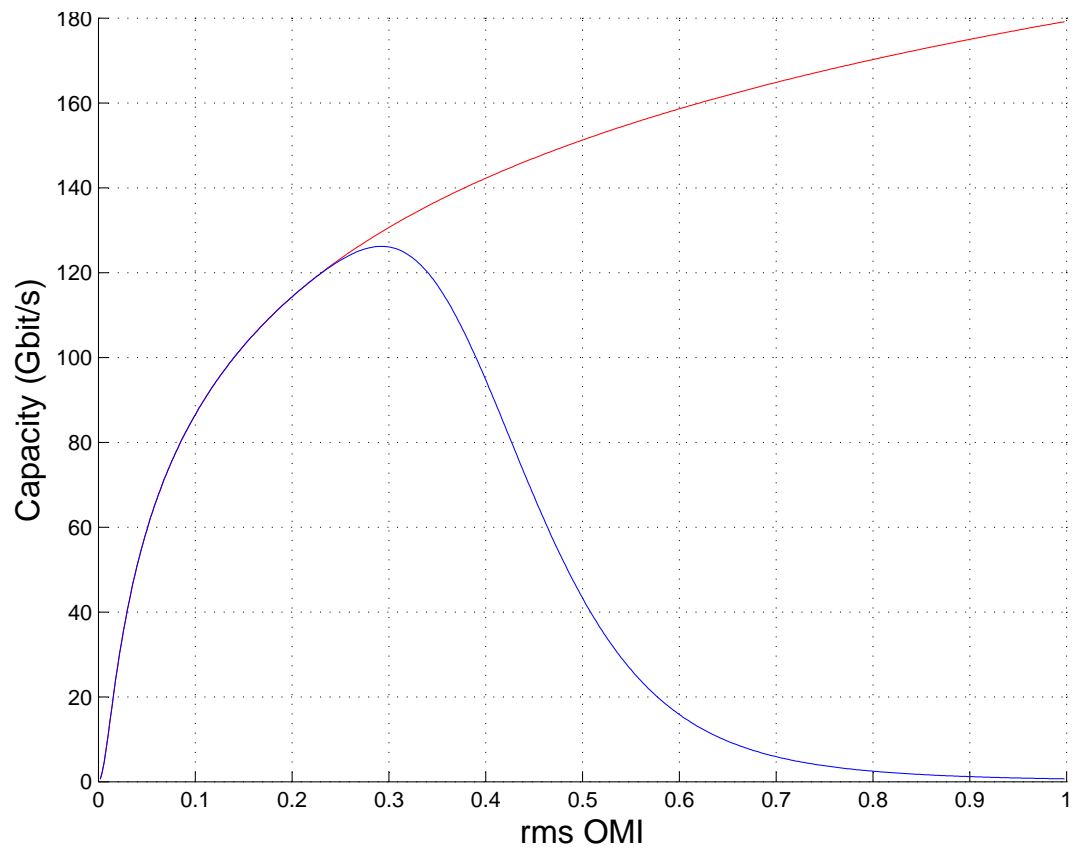


Figure 4.44: Laser diode capacity vs OMI with RIN and clipping noise (blue curve) and linear channel bound (red curve). $K = 16$; $B = 14$ GHz; $I_b - I_{th} = 50$ mA.

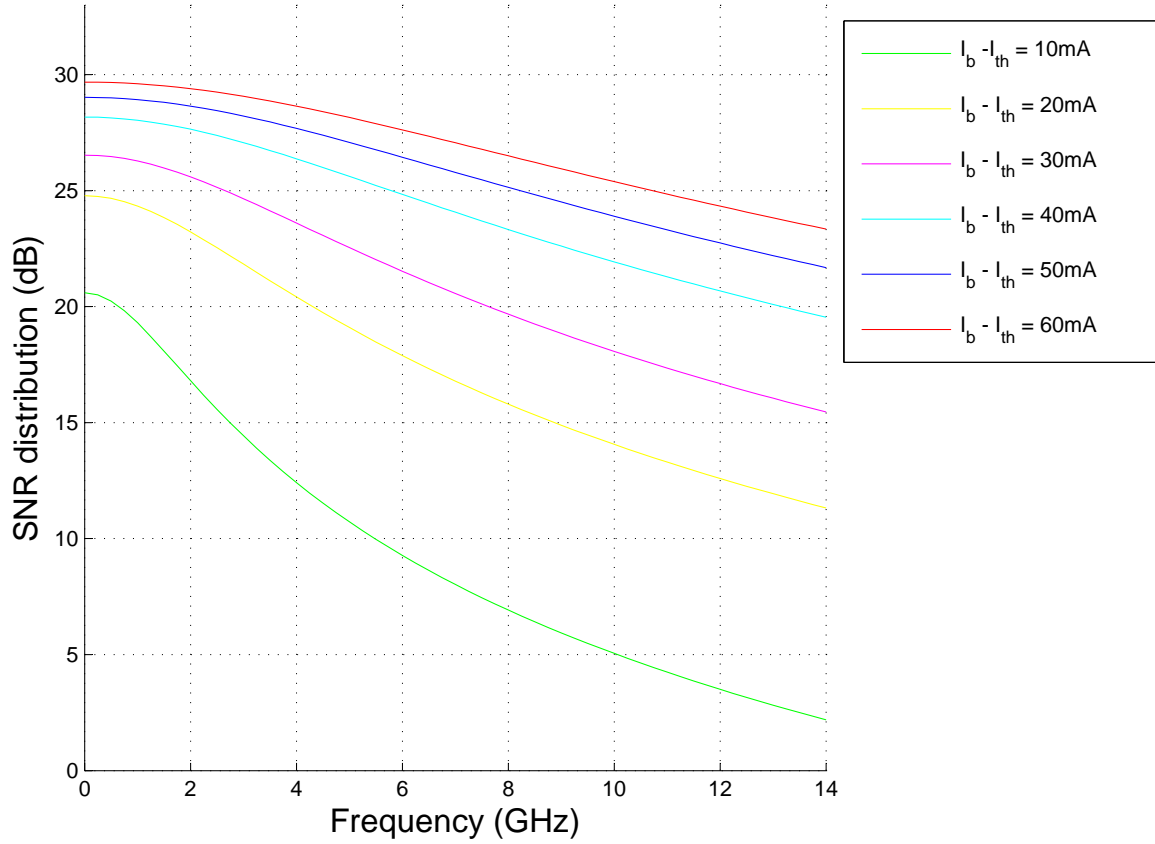


Figure 4.45: Signal-to-RIN ratio distribution for a flat (single-sided) input signal power spectral density μ^2/B over the frequency band $(0, B)$. $\mu = 0.13$; $B = 14$ GHz.

values. Keeping the system in the linear channel regime while being slightly suboptimal in terms of achievable capacity makes the design of codes and modulations approaching the capacity limit more intuitive following known Gaussian channel results.

4.6.5 Laser SNR distribution and water-filling optimum

In the context of the linear Gaussian channel regime the model can be refined by taking into account the linearized EO frequency response of the laser as well as the actual shape of RIN spectral density. With a set input signal OMI constraint the capacity can be optimized by shaping the input signal power spectrum according to the water-filling procedure.

SNR for flat input signal power density Assuming first that power spectral density of the signal process X is flat over the frequency interval $(0, B)$ taking into account the laser EO response and the RIN power spectral density function the signal-to-noise ratio distribution can be expressed as

$$\text{snr}(\omega) = \frac{\mu^2 P_0}{2B 2R_{\text{sp}}} \frac{\omega_r^4 + 4(\omega_r^2 + \Gamma^2)\Gamma^2}{\omega^2 + \Gamma_N^2}.$$

A flat signal spectral density function corresponds to the case where equal power is put into each RF carrier channel. SNR distributions for different bias currents when $\mu = 0.13$ and $B = 14$ GHz are shown in Fig. 4.45. In particular the SNR levels predicted by this model match very well the SNR levels for the 16 carriers computed through a complete link simulation model and presented in Fig. 5.2 (the red curve in Fig. 4.45 has to be compared with the SNR levels of the 16 channels for an OMI of 13% in Fig. 5.2). Matching is not so good for low bias currents very likely because the present model does not take into account additional noise contributions due to nonlinear mixing.

The channel capacity under the linear assumption can be more precisely evaluated with the expression

$$C = \int_0^B \log_2(1 + \text{snr}(2\pi f)) df.$$

For $\mu = 0.13$ and $B = 14$ GHz at a bias of 50 mA above threshold the computed capacity value is 136 Gb/s to be compared with the estimates of the previous section that were evaluated using an upper bound for the RIN power spectral density and were not taking into account the details of the laser frequency response.

Optimal input signal power density and capacity Assuming for a moment that no bandwidth restriction applies (absence of laser package sharp cut-off frequency, infinite bandwidth photodiode, etc.) we can look for the absolute optimum for the channel capacity under the constraint of a fixed OMI (for a fixed bias current) in linear Gaussian channel regime as given by the “water-filling” algorithm. Using the laser linearized response and RIN spectral density function the optimum signal power spectral density can be derived and the channel capacity is given by

$$C = \int_0^{\omega_M} \log_2 \left(1 + \frac{\omega_M^2 - \omega^2}{\Gamma_N^2 + \omega^2} \right) \frac{d\omega}{2\pi},$$

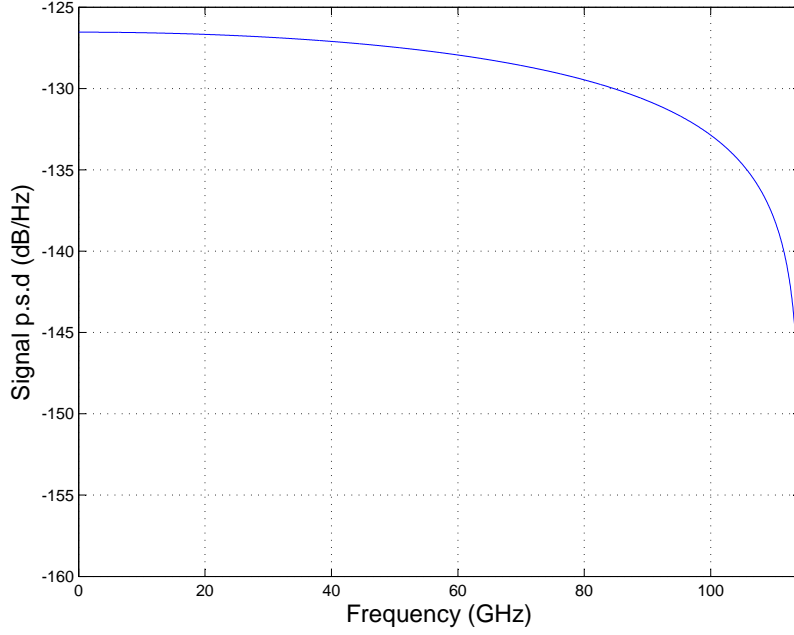


Figure 4.46: Optimal input signal power spectral density for the laser channel. $\mu = 0.13$; $I_b - I_{th} = 50$ mA.

where $\omega_M = (3\pi Q\mu^2)^{1/3}$ with $Q = \frac{P_0}{2R_{sp}} (\omega_r^4 + 4(\omega_r^2 + \Gamma^2)\Gamma^2)$.

As an example the capacity-optimal signal power spectral density and the associated signal-to-RIN distribution are shown in Fig. 4.46 and Fig. 4.47 respectively. These results highlight the fact that, in a linear regime, the laser resonance itself does not constitute an intrinsic barrier to the efficient modulation of the laser diode despite the steep roll-off in the laser linear response. As a matter of fact RIN is subject to a similar roll-off combined with a quadratic enhancement factor that provides the true limitation.

More realistic “water-filling” optimization can be performed under a hard bandwidth constraint. Furthermore once the fiber length is increased receiver noise with a flat (or shaped by other link elements) spectral density becomes dominant making the previous results of relevance only in the case of short transmitter-limited links. For longer fiber link length uniform distribution of signal power over the available frequency band is the capacity-optimal distribution.

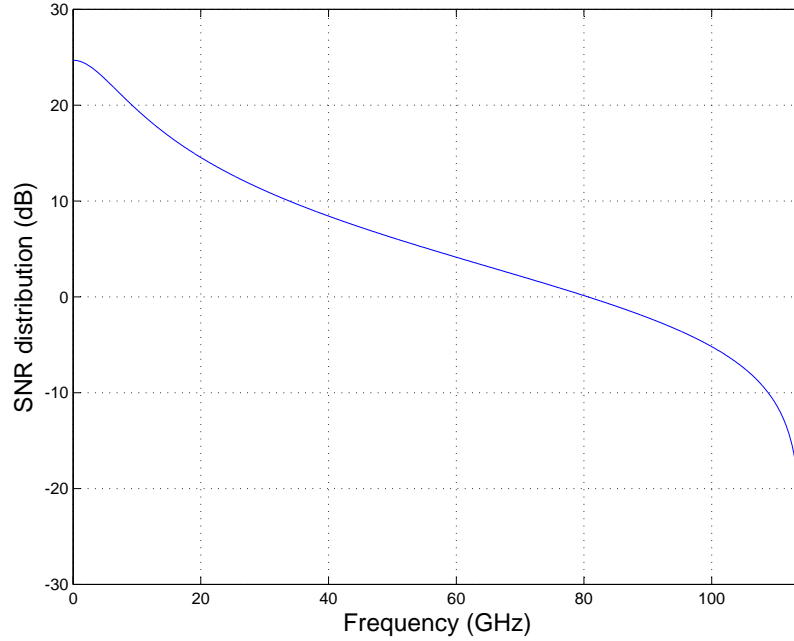


Figure 4.47: Optimal signal-to-RIN ratio distribution. $\mu = 0.13$; $I_b - I_{th} = 50$ mA.

4.6.6 Discussion

The simple information channel model presented provide insightful results regarding the transmission system capacity. Even though some laser non-linear dynamics effects are not taken into account and fiber non-linear impairments are assumed to have been avoided by a precise tuning to the fiber zero-dispersion wavelength the derived achievable spectral density is well above 6 b/s/Hz. This is more than double the effective bandwidth efficiency targeted in this work. Yet the implicit assumption is that the signal power spectrum can efficiently fill the available bandwidth (by having “brick-wall” baseband filters for each channel in an SCM scheme). This is not the case in practice and packing carrier channels close to each other induces interference between channels (a multi-channel capacity analysis could quantify such effects on the information channel capacity). Nonetheless the digital signal processing structures presented in Sec. 3.3 can reduce these interferences and bring implementable systems closer to theoretically achievable capacities when combined with powerful channel coding.

4.7 Conclusions

For the proposed channel used to transmit an SCM electrical signal and composed of a DML, single-mode fiber and a photodiode connected on each side to electrical amplification and buffer stages, impairments have been categorized as linear or nonlinear. It has been shown that a combination of laser chirp and fiber dispersion can result in an alteration of the signal power distribution among channels at the output of the system with consequences on the signal to noise ratio in each channel. These linear effects depend on the sign of the fiber group velocity dispersion at the laser operating wavelength and do not necessarily vary monotonically with fiber length. Nonlinear effects related to the interplay of chirp and chromatic dispersion do not depend on the sign of the GVD at the carrier wavelength. Their adverse impact (increase in CSO and CTB) increases monotonically with fiber length. Such qualitative results will be echoed in the simulation results presented in the next chapter. The laser diode is a nonlinear device and needs to be operated in a regime that minimizes nonlinearities.

Laser noise is the dominant source of noise at short distances (less than 20 km) whereas receiver shot and thermal noise dominate at higher distances. Signal-to-noise ratio requirements when considering QAM-16 multilevel modulation on each RF carrier is 25 dB. It can be lowered to 19 dB when using forward-error correction. Allocating parts of the power budget to nonlinear distortions which appear as noise in each electrical subcarrier band and placing a limit to the contribution of each transmission link component to nonlinear distortion equal to -35 dB for its CSO and -40 dB for its CTB, it appears that the limiting impairment, besides laser nonlinear dynamics, is the combination of chromatic dispersion and laser chirp. This in turn translates into how close the laser output wavelength needs to be compared to the fiber zero-dispersion point.

Link component models, some of which have been introduced in this chapter, have been gathered in a transmission system numerical simulation platform presented in the following chapter.

Chapter 5

Application: a low-cost 40G Transceiver

This chapter presents the design of a simulation platform based on models developed in the previous chapters for the purpose of proving the feasibility of a 40 Gb/s transmission using low-cost optical components (10 Gb/s DML and photodiode). Simulation results permit the solidification of the system definition previously based on high level simulations and critical parameters numerical estimates. In particular system implementation specifications can be derived. In order to prove that implementation challenges for the defined system can be overcome, the measurement results of a 3.6 mm² single-channel QAM transceiver test chip designed in CMOS technology are presented. This test chip, while still on the wafer probe station, was included in a basic transmission prototype composed of packaged DML and photodiode modules, electrical amplification stages and an SMF piece.

5.1 Numerical simulation platform and performance analysis

5.1.1 Introduction

The optimization of a frequency division multiple access transmission system example is discussed on page 335 of [BB99]:

The choice of [system] parameters is usually accomplished through a cut-and-try approach, which requires repeated analyses of the system and, hence, the availability of a tool to quickly evaluate system performance.

Due to the complexity of the system presented in this dissertation and the interdependency between various discrete and continuous parameters, this very same approach was adopted indeed. It was felt that an iterative procedure based on a complete simulation tool would allow the determination of system performance and help make the appropriate system architecture and parameter choices. Such a tool would also form the basis for further analysis and understanding of how well-understood subsystems when studied by themselves interact once integrated with each other.

However some parameters were already constrained by the goals the present system had to achieve that motivated its design in the first place. In particular the primary constraints were economical and technological and defined by the ability to use cost-effective components and technologies. These core constraints translate into a hard bound on the total available bandwidth (less than 15 GHz) which comes at a big premium, maximum signal processing speed (clock speed comfortably less than 1 GHz), system complexity (integration, circuit and module size) and technology (maximum sustainable voltages and peak-to-average ratio, transistors maximum operating frequency). This actually provides a starting point for the cut-and-try design methodology.

System parameter	Parameter value
Symbol constellation type and size	QAM-16
Symbol rate	666 Mbaud
Number of RF carrier channels	16
Carrier frequency spacing	833 MHz
Baseband analog pulse shaping filter	3 rd -order Butterworth, 416 MHz cut-off
Directly modulated laser bias current	Between 5 and 60 mA above threshold
Optical modulation index	Between 10 and 30% rms
Single mode fiber length	Between 2 and 40 km

Table 5.1: Summary of system parameters for a low-cost 40 Gb/s system.

Given that signal bandwidth had to be divided by approximately 4 compared to basic NRZ signalling in order to transmit 40 Gb/s along with any channel coding overhead, the symbol constellation had to be composed of at least 16 points. Starting now with QAM16 constellations the constraints on the digital signal processing speed translate into the necessity for the symbol rate to be less than 1 Gbaud which requires that the symbol flow be divided among at least 16 parallel channels. Parallelism eases digital signal processing but has an adverse effect on the combined signal peak-to-average ratio: for the same

signal power, and signal to noise ratio at the receiver everything else remaining the same, the peak signal amplitude increases with the number of channels as explained in Sec. 3.2. This finally encounters analog front-end implementation as well as laser nonlinear clipping issues if arbitrarily increased. Carrier spacing was initially set to a value of 833 MHz. This is above the minimum theoretical spacing equal to twice the Nyquist frequency (333 MHz here). This spacing value was chosen in order to get high spectral efficiency with manageable inter-channel cross-talk when using 3rd-order Butterworth pulse shaping filters setting reasonable analog front-end challenges. Table 5.1 summarizes the initial system parameter settings for the system feasibility verification and operation optimization procedure. Most of the initial values presented were determined through initial high-level simulations using the MATLAB computing language beyond the high-level explanations provided.

The analysis of simulation results is expected to allow the identification of critical dimensions along which design efforts have to be applied. For instance, if it were found that reliable transmission is limited by inter-channel cross-talk despite the usage of an advanced DSP architecture for its cancellation, transmit filter design could be further constrained. This would make the actual implementation more challenging though.

5.1.2 A complete system simulation platform in C

Table 5.2 summarizes the subsystem and component characteristics that were modelled and included in the system simulation platform implemented in C code for reduced computation time. The last column in that table provides pointers to relevant sections in this dissertation. Some effects were not initially included in the simulation platform since it was deemed that they did not add significant insight in the system operation for the additional computation time and complexity they would require and could be controlled with proper system integration or existing components redesign. These include in particular effects related to electrical impedance mismatch and some electrical package effects in the range of frequencies considered that could affect the integrity of signals transmitted between electrical subsystems.

5.1.3 Simulation results

Since the directly modulated laser was determined in a previous analysis to be a critical component in the communication chain even at minimal optical transmission distance the

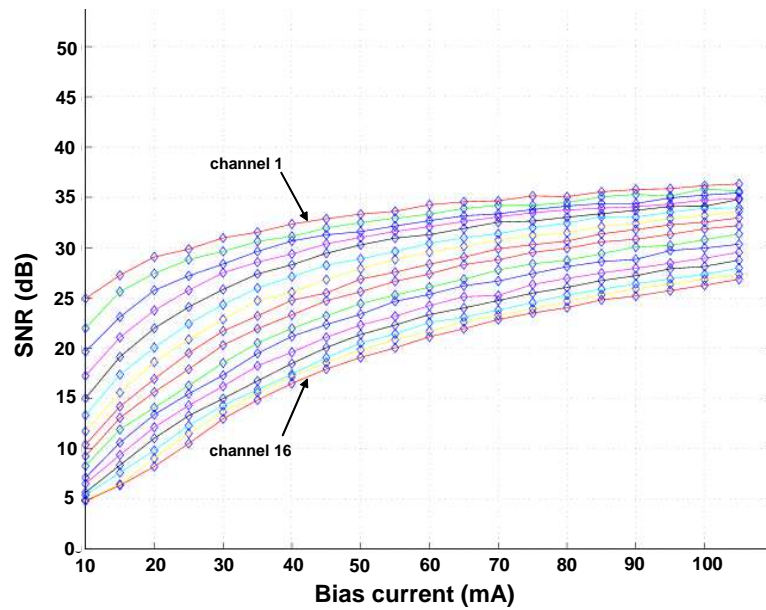


Figure 5.1: Variations of the SNR for the 16 channels with bias current for a fixed OMI of 15% in an optical back-to-back configuration.

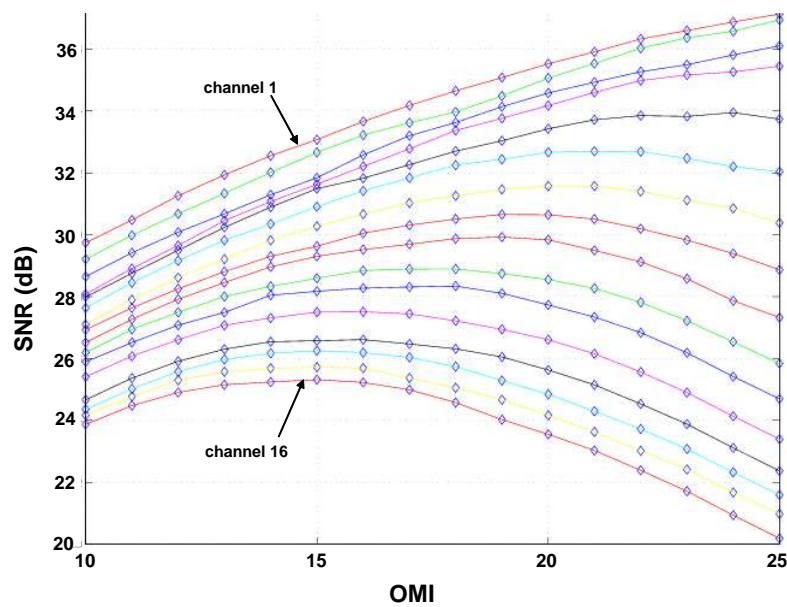


Figure 5.2: Variations of the SNR for each of the 16 channels with the total OMI (in % of the average optical power) for a laser bias current of 80 mA above threshold in an optical back-to-back configuration.

System component	Characteristics included in simulation platform	Reference in this work
Analog circuit models	Filter shapes and bandwidths Linearity of amplifiers, filters and mixers Circuit noise	Sec. 4.3.2
Laser	Laser die electro-optical response Laser intensity and phase noise Zero-dispersion wavelength detuning	Sec. 4.5.1 & 4.5.4 Sec. 4.5.2 & 4.5.4 Sec. 4.3.1
Optical fiber	SMF with PMD and chromatic dispersion	Sec. 2.3.5
p-i-n photoreceiver and receiver amplification	Responsivity Bandwidth Noise Transimpedance	
Equalization and cross-talk cancellation DSP	FIR filters length Number of cross-talk cancellation filters	Sec. 3.3.3 Sec. 3.3.2
Timing, carrier recovery	Digital architecture; closed recovery loop combined with DSP	

Table 5.2: Subsystem characteristics captured in the simulation platform implemented in C. The last column provides references to related developments in this dissertation.

determination of its proper operation conditions motivated a set of simulation runs in an optical back-to-back configuration. Laser bias current and optical modulation index (OMI) were the parameters to be optimized. It has been established in Sec. 4.5.5 through a combination of experimental and simulation results that both linearity and noise characteristics of the laser improve when increasing the bias current in the allowed range. The existence of an optimal optical modulation index value is expected given the laser noise and nonlinearity behavior. When the OMI increases signal to relative intensity noise increases while signal to nonlinear distortion decreases.

Fig. 5.1 and 5.2 show the results of several simulation runs all performed in back-to-back optical configuration. These figures present the SNR estimates for each of the 16 channels expressed in decibels ($\text{SNR}_{\text{dB}} = 10 \log_{10}(\text{SNR})$). More precisely the SNR estimate

for channel k is computed by forming the ratio:

$$\frac{\sum_{q=0}^{N-1} |\check{s}_{n+q,k}|^2}{\sum_{q=0}^{N-1} |\check{s}_{n+q,k} - \hat{s}_{n+q,k}|^2},$$

where the notations of Sec. 3.3 are used to designate the sequence $(\hat{s}_{n,k})$ of received samples in channel k at the output of the baseband DSP stage and the sequence $(\check{s}_{n,k})$ of received symbols after the decision stage. N is an integer number of samples sufficiently large to provide good estimates and n represents the discrete time at which the computation is started. As a matter of fact the actual transmission of QAM-16 symbols is occurring only after the transmission of a set of training quaternary-phase-shift-keying (QPSK or PSK-4) sequences in all channels obtained by retaining the four corner symbols of the QAM-16 constellation. At the end of the training sequence adaptive DSP as well as timing and carrier recovery have converged. n is chosen to correspond to the end of the training sequence transmission and the beginning of the actual 40 Gb/s transmission.

Fig. 5.1 is obtained by varying the laser bias current for an rms optical modulation index set to 15%. The obvious result in this case is the improvement of the system performance with increasing bias current explained by the reduction of RIN and improvement of laser linearity. We note also the disparity of performance among channels. The channels at lower frequencies exhibit a better SNR than the channels at higher frequencies when the total signal power distribution between channels is flat, which is in accordance with the analysis of Sec. 4.6.

Fig. 5.2 displays the variations of system performance with the total rms OMI for a fixed bias current of 80 mA above the laser threshold. All the channels do not behave similarly in the range of modulation indexes considered here. In particular the identification of the optimal optical modulation index resulting from the trade-off between laser noise and nonlinearity penalties leads to different results depending upon the channel. Higher frequency channels that were seen to be more affected by relative intensity noise are also more sensitive to nonlinearities. The worst case criterion would lead to an optimum for a value of 15% whereas a criterion based on the maximization of the total SNR obtained by the addition of the SNRs of all channels would lead to an optimum located closer to 20%. We note that an OMI of 13% (100%/PAR, where PAR is 7.6 for 16 carriers modulated with QAM-16 symbol constellations as explained in Sec. 3.2.1) corresponds to the point above which the simple adiabatic model with strictly linear dependence of the output power with

the bias current above threshold predicts that signal clipping starts.

Multiple other runs were performed once the laser bias current and optical modulation index were fixed. Even though fiber can have an impact on the optimal choice for these parameters reasonable back-to-back values were chosen and kept fixed for simulations with non-zero fiber length and possible laser de-tuning (the commercial 1310 nm DFB DML used operates at a wavelength guaranteed to remain between 1290 nm and 1320 nm where the GVD is approximately $+2 \text{ ps}^2/\text{km}$ and $-2 \text{ ps}^2/\text{km}$ respectively). Table 5.3 summarizes results obtained for different fiber lengths. Observations from the plots of the received electrical signal power spectrum motivated the definition of the link electro-opto-electrical response of the link. The purpose was to explain “anomalous” variations of the SNR per channel not explained when only taking into account the nonlinear effects due to chirp and dispersion. The latter are independent from the sign of β_2 .

Fiber length		0 km	2 km	10 km	40 km
SNR before equalization	$\lambda_0 = 1290 \text{ nm}$ ($\beta_2(\lambda_0) = +2 \text{ ps}^2/\text{km}$)	22 dB	22 dB	21 dB	14 dB
	$\lambda_0 = 1330 \text{ nm}$ ($\beta_2(\lambda_0) = -2 \text{ ps}^2/\text{km}$)	22 dB	22 dB	18 dB	10 dB
SNR after equalization	$\lambda_0 = 1290 \text{ nm}$ ($\beta_2(\lambda_0) = +2 \text{ ps}^2/\text{km}$)	28 dB	28 dB	25 dB	15 dB
	$\lambda_0 = 1330 \text{ nm}$ ($\beta_2(\lambda_0) = -2 \text{ ps}^2/\text{km}$)	28 dB	27 dB	23 dB	10 dB

Table 5.3: Computed SNR averaged over the 16 channels for different fiber lengths with a DGD equal to the mean DGD for a fiber with a PMD coefficient of $1 \text{ ps}/\sqrt{\text{km}}$ and in a worst case SOP configuration. Results are shown before and after the equalization and cross-talk cancellation stage for extremal cases of laser de-tuning ($\lambda_0 = 1290 \text{ nm}$ and $\lambda_0 = 1330 \text{ nm}$).

5.1.4 Analysis, SNR requirements and forward-error correction

We assuming that the overall noise and nonlinearity contributions result in a random disturbance that follows a Gaussian distribution. The SNR estimates provided by the simulation platform can be readily used to determine the bit error rate through the following relationship valid for the QAM-16 constellation for small error probabilities with the appropriate bit to symbol mapping:

$$P_b \approx \frac{3}{2} \operatorname{erfc} \left(\sqrt{\text{SNR}/10} \right).$$

Coding scheme	Overhead	Required SNR
No FEC	No overhead	25 dB
RS(255,239)	7%	19 dB
Turbo block code	15%	15 dB

Table 5.4: Comparison of overhead and required SNR at a BER of 10^{-15} for a system without FEC, with Reed-Solomon(255,239) and with a Turbo block code.

This means that for a bit-error rate (BER) of 10^{-12} the minimum SNR requirement is 24 dB and for a BER of 10^{-15} it is 25 dB. SNR requirements can be relaxed when using forward-error correction (FEC) codes which is a widely used technique even for optical communications at speeds of 10 Gb/s and beyond [AHS⁺02]. Table 5.4 summarizes the SNR requirements at a BER of 10^{-15} when using a widely used block code RS(255,239) that is specified by the ITU for submarine optical communications and a Turbo block code with higher gain but higher overhead as well. RS(255,239) has been assumed in the design of the system and a 7% overhead had to be taken into account for specifications such as pulse shaping filters bandwidth and carrier spacing with a total raw throughput of 43 Gb/s. This overhead which *a priori* adds constraints to the system implementation brings enormous benefits.

Simulation results, some of which were presented in the previous section, show that with the choice of parameters displayed in table 5.1, a laser bias current of 60 mA above threshold, a total rms OMI of 18% and the usage of FEC reliable transmission is possible at 40 Gb/s over at least 10 km of SMF.

It is also apparent that several straightforward improvements can be implemented. In particular, with the constraint that the total electrical signal power should remain the same, signal power can be unevenly allocated among channel. A simple tilt of the RF carrier power grid to favor higher frequency channels would bring the SNR in each channel close to the same level close to 29 dB instead of a worst case channel around 25 dB.

5.1.5 Conclusions and system specifications

Using a combination of analysis and numerical simulations a complete set of specifications could be prepared for the actual implementation of a prototype of the system with an RF

carrier frequency map as specified in Sec. 3.2.2. Albeit system simulation and analysis bring proof of the system feasibility, it also has to be implementable using low-cost and widely available CMOS circuit technology. Using the specifications resulting from the simulations and analysis presented in this dissertation, the High Speed Communications VLSI Research team implemented a test chip presented in the following section.

5.2 Circuit design challenges and test chip

5.2.1 Test chip goals

The reduction in bandwidth resulting from the usage of multilevel signalling makes conceivable the usage of standard and cost-effective CMOS technology to implement a 40 Gb/s SCM system that we validated through thorough modelling and system simulation. Yet major technical challenges remain in the design of the SCM analog radio-frequency (RF) front-end. In order to prove that the most challenging integrated circuit functions can be implemented our team designed a QAM transceiver test chip.

This section explains what these design challenges are. The test chip architecture is subsequently presented and measurements of its operation are outlined. The design of a one-channel system prototype comprising the QAM transceiver test chip connected to the complete optical channel including 30 km of SMF is finally described.

5.2.2 Main CMOS design challenges

The main CMOS circuit implementation challenges were identified as being:

- the design of highly linear mixers operating at high frequencies (IMD3 less than -42 dB and phase shifters at frequencies close to 14 GHz),
- the design of high-linearity (combined CSO and CTB distortions less than -36 dB at 100 mV_{rms} when being used with all 16 carriers) and high-bandwidth (3-dB bandwidth above 16 GHz) input and output buffers,
- the integration of all these functionalities on a single die.

Fig. 5.3 shows a block diagram of the QAM transceiver test chip. This test chip gathers modulation-demodulation functions for channel 16 at a carrier frequency of 13.32 GHz, the most challenging and highest frequency channel. Its transmit path is composed of:

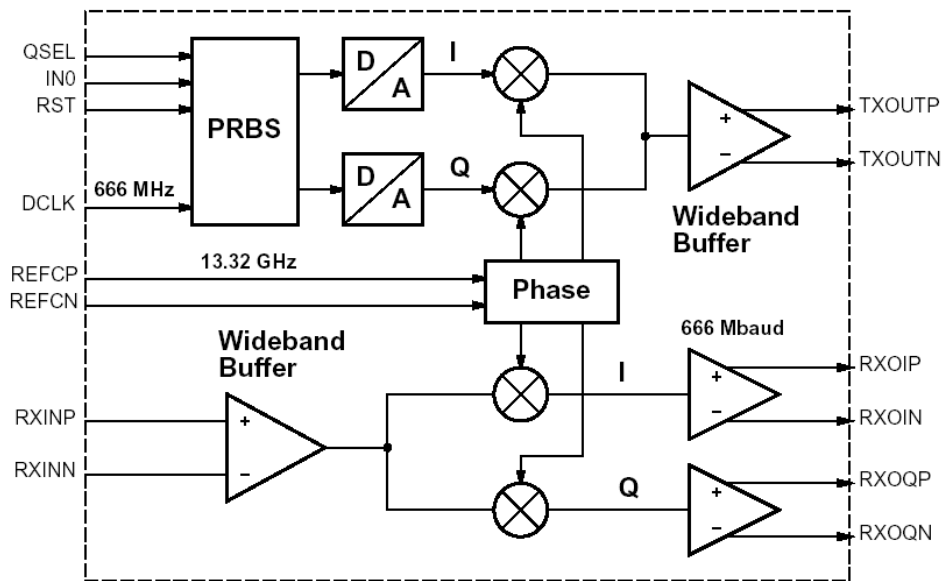


Figure 5.3: Test chip block diagram. PRBS: pseudo-random bit sequence generator; D/A: digital-to-analog conversion stage.

- an on-chip PRBS generator and data scrambler clocked by a 666 MHz external digital clock provided through the DCLK port. RST serves as a reset input and QSEL allows the switching from the generation of a QAM-16 to a QPSK signal for testing purposes,
- two two-bit digital to analog converters (D/A) producing in-phase (I) and quadrature (Q) baseband data signals,
- in-phase and quadrature up-conversion mixers modulating the transmit baseband signals with a carrier at 13.32 GHz,
- a $50\ \Omega$ -matched wideband buffer driving the passband transmit signal through the differential output port TXOUTP/TXOUTN.

Its receive path is composed of:

- a wideband buffer receiving the input passband signal from the differential input port RXINP/RXINN,
- two down-conversion mixers demodulating the received passband signal into baseband I and Q signals,

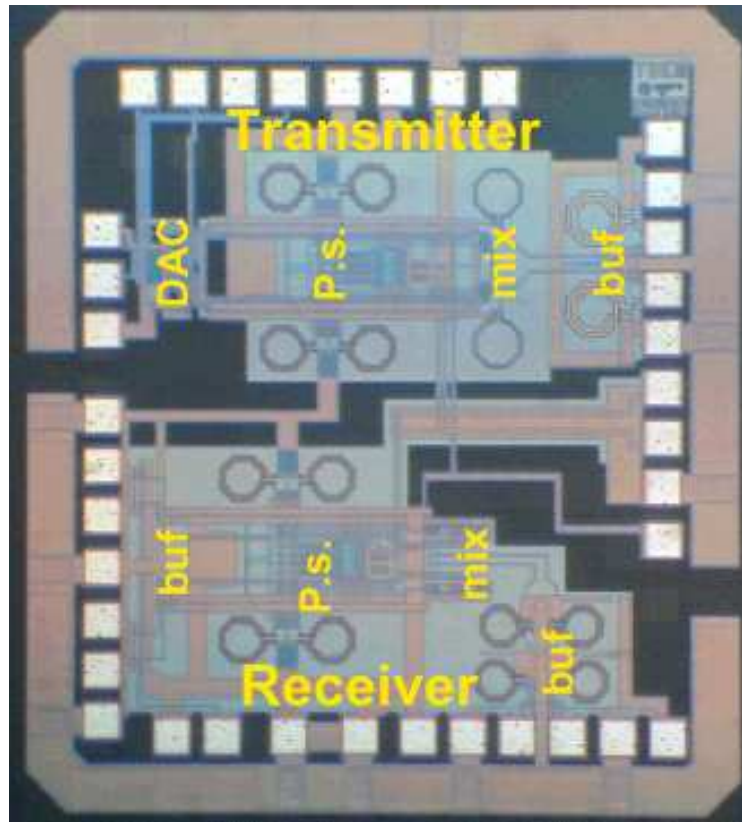


Figure 5.4: Test chip die photo. DAC: digital-to-analog converter; P.s.: phase shifter; mix: mixer; buf: buffer.

- two baseband buffers for the received I and Q signals that drive two differential output ports RXOIP/RXOIN and RXOQP/RXOQN.

A common phase shifter derives the in-phase and quadrature-phase carrier signals from a reference signal provided by an external local oscillator through the ports REF_{CP}/REF_{CN}.

5.2.3 QAM transceiver CMOS test chip

Fig. 5.4 shows a photograph of the implemented QAM transceiver test chip where transmitter and receiver paths have been annotated to make the identification of the different functional blocks defined in Fig. 5.3 easier. This chip was implemented in 0.14- μm , 1.5-V CMOS technology. Its total area is 3.6 mm² and its power consumption 340 mW.

5.2.4 Testchip and optical subsystem measurement setup

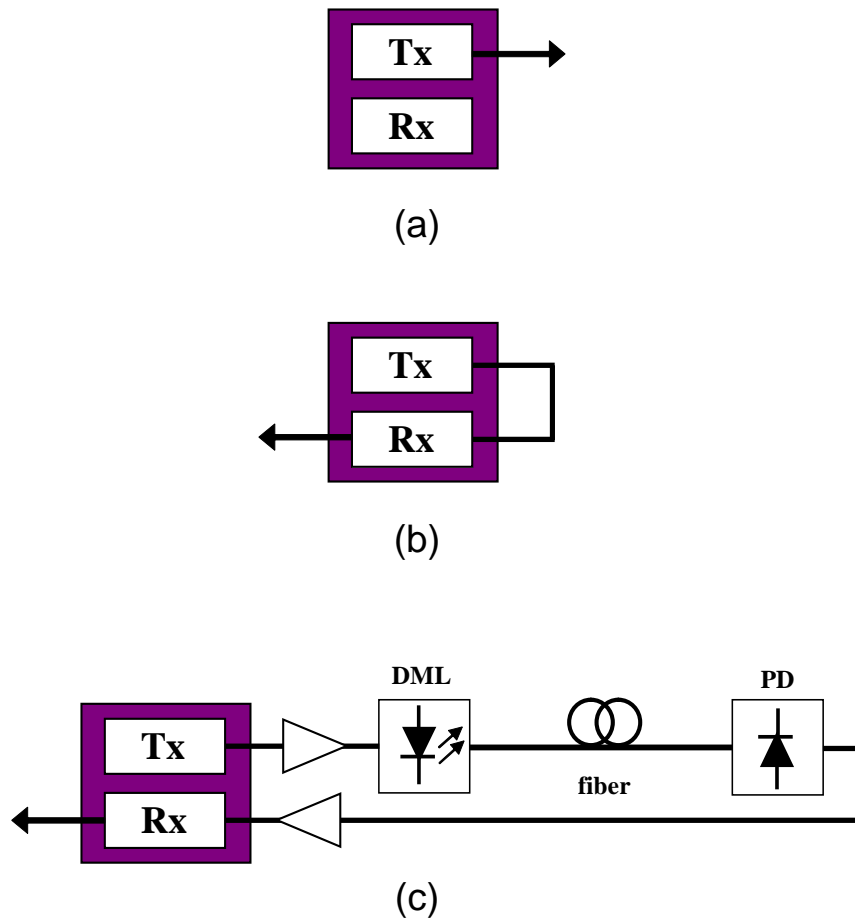


Figure 5.5: Test chip measurement configurations: (a) measurement of test chip output power spectrum, (b) observation of back-to-back QAM constellation, (c) observation of constellation after fiber optic transmission.

Fig. 5.5 shows the three basic laboratory measurement setup configurations that were implemented in order to verify the test chip correct operation and create a simple prototype of the system. The properties of the QAM transmitter were first measured (Fig. 5.5(a)) and more specifically the spectral properties of the output passband QAM-16 signal were checked. A back-to-back modulation/demodulation operation (Fig. 5.5(b)) was then demonstrated and operation parameters were adjusted to prepare for the implementation of an illustrative system prototype (Fig. 5.5(c)).

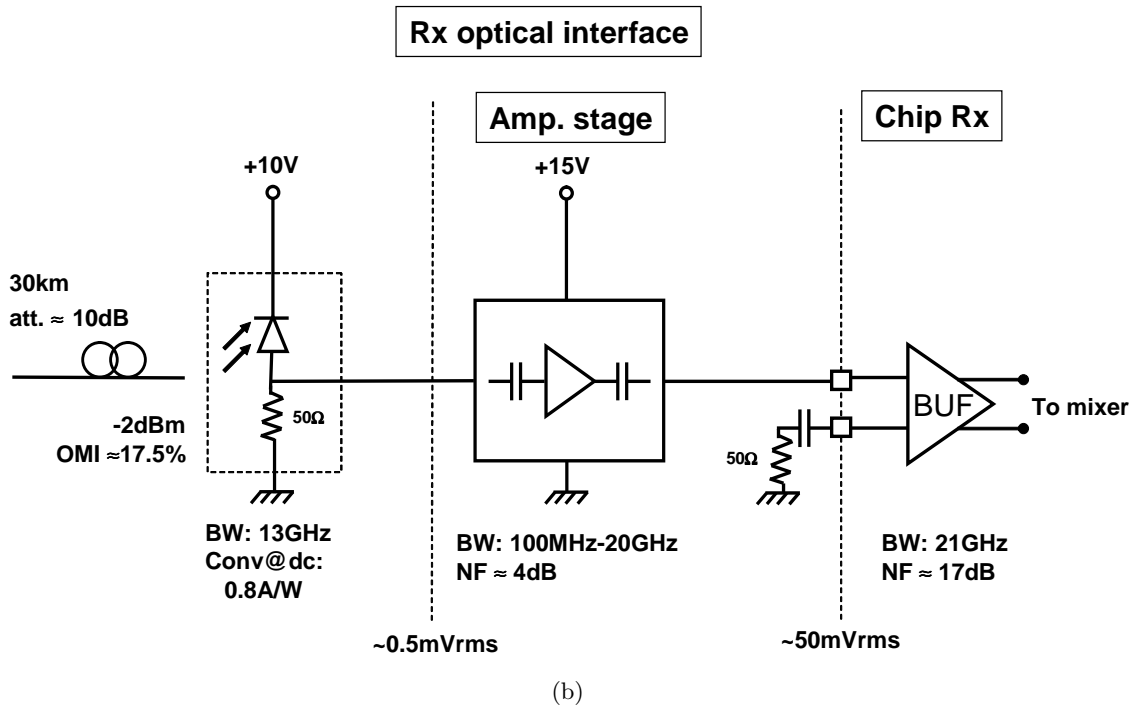
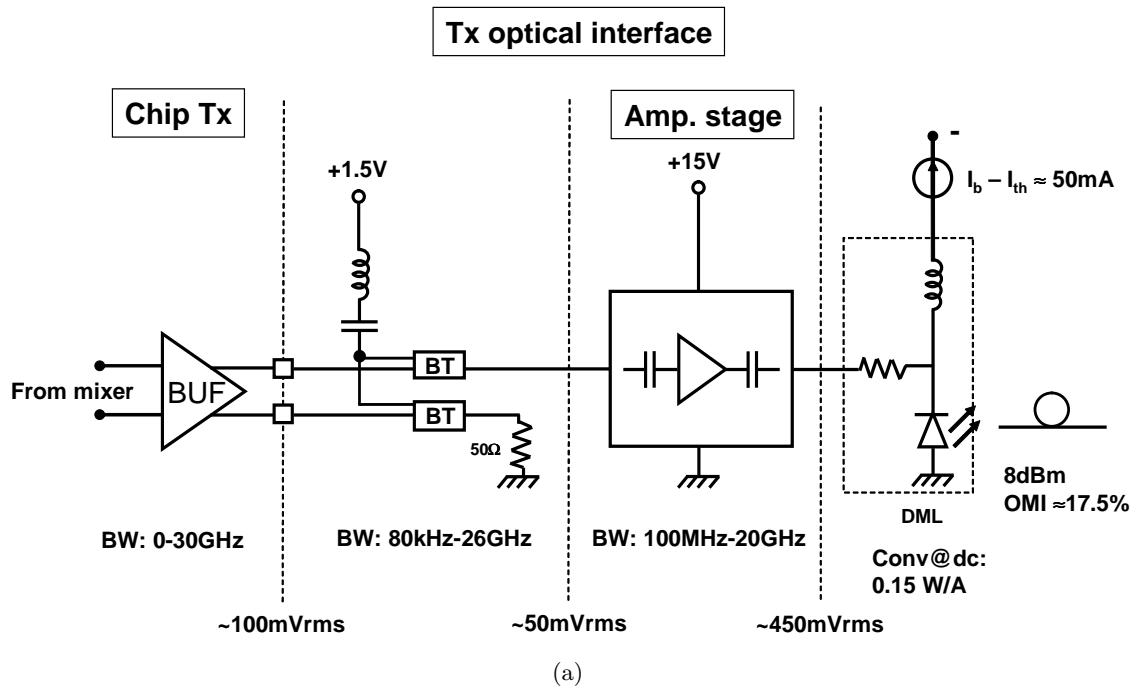


Figure 5.6: (a) Transmit electro-optical and (b) receive opto-electrical interfaces. BT: bias T; BUF: buffer.

Fig. 5.6 shows details of the transmit and receive paths of the QAM transmission prototype including signal levels at intermediate interfaces, bandwidth of off-chip electrical components and optical signal levels. In this illustrative experiment an optical modulation index of 17.5% for the 16-QAM16 signal was applied to the only channel available here and the total fiber length used was 30 km. Fig. 5.6(a) shows the on-chip transmit output buffer connected to a biasing and differential-to-single-ended conversion stage, an amplification stage and the packaged directly modulated laser modelled in Sec.4.5 biased at 50 mA above threshold and coupled to an SMF thanks to an integrated fiber pigtail output and a standard fiber connector. Fig. 5.6(b) shows the fiber coupled to a packaged, high-power 50 Ω -terminated p-i-n photodiode connected to a low-noise amplification stage, itself connected to the on-chip receive input buffer through a single-ended to differential stage.

5.2.5 Measurement results

Fig. 5.7 shows the power spectrum of the signal at the output of the chip transmitter. Its shape is as expected except for undesirable spurs at frequency offsets around the center frequency of 13.32 GHz at multiple of the symbol rate, 666 MHz. These discrete spectral components are likely to be the result of baseband signal level imbalances as the calculation of the theoretical signal power spectrum suggests in that case. In QAM-16 mode the PAR is approximately equal to 1.9 for a single channel. Measured single-ended output signal levels were about 100 – 130 mV_{pp} at the end of RF cables attached to the chip probes.

In a back-to-back electrical setup the I and Q receiver differential output voltages were about 100 – 150 mV_{pp}. The observed QAM-16 constellations showed a fairly large amount of noise (Q factor of approximately 3.5 translating into BER $\approx 10^{-4}$). Lowering of the data clock to 166.5 MHz lead to a noticeable improvement ($Q \approx 4.5$ and BER $\approx 10^{-6}$) suggesting that most of the noise contribution was data dependent and due to ISI. The bandwidth bottleneck was ulteriorly identified within the chip and corrected in the design.

Fig. 5.8(a) shows a back-to-back optical QAM-16 constellation measurement after connecting the test chip receiver I and Q outputs to the controls of the horizontal and vertical axes respectively of an oscilloscope. Fig. 5.8(b) shows the same measurement after inserting up to 30 km of fiber in the optical transmission path. Almost no degradation in SNR could be observed from 0 to 30 km of fiber and the BER at 30 km can be estimated from $Q \approx 3$ as being BER $\approx 10^{-3}$. The main source of BER degradation was ISI as previously identified in

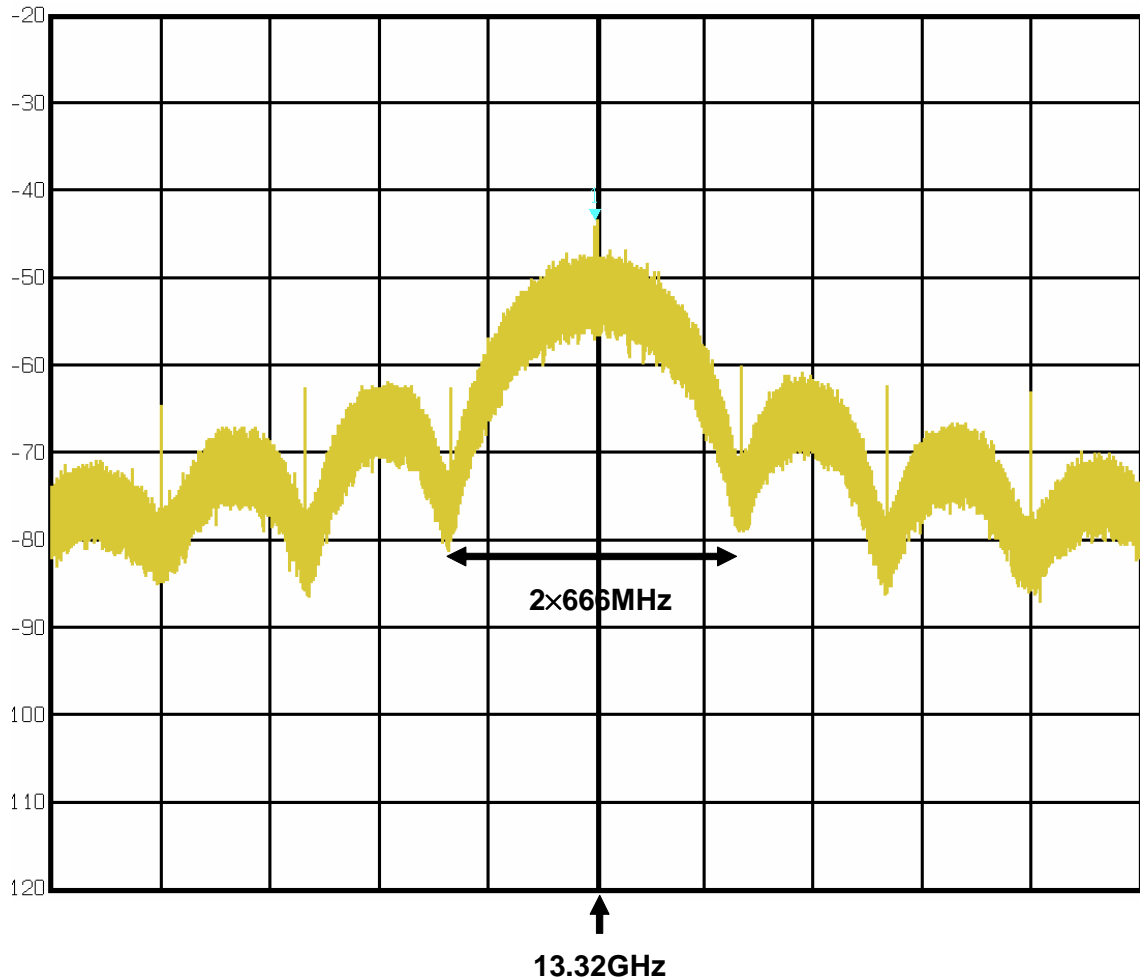
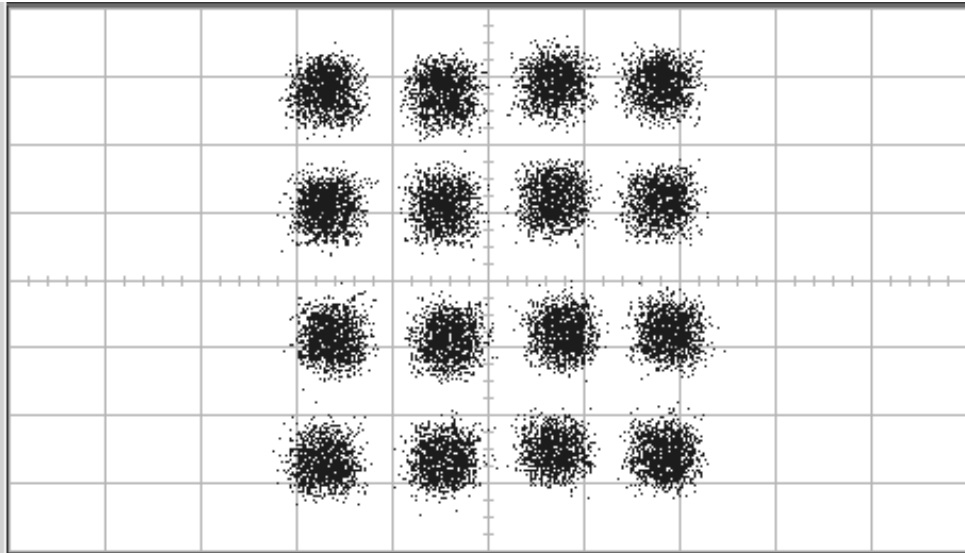


Figure 5.7: Test chip transmitter electrical output power spectrum.

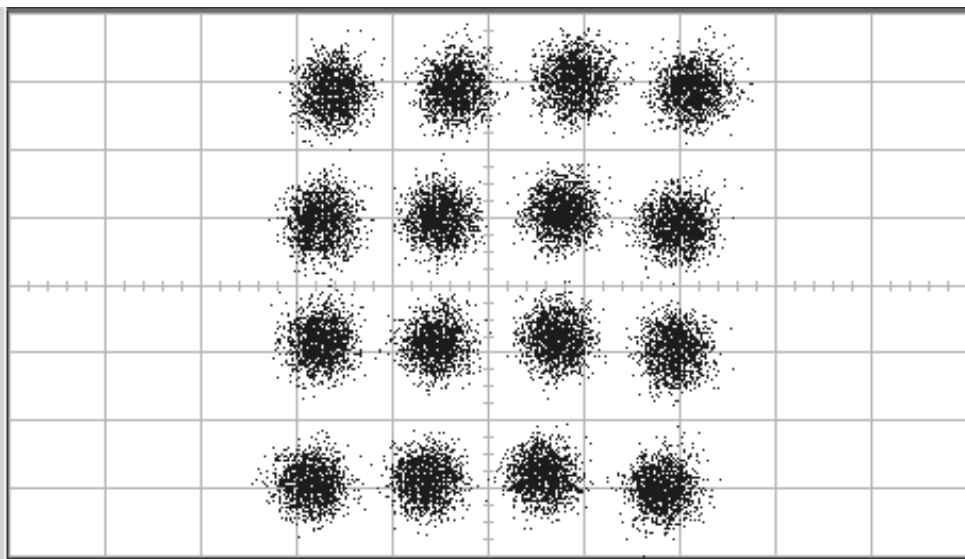
the back-to-back electrical measurements. Reduction of the data clock rate made possible the estimation of the BER which was effectively close to 10^{-5} in a design free of bandwidth bottleneck.

5.2.6 Discussion

Table 5.5 summarizes the characteristics of the test chip designed to prove that the implementation and integration of challenging RF front-end functions is indeed possible. The test chip is operational at design supply currents, bias currents and voltage levels. Issues encountered could be easily solved in future designs. The transmission of the highest fre-



(a)



(b)

Figure 5.8: Measured QAM-16 constellations: (a) optical back-to-back, and (b) after 30 km of single-mode fiber.

Technology	0.14 μm , 1.5 V CMOS
Area	3.6 mm ²
Power	340 mW
Modulation	QAM-16 or QPSK
Carrier frequency	13.32 GHz
Bit rate	2.664 Gb/s (QAM16 mode)

Table 5.5: QAM transceiver test chip characteristics summary.

quency microwave channel using the test chip, a directly modulated laser and 30 km of SMF and a p-i-n photodiode was demonstrated. Other individual functionalities such as the local oscillator were the subject of other test chips not presented in this dissertation and gave very encouraging results as far as stand-alone design and VLSI integration are concerned.

The implementation of the most challenging IC functionalities is thus practical using standard and economical technology. The next steps in the design of a full prototype would include the integration of a local oscillator providing a pure reference signal for the derivation of all 16 carriers, the integration of phase-shifting and mixing functionalities for the other 15 channels similar to the ones presented here and the implementation of digital clock and data recovery thus allowing digital data transmission at 40 Gb/s.

5.3 Conclusions

Simulation results backed by system analysis have proven the feasibility of a 40 Gb/s optical transmission system using low-cost and widely available integrated optical components. The transmission of a single microwave channel (concentrating the target total signal power) was demonstrated through 30 km of SMF using a test chip that constitutes the highest-speed integrated CMOS QAM transceiver to our knowledge when this dissertation was being written.

Other circuit design elements were implemented and tested separately such as a local oscillator for reference carrier generation showing suitable characteristics. Future design goals would include the integration of all 16 channels on a single die and a fiber transmission prototype including such a multi-carrier transceiver and the design of a transponder similar to what is shown in Fig. 5.9.

Potential applications for the system span different types of short reach low-cost inter-

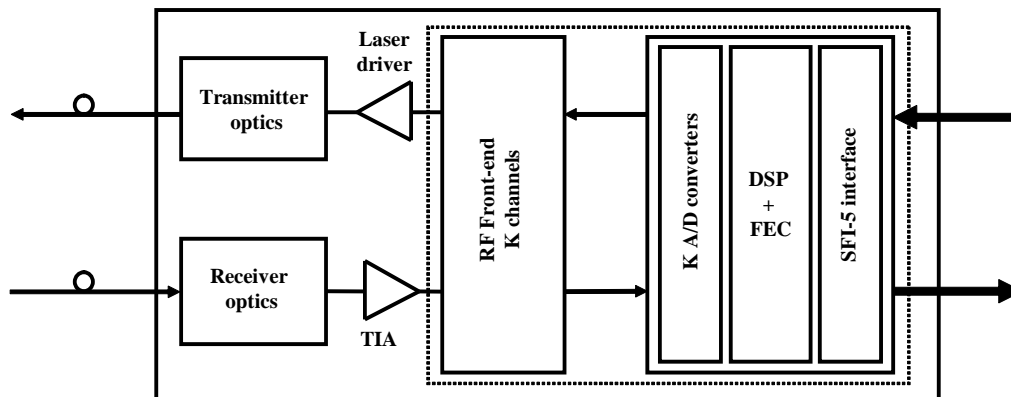


Figure 5.9: Bandwidth efficient modulation optical transponder concept.

connects [SSC⁺03]. Preliminary cost structure analyses have shown that such a transponder would be competitive against current data center and short reach 40 Gb/s solutions. These current solutions include:

- parallel optical interfaces (POI) using VCSEL arrays and multi-mode fiber ribbons limited to distances of a few hundred meters. Fiber ribbon and installation cost is fifty times higher than single-mode fiber and the central offices installed base is mostly composed of single-mode fiber.
- 40 Gb/s coarse wavelength division multiplex (CWDM) which multiplies the cost of 10 Gb/s by duplicating optical components.

Chapter 6

Conclusions and Suggestions for Future Work

6.1 Conclusions

This dissertation has focused on the design of a single-wavelength short reach optical communication system using low cost optical components and IC technology supporting capacities of 40 Gb/s and beyond. It is based on the usage of bandwidth efficient modulation and digital signal processing techniques.

Time varying dispersive effects such as polarization mode dispersion have a dramatic impact on simple and widely used OOK signaling at increased data rates. Even though newly manufactured single-mode fibers exhibit very low levels of PMD it can still be very high for installed fibers. Electrical signal processing solutions exist but are rate-dependent and reach technological and power dissipation barriers at higher speeds. Optical dispersion compensation is fairly rate-independent and covers multiple wavelengths. However it is a costly solution for short links and still requires to be combined with data recovery integrated-circuits designed with expensive semiconductor technologies that are needed to handle the line rates for multi-gigabit per second transmission using OOK. This is not compatible with the low costs required by application spaces based on short optical links.

Departing from OOK signaling, this research work has proposed the usage of sub-carrier multiplexing with multilevel signaling as a bandwidth efficient modulation format. Multilevel signaling reduces the electrical signal bandwidth occupation. Combined with sub-carrier multiplexing digital information is transmitted over multiple digital RF channels in

parallel at a lowered signaling rate. Motivated by the constraints of the targeted application this change of modulation format trades transmitted signal power for bandwidth and signaling speed. Constraints on the latter determine the minimum number of levels and channels for a targeted throughput of 40 Gb/s in less than 14 GHz bandwidth. Increasing these numbers lowers bandwidth and signaling rate even further but at the cost of increased signal-to-noise ratio requirements and sensitivity to distortions.

With lowered maximum signal frequencies cost-effective, power-efficient and reliable CMOS technology can be used for data recovery and processing. The implementation of analog RF functions in CMOS remains challenging though. Frequency multiplexed wireless applications impose strong orthogonality requirements for the purpose of reliable recovery of data. These requirements increase analog front-end design constraints and limit the effective bandwidth efficiency of the modulation scheme. This research work proposed a novel adaptive digital signal processing structure for inter-channel and inter-symbol interference cancellation. Such a scheme can greatly relax constraints on pulse shaping, RF carrier positions and other system implementation parameters that are even more difficult to meet than in wireless applications.

The design of an optical communication system based on electrical sub-carrier multiplexing and multilevel signaling has been outlined. The optical link is composed of optoelectronic components that are all commercially available and can be produced with high yield and in a cost-effective manner. Namely, a directly modulated laser used for “digital” 10 Gb/s applications, standard single-mode fiber and a p-i-n photodiode with appropriate electrical amplification stages are utilized. Thanks to the notion of EOE response of the fiber link we could show that linear impairments have a measurable impact on the system with increasing fiber length but remain limited with realistic laser wavelength accuracy requirements. Link nonlinear impairments due to combinations of laser chirp and fiber phase-to-intensity modulation conversions have been quantified in terms of RF intermodulation distortions. These results together with noise level estimates motivated the precise modelling of the semiconductor laser. The numerical implementation of the model for this critical component was validated using relative intensity noise measurements and two-tone test measurements. Theory, simulation and measurement results indicated that high laser bias currents within normal range of operation improve laser linearity and noise behavior.

The design of a complete simulation platform has been presented including models for the optical link components, analog circuit components, digital signal processing and closed-

loop carrier and timing recovery. This simulation platform combined with analysis yielded the optimization of system parameter settings. For the chosen directly modulated laser an optical modulation index of 18% and a laser bias current of approximately 60 mA have been recommended by trading-off relative intensity noise-related signal to noise ratio with laser nonlinearity distortion. Those results have proved the feasibility of the intended system transmitting 40 Gb/s using 10 Gb/s optical components and 16-point QAM modulation over 16 RF carrier channels. Strategies for improving system performance could also be defined by uneven distribution of power or allocation of bits among RF channels. With reasonable laser wavelength accuracy requirements, the link length can be extended above 10 km keeping the bit-error-rate below 10^{-15} when using low-overhead forward error correction codes.

The definition of a simple information channel model has provided insight into the ultimate bound on achievable throughputs with such a system. Even when limiting the input signal power to remain in a quasi-linear regime spectral efficiencies in excess of 6 b/s/Hz can be reached for short transmitter-limited links.

An integrated QAM-16 transceiver CMOS test chip has been designed according to specifications derived from this research work. The test chip has been implemented in 0.14- μm , 1.5 V CMOS technology, occupying 3.6 mm² of surface area and consuming 340 mW. To the author and the design team's knowledge this constitutes the highest speed integrated CMOS QAM modulator/demodulator ever implemented. Using this test chip a single-channel system prototype has been implemented and successful transmission has been performed over 30 km of single mode fiber.

6.2 Future work

A future prototype development could include the design of a full 16 QAM-16 CMOS transceiver with an on-chip local oscillator and external A/D conversion for the initial test of DSP and data recovery algorithms in software or using field programmable gate array (FPGA) circuits.

Chapter 5 showed that the widely used RS(255,239) forward error correcting code allows the extension of the operating distance without strengthening laser wavelength constraints. If low overhead error correction codes specific to the modulation and channel at the center of this research work could be designed exhibiting increased coding gain, operating distance could be extended. Furthermore, lower cost optical components such as uncooled lasers

could potentially be used. This is an area that should certainly be investigated.

Chapter 4 defined an optical link channel for the targeted high-capacity low-cost short reach application. The system represented in Fig. 3.2 could be extended to different application spaces. In particular, initial results not presented in this dissertation show that, if effective predistortion schemes can be implemented when using a Mach-Zehnder-based single-sideband optical modulator, impairments due to chromatic dispersion and chirp can be avoided altogether without using any form of dispersion compensation. The system would be scalable in the optical domain by the usage of DWDM with potentially increased optical spectral efficiency. The impact of optical amplifiers nonlinearities and optical filters design characteristics should be investigated.

Finally channel capacity bounds were derived for a laser diode when taking into account its linearized response (small-signal, wide-band assumptions) and clipping distortions (large signal, quasi-static assumptions). A more accurate model should be developed that includes dynamic nonlinear distortions resulting in inter-channel mixing. Volterra series and frequency dependent Volterra kernels derived from the laser rate equations ([HTLLAD94, SO96]) could make it possible to define such a model and refine the channel capacity estimate as well as determine its dependence upon modulation, index, laser design parameters and fiber length.

Appendix A

Fiber Birefringence

This appendix provides definitions and developments regarding fiber birefringence and dispersion useful for Chap. 2 and Appendix D. The two orthogonally polarized modes of a single mode fiber are degenerate (they propagate exactly the same way) under ideal conditions. In practice, irregularities such as random variations in the core shape, random non-symmetrical stress fields in the glass around the core region (intrinsic perturbations) or random external force induced stresses (extrinsic perturbations) along the fiber length randomly mix the polarization components and scramble the polarization of the incident light as it propagates through the fiber. This appendix makes use of the following vectorial representation of the optical field:

$$\vec{E}(\vec{r}, t) = \text{Re} \left(G(x, y) A(z, t) e^{-i\beta_0 z} e^{i\omega_0 t} \right),$$

where ω_0 is the optical carrier angular frequency and $\frac{\omega_0}{\beta_0}$ its phase velocity. $A = \begin{pmatrix} A_x \\ A_y \end{pmatrix}$ is normalized so that $|A|^2 = |A_x|^2 + |A_y|^2$ represents the optical power. $G(x, y)$ represents the field mode distribution over the fiber section. $A = B^*$ represents here the “light field” referred to in Section 2.2.1.

A.1 Representation of lumped and infinitesimal birefringent elements

Taking a system point of view, it is assumed that the system under study relates the optical field at its output ($z=L$) to the optical field at its input ($z=0$) in the following way:

$$\tilde{A}_{\text{out}}(\omega) = e^{h(\omega)}U(\omega)\tilde{A}_{\text{in}}(\omega), \quad (\text{A.1})$$

where, for all relative angular frequencies ω , $U(\omega)$ is an element of $SU(2)$, the set of special unitary matrices (i.e., 2x2 complex unitary matrices with unit determinant). From their defining properties we can see that special unitary matrices act by only modifying the relative phase and amplitude of the components of vectors when expressed in a certain basis of \mathbb{C}^2 . They do not change the norm of vectors (unitary property) and do not add a common phase to the components (unit determinant property). The effects of the waveguide on the norm and phase variations of the optical field are accounted for respectively by the real part and imaginary part of $h(\omega)$. If we use the decomposition $A = a|s\rangle$ presented in Sec. 2.2.1 on page 11, we can relate input and output Jones vectors

$$|s_{\text{out}}\rangle = U|s_{\text{in}}\rangle.$$

As a matter of fact U relates SOP's (equivalence classes of Jones vectors as presented in Sec. 2.2.1) since it commutes with any phase term. In mathematical terms we can define an action of the group $SU(2)$ on the set of SOP's. SOP's can be represented by points on the Poincaré sphere (see page 14). Hence $SU(2)$ naturally acts on the Poincaré sphere itself. More precisely the mapping of the set of SOP's on the Poincaré sphere naturally defines a map ρ from $SU(2)$ to $SO(3)$, the special orthogonal group formed by the rotation matrices of the real space \mathbb{R}^3 ,

$$\begin{aligned} SU(2) &\longrightarrow SO(3) \\ U &\longmapsto R = \rho(U) \end{aligned}$$

with, for every Jones vector $|s\rangle$, $R\langle s|\vec{\sigma}|s\rangle = \langle s|U^\dagger\vec{\sigma}U|s\rangle$.

Two basic properties make the definition of this map explicit and very useful when making calculations. In the following lines I_2 designates the 2x2 identity matrix and $\vec{\sigma}$ the column of Pauli matrices defined on page 14. The exponential of matrices is defined by its series expansion.

property 1 For all U in $SU(2)$ there is a real number θ and a unit length vector $\vec{n} \in \mathbb{R}^3$ such that $U = e^{-i\theta\vec{n}\cdot\frac{\vec{\sigma}}{2}} = \cos(\theta/2)I_2 - i \sin(\theta/2)\vec{n}\cdot\vec{\sigma}$. And every matrix of the form $e^{-i\theta\vec{n}\cdot\frac{\vec{\sigma}}{2}}$ is an element of $SU(2)$.

If we decide to notate $R(\theta, \vec{n})$ the matrix of the rotation defined by the angle θ and unit length axis vector \vec{n} expressed in the canonical basis of \mathbb{R}^3 we have the following property.

property 2 $\rho\left(e^{-i\theta\vec{n}\cdot\frac{\vec{\sigma}}{2}}\right) = R(\theta, \vec{n}) = e^{\theta(\vec{n}\times)}$
where $\vec{n}\times = \begin{pmatrix} 0 & -n_3 & n_2 \\ n_3 & 0 & -n_1 \\ -n_2 & n_1 & 0 \end{pmatrix}$ if $\vec{n} = \begin{pmatrix} n_1 \\ n_2 \\ n_3 \end{pmatrix}$.

One immediate comment is that the map ρ is onto but not one-to-one since we clearly have, for all U in $SU(2)$, $\rho(-U) = \rho(U)$.

A.1.1 Examples: elementary rotations.

Let $\vec{e}_1 = \begin{pmatrix} 1 \\ 0 \\ 0 \end{pmatrix}$, $\vec{e}_2 = \begin{pmatrix} 0 \\ 1 \\ 0 \end{pmatrix}$ and $\vec{e}_3 = \begin{pmatrix} 0 \\ 0 \\ 1 \end{pmatrix}$ be the canonical basis vectors of \mathbb{R}^3 .

$$\begin{aligned} \begin{pmatrix} e^{-i\theta/2} & 0 \\ 0 & e^{i\theta/2} \end{pmatrix} = e^{-i\theta\frac{\sigma_1}{2}} &\quad \mapsto \quad R(\theta, \vec{e}_1) = \begin{pmatrix} 1 & 0 & 0 \\ 0 & \cos(\theta) & -\sin(\theta) \\ 0 & \sin(\theta) & \cos(\theta) \end{pmatrix} = e^{\theta(\vec{e}_1 \times)} \\ \begin{pmatrix} \cos(\theta/2) & -i \sin(\theta/2) \\ -i \sin(\theta/2) & \cos(\theta/2) \end{pmatrix} = e^{-i\theta\frac{\sigma_2}{2}} &\quad \mapsto \quad R(\theta, \vec{e}_2) = \begin{pmatrix} \cos(\theta) & 0 & \sin(\theta) \\ 0 & 1 & 0 \\ -\sin(\theta) & 0 & \cos(\theta) \end{pmatrix} = e^{\theta(\vec{e}_2 \times)} \\ \begin{pmatrix} \cos(\theta/2) & -\sin(\theta/2) \\ \sin(\theta/2) & \cos(\theta/2) \end{pmatrix} = e^{-i\theta\frac{\sigma_3}{2}} &\quad \mapsto \quad R(\theta, \vec{e}_3) = \begin{pmatrix} \cos(\theta) & -\sin(\theta) & 0 \\ \sin(\theta) & \cos(\theta) & 0 \\ 0 & 0 & 1 \end{pmatrix} = e^{\theta(\vec{e}_3 \times)} \end{aligned}$$

This representation of the group $SU(2)$ gives a powerful way to build mental images of the effect of birefringent optical elements on the SOP of a polarized light beam. The vector $\theta\vec{n}$ itself sums up all the information about the birefringent optical element. In general this vector is a function of different parameters (frequency in the above described case).

A.2 Spatial variations and birefringence vector

One important result about special unitary matrices is that there exists an orthonormal basis of eigenvectors and the corresponding eigenvalues are of unit modulus and complex conjugate. Consequently the orthonormal eigenbasis of a birefringence matrix determines a unique couple of SOP's (except in the degenerate case where both eigenvalues are equal to 1): the eigenstates of the associated birefringent system. Physically this means that for any birefringent optical element there exist two orthogonal SOP's that are transmitted unchanged. It is important to notice that, in general, the $SU(2)$ matrix associated with a birefringent optical element is frequency dependent and that the previous result is valid at each frequency value.

Imagining that a certain continuous optical system is the concatenation of an infinite number of infinitesimal birefringent elements along a z coordinate, we can consider the Jones matrix resulting from the concatenation from 0 to z , $U(z, \omega)$. The following heuristic arguments lead to a definition of the local birefringence vector and give the partial differential equation describing the propagation of a light beam in such a birefringent waveguide:

$$\begin{aligned}\tilde{A}(z + dz, \omega) &= U(z + dz, \omega)\tilde{A}(0, \omega) \\ \tilde{A}(z, \omega) &= U(z, \omega)\tilde{A}(0, \omega).\end{aligned}$$

Hence

$$\tilde{A}(z + dz, \omega) = U(z + dz, \omega)U^{-1}(z, \omega)\tilde{A}(z, \omega),$$

and

$$\tilde{A}(z + dz, \omega) - \tilde{A}(z, \omega) = (U(z + dz, \omega) - U(z, \omega))U^{-1}(z, \omega)\tilde{A}(z, \omega).$$

This justifies the following equation for describing the evolution of the optical field when propagating in a linear birefringent waveguide:

$$\frac{\partial \tilde{A}}{\partial z} = \frac{\partial U}{\partial z}U^{-1}\tilde{A}. \quad (\text{A.2})$$

The matrix $\frac{\partial U}{\partial z}U^{-1}$ has interesting properties. From the characteristic properties of special unitary matrices, it can be derived that $i\frac{\partial U}{\partial z}U^{-1}$ is a Hermitian, traceless matrix. Now the Pauli matrices form a \mathbb{R} -basis of the vector space composed of the Hermitian and traceless 2x2 matrices. In other words there exists a vector $\vec{\beta}$ of \mathbb{R}^3 such that $i\frac{\partial U}{\partial z}U^{-1} =$

$\frac{1}{2}\vec{\beta}\cdot\vec{\sigma} = \frac{1}{2}(\beta_1\sigma_1 + \beta_2\sigma_2 + \beta_3\sigma_3)$. The column of Pauli matrices $\vec{\sigma}$ is as defined on page 14. The operator \cdot has formally the same action as the canonical scalar product in \mathbb{R}^3 and gives a short way of writing a linear combination of Pauli matrices. Writing parameter dependencies explicitly the following defines the *local birefringence vector* $\vec{\beta}$:

$$\boxed{i\frac{\partial U}{\partial z}(z, \omega)U^{-1}(z, \omega) = \frac{1}{2}\vec{\beta}(z, \omega)\cdot\vec{\sigma}}$$

Equation (A.2) becomes:

$$\frac{\partial \tilde{A}}{\partial z} + i\frac{1}{2}\vec{\beta}\cdot\vec{\sigma}\tilde{A} = 0. \quad (\text{A.3})$$

The birefringence vector $\vec{\beta}$ can be related to the eigenstates of infinitesimal elements forming the continuous system. For an element between z and $z + dz$ (omitting the implicit frequency dependence)

$$\begin{aligned} \tilde{A}(z + \Delta z) &= \tilde{A}(z) + \frac{\partial \tilde{A}}{\partial z}(z)\Delta z + o(\Delta z) \\ &= \left(I_2 - i\frac{1}{2}\vec{\beta}(z)\cdot\vec{\sigma}\Delta z\right)\tilde{A}(z) + o(\Delta z) \\ &= e^{-i\Delta z\vec{\beta}\cdot\frac{\vec{\sigma}}{2}}\tilde{A}(z) + o(\Delta z). \end{aligned}$$

The matrix $e^{-i\Delta z\vec{\beta}\cdot\frac{\vec{\sigma}}{2}} = I_2 - i\frac{1}{2}\vec{\beta}(\Delta z)\cdot\vec{\sigma}\Delta z + o(z)$ is the special unitary matrix associated with the infinitesimal birefringent element between z and $z + \Delta z$. The associated rotation matrix is $e^{\Delta z(\vec{\beta}\times)}$. If $\vec{\beta}(z)$ is non zero, $\vec{n}(z) = \frac{\vec{\beta}(z)}{|\vec{\beta}(z)|}$ is a point of the Poincaré sphere. The rotation matrix can be written $e^{\Delta z|\beta(z)|(\vec{n}(z)\times)}$ and $\vec{n}(z)$ and $-\vec{n}(z)$ represent two orthogonal¹ SOP's. They are the eigenstates of this birefringent element. In this infinitesimal context, $\vec{n}(z)$ and $-\vec{n}(z)$ are called *local eigenaxes* of the birefringent optical system at point z .

Using the decomposition $\tilde{A} = \|\tilde{A}\| |s\rangle$, equation (A.3) implies that $\|\tilde{A}(z)\|$ is constant and the following equation describes the evolution of $|s\rangle$:

$$\boxed{\frac{\partial |s\rangle}{\partial z} + i\frac{1}{2}\vec{\beta}\cdot\vec{\sigma}|s\rangle = 0} \quad (\text{A.4})$$

This equation can be translated into an equivalent one involving Stokes space quantities.

¹The Jones vectors are orthogonal and the Poincaré sphere points are antipodal.

The evolution with z of the SOP in Stokes space is given by

$$\frac{\partial \vec{S}}{\partial z} = \vec{\beta} \times \vec{S}. \quad (\text{A.5})$$

If $\vec{\beta}(z)$ were actually a constant, the SOP $\vec{S}(z)$ would have a precession movement around the axis defined by the birefringence vector and would describe a circle on the Poincaré sphere. The length-period $L_B = 2\pi/|\vec{\beta}|$ of this precession movement is called the *beat length* of the birefringent system. This length scale characterizes the strength of the birefringence phenomenon.

By making a few assumptions on the birefringence vector a time-domain differential equation that describes the evolution of the optical field in a waveguide with distributed birefringence can be derived. Recalling here that every quantity of concern is supposed to be defined in the vicinity of the angular frequency ω_0 that corresponds to the vacuum wavelength $\lambda_0 = \frac{2\pi c}{\omega_0}$ of a modulated optical carrier. In the approach that consists in looking for an “evolution” equation for the propagating signal, the assumption of a narrow-band modulating signal allows the Taylor-expansion every frequency dependent quantity in the vicinity of the center frequency. Doing this with the birefringence vector $\vec{\beta}(z, \omega) = 2b(z, \omega)\vec{n}(z, \omega)$ gives

$$\vec{\beta}(z, \omega) = \vec{\beta}(z, 0) + \frac{\partial \vec{\beta}}{\partial \omega}(z, 0)\omega + o(\omega).$$

If it can be further assumed that the direction \vec{n} does not depend on ω and that the birefringence strength does not depend on z , two constants $b = b(0)$ and $b' = \frac{db}{d\omega}(0)$ can be used to write

$$\vec{\beta}(z, \omega) = 2b\vec{n}(z) + 2b'\vec{n}(z)\omega + o(\omega).$$

Not taking into account terms of order more than one, equation (A.3) becomes

$$\frac{\partial \tilde{A}}{\partial z} + ib\vec{n} \cdot \vec{\sigma} \tilde{A} + b'\vec{n} \cdot \vec{\sigma} i\omega \tilde{A} = 0.$$

This can now be translated in the time domain equation

$$i\frac{\partial A}{\partial z} - b\vec{n} \cdot \vec{\sigma} A + ib'\vec{n} \cdot \vec{\sigma} \frac{\partial A}{\partial t} = 0.$$

Using now a representation of the optical field consistent with the definition of the Fourier

transform in [Agr95b] and every article dealing with the nonlinear Schrödinger equation, $\widehat{B}(z, \omega) = \widetilde{A}^*(z, \omega)$, the following differential equation rules the evolution of B :

$$i \frac{\partial B}{\partial z} + \underbrace{b \vec{n} \cdot \vec{\sigma} B}_{\text{Lowest order birefringence}} + \underbrace{ib' \vec{n}' \cdot \vec{\sigma} \frac{\partial B}{\partial t}}_{\text{PMD source}} = 0.$$

As will be seen at the end of Sec. A.4, there is no polarization-mode dispersion (polarization-dependent group delay) if the local birefringence vector does not actually have a frequency dependence.

A.3 Frequency variations and polarization-mode dispersion vector

The z dependence of the U matrix leads to the definition of the local birefringence vector $\vec{\beta}$. We proceed exactly the same way to define the *PMD vector* $\vec{\tau}$ related to the ω dependence of U . As $i \frac{\partial U}{\partial \omega} U^{-1}$ is traceless and Hermitian, there exists a vector of \mathbb{R}^3 , $\vec{\tau}$, such that $i \frac{\partial U}{\partial \omega} U^{-1} = \frac{1}{2} \vec{\tau} \cdot \vec{\sigma}$. With a parameter dependence explicitly expressed, the defining relationship reads:

$$\boxed{i \frac{\partial U}{\partial \omega}(z, \omega) U^{-1}(z, \omega) = \frac{1}{2} \vec{\tau}(z, \omega) \cdot \vec{\sigma}}$$

The system (*output*) *PMD vector* is defined by $\vec{\tau}_{\text{out}}(\omega) = \vec{\tau}(L, \omega)$. It is often useful to have input-referred quantities. This justifies the definition of the input PMD vector of the fiber, $\vec{\tau}_{\text{in}} = R^{-1} \vec{\tau}_{\text{out}}$ (where R is the rotation matrix associated with $M = U(L, \cdot)$). This sets another differential equation verified by the SOP in the Jones representation:

$$\boxed{\frac{\partial |s\rangle}{\partial \omega} + i \frac{1}{2} \vec{\tau} \cdot \vec{\sigma} |s\rangle = 0} \quad (\text{A.6})$$

The corresponding equation for the SOP in Stokes space is

$$\frac{\partial \vec{S}}{\partial \omega} = \vec{\tau} \times \vec{S}. \quad (\text{A.7})$$

A.4 Dynamical polarization-mode dispersion equation

This section describes characteristic properties of the birefringence and PMD vectors as well as a fundamental relationship between them. In this paragraph those properties and relationships are proven in a very concise way using some fundamental properties of $SU(2)$ matrices and Pauli matrices. Very useful properties of the Pauli matrices (see [GK91] for more) are given below.

property 3 For \vec{a} and \vec{b} in \mathbb{R}^3 ,

$$\begin{aligned}\vec{\sigma}(\vec{a} \cdot \vec{\sigma}) &= \vec{a}I_2 + i\vec{a} \times \vec{\sigma} \\ (\vec{a} \cdot \vec{\sigma})\vec{\sigma} &= \vec{a}I_2 - i\vec{a} \times \vec{\sigma} \\ (\vec{a} \cdot \vec{\sigma})(\vec{a} \cdot \vec{\sigma}) &= |\vec{a}|^2 I_2 \\ (\vec{a} \cdot \vec{\sigma})(\vec{b} \cdot \vec{\sigma}) &= (\vec{a} \cdot \vec{b})I_2 + i(\vec{a} \times \vec{b}) \cdot \vec{\sigma} \\ (\vec{a} \cdot \vec{\sigma})\vec{\sigma}(\vec{b} \cdot \vec{\sigma}) &= 2\vec{a}(\vec{a} \cdot \vec{\sigma}) - |\vec{a}|^2 \vec{\sigma},\end{aligned}$$

where \times designates the formal vector product.

If we now consider that U , and consequently $R = \rho(U)$, is a smooth function of two parameters z and ω it is of interest to define the local birefringence and PMD vectors. Starting from the definition of the rotation matrix R associated with the birefringence matrix U we have:

$$\text{For all } \vec{S} = \langle s | \vec{\sigma} | s \rangle, \quad R\vec{S} = \langle s | U^\dagger \vec{\sigma} U | s \rangle. \quad (\text{A.8})$$

The equation $\frac{\partial U}{\partial z} + \frac{i}{2}\vec{\beta} \cdot \vec{\sigma} U = 0$ defining the birefringence vector and the properties of the Pauli matrices give the following sequence of inferences:

$$\begin{aligned}\frac{\partial R}{\partial z} \vec{S} &= \langle s | \frac{\partial U}{\partial z}^\dagger \vec{\sigma} U | s \rangle + \langle s | U^\dagger \vec{\sigma} \frac{\partial U}{\partial z} | s \rangle \\ &= \langle s | U^\dagger \frac{i}{2} \left((\vec{\beta} \cdot \vec{\sigma}) \vec{\sigma} - \vec{\sigma} (\vec{\beta} \cdot \vec{\sigma}) \right) U | s \rangle \\ &= \langle s | U^\dagger (\vec{\beta} \times \vec{\sigma}) U | s \rangle \\ &= (\vec{\beta} \times) R\vec{S}.\end{aligned}$$

Hence

$$\boxed{\frac{\partial R}{\partial z} R^{-1} = \vec{\beta} \times}$$

The same sequence of arguments starting from a derivative relative to ω and using the defining equation for the PMD vector $\frac{\partial U}{\partial \omega} + \frac{i}{2}\vec{\tau} \cdot \vec{\sigma} U = 0$ lets

$$\boxed{\frac{\partial R}{\partial \omega} R^{-1} = \vec{\tau} \times}$$

As the SOP $\vec{S}(z, \omega)$ of the beam of light at point z in the fiber is given by

$$\vec{S} = R\vec{S}_{\text{in}}.$$

We get

$$\boxed{\frac{\partial \vec{S}}{\partial z} = \vec{\beta} \times \vec{S}} \quad (\text{A.9})$$

and

$$\boxed{\frac{\partial \vec{S}}{\partial \omega} = \vec{\tau} \times \vec{S}} \quad (\text{A.10})$$

It is apparent that the definitions and properties of those two vectors are very similar. Similar vectors could be defined related to the infinitesimal variations of the birefringence matrix of a system with other parameters it can depend upon. Such vectors are named *Dynamic Eigenstate* (DES) vectors and some other cases of parameter dependence are studied (temperature, rotation angle,...) in [SK01].

PMD and birefringence are related to each other through an equation first derived by C. J. Poole (reproduced in [GK91]). This paragraph proposes an alternate derivation for this equation, starting from the definition of the birefringence and PMD vectors:

$$\begin{cases} \frac{\partial U}{\partial z} + \frac{i}{2}\vec{\beta} \cdot \vec{\sigma} U = 0 \\ \frac{\partial U}{\partial \omega} + \frac{i}{2}\vec{\tau} \cdot \vec{\sigma} U = 0 \end{cases}$$

Frequency derivation of the first relation gives

$$\frac{\partial}{\partial z} \left(\frac{\partial U}{\partial \omega} \right) + \frac{i}{2} \frac{\partial \vec{\beta}}{\partial \omega} \cdot \vec{\sigma} U + \frac{i}{2} \vec{\beta} \cdot \vec{\sigma} \frac{\partial U}{\partial \omega} = 0.$$

One use of the second relation lets

$$-\frac{i}{2} \frac{\partial}{\partial z} (\vec{\tau} \cdot \vec{\sigma} U) + \frac{i}{2} \frac{\partial \vec{\beta}}{\partial \omega} \cdot \vec{\sigma} U + \frac{i}{2} \vec{\beta} \cdot \vec{\sigma} \frac{\partial U}{\partial \omega} = 0,$$

and then

$$\frac{\partial \vec{\tau}}{\partial z} \cdot \vec{\sigma} U + \vec{\tau} \cdot \vec{\sigma} \frac{\partial U}{\partial z} - \frac{\partial \vec{\beta}}{\partial \omega} \cdot \vec{\sigma} U - \vec{\beta} \cdot \vec{\sigma} \frac{\partial U}{\partial \omega} = 0.$$

Another use of the each of the two relations together with the properties of the Pauli matrices gives the following sequence of inferences:

$$\begin{aligned} \frac{\partial \vec{\tau}}{\partial z} \cdot \vec{\sigma} &= -\vec{\tau} \cdot \vec{\sigma} \frac{\partial U}{\partial z} U^{-1} + \frac{\partial \vec{\beta}}{\partial \omega} \cdot \vec{\sigma} + \vec{\beta} \cdot \vec{\sigma} \frac{\partial U}{\partial \omega} U^{-1} \\ &= \frac{i}{2} (\vec{\tau} \cdot \vec{\sigma}) (\vec{\beta} \cdot \vec{\sigma}) + \frac{\partial \vec{\beta}}{\partial \omega} \cdot \vec{\sigma} - \frac{i}{2} (\vec{\beta} \cdot \vec{\sigma}) (\vec{\tau} \cdot \vec{\sigma}) \\ &= \frac{\partial \vec{\beta}}{\partial \omega} \cdot \vec{\sigma} + \frac{i}{2} \left((\vec{\tau} \cdot \vec{\sigma}) (\vec{\beta} \cdot \vec{\sigma}) - (\vec{\beta} \cdot \vec{\sigma}) (\vec{\tau} \cdot \vec{\sigma}) \right) \\ &= \frac{\partial \vec{\beta}}{\partial \omega} \cdot \vec{\sigma} + \frac{i}{2} \left(((\vec{\tau} \cdot \vec{\beta}) I_2 + i(\vec{\tau} \times \vec{\beta}) \cdot \vec{\sigma}) - ((\vec{\beta} \cdot \vec{\tau}) I_2 + i(\vec{\beta} \times \vec{\tau}) \cdot \vec{\sigma}) \right) \\ &= \left(\frac{\partial \vec{\beta}}{\partial \omega} + \vec{\beta} \times \vec{\tau} \right) \cdot \vec{\sigma}. \end{aligned}$$

Hence

$$\frac{\partial \vec{\tau}}{\partial z} = \frac{\partial \vec{\beta}}{\partial \omega} + \vec{\beta} \times \vec{\tau}.$$

From a formal point of view, considering z and ω as dummy variables expressing the parameter dependence of U , the vector functions $\vec{\beta}$ and $\vec{\tau}$ are completely equivalent as they both describe the infinitesimal variation of U with its parameters. This symmetry appears in the dynamical PMD equation once written as follows:

$$\boxed{\frac{\partial \vec{\tau}}{\partial z} - \frac{\partial \vec{\beta}}{\partial \omega} + \vec{\tau} \times \vec{\beta} = \vec{0}} \quad (\text{A.11})$$

But the physical basis of the mathematical model does not keep this symmetry. The physical model makes explicit the variations of the local birefringence $\vec{\beta}$. The dynamical PMD equation is subsequently used to deduce $\vec{\tau}$ given the initial conditions: for all ω , $\vec{\tau}(0, \omega) = \vec{0}$. Two examples of this methodology are given hereafter.

Examples:

- What if we assume that the local birefringence vector $\vec{\beta}$ does not depend on ω ? In this case the dynamical PMD equation becomes $\frac{\partial \vec{\tau}}{\partial z} = \vec{\beta} \times \vec{\tau}$ with the initial condition $\vec{\tau}(0, \omega) = \vec{0}$ for all ω and the solution is clearly $\vec{\tau}(z, \omega) = \vec{0}$ for all z and ω . This shows that this is indeed the frequency dependence of the local birefringence vector that generates polarization-mode dispersion (PMD).

- We introduce here a possible model for a piece of highly birefringent fiber (HiBi fiber) with fast and slow axes represented in the Stokes space by the unit length vector \vec{n} . We assume that local birefringence is deterministic and constant over the fiber length with the following dependence:

$$\vec{\beta} = 2(b_0 + b'_0\omega)\vec{n}.$$

The solution of the dynamical equation is then $\vec{\tau}(z, \omega) = 2b'_0 z \vec{n}$. The PMD vector of the fiber piece is $\vec{\tau}_{\text{out}} = 2b'_0 L \vec{n}$ and has no frequency dependence. Furthermore the DGD $\tau = |\vec{\tau}_{\text{out}}|$ increases linearly with the fiber length L . The Jones matrix M of the HiBi fiber piece is then

$$M(\omega) = e^{-iL\vec{\beta} \cdot \frac{\vec{\sigma}}{2}} = e^{-i2b_0 L \vec{n} \cdot \frac{\vec{\sigma}}{2}} e^{-i2b'_0 L \omega \vec{n} \cdot \frac{\vec{\sigma}}{2}} = e^{-i2b_0 L \vec{n} \cdot \frac{\vec{\sigma}}{2}} e^{-i\omega \vec{\tau}_{\text{out}} \cdot \frac{\vec{\sigma}}{2}}.$$

The first term changes the SOP of light with no frequency dependence. The second term introduces a polarization-dependent linear frequency dependence and will be responsible for different travelling speeds for pulses with different SOP's at the fiber input.

As mentioned in the body of this dissertation this equation is the basis for the derivation of the PMD vector statistics when considering a single-mode fiber with random birefringence as developed in the fundamental article [FP91].

Appendix B

Fiber Electro-opto-electrical Response Calculations

The first part of this appendix presents detailed calculations for the electro-opto-electrical (EOE) response of an optical system used in particular in the discussions of Sec 4.2. The second part models the phase-to-intensity ratio of a directly modulated laser necessary for the derivation of the EOE response with such an electro-optical converter. The notations used are as introduced in Sec. 4.2.2 and 4.2.3.

B.1 Fiber response

All calculations are done up to the first order in the less than unity real number \bar{m} as defined on page 74. We write the optical field $e(t) = \sqrt{P_0}E(t)|s_{\text{in}}\rangle$ where $E(t) = \sqrt{1+m(t)}e^{i\phi(t)}$. The input-output relationship for the optical system is expressed in the frequency domain by $\tilde{e}_{\text{out}}(\omega) = T(\omega)\tilde{e}_{\text{in}}(\omega)$ where $T(\omega) = H(\omega)M(\omega)$ as defined on page 76. The optical field at the output of the optical system is then such as

$$e_{\text{out}}(t) = \sqrt{P_0} \int H(\omega)\tilde{E}(\omega)M(\omega)|s_{\text{in}}\rangle e^{i\omega t} \frac{d\omega}{2\pi}.$$

Expressing the field amplitude E up to the first order in \bar{m} , $E(t) \approx 1 + \frac{1}{2}m(t) + i\phi(t) = 1 + (\frac{1}{2}\delta + i\eta)*m(t)$ where η is the phase-to-intensity ratio impulse response function. In the

frequency domain $\tilde{E}(\omega) \approx \delta(\omega) + (\frac{1}{2} + i\tilde{\eta}(\omega))\tilde{m}(\omega)$. The detected optical power is now

$$\begin{aligned} P_{\text{out}}(t) &= |e_{\text{out}}(t)|^2 \\ &= P_0 \iint H^*(\omega') \tilde{E}^*(\omega') H(\omega) \tilde{E}(\omega) e^{i(\omega-\omega')t} \frac{d\omega}{2\pi} \frac{d\omega'}{2\pi} \end{aligned}$$

and neglecting order 2 in \bar{m}

$$P_{\text{out}}(t) \approx P_0 \left(\underbrace{1}_{\text{dc-dc mixing}} + \int H^*(\omega') \left(\frac{1}{2} - i\tilde{\eta}^*(\omega') \right) \tilde{m}^*(\omega') e^{-i\omega't} \frac{d\omega'}{2\pi} + \underbrace{\int H(\omega) \left(\frac{1}{2} + i\tilde{\eta}(\omega) \right) \tilde{m}(\omega) e^{i\omega t} \frac{d\omega}{2\pi}}_{\text{signal-dc mixing}} \right).$$

Since $m(t)$ is a real signal and η is a real filter, we have the conjugate symmetry property:

$$\begin{aligned} \tilde{m}^*(\omega) &= \tilde{m}(-\omega) \\ \tilde{\eta}^*(\omega) &= \tilde{\eta}(-\omega) \\ \tilde{\phi}^*(\omega) &= \tilde{\phi}(-\omega). \end{aligned}$$

The detected output power approximation is now

$$P_{\text{out}}(t) \approx P_0 \left(1 + \int \left(\underbrace{\frac{H(\omega) + H^*(-\omega)}{2}}_{H_e(\omega)} + 2i \underbrace{\frac{H(\omega) - H^*(-\omega)}{2}}_{H_o(\omega)} \tilde{\eta}(\omega) \right) \tilde{m}(\omega) e^{i\omega t} \frac{d\omega}{2\pi} \right),$$

and consequently

$$\boxed{\tilde{m}_{\text{out}}(\omega) = H_f(\omega)\tilde{m}(\omega) \quad \text{with} \quad H_f(\omega) = H_e(\omega) + 2iH_o(\omega)\tilde{\eta}(\omega)}$$

B.2 Phase-to-intensity ratio and laser electro-optical response

An extensive use of the laser rate equations detailed in Sec. 4.5 is made throughout this section.

B.2.1 Preliminary developments

The deterministic¹ rate equations for a monomode semiconductor laser are as presented in Sec. 4.5.1:

$$\begin{cases} \frac{dN}{dt} &= i_L - G(N, P)P - R_{\text{rec}}(N) \\ \frac{dP}{dt} &= (G(N, P) - \alpha_L)P + R_{\text{sp}}(N) \\ \frac{d\phi}{dt} &= \frac{\alpha}{2}(G_0(N) - \alpha_L) \end{cases}$$

where N is the electron density, P is the photon density, ϕ is the phase of the optical field produced by the laser, i_L is the injected current in number of electrons per unit time, G is the laser gain, α_L is the loss coefficient which includes mirror and inside cavity material loss, R_{sp} is the rate of creation of photons due to spontaneous emission and R_{rec} the rate of “destruction” of electrons through different electron-hole recombination processes. α is the *linewidth broadening factor* and $G_0(N)$ is the *unsaturated gain*. The gain G is related to the unsaturated gain G_0 through a gain compression relationship $G(N, P) = G_0(N)/(1 + \varepsilon P)$ where ε is the *gain compression factor*.

From the rate equations we can infer

$$\frac{d\phi}{dt} = \frac{\alpha}{2}(G - \alpha_L + G_0 - G) = \frac{\alpha}{2}\left(\frac{1}{P}\frac{dP}{dt} - \frac{R_{\text{sp}}}{P} + G_0 - \frac{G_0}{1 + \varepsilon P}\right).$$

Above the laser threshold we make the approximations that N stays close to its threshold value, that is to say $N \approx N_{\text{th}}$, and that (non-random) power variations due to spontaneous emission are greatly smaller than the overall power variations, i.e., $\frac{R_{\text{sp}}}{P} \ll \left|\frac{1}{P}\frac{dP}{dt}\right|$. We further assume that gain compression is small, i.e., $\varepsilon P \ll 1$. With these assumptions the following approximation for the optical field phase variations can be obtained:

$$\frac{d\phi}{dt} \approx \frac{\alpha}{2}\left(\frac{1}{P}\frac{dP}{dt} + \underbrace{G_0\varepsilon P}_{\kappa}\right),$$

where $\kappa = G_0(N)\varepsilon \approx G_0(N_{\text{th}})\varepsilon$ and the product κP is an angular frequency. It is sometimes referred to as the *cross-over frequency* between the adiabatic and transient regimes of the laser chirp. A more rigorous derivation of this expression can be found at the same time as the laser EOE response when linearizing the laser rate equations.

¹Spontaneous emission and charge carriers number fluctuations are not taken into account here.

B.2.2 Laser phase to Intensity Ratio and EO response

For steady state conditions (N_0, P_0) , the laser mode angular frequency incurs an offset is given by

$$\Delta\omega_0 = \frac{\alpha}{2}(G_0(N_0) - \alpha_L).$$

The rate equations can be linearized in the vicinity of a steady state, $N(t) = N_0 + n(t)$, $P(t) = P_0 + p(t)$ and $\phi(t) = \Delta\omega_0 t + \varphi(t)$ for a small input signal $I(t) = I_b + i_s(t)$,

$$\begin{cases} \frac{dn}{dt} &= -\Gamma_N n - C_{NP} p + i_s(t) \\ \frac{dp}{dt} &= -\Gamma_P p + C_{PN} n \\ \frac{d\varphi}{dt} &= \Delta\phi n \end{cases}$$

where Γ_N , Γ_P , C_{NP} and C_{PN} are as defined in Sec. 4.5.4. The first two equations are coupled with each other and phase variations are determined by the electron number variable independently. The carrier density to frequency coupling coefficient is given by

$$\Delta\phi = \frac{\alpha}{2} G_N (1 + \varepsilon P_0).$$

The free motion of this linear system is obtained when setting $i_s(t)$ to 0 and looking for a solution of the form e^{st} . It is characterized by its *damping coefficient* $\Gamma = (\Gamma_N + \Gamma_P)/2$ and *free oscillation frequency* $\omega_{\text{free}} = 2\pi f_{\text{free}} = \sqrt{C_{PN}C_{NP} - \Gamma^2}$. When $i_s(t)$ is non-zero we get the system frequency response

$$\begin{cases} \tilde{n}(\omega) &= \frac{i\omega + \Gamma_P}{-\omega^2 + i(\Gamma_N + \Gamma_P)\omega + C_{PN}C_{NP}} \tilde{i}_s(\omega) \\ \tilde{p}(\omega) &= \frac{C_{PN}}{-\omega^2 + i(\Gamma_N + \Gamma_P)\omega + C_{PN}C_{NP}} \tilde{i}_s(\omega) \\ \tilde{\varphi}(\omega) &= \frac{\Delta\phi}{i\omega} \tilde{n}(\omega) \end{cases}$$

where the Fourier transform of a function f is defined by $\tilde{f}(\omega) = \int f(t)e^{-i\omega t} dt$. Maximizing the magnitude of the denominator of the ratio $\frac{\tilde{p}}{\tilde{i}_s}$ we get the *resonance frequency* of the system $\omega_r = 2\pi f_r = \sqrt{C_{PN}C_{NP} - 2\Gamma^2} = \sqrt{\omega_{\text{free}}^2 - \Gamma^2}$.

Since $C_{NP}\tilde{n}(\omega) = (i\omega + \Gamma_P)\tilde{p}(\omega)$ the relationship between phase and power variations is now

$$\tilde{\varphi}(\omega) = \frac{\Delta\phi P_0}{C_{PN}} \left(1 + \frac{\Gamma_P}{i\omega}\right) \frac{\tilde{p}(\omega)}{P_0}.$$

Remembering our definition of the input signal to the optical system, we clearly have $p(t) = P_0 m(t)$ the phase-to-intensity-ratio (PIR) of the laser is given by the following expression:

$$\tilde{\eta}(\omega) = \frac{\Delta_\phi P_0}{C_{PN}} \left(1 + \frac{\Gamma_P}{i\omega}\right).$$

Making the same assumption as stated on page 171 should yield the same result. That is to say N stays close to its threshold value N_{th} , and the (non-random) power variations due to spontaneous emission are greatly smaller than the overall power variations, i.e., in this context $|R_{sp}^N| \ll |G_N P_0|$. Further assuming that gain compression is small, i.e., $\varepsilon P_0 \ll 1$,

$$\begin{aligned} \frac{\Delta_\phi P_0}{C_{PN}} &= \frac{\alpha}{2} \frac{1 + \varepsilon P_0}{1 + \frac{R_{sp}^N}{G_N P_0}} \\ &\approx \frac{\alpha}{2}, \end{aligned}$$

and

$$\begin{aligned} \Gamma_P &= \alpha_L - G - G_P P_0 \\ &= \frac{1}{P_0} \left(R_{\text{sp}}(N_0) + \varepsilon P_0 \frac{G_0(N_0) P_0}{(1 + \varepsilon P_0)^2} \right). \end{aligned}$$

If the steady state point is high enough above threshold but such that it is true that $\varepsilon P_0 \ll 1$ then $\Gamma_P \approx \varepsilon G_0 P_0 = \kappa P_0$. This is consistent with the simpler derivation of the previous section and gives for the PIR

$$\tilde{\eta}(\omega) = \frac{\alpha}{2} \left(1 + \frac{\kappa P_0}{i\omega}\right).$$

The linearized rate equations and the parameters defined page 172 allow the derivation of the electro-optical frequency response of the laser

$$H_{EO}(\omega) = \frac{K C_{PN}}{-\omega^2 + 2\Gamma i\omega + \omega_r^2 + 2\Gamma^2},$$

where the scaling factor K is now used to express the response in W/A. The amplitude of the frequency response for different bias currents is shown in Fig. 4.18 on page 106.

B.2.3 Laser chirp numerical values

In this section a few numerical values that stem from the laser rate equations parameters are computed. According to the PIR expression an approximation of the instantaneous

optical carrier frequency relative to the steady state frequency is given by

$$\Delta f(t) \approx \frac{\alpha}{4\pi} \frac{dm}{dt}(t) + \frac{\gamma_{adiab}}{2\pi} m(t),$$

where $\gamma_{adiab} = \frac{\alpha}{2} \kappa P_0$ is the *adiabatic chirp coefficient*. Assuming that the laser is operating above threshold in the linear portion of the I-P curve the steady-state power is given by $P_0 \approx \frac{I_{bias} - I_{th}}{\alpha_L}$. Knowing that $G_0(N_{th}) = \alpha_L$ by definition and that $\kappa \approx G_0(N_{th})\varepsilon$ we have $\gamma_{adiab} \approx \frac{\alpha}{2} \varepsilon (I_{bias} - I_{th})$.

Laser sample measurements give $\alpha = 2.7$ and $\varepsilon = 0.59 \text{ pC}^{-1}$. Hence $\frac{1}{2\pi} \frac{\gamma_{adiab}}{I_{bias} - I_{th}} \approx 127 \text{ MHz/mA}$ and $\frac{1}{2\pi} \frac{\kappa P_0}{I_{bias} - I_{th}} \approx 93 \text{ MHz/mA}$. If we now consider a bias current such as $I_{bias} - I_{th} = 50 \text{ mA}$ then $\frac{1}{2\pi} \gamma_{adiab} \approx 6.34 \text{ GHz}$ and $\frac{1}{2\pi} \kappa P_0 \approx 4.69 \text{ GHz}$.

Appendix C

Laser Noise Formulation with (N , E) Variables

In this short appendix the noise processes modelling the noise sources appearing in the laser rate equations using carrier number N and optical phasor E are derived from elementary considerations. The notations and terminology of this appendix are as introduced in Sec. 4.5.1 and 4.5.2.

C.1 Heuristics of the random evolution of E

As no clear expression for the power and structure of the noise sources when expressing the laser rate equations in (N, E) variables has been found in the literature we derived it from the following considerations.

Henceforth we deal with dimensionless quantities and the intensity-related photon number variable P equals $|E|^2$. We want to describe how the classical electromagnetic field is modified when one “photon” is produced through spontaneous emission. We assume that when produced a “spontaneous-emission photon” adds a random phase contribution which can be represented by a random variable with a uniform distribution over $(0, 2\pi)$. We also assume that the average density of such events on the time line is $R_{\text{sp}}(N)$. This can be stated by the following expression for the accumulated contribution of spontaneous emission

to the internal electrical field phasor:

$$E_t^{sp} = \sum_{n \in \mathbb{N}} e^{i\phi_n} H(t - t_n),$$

where (t_n) is the random sequence of times when spontaneous emission events occur, (ϕ_n) is the sequence of random phases and H is the Heaviside distribution. Which leads to modelling the phenomenon by a random walk (Brownian motion) in the complex plane. The real and imaginary part of the process are uncorrelated real Brownian motions with a diffusion coefficient of $R_{sp}(N)/2$ each. The electromagnetic field can now be modelled by an Ito process driven by the following stochastic differential equation:

$$dE_t = \frac{1}{2}(\tilde{G}(N_t, |E_t|^2) - \alpha_L)E_t dt + dE_t^{sp}.$$

C.2 Ito stochastic calculus for the determination of the carrier noise process

Ito's calculus [KGP00] allows the determine of the stochastic differential equation driving $P = E^*E$,

$$\begin{aligned} d(E_t^*E_t) &= E_t^*dE_t + dE_t^*E_t + \text{Cov}_t(dE_t^*, dE_t) \\ &= (G(N_t, |E|^2) - \alpha_L)|E_t|^2 dt + E_t^*dE_t^{sp} + E_t dE_t^{sp*} + R_{sp}(N_t)dt, \end{aligned}$$

which gives

$$dP_t = \left((G(N_t, P_t) - \alpha_L)P_t + R_{sp}(N_t) \right) dt + dP_t^{sp},$$

where by identification $dP^{sp} = E^*dE^{sp} + EdE^{sp*}$. This formula is consistent with what is stated in [Hen86] and [AD93] since it can be verified that the previously defined random process (approximately Gaussian if the output power is high enough so that field relative variations due to spontaneous emission are small) has a diffusion coefficient equal to $2R_{sp}(N)P$. Finally by considering that the main mechanism that leads to carrier number fluctuation is spontaneous emission in the laser mode we get $dN^{sp} = -dP^{sp}$. (When this assumption is not valid dN^{sp} can be written as the sum of $-dP^{sp}$ and an independent noise process with diffusion coefficient equal to $2R_{rec}(N)$).

Appendix D

Fiber Dispersion Impact on On-Off Keying Optical Communication Systems and Mitigation Techniques

Most digital optical communication systems be they for LAN, MAN, WAN or intercontinental long-haul applications are based on the simple on-off keying (OOK) modulation scheme where a transmitted bit value of 1 is encoded into a light pulse and a bit value of 0 is encoded into the absence of a light pulse in allocated time slots of same size T , the bit period. Its extensive use is mostly due to its robustness and simplicity that makes possible the design of transceivers at speeds in excess of several gigabits per second. This class of modulation formats make also an efficient usage of optical power. This denomination actually covers several types of modulations such as Non-Return to Zero (NRZ) and Return to Zero (RZ) with different duty cycles.

This appendix starts by presenting a simple method for quantifying the impact of fiber dispersion on the performance of a digital OOK optical communication system that will be mostly used in D.4.5. It serves as a simple and intuitive analysis tool. It makes use of the notion of power penalty of an optical communication system with impairments. The bit-error rate (BER) which is the ultimate measure of the system performance can be analytically expressed in basic cases [Agr95a]. But its evaluation is difficult whenever there is inter-symbol interference (ISI) due to fiber dispersive effects in particular. The system power penalty is amenable to simple analytical calculations and can be expressed

as a function of fiber dispersion parameters in return for a few simplifying assumptions. It then reveals insightful system parameter dependencies as well as scaling rules (fiber span length increase, data rate increase, etc) in a dispersion-limited (as opposed to power-limited) system.

There already exists a number of signal processing techniques. Some are specified in the standards of existing networking technologies or are part of commercial systems that allow the mitigation or cancellation of adverse effects due to fiber dispersion. They fall into two broad categories: electrical domain compensation and optical domain compensation. The choice of a specific solution trades off system cost, handling of high data rates, reliability and availability of the basic technology. Optical compensation techniques have the advantage of not requiring high-speed integrated circuit (IC) technology. However they often lack flexibility and are costly compared to electronic compensation in LAN/MAN point-to-point applications where electrical/optical and optical/electrical conversion is a given. But even the affordability and flexibility of electronic solutions can be challenged when data rates reach 10 Gb/s and beyond.

A final section presents experimental results and analyses in the implementation of a simple optical domain PMD compensator. This study was conducted in collaboration with Dr. Martin Fischer of Agere's Advanced Photonics Research Group who implemented the experimental setups presented here.

D.1 Polarization-mode dispersion vector and pulse signal

D.1.1 Definitions and preliminary results

We present here results first introduced in [Kar98], [Shi99] and [Shi00], and give a proof for each of them.

We start with a model of the transfer matrix of an SMF¹ $T(\omega) = e^{-\frac{\alpha}{2}L}e^{-i\beta(\omega)L}M(\omega)$. The optical signal is represented by the optical field $A(z, t)$. $\|A(z, t)\|^2$ is the optical power that goes at time t through the section at point z . We define the *normalized waveform* $e(z, t)$ of the optical signal,

$$e(z, t) = \frac{A(z, t)}{(\int \|A(z, t)\|^2 dt)^{1/2}},$$

¹This could be applied to any distributed optical system.

where $\int \|A(z, t)\|^2 dt$ is the total energy crossing the section at point z .

We also define *time moments* $\langle t^n \rangle_z$ associated with the optical signal at point z :

$$\text{For } n \in \mathbb{N}, \langle t^n \rangle_z = \int e^\dagger(z, t) t^n e(z, t) dt.$$

Properties of the Fourier transform ($\frac{\partial e}{\partial t} = i\omega \tilde{e}$ and $\tilde{t}e = i\frac{\partial}{\partial \omega} \tilde{e}$) and the Parseval theorem give

$$\begin{aligned} \langle t^0 \rangle &= \int \|e\|^2 dt = \int \|\tilde{e}\|^2 \frac{d\omega}{2\pi} = 1 \\ \langle t \rangle &= \int e^\dagger t e dt = i \int \tilde{e}^\dagger \frac{\partial \tilde{e}}{\partial \omega} \frac{d\omega}{2\pi} \\ \langle t^2 \rangle &= \int e^\dagger t^2 e dt = \int \|\frac{\partial \tilde{e}}{\partial \omega}\|^2 \frac{d\omega}{2\pi}. \end{aligned}$$

We use the complex amplitude-SOP decomposition $\tilde{e}(z, \omega) = \tilde{x}(z, \omega) |s\rangle_{(z, \omega)}$ and have

$$\begin{cases} \tilde{x}_{\text{out}}(\omega) = e^{-i\beta(\omega)L} \tilde{x}_{\text{in}}(\omega) \\ |s_{\text{out}}\rangle = M |s_{\text{in}}\rangle \end{cases}$$

The z -independence of $\|\tilde{e}(z, \omega)\|$ can be inferred from the form of the transmission matrix T :

$$\|\tilde{e}(z, \omega)\| = \|\tilde{e}_{\text{out}}(\omega)\| = \|\tilde{e}_{\text{in}}(\omega)\| = g(\omega),$$

where $g^2(\omega)$ is the *normalized spectrum* of the signal. It gives the frequency-domain distribution of the energy of the signal. The unit mass measure $\frac{1}{2\pi} g^2$ will be extensively used to express the average of frequency dependent quantities. In the following paragraph we will note $[\bullet] = \int g^2 \bullet \frac{d\omega}{2\pi}$. In a way similar to probability notations we will note $\text{Var}[\bullet] = [(\bullet - [\bullet])^2]$ and $\text{Cov}[\bullet, \star] = [(\bullet - [\bullet])(\star - [\star])]$.

We first derive an expression for the time moments $\langle t \rangle$ and $\langle t^2 \rangle$ related to our transfer matrix model. We recall the definition of the output and input PMD vector $\frac{dM}{d\omega} M^\dagger = -\frac{i}{2} \vec{\tau}_{\text{out}} \cdot \vec{\sigma}$ and $M^\dagger \frac{dM}{d\omega} = -\frac{i}{2} \vec{\tau}_{\text{in}} \cdot \vec{\sigma}$. As phase and magnitude variations of our signal will play an important role we write

$$\begin{cases} \tilde{x}_{\text{in}}(\omega) = g(\omega) e^{i\psi(\omega)} \\ \tilde{x}_{\text{out}}(\omega) = g(\omega) e^{i\phi(\omega)} \end{cases} \quad \text{with } \phi(\omega) = \psi(\omega) - \beta(\omega)L.$$

We also define the input and output *intrinsic group delays* by $\tau_g^{\text{in}} = -\frac{d\phi}{d\omega}$ and $\tau_g^{\text{out}} = -\frac{d\psi}{d\omega}$. The *common group delay* of the fiber link is given by $\tau_g^f = \frac{L}{v_g} = \frac{d\beta}{d\omega} L$ where v_g is the

common group velocity. We have from our input/output relationship

$$\tau_g^{\text{out}} = \tau_g^{\text{in}} + \tau_g^f.$$

With the help of our definitions we can get useful expressions for the first and second order time moments:

$$\begin{aligned} \langle t \rangle_{\text{in}} &= [\tau_g^{\text{in}}] \\ \langle t \rangle_{\text{out}} &= [\tau_g^{\text{out}}] + \frac{1}{2} [\vec{\tau}] \cdot \vec{S} \\ \langle t^2 \rangle_{\text{in}} &= [(\tau_g^{\text{in}})^2] + [(\frac{d}{d\omega} \ln(g))^2] \\ \langle t^2 \rangle_{\text{out}} &= [|\tau_g^{\text{out}} \vec{S} + \frac{1}{2} \vec{\tau}|^2] + [(\frac{d}{d\omega} \ln(g))^2], \end{aligned}$$

and for the input and output *mean-square width* of the optical waveform:

$$\begin{aligned} \delta_{\text{in}}^2 &= \langle (t - \langle t \rangle_{\text{in}})^2 \rangle_{\text{in}} = \delta_0^2 + \text{Var}[\tau_g^{\text{in}}] \\ \delta_{\text{out}}^2 &= \langle (t - \langle t \rangle_{\text{out}})^2 \rangle_{\text{out}} = \delta_0^2 + [|\tau_g^{\text{out}} \vec{S} + \frac{1}{2} \vec{\tau}|^2] - \left([\tau_g^{\text{out}}] + \frac{1}{2} [\vec{\tau} \cdot \vec{S}] \right)^2, \end{aligned}$$

where $\delta_0^2 = [(\frac{d}{d\omega} \ln(g))^2] = \int (\frac{dg}{d\omega})^2 \frac{d\omega}{2\pi}$ is the *intrinsic mean-square pulse width*. It is the minimum pulse width attainable by signals having exactly the same frequency power distribution but different phase variations. It is important to note that in all the previous expressions $\vec{\tau}$ and \vec{S} can either refer simultaneously to input or output quantities since they appear in rotation invariant combinations. The following derivation of those expressions will use input referred quantities.

The derivation of the expression of $\langle t \rangle_{\text{in}}$ is straightforward. For $\langle t \rangle_{\text{out}}$ we have

$$\begin{aligned} \langle t \rangle_{\text{out}} &= i \int \tilde{x}_{\text{out}}^* \langle s_{\text{out}} | \frac{d}{d\omega} (\tilde{x}_{\text{out}} | s_{\text{out}}) \rangle \frac{d\omega}{2\pi} \\ &= i \int \left(g^2 \langle s_{\text{out}} | \frac{d}{d\omega} (|s_{\text{out}}\rangle) + \tilde{x}_{\text{out}}^* \frac{d}{d\omega} (\tilde{x}_{\text{out}}) \right) \frac{d\omega}{2\pi} \\ &= i \int \left(g^2 \langle s_{\text{in}} | M^\dagger \frac{dM}{d\omega} | s_{\text{in}} \rangle + \frac{1}{2} \frac{dg^2}{d\omega} + i \frac{d\phi}{d\omega} g^2 \right) \frac{d\omega}{2\pi} \\ &= - \int g^2 \left(\frac{d\phi}{d\omega} - \frac{1}{2} \vec{\tau}_{\text{in}} \cdot \vec{S}_{\text{in}} \right) \frac{d\omega}{2\pi} + \underbrace{\frac{i}{2} \int \frac{dg^2}{d\omega} \frac{d\omega}{2\pi}}_{=0}. \end{aligned}$$

For the second-order time moments we have

$$\langle t^2 \rangle_{\text{in}} = \int \left\| \frac{d\tilde{x}_{\text{in}}}{d\omega} | s_{\text{in}} \rangle \right\|^2 \frac{d\omega}{2\pi} = \int \left| ig \frac{d\psi}{d\omega} + \frac{dg}{d\omega} \right|^2 \frac{d\omega}{2\pi} = \int g^2 \left(\frac{d\psi}{d\omega} \right)^2 \frac{d\omega}{2\pi} + \int \left(\frac{dg}{d\omega} \right)^2 \frac{d\omega}{2\pi},$$

and

$$\begin{aligned}
\langle t^2 \rangle_{\text{out}} &= \int \left| \left| \frac{d}{d\omega} (\tilde{x}_{\text{out}} M |s_{\text{in}}) \right| \right|^2 \frac{d\omega}{2\pi} \\
&= \int \left| \left| \frac{d\tilde{x}_{\text{out}}}{d\omega} M |s_{\text{in}} \right\rangle + \tilde{x}_{\text{out}} \frac{dM}{d\omega} |s_{\text{in}} \right\rangle \right|^2 \frac{d\omega}{2\pi} \\
&= \int \left| \left| \frac{d\tilde{x}_{\text{out}}}{d\omega} |s_{\text{in}} \right\rangle + \tilde{x}_{\text{out}} M^\dagger \frac{dM}{d\omega} |s_{\text{in}} \right\rangle \right|^2 \frac{d\omega}{2\pi} \\
&= \int \left(\left| \frac{d\tilde{x}_{\text{out}}}{d\omega} \right|^2 + g^2 \langle s_{\text{in}} | (M^\dagger \frac{dM}{d\omega})^\dagger M^\dagger \frac{dM}{d\omega} |s_{\text{in}} \rangle + 2 \operatorname{Re} \left(\langle s_{\text{in}} | \frac{d\tilde{x}_{\text{out}}}{d\omega} \tilde{x}_{\text{out}} M^\dagger \frac{dM}{d\omega} |s_{\text{in}} \rangle \right) \right) \frac{d\omega}{2\pi} \\
&= \int \left(\left| \frac{d\tilde{x}_{\text{out}}}{d\omega} \right|^2 + g^2 \langle s_{\text{in}} | \frac{1}{4} \underbrace{(\vec{\tau}_{\text{in}} \cdot \vec{\sigma})(\vec{\tau}_{\text{in}} \cdot \vec{\sigma})}_{=|\vec{\tau}_{\text{in}}|^2} |s_{\text{in}} \rangle + 2 \operatorname{Re} \left(\frac{d\tilde{x}_{\text{out}}}{d\omega} \tilde{x}_{\text{out}} \langle s_{\text{in}} | - \frac{i}{2} \vec{\tau}_{\text{in}} \cdot \vec{\sigma} |s_{\text{in}} \rangle \right) \right) \frac{d\omega}{2\pi} \\
&= \int \left(\left(\frac{dg}{d\omega} \right)^2 + g^2 \left(\frac{d\phi}{d\omega} \right)^2 + g^2 \frac{|\vec{\tau}_{\text{in}}|^2}{4} - 2g^2 \vec{\tau}_{\text{in}} \cdot \vec{S}_{\text{in}} \frac{d\phi}{d\omega} \right) \frac{d\omega}{2\pi} \\
&= \int g^2 \left| \frac{d\phi}{d\omega} \vec{S}_{\text{in}} - \frac{1}{2} \vec{\tau}_{\text{in}} \right|^2 \frac{d\omega}{2\pi} + \int \left(\frac{dg}{d\omega} \right)^2 \frac{d\omega}{2\pi}.
\end{aligned}$$

D.1.2 PMD vector of a pulse and polarization dependent group delays

The energy of a physical pulse observed at one point in space is not concentrated at one point in time. We define the arrival time of the pulse at this point in space as the mean of the time variable t weighted by the time-distribution of the energy of the pulse, $\|e(z, t)\|^2 = e^\dagger(z, t)e(z, t)$, that is to say the normalized pulse power at point z . The propagation time of the pulse through the fiber is then given by

$$t_{\text{prop}} = \langle t \rangle_{\text{out}} - \langle t \rangle_{\text{in}} = [\tau_g^f] + \frac{1}{2} [\vec{\tau} \cdot \vec{S}] = [\tau_g^f] + \frac{1}{2} [\vec{\tau}_{\text{in}}] \cdot \vec{S}_{\text{in}},$$

where we can define the (input) PMD vector associated with the pulse waveform by

$$\vec{\tau}_p = [\vec{\tau}_{\text{in}}].$$

If this quantity is nonzero, we can define the slow PSP of the pulse, $\vec{p}_p = \frac{\vec{\tau}_p}{|\vec{\tau}_p|}$, and the fast PSP of the pulse, $\vec{q}_p = -\vec{p}_p$. We see here that, if $\vec{\tau}_p$ is nonzero, the propagation time depends on the input SOP of the pulse and that it has a unique absolute maximum and a unique absolute minimum that are respectively attained if the pulse is sent on its slow PSP or its fast PSP:

$$t_{\text{slow}} = t_{\text{com}} + \frac{1}{2} \tau_p \quad \text{and} \quad t_{\text{fast}} = t_{\text{com}} - \frac{1}{2} \tau_p$$

where $t_{\text{com}} = [\tau_g^f]$ is the common propagation time and $\tau_p = |\vec{\tau}_p| = |[\vec{\tau}_{\text{in}}]|$ is the pulse Differential Group Delay (DGD) for the fiber of interest. The delay between a pulse sent

on the slow PSP and one sent on the fast one is equal to the DGD (hence the name) as illustrated in Fig. 2.8.

D.1.3 Pulse width evolution

In digital optical communication systems, information is encoded in a sequence of light pulses. The narrower the pulse, the higher the information throughput. Yet narrow pulses generate a broadband signal that is more sensitive to dispersion effects that increase their width after propagation. The overlapping of pulses generates inter-symbol interference (ISI) and degrades system performance. The study of the evolution of the width of light pulses is consequently of paramount importance to quantify the effects of dispersion on the performance of the communication system and to minimize them.

At the fiber input the width of the pulse can be related to its frequency-domain phase variations and energy distribution:

$$\delta_{\text{in}}^2 = \delta_0^2 + \text{Var}[\tau_g^{\text{in}}],$$

where $\delta_0^2 = [(\frac{d}{d\omega} \ln(g))^2]$ is the minimal pulse width and $\text{Var}[\tau_g^{\text{in}}] = [(\frac{d\psi}{d\omega})^2] - [\frac{d\psi}{d\omega}]^2 = \int g^2 (\frac{d\psi}{d\omega})^2 \frac{d\omega}{2\pi} - \left(\int g^2 \frac{d\psi}{d\omega} \frac{d\omega}{2\pi} \right)^2$ is the frequency variance of the signal chirp. Expanding the expression previously obtained for the output pulse width:

$$\delta_{\text{out}}^2 = \delta_0^2 + \text{Var}[\tau_g^{\text{out}}] + \frac{1}{4} \left([|\vec{\tau} \times \vec{S}|^2] + \text{Var}[\vec{\tau} \cdot \vec{S}] \right) + \text{Cov}[\tau_g^{\text{out}}, \vec{\tau} \cdot \vec{S}],$$

with $\tau_g^{\text{out}} = \tau_g^{\text{in}} + \tau_g^f$. The difference of those two quantities can be written:

$$\delta_{\text{out}}^2 - \delta_{\text{in}}^2 = \text{Var}[\tau_g^f] - 2 \text{Cov}[\tau_g^{\text{in}}, \tau_g^f] + \frac{1}{4} \left([|\vec{\tau} \times \vec{S}|^2] + \text{Var}[\vec{\tau} \cdot \vec{S}] \right) + \text{Cov}[\tau_g^{\text{out}}, \vec{\tau} \cdot \vec{S}]$$

The first two terms give the impact of fiber chromatic dispersion and chirp on the pulse width evolution. The second term describes the effect of PMD alone. The last term is the contribution to the pulse width evolution of the interaction of chirp and chromatic dispersion with PMD. It can be readily noted that if the PMD vector is constant over the frequency range where the signal spectral power is non-zero this expression reduces to $\delta_{\text{out}}^2 - \delta_{\text{in}}^2 = \text{Var}[\tau_g^f] - 2 \text{Cov}[\tau_g^{\text{in}}, \tau_g^f] + \frac{1}{4} [|\vec{\tau} \times \vec{S}|^2]$. In this case the only important parameters are chirp, chromatic dispersion and the relative position of the input SOP and the input

PMD vector. Let's be more precise. We now want to know which (input) SOP's minimize and maximize the output pulse width. Let $F(\vec{S}) = -\frac{1}{4}(\vec{\tau}_p \cdot \vec{S})^2 + \text{Cov}[\tau_g^{\text{in}} + \tau_g^f, \vec{\tau}_{\text{in}}] \cdot \vec{S}$ be the contribution of $\delta_{\text{out}}^2 - \delta_{\text{in}}^2$ that depends on \vec{S} and $N(\vec{S}) = |\vec{S}|^2$. The problem to solve is to find the extrema of the smooth function F on the smooth surface $N(\vec{S}) = 1$ (Poincaré sphere). As F is a continuous function of \vec{S} and the surface $N(\vec{S}) = 1$ is compact, F has an absolute maximum and an absolute minimum on the sphere. A necessary condition verified by the extremal points is that they make the gradients of F and N colinear:

$$\begin{cases} \vec{\nabla}F(\vec{S}) = -\frac{1}{2}(\vec{\tau}_p \cdot \vec{S})\vec{\tau}_p + \text{Cov}[\tau_g^{\text{in}} + \tau_g^f, \vec{\tau}_{\text{in}}] \\ \vec{\nabla}N(\vec{S}) = 2\vec{S} \end{cases}$$

This means that \vec{S} has to be aligned with the vector $(\vec{\tau}_p \cdot \vec{S})\vec{\tau}_p - 2\text{Cov}[\tau_g^{\text{in}} + \tau_g^f, \vec{\tau}_{\text{in}}]$.

In general the solutions have no reason to be aligned with $\vec{\tau}_p$ so we do not necessarily have minimization of the pulse width for the PSP's. But there are cases when the term $\text{Cov}[\tau_g^{\text{in}} + \tau_g^f, \vec{\tau}_{\text{in}}]$ is zero. For instance the PMD vector can have no frequency variations over the signal spectrum or the effects of chromatic dispersion in the fiber and initial chirp of the pulse can cancel each other. If this is the case F varies as the opposite of the square of the distance to the plane orthogonal to $\vec{\tau}_p$. F is then minimal on the sphere for the PSP's and maximal for all the points of the equator defined by the intersection of the sphere and the plane orthogonal to the PSP's.

D.1.4 Frequency-moments expansions and approximations

We first define the *frequency moments* of the signal:

$$\text{For } n \in \mathbb{N}, [\omega^n] = \int g^2 \omega^n \frac{d\omega}{2\pi}.$$

We assume that we can Taylor-expand quantities in the vicinity of the mean frequency $\bar{\omega} = [\omega]$ of the modulating signal:

$$\vec{\tau}_{\text{in}}(\omega) = \vec{\tau}_{\text{in}}(\bar{\omega}) + \vec{\tau}'_{\text{in}}(\bar{\omega})(\omega - \bar{\omega}) + \frac{1}{2}\vec{\tau}''_{\text{in}}(\bar{\omega})(\omega - \bar{\omega})^2 + o((\omega - \bar{\omega})^2).$$

In general, g^2 is symmetric (except for instance for Single Side Band (SSB) signals) and $\bar{\omega} = 0$. In this case $\vec{\tau}_{\text{in}}(\bar{\omega})$ is consequently equal to $\vec{\tau}_{\text{in}}(0)$, the PMD vector of the fiber at the center of the frequency band. The PMD vector of the signal can be expanded the following

way:

$$\vec{\tau}_p(\omega) = [\vec{\tau}_{\text{in}}(\omega)] = \vec{\tau}_{\text{in}}(\bar{\omega}) + \frac{1}{2}\vec{\tau}_{\text{in}}''(\bar{\omega}) \text{Var}[\omega] + [o((\omega - \bar{\omega})^2)],$$

where $\text{Var}[\omega] = [(\omega - \bar{\omega})^2]$ is the frequency-variance of the signal frequency.

We have the following result about the second order expansion of the pulse width increase due to PMD:

$$\begin{array}{l} \delta_{\text{out}}^2 = \delta_0^2 + \delta_1^2 + \delta_2^2 + [o((\omega - \bar{\omega})^2)] \\ \text{with } \begin{cases} \delta_0^2 = \left[\left(\frac{d}{d\omega} \ln(g) \right)^2 \right] = \int \left(\frac{dg}{d\omega} \right)^2 \frac{d\omega}{2\pi} \\ \delta_1^2 = \frac{1}{4} \left(\vec{\tau}_p^{(2)} \times \vec{S}_{\text{in}} \right)^2 = \frac{1}{4} \left(\left(\vec{\tau}_p^{(2)} \right)^2 - \left(\vec{S}_{\text{in}} \cdot \vec{\tau}_p^{(2)} \right)^2 \right) \\ \delta_2^2 = \left(\phi''(\bar{\omega}) - \frac{1}{2}\vec{\tau}_{\text{in}}'(\bar{\omega}) \right)^2 \text{Var}[\omega] \end{cases} \end{array}$$

where $\vec{\tau}_p^{(2)} = \vec{\tau}_{\text{in}}(\bar{\omega}) + \frac{1}{2}\vec{\tau}_{\text{in}}''(\bar{\omega}) \text{Var}[\omega]$ is the second-order approximation of the PMD vector relative to the signal.

To prove this result we assume that $\bar{\omega} = 0$ without loss of generality. We have the following Taylor expansion of the derivative of the phase of the signal at the fiber output:

$$\frac{d\phi}{d\omega}(\omega) = \phi'(0) + \phi''(0)\omega + \frac{1}{2}\phi'''(0)\omega^2 + o(\omega^2).$$

We then compute an expansion of the output pulse width δ_{out}^2 from which we have subtracted the intrinsic pulse width of the signal $\delta_0^2 = \int \left(\frac{dg}{d\omega} \right)^2 \frac{d\omega}{2\pi}$:

$$\begin{aligned} \delta_{\text{out}}^2 - \delta_0^2 &= \left[\left(\frac{d\phi}{d\omega} \vec{S}_{\text{in}} - \frac{1}{2}\vec{\tau}_{\text{in}} \right)^2 \right] - \left[\left(\frac{d\phi}{d\omega} - \frac{1}{2}\vec{\tau}_{\text{in}} \cdot \vec{S}_{\text{in}} \right)^2 \right] \\ &= \left[\left((\phi'(0)\vec{S}_{\text{in}} - \frac{1}{2}\vec{\tau}_{\text{in}}(0)) + (\phi''(0)\vec{S}_{\text{in}} - \frac{1}{2}\vec{\tau}_{\text{in}}'(0))\omega + \frac{1}{2}(\phi'''(0)\vec{S}_{\text{in}} - \frac{1}{2}\vec{\tau}_{\text{in}}''(0))\omega^2 + o(\omega^2) \right)^2 \right] \\ &\quad - \left[\left((\phi'(0) - \frac{1}{2}\vec{\tau}_{\text{in}}(0) \cdot \vec{S}_{\text{in}}) + (\phi''(0) - \frac{1}{2}\vec{\tau}_{\text{in}}'(0) \cdot \vec{S}_{\text{in}})\omega + \frac{1}{2}(\phi'''(0) - \frac{1}{2}\vec{\tau}_{\text{in}}''(0) \cdot \vec{S}_{\text{in}})\omega^2 + o(\omega^2) \right)^2 \right] \\ &= \frac{1}{4} \left((\vec{\tau}_{\text{in}}(0))^2 - (\vec{\tau}_{\text{in}}(0) \cdot \vec{S}_{\text{in}})^2 \right) + \frac{1}{4} \left(\vec{\tau}_{\text{in}}(0) \cdot \vec{\tau}_{\text{in}}''(0) - (\vec{\tau}_{\text{in}}(0) \cdot \vec{S}_{\text{in}}) (\vec{\tau}_{\text{in}}''(0) \cdot \vec{S}_{\text{in}}) \right) [\omega^2] \\ &\quad + \left(\phi''(0)\vec{S}_{\text{in}} - \frac{1}{2}\vec{\tau}_{\text{in}}'(0) \right) [\omega^2] + [o(\omega^2)], \end{aligned}$$

which leads to the result when using the definition of $\vec{\tau}_p^{(2)}$.

From this we can also infer a lower order expansion of δ_{out}^2 that reveals what is called a “first-order PMD” effect:

$$\delta_{\text{out}}^2 = \delta_0^2 + \frac{1}{4} |\vec{\tau}_{\text{in}}(\bar{\omega}) \times \vec{S}_{\text{in}}|^2 + [o(\omega - \bar{\omega})].$$

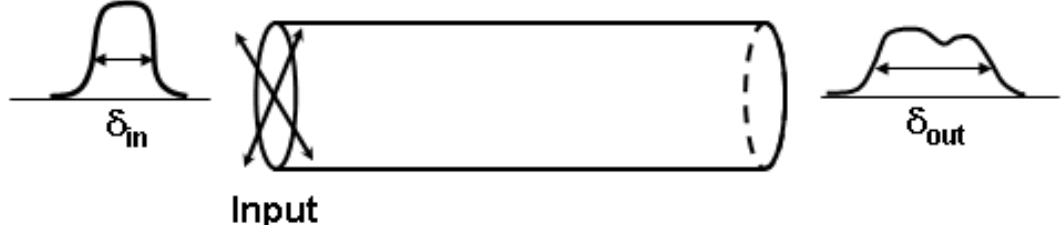


Figure D.1: Dispersion induced pulse spreading.

Neglecting terms of order more than one and assuming that $\bar{\omega} = 0$, we can say that the output pulse width is minimal when the pulse signal is sent on one of the (input) PSP's (the value of which is considered at the center on the frequency band). In the second-order frequency moments expansion, δ_1^2 is the modified first-order PMD effect and actually includes second order effects in the definition of $\vec{\tau}_p^{(2)}$. This term vanishes if the input SOP \vec{S}_{in} is equal to $\vec{q}_p^{(2)}$ (second-order approximation of the fast PSP) or its opposite $\vec{p}_p^{(2)}$ (second-order approximation of the slow PSP). The term δ_2^2 comprehends the effects of chromatic dispersion and input pulse chirp included in $\phi'' = \psi'' - \beta_2 L$. It is also clear from this expression that chromatic-dispersion and chirp effects interact with the PMD effects: depending on the relative positions of the input SOP and the first derivative of the PMD vector those effects can either add or subtract. This suggests that frequency dependence of the PMD vector has effects close to chirp and chromatic dispersion on the spreading of light pulses. If there is no chirp and no frequency dependence of the PMD vector, we have $\delta_2 = |\beta_2| L \Delta\omega$ and if $\phi''(\bar{\omega}) = 0$, $\delta_2 = \frac{1}{2} |\vec{\tau}'_{\text{in}}(\bar{\omega})| \Delta\omega$ where $\Delta\omega$ is the rms width of the frequency band occupied by the signal. Those expressions relate pulse spreading due to every cause of dispersion and give the scaling of the induced effects when we consider signals occupying different bandwidths. They can be used to compute related transmission power penalties as is done in Section D.2.

D.2 Dispersion-induced power penalty in on-off keying optical systems

As optical pulse spreading is the main source of ISI in digital OOK optical systems the approximation of the previous section can be used to quantify the impact of fiber dispersion on an optical OOK transmission system performance. We assume here that the input pulse does not bear any chirp² and that the pulse power spectrum is centered on the optical carrier. An approximate expression of the output rms pulse width δ_{out} up to the second order in the rms spectrum width $\Delta\omega$ of the signal optical signal is derived in Appendix D.1:

$$\delta_{\text{out}}^2 \approx \delta_{\text{in}}^2 + \delta_1^2 + \delta_2^2$$

$$\text{with } \begin{cases} \delta_1^2 = \frac{1}{4} |\vec{\tau}_{\text{in}}(0) \times \vec{S}_{\text{in}}|^2 = \frac{1}{4} (|\vec{\tau}_{\text{in}}(0)|^2 - (\vec{S}_{\text{in}} \cdot \vec{\tau}_{\text{in}}(0))^2) \\ \delta_2^2 = (\beta_2 L \vec{S}_{\text{in}} + \frac{1}{2} \vec{\tau}'_{\text{in}}(0))^2 \Delta^2 \omega \end{cases}$$

where δ_{in}^2 is the input mean-square pulse width, \vec{S}_{in} is the input SOP, $\vec{\tau}_{\text{in}}(0)$ and $\vec{\tau}'_{\text{in}}(0)$ are the value of the PMD vector and its first derivative respectively at the center of the frequency band, β_2 is the GVD parameter and L the fiber piece length. In order to slightly simplify our discussion we have assumed here that $|\vec{\tau}'_{\text{in}}(0)| \Delta^2 \omega \ll |\vec{\tau}_{\text{in}}(0)|$ (*i.e.* we have neglected order-3 PMD effects compared to order-1 PMD effects). The contributions to pulse spreading δ_1^2 and δ_2^2 are expressed in terms of input-referred quantities but can be translated into output-referred quantities the statistics of which are presented in Sec. 2.3.4. This is done by noting that these expressions are rotationally invariant and by considering the value of the fiber rotation matrix at the center of the frequency band $R = R(L, 0)$ ³:

$$\begin{aligned} \vec{S}_0 &= R \vec{S}_{\text{in}} \\ \vec{\tau}_0 &= R \vec{\tau}_{\text{in}}(0) \\ \vec{\tau}'_0 &= R \vec{\tau}'_{\text{in}}(0), \end{aligned}$$

²This could not be the case in reality but taking this effect into account would amount to combining a chirp term to the chromatic dispersion term we have here. All other considerations would remain the same.

³In general $\vec{\tau}''(0) = \vec{\tau}(0) \times \vec{\tau}'(0) + R \vec{\tau}''_{\text{in}}(0) \neq R \vec{\tau}''_{\text{in}}$.

where the subscript 0 denotes the value of output-referred quantities at the center of the frequency band. With the above notations,

$$\begin{aligned}\delta_1^2 &= \frac{1}{4}|\vec{\tau}_0 \times \vec{S}_0|^2, \\ \delta_2^2 &= (\beta_2 L \vec{S}_0 + \frac{1}{2}\vec{\tau}'_0)^2 \Delta^2 \omega.\end{aligned}$$

In digital optical systems a time slot is allocated for each bit of information encoded as an optical pulse (or its absence). Because of noise sources and the very quantized nature of light the detection system makes errors. The higher the optical power used for the transmission, the lower the Bit Error Rate (BER). Yet, apart from optical loss, dispersion is another source of degradation of the performances of the system. It gives rise to a power penalty and a BER increase. As suggested in [PTCF91] and [Shi00] we have the following approximate expression for the power penalty \mathcal{P}_{dB} in dB at a given baseline BER due to the spreading of digital pulses:

$$\mathcal{P}_{dB} \propto \frac{\delta_{\text{out}}^2 - \delta_0^2}{\delta_0^2} \approx \frac{\delta_1^2 + \delta_2^2}{\delta_0^2} \quad (\text{in dB}). \quad (\text{D.1})$$

This results from the following intuitive mechanism. When a pulse width broadens pulse energy in the allocated time slot diminishes and leaks into adjacent slots. We can see that in the worst case bit sequence $\dots 101010 \dots$ the level of 1's is lowered and the level of 0's is heightened in front of the receiver decision circuit resulting in closure of the digital eye. This translates into power penalty, that is to say the received optical power needs to be increased to obtain the same BER as the unimpaired system.

The structure of Eq. D.1 provides good insight into fiber dispersion contribution to the system performance degradation. We can first note that chromatic dispersion and second-order PMD contribute the same way to the system power penalty. If we let D_b be the bit-rate and $T = 1/D_b$ be the bit-period we have $\delta_0^2 \propto T^2 = \frac{1}{D_b^2}$ and $\Delta^2 \omega \propto D_b^2$. The proportionality coefficients depend on the pulse shape. The expression for the power penalty becomes

$$\mathcal{P}_{dB} = \mathcal{A} \frac{1}{4} \left((\vec{\tau}_0)^2 - (\vec{S}_0 \cdot \vec{\tau}_0)^2 \right) D_b^2 + \mathcal{B} \left(\beta_2 L \vec{S}_0 + \frac{1}{2} \vec{\tau}'_0 \right)^2 D_b^4, \quad (\text{D.2})$$

where \mathcal{A} and \mathcal{B} depend on the data format and the receiver structure and the chosen baseline BER. They could be determined either by simulations or experiments. \mathcal{A} can be determined from the measurement of the performance of links with first-order PMD only and \mathcal{B} can be

Format	\mathcal{A}	\mathcal{B}
NRZ	30 [Nel01], [Jop99]	85 [Shi00]

Table D.1: Values of the coefficients \mathcal{A} and \mathcal{B} in Eq. D.1 for a baseline BER of 10^{-9} .

determined from links with chromatic dispersion only. Some values found in the literature are presented in table D.1.

The actual values for PMD parameters are not known *a priori* as opposed to the GVD fixed value. Yet we have statistical models allowing us to make probabilistic inferences. The PMD statistics is scaled by the mean PMD. For fibers of practical length mean PMD scales as the square-root of the fiber length:

$$\sqrt{E(\bar{\tau}^2)} = D_{\text{pmd}}\sqrt{L},$$

where the coefficient D_{pmd} is specified by optical fiber manufacturers in ps/ $\sqrt{\text{km}}$.

If we consider that \vec{S}_{in} has a fixed value and PMD follows probability distributions shown in table 2.1 on page 28. The average power penalty expressed in terms of the previously mentioned quantities becomes

$$E(\mathcal{P}_{dB}) \approx \mathcal{A}\frac{1}{6}\left(D_{\text{pmd}}\sqrt{L}\right)^2 D_b^2 + \mathcal{B}\left((\beta_2 L)^2 + \frac{1}{12}(D_{\text{pmd}}\sqrt{L})^4\right) D_b^4.$$

We first note that the average impact of first-order PMD effects scale linearly with the fiber length L and quadratically with the bit rate D_b . Chromatic dispersion and second-order PMD effects scale quadratically with the fiber length and with the fourth power of the bit rate. If we combine link length and bit rate we get the following form for the average power penalty:

$$E(\mathcal{P}_{dB}) \approx \mathcal{C}(LD_b^2) + \mathcal{D}(LD_b^2)^2,$$

where \mathcal{C} and \mathcal{D} are positive constants depending on the fiber PMD and chromatic dispersion parameters, pulse shape and receiver structure. This expression indicates that a constant power penalty should be equivalent to a constant LD_b^2 product. It means that if we set a dispersion power penalty limit for our system the maximum achievable length for a dispersion-limited system is divided by 4 when the bit rate is doubled.

This expression can serve as a good tool for a high-level analysis of the scaling of optical

fiber networks when the bit rate is changed for instance. It should give a view on where critical performance limits will be reached when upgrading a LAN or MAN network base to higher throughputs, or when migrating an optical communication technology to a different fiber base (usage of old dark fibers, etc). For instance knowing that a 10 Gb/s (unchirped) NRZ system is limited by chromatic dispersion at 1550 nm to approximately 80 km we can assess that a 40 Gb/s NRZ system should be limited to around 5 km without any chromatic dispersion compensation device and with a similar receiver design.

We will be making an extensive usage of the notion of power penalty and Eq. D.1 as a tool for analyzing the relative performance of different configurations of a PMD compensation system studied in Sec. D.4.

D.3 Fiber dispersion compensation solutions

D.3.1 Introduction

Techniques for the compensation of the effects of fiber dispersion on OOK signals have been extensively studied. They fall into two main categories:

- Electronic equalization which is very flexible but is limited by data rate dependence and integrated-circuits technology speed limits.
- Optical compensation which is data rate independent to some extent but leads to complex and expensive systems.

D.3.2 Electronic equalization

Adaptive electronic equalization has been widely used in communication applications such as voice-band modems, wireless, digital subscriber lines, and ISDN, and even at rates close to 1 Gb/s in disk drives. However, implementation of equalization at rates exceeding 10 Gb/s for optical applications is not so straightforward. Previous work [Kas82] proposed the general concept of electrical compensation of differential-mode delay (DMD) in multi-mode fibers and [FGL⁺00, BBT00, BBK00] reported board-level implementations of electrical equalization at 10 Gb/s.

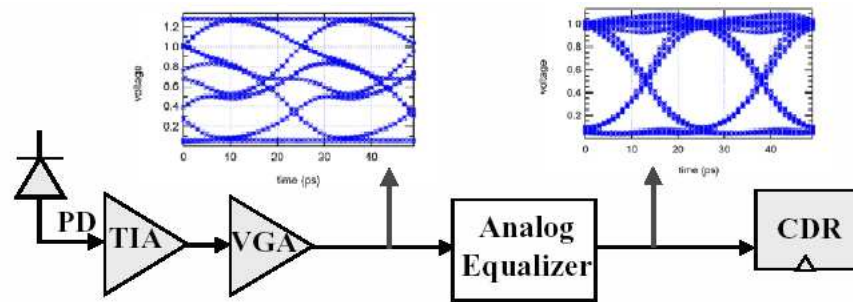
FFE and DFE In high-speed digital equalization the main challenge resides in the design of a 10 GS/s and above analog-to-digital converter (ADC). Therefore purely analog equalization can be a more practical alternative to digital equalization.

A silicon-proven equalization structure makes use of two *finite-impulse response* (FIR) filters, one in front of the decision circuit and called *feed-forward equalizer* (FFE a.k.a *transversal filter*), and a second one providing feedback from the output of the decision circuit and called decision feedback equalizer (DFE). Since the decision circuit is part of the DFE it is categorized as a non-linear equalizer and allows the removal of non-linear ISI depending on already decided bits from the bit under decision (or equivalently to modify the decision threshold based on previously decided bits). The disturbance caused by a given bit value on the signal value used for the decision of following bits is called *post-cursor ISI*. The disturbance on the signal value used for the decision of previous bits is called *pre-cursor ISI*. The DFE removes postcursor ISI with minimal noise enhancement while the FFE removes precursor ISI with potential noise enhancement effects.

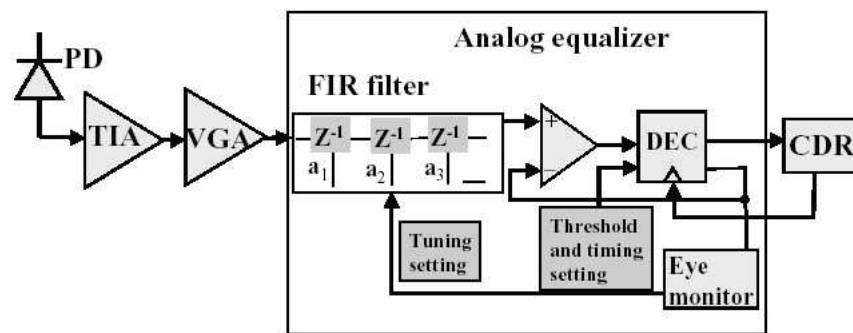
In Fig. D.2(a) we show an analog FFE inserted within a conventional direct detection receiver path formed by a photodiode, a linear transimpedance amplifier (TIA), a linear variable gain amplifier (VGA), and clock and data recovery (CDR) functions. Fig. D.2(b) shows some of the internal details of the analog equalizer, implemented using analog delay lines, wide-band digitally programmable multipliers, and a digital tap adaptation algorithm. Tap adaptation can be performed using the least-mean square (LMS) algorithm or eye monitoring techniques [BBK00]. Such an equalizer can be used for extending the distances of 10 Gb/s bit streams over MMF up to 300 m, and compensating up to 50 ps DGD for an SMF, allowing the increase of operating distances of SONET/SDH and 10-Gb Ethernet networks.

A 5-tap analog FFE was implemented in a 0.25- μm SiGe technology. The chip is shown in Fig. D.3 where a delay-locked loop, 4 delay lines and 5 taps are apparent. The chip size is $2.5 \times 2.5 \text{ mm}^2$. The equalizer operation was tested in an experiment where the NRZ signal bit-rate was 10 Gb/s, the SMF channel with first-order PMD (DGD of 50 ps) was emulated using a PMD emulator, and the receiver had a bandwidth of less than 10 GHz. In a worst case configuration where the input SOP is equally projecting on each input PSP the equalizer manages to open a completely closed eye as shown in Fig. D.4.

We have seen that the effects of first-order PMD are linear in the electrical domain after direct detection. Yet chromatic dispersion and higher-order PMD lead to non-linear ISI in



(a) Analog equalization simulation results



(b) Analog feed-forward equalizer architecture

Figure D.2: Analog fiber equalizer: (a) simulation results, (b) feed-forward equalizer (FFE) architecture with control loop based on eye monitoring. PD: Photodiode; TIA: Transimpedance amplifier; VGA: Variable gain amplifier; CDR: Clock and data recovery.

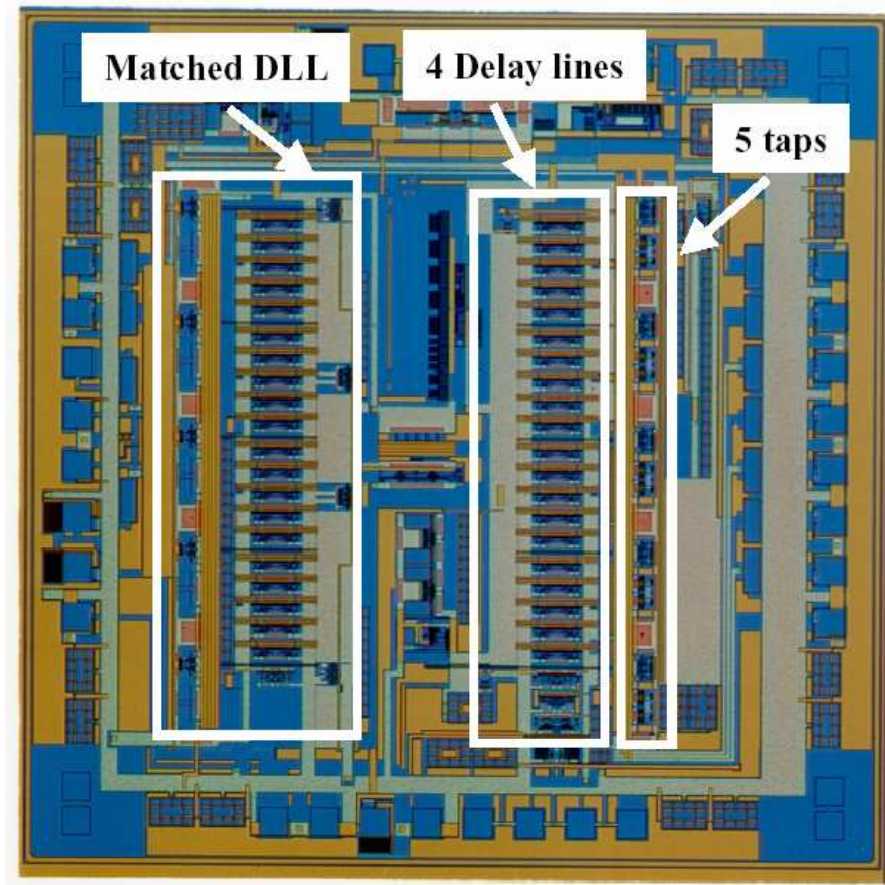
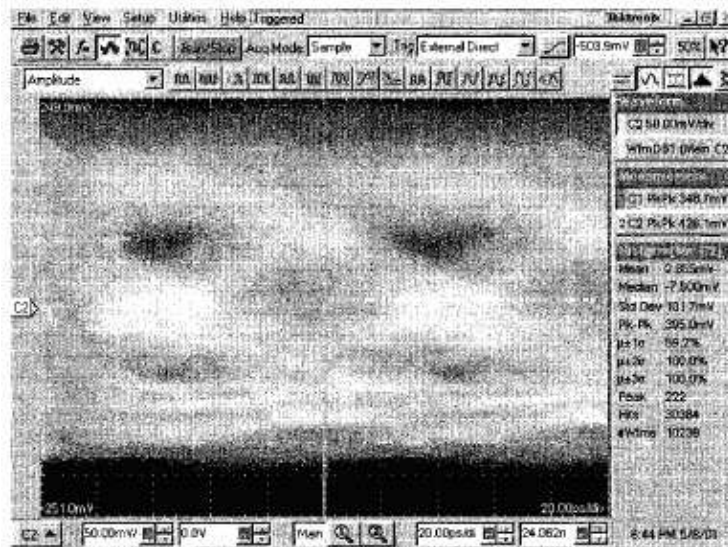
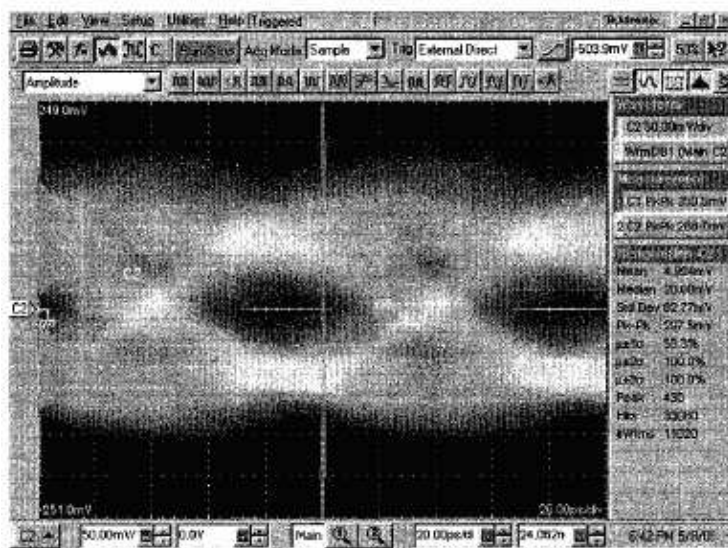


Figure D.3: Micrograph of the analog FIR FFE described in Fig. D.2.



(a)



(b)

Figure D.4: Equalization of a 10 Gb/s NRZ signal impaired by PMD (using a PMD emulator) with the analog FIR FFE showed in Fig. D.2: (a) optical channel output (equalizer input), (b) equalizer output.

the electrical domain. The improvement that an stand-alone FFE can bring is consequently limited and can be improved by the usage of a DFE or a more general nonlinear canceller (NLC) [KW91, WK92]. The high-speed integrated implementation of a DFE or NLC is limited by the existence of a loop in the design. This bottleneck can be broken in return for additional complexity by implementing look-ahead techniques where the results of ISI cancellation in the current signal value are computed in parallel for each possible previous bit values. The loop is now reduced to selecting the correct result right before the decision device.

Maximum likelihood detection *Maximum likelihood sequence estimation* (MLSE) is the optimum receiver electrical signal processing technique for ISI compensation. It estimates each transmitted bit from multiple received signal samples. MLSE is commonly used in disk drives. However, as opposed to disk-drive applications where the recording channel can be characterized beforehand, optical channels are not known a priori and are time varying. This requires channel estimation and flexible trellis decoding (or adaptive Viterbi decoding).

If we assume that high-speed A/D conversion is possible at high rates of 10 GS/s (using interleaved A/D conversion [AHS⁺02]) this solution can be implemented by using parallel processing techniques. Yet design challenges are extreme and approximate solutions have been proposed and have only been proven with discrete components [WK91].

D.3.3 Optical compensation

Chromatic dispersion compensation [Li01] reviews and compares numerous chromatic dispersion compensation techniques in the context of high-capacity DWDM systems. The usage of *dispersion compensating fiber* (DCF) provides simple and satisfactory compensation. For single wavelength links over short distances the usage of laser sources in the vicinity of the standard single mode fiber zero-dispersion point is the solution prevailing in most available communication systems.

PMD compensation The general idea of a polarization mode dispersion compensator is to either prevent or undo the effect of PMD caused by the transmission system. The simplest and most common ways of attempting to achieve this goal are described in this section.

One can get a feel for the problems and complexities involved in building such a device by reexamining how PMD affects a transmitted signal. Since PMD acts on the optical field amplitude, it is a natural approach to try to counter-act this effect using optical methods. As stated in Eq. (2.10), for linear propagation through a fiber the electric field amplitude evolves as

$$\tilde{A}_{\text{out}}(\omega) = T(\omega)\tilde{A}_{\text{in}}(\omega).$$

If one can find an optical medium with a transmission matrix

$$T_{\text{comp}}(\omega) = T^{-1}(\omega),$$

then the effect of PMD can be reversed by inserting this device after the transmission path, since

$$\tilde{A}_{\text{final}}(\omega) = T_{\text{comp}}(\omega)\tilde{A}_{\text{out}}(\omega) = T^{-1}(\omega)T(\omega)\tilde{A}_{\text{in}}(\omega) = \tilde{A}_{\text{in}}(\omega).$$

Several challenges have to be overcome if such an element were to be constructed:

- The transmission matrix T_{comp} is frequency dependent. This means the compensator cannot be a simple rotation of the light polarization. This is quite obvious, since even to first order a pulse delay needs to be compensated. Additionally the frequency dependence has to be matched to the fiber transmission matrix. Since this dependence in general is quite complicated, an approximation to the ideal case must be made.
- The fiber transmission matrix T varies randomly with environmental parameters and therefore with time. As a consequence the compensator matrix has to vary in time as well. This requires a real-time tracking mechanism.
- Since an approximation to T_{comp} has to be found one has to ensure that a continuous change in the fiber matrix can be compensated by a continuous change in the compensator matrix. To make this point might seem a little exaggerated. It will, however, have severe consequences on the performance, as will be elaborated later.
- Besides the fundamental problems stated above there is the practical one of actually obtaining information about the fiber transmission matrix to be compensated. The matrix $T(\omega)$ cannot be measured without interfering with the input signal into the fiber. What is typically done instead is to add the variable compensator after the fiber and measure the effect of PMD after the combined system ‘fiber+compensator’. One

then adjusts the compensator to minimize this effect. This minimization approach raises another set of problems, some of which are addressed later in this section.

In the remainder of this section we will describe the most basic architectures for compensation and compare their general features. This will illuminate the choice we made for the implementation of our compensator. We will then describe in more detail the experimental setup.

PSP alignment The simplest way to avoid first order PMD effects in a fiber to occur is to align the light polarization launched into the fiber along one of the principal states of polarization (PSP). Since the PSP vectors in a fiber link vary randomly, the input polarization has to be constantly adjusted to track these changes. A schematic of this method is shown in Fig. D.5. In this setup the effect of PMD on the transmitted signal is measured

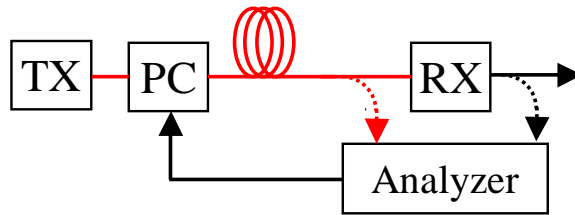


Figure D.5: PMD Compensator based on PSP alignment on the transmitter side.

either optically or electronically by the *analyzer*, as will be described later in this section. This information is then used to adjust the polarization controller (PC) on the input side. If only first order PMD effects are considered, the degradation of the signal is at a minimum when the input polarization is aligned with the PSP. The action of the feedback loop is to drive the system to this minimum state.

The effect of the PSP alignment is to prevent the occurrence of first order PMD effects. However, a shortcoming of this technique is the fact that it does not address the effect of higher order PMD. Even when the input polarization is aligned with a PSP there will still be signal distortion due to higher order PMD.

From an implementation standpoint the main reason why this technique is not the method of choice is that the feedback loop encompasses the entire transmission line. The error signal - the measure of the degradation due to PMD - is derived after the fiber span,

whereas the launched polarization has to be adjusted at the transmitter. This requires that the control information be sent over the entire transmission distance from the receiver back to the transmitter, complicating the setup in real applications tremendously. In addition, the operation speed of the loop is limited by the signal delay through the loop. For links of several hundreds of kilometers length this can ultimately limit the speed to several hundred Hertz.

DGD reduction The schematic of the simplest optical (post-)compensator⁴ is shown in Fig. D.6. In this setup, all elements of the compensator are located at the receiver end of

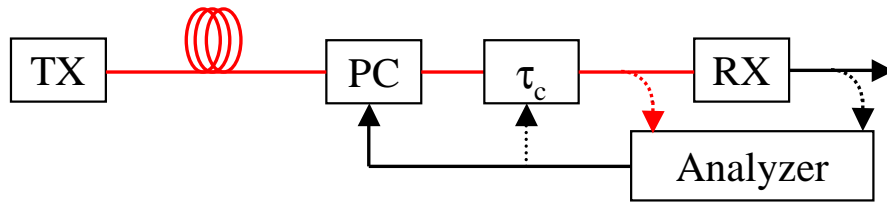


Figure D.6: First order PMD compensator.

the span. This allows for a more compact and easier to control implementation. The core of the compensator is a section of birefringent material (τ_c) inserted after the fiber span. A polarization controller allows a variable rotation of the polarization after the fiber with respect to the birefringent section. Most commonly the birefringent section consists of either a section of polarization maintaining fiber (PMF or HiBi fiber) or a packaged birefringent crystal. These implementations of τ_c have a fixed value of differential group delay (DGD). An implementation for a variable DGD is depicted in Fig. D.7. Here a polarization beam splitter (PBS) is used to split two orthogonal polarizations into two paths and recombine them after travelling a certain distance. The path length difference can be dynamically adjusted by varying the position of the reflectors in one of the paths.

The setup described in Fig. D.6 is potentially capable of completely eliminating the effect of first order PMD (hence the name). There are two operating modes of this compensator which can best be explained by illustrating the concatenation of PMD vectors as in Fig. D.8. The vector $\vec{\tau}_F$ denotes the fiber PMD vector and $\vec{\tau}_C$ the PMD vector of the compensating section. The total PMD vector $\vec{\tau}_{in}$ is the sum of the two component vectors⁵. Rotating

⁴Post' here means to undo the effect after they have occurred.

⁵To be exact, $\vec{\tau}_{in} = \vec{\tau}_F + R_F^{-1} R_{PC}^{-1} \vec{\tau}_C$. All PMD vectors are input-referred quantities.

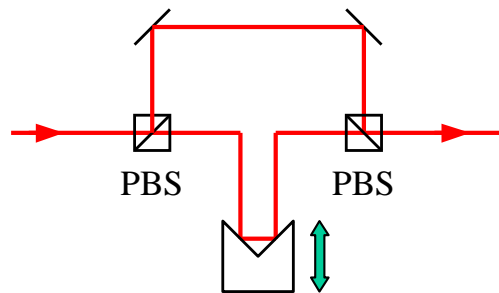


Figure D.7: Variable DGD section based on path length difference.

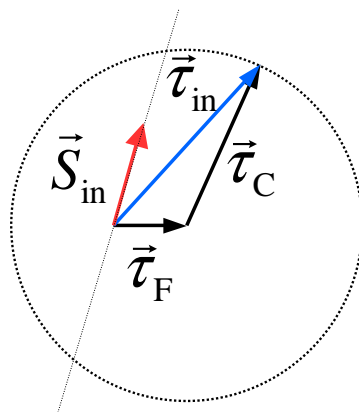


Figure D.8: Concatenation of PMD vectors in a first order PMD compensator.

the polarization controller allows the second vector to rotate through the entire sphere. \vec{S}_{in} denotes the input polarization into the link. As we can see from this illustration, there are two possible ways to eliminate first order PMD effects:

1. Align the polarization controller such that $\vec{\tau}_{\text{C}} = -\vec{\tau}_{\text{F}}$, leading to $\vec{\tau}_{\text{in}} = 0$. The idea here is to choose a birefringent section with an amount of DGD that is equal to that of the fiber. If the polarization controller maps the fast PSP of the fiber onto the slow PSP of the compensating section and vice versa, then the compensating section undoes the PMD effect of the fiber section. Effectively it slows down the component of the pulse that has travelled faster in the fiber with respect to the other component so that both arrive at the receiver at the same time to reconstruct the original pulse. This is obviously only possible if the magnitudes of the vectors (DGD) are the same. This is the major advantage of a compensator section with variable DGD, since it can be adjusted dynamically to match the randomly varying DGD of the fiber.
2. Align the polarization controller such that $\hat{\tau}_{\text{in}} = \pm \hat{S}_{\text{in}}$, i.e., the input polarization is aligned with one of the PSP's of the combined system "fiber + compensator". This eliminates the pulse splitting due to first order PMD. There is only a guaranteed solution for this condition if $\tau_{\text{C}} \geq \tau_{\text{F}}$. For $\tau_{\text{C}} < \tau_{\text{F}}$ there might or might not exist a polarization controller setting to satisfy this condition, depending on the input polarization with respect to the fiber PSP.

The fact that there are more than one solutions to eliminate (or minimize) the first order PMD effect poses a problem. As an example, assume that the DGD's of fiber and compensator are roughly equal and the feedback loop drives the system towards the minimum PMD effect according to the first item above (cancellation of the total DGD). If the fiber DGD now diminishes and the DGD of the compensator is fixed, the cancellation approach can no longer completely eliminate the PMD effect. Even though the effect could be compensated by switching to the second method (aligning the PSP to the input polarization) the feedback loop has no knowledge of this (better) solution. It keeps trying to minimize the PMD effect according to the current state, not realizing that the minimization is towards a local rather than a global minimum. Even if it could be made aware of the existence of a better solution, it might not be able to find its way to the new configuration without crossing a region that offers little compensation or in the worst case intensifies the PMD effect. This local minimum trap is most pronounced in a setup with a compensating section with fixed

DGD and is largely eliminated if a variable DGD section is used.

Another downside of this setup is that it does not specifically address higher order PMD effects. In fact, in an attempt to eliminate first order effects it might “inadvertently” create higher order effects. Even though this fact can be utilized to cancel higher order PMD partially it comes at the expense of first order compensation.

More elaborate schemes One natural way to simultaneously include first and higher order PMD effects into the compensation scheme can be achieved by using a compensator that itself has an adjustable component of first and higher order PMD. This is merely a restatement of the comment above that the inverse transmission matrix has to be approximated by an appropriate arrangement of the compensator. Clearly a compensator consisting of one birefringent section cannot compensate for all higher order terms generated by a real fiber. To get a better approximation, several birefringent sections can be concatenated, separated by polarization controllers as indicated in Fig. D.9. Having many (possibly even adjustable)

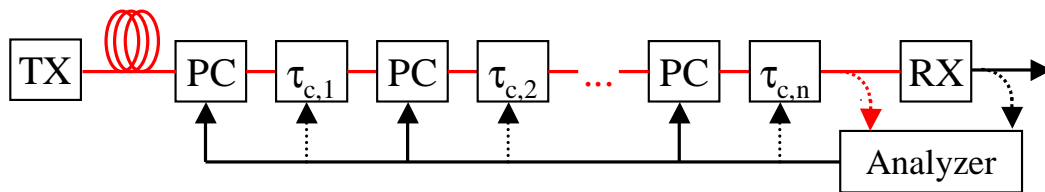


Figure D.9: Higher order compensator consisting of a concatenation of several birefringent sections.

birefringent sections allows for a close match of the generated transmission matrix to the desired one. However, the major drawback of this arrangement is complexity. For each section comprised of a polarization controller (PC) and a birefringent section there are a number of variables that need to be controlled. As mentioned previously it is not possible to measure the transmission matrix directly during an ongoing transmission. Therefore, the analyzer determining the effect of PMD on the transmission must make its judgement based on a limited number of measurable quantities like optical/electrical spectrum, degree of polarization etc. Since a unique mapping of the control parameters onto the effect on the measured quantities is not possible, one again needs to resort to an iterative, multidimensional minimization technique. This is similar to the first order compensator described above, but with an increased number of free parameters to adjust. This leads to a very

complex (and in most cases expensive) implementation.

D.3.4 Discussion

A comparison between optical compensation techniques is given by Sunnerud et al. [Sun02]. The authors compare the pulse broadening and associated outage probability reduction by performing transmission simulations. Compensator arrangements studied range from simple PSP alignment to multistage PMD compensators. A more detailed comparison of a first order compensator with a fixed vs. variable DGD section is given by Yu and Willner [YW02]. In particular, the authors address the problem of trapping in local minima. Here too, the results are derived from simulations. Bülow gives an outline of the comparison of various electronic compensation techniques with optical techniques [Bül02].

D.4 Fixed-DGD optical PMD compensator

D.4.1 Introduction

For the purpose of justifying our choice of compensator to implement in the experiment we briefly emphasize the key features described previously for the relevant compensator types. We take into account the issues that would arise if an actual commercialization of such a setup were to be considered. This list is therefore biased to some extent by our view of the overall application space for PMD compensators.

- **Electronic compensator:** The main advantages of this all-electrical approach are potentially low cost and a compact size due to the possibility of integration into the receiver. The major drawback is that the electronics operates at the data rate, making operation at 40 Gb/s challenging to say the least. Even though 10 Gb/s devices have been demonstrated, devices at 40 Gb/s are still to be developed. Optical compensation methods, on the other hand, are less dependent on the bit rate.
- **PSP alignment:** Compared to other optical compensation techniques with equal or better performance the necessity to extend the feedback loop from the receiver to the transmitter makes this approach unpractical for real applications.
- **First order compensator:** In our view this approach gives the best performance for the complexity and cost involved. From a performance perspective a variable DGD

section is most desirable. However, we are not aware of a simple, robust and cost-effective way to implement such a variable birefringent section. For this reason a fixed DGD section was chosen.

- **Higher order compensator:** The improved performance when utilizing multiple birefringent sections does in our opinion not offset the increased complexity and cost of this configuration. Compensators with one birefringent section can compensate to some extent higher order at the expense of first order PMD effects, reducing the demand for pure higher order compensators.

The optical compensator of choice for our experiment is a first order compensator as described in Sec. D.3.3. A simplified block diagram of the experimental setup is given in Fig. D.10.

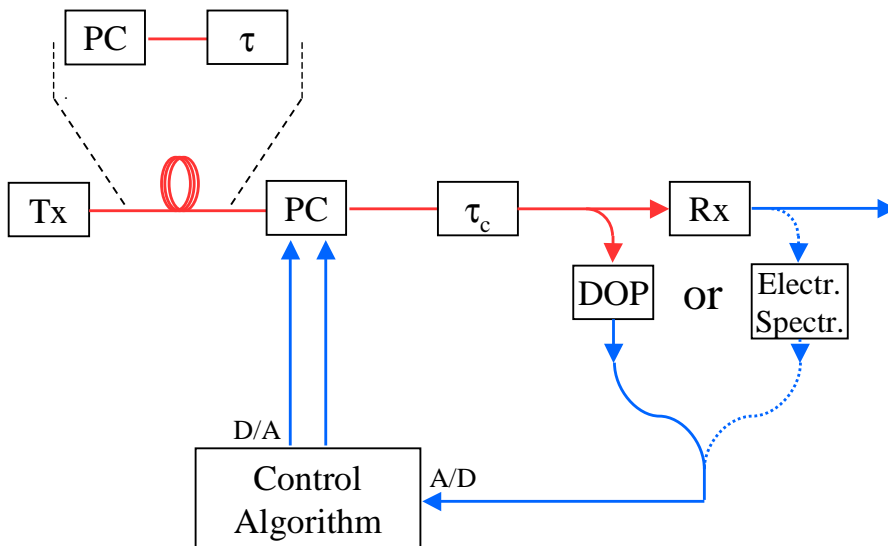


Figure D.10: Simplified block diagram of the experimental setup.

D.4.2 PMD compensator structure

Error signals Even though the actual compensation in this first order compensator is performed in the optical domain, the information about the impact on the signal quality caused by PMD can be obtained either optically or electrically. Here we describe two

ways of extracting this error signal. Both were implemented in the experiment and their performance was compared. Other feedback signals could be used based on the computation of a pseudo-BER or other eye monitoring techniques [SD89, KWOY89, BBK00].

Degree of polarization The degree of polarization (DOP, the length of the time-averaged Stokes vector) gives a measure of the PMD effect. An intuitive explanation for this dependence can be obtained by considering the first order PMD effect in the time domain. At the fiber output, two pulses with orthogonal polarizations arrive with a time delay of τ . At the rising edge the pulse is purely polarized along one PSP. In the overlap region the polarization will be at an angle between the PSP's before switching to the other PSP at the trailing edge. Even though at every instant the pulse is completely polarized time averaging leads to an effective shortening of the Stokes vector.

Typically, the DOP is acquired by an arrangement of 4 photodiodes, measuring the Stokes parameters S_0, S_1, S_2 and S_3 of the incoming light. The low bandwidth (tens of kHz) achieves the time averaging. In the experimental setup, a commercial polarization analyzer (Agilent 8509C) is used. This device can measure the Stokes parameters and output an analog voltage proportional the DOP.

To calibrate the effect of PMD in our system we measure the DOP degradation caused by first order PMD. The expression for the average DOP after passing through a first order DGD element is

$$\text{DOP} = |\vec{s}| = \sqrt{|\vec{S}_{\parallel}|^2 + G(\tau)^2 |\vec{S}_{\perp}|^2}$$

where \vec{S}_{\parallel} is the projection of the input SOP on the PSP's axis in Stokes space, \vec{S}_{\perp} is the projection of the input SOP on the plane orthogonal to the PSP's, G is the input optical waveform autocorrelation function.

We can introduce γ as the fraction of the power in one PSP over the total power. This allows us to write

$$\begin{aligned} |\vec{S}_{\parallel}|^2 &= (2\gamma - 1)^2, \\ |\vec{S}_{\perp}|^2 &= 4\gamma(1 - \gamma). \end{aligned}$$

For a square wave non-return-to-zero (NRZ) pulse train one can easily calculate the corre-

lation function $G(\tau)$ to be:

$$G(\tau) = \begin{cases} 1 - \frac{1}{2} \frac{\tau}{T} & \text{for } \tau < T \\ \frac{1}{2} & \text{for } \tau \geq T \end{cases}$$

where τ is the DGD and T is the bit period. Even though the pulses we use in the transmission experiment are not square (the pulses are typically modelled as raised-cosine), this reference expression is still useful in comparing qualitative features.

As an operation verification we measured the DOP of a signal that was distorted by first order PMD. Simultaneously we recorded the bit error ratio (BER) of the transmitted signal. We performed the experiment at roughly equal powers in each PSP which is the case that leads to the worst first-order PMD performance degradation. The result of this test is displayed in Fig. D.11. Part (a) shows the effect of PMD on the DOP measured after transmission. As a guideline we also indicated the expected dependence for a perfect square wave at $\gamma = 0.5$. The fact that the DOP does not reach 50% is most likely an indication of unequal powers in the PSP's. In addition, the DOP does not reach 100% due to unpolarized amplified spontaneous emission (ASE) from the erbium doped fiber amplifier (EDFA) used to increase the optical power level.

The BER is the quantity that ultimately has to be minimized. Since the BER cannot be measured quickly enough to be used in a feedback loop one has to resort to another observable that shows a correlation to the BER. The impact of the introduced DGD on the BER of the transmission is indicated in part (b), where the BER is plotted versus the measured DOP. This graph shows a monotonic increase of the BER with decreasing DOP. This fact allows us to use the DOP as a measurement function to derive a control signal at least when only first-order PMD is present in the link. Maximization of the DOP should therefore minimize the BER of the link.

Electrical spectrum probing The DOP as described above is derived by tapping off part of the optical data signal and analyzing it. Another possibility is to let a high speed data receiver convert the signal to the electrical domain and investigate the electrical spectrum. If the compensator is co-located with the data receiver this can offer the advantage of reduced cost, since no additional optical components are needed.

Here we estimate the effect of first order PMD on the electrical spectrum. The power

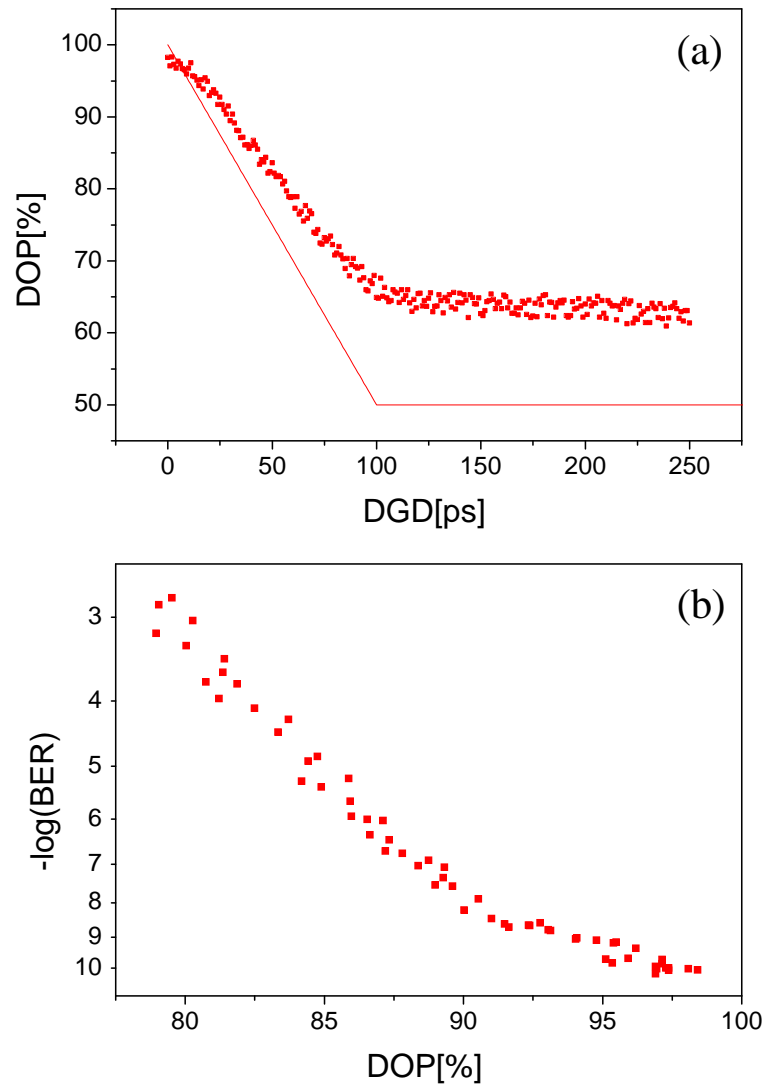


Figure D.11: Calibration of the DOP. Part (a) shows the effect of first order PMD on the DOP and part (b) shows the correlation with the BER.

density spectrum P measured after the receiver can be expressed in terms of the squared magnitude of the Fourier transform of an individual pulse photocurrent waveform $i(t)$ and the power spectral density $S_{aa}(\omega)$ of the stationary sequence of data symbols (a_k) being transmitted as $P_i(\omega) = \frac{1}{T} S_{aa}(\omega) |\tilde{i}(\omega)|^2$.

The photocurrent waveform of a signal distorted by first order PMD can be written as

$$i(t) = \gamma i_0(t) + (1 - \gamma) i_0(t + \tau),$$

where i_0 is the intensity of the undistorted signal. We therefore can write the power spectral density as

$$\begin{aligned} |\tilde{i}(\omega)|^2 &= \left| \int \{\gamma i_0(t) + (1 - \gamma) i_0(t + \tau)\} e^{-i\omega t} dt \right|^2 \\ &= |\gamma + (1 - \gamma) e^{-i\omega\tau}|^2 \left| \int i_0(t) e^{-i\omega t} dt \right|^2 \\ &= [1 - 4\gamma(1 - \gamma) \sin^2(\omega\tau/2)] |\tilde{i}_0(\omega)|^2. \end{aligned}$$

We can now normalize the spectrum to the undistorted case, resulting in

$$P_{\text{rel}}(\omega) = 1 - 4\gamma(1 - \gamma) \sin^2(\omega\tau/2). \quad (\text{D.3})$$

As an operation verification we measured the power spectral density of the electronic signal that was distorted by first order PMD. The spectrum was recorded with a spectrum analyzer and the components at various frequencies were extracted from the trace. It is important to note that the receiver has to be a linear device for the above treatment to apply. A limiting amplifier for example would not be appropriate. Simultaneously we recorded the bit error rate (BER) of the transmitted signal. The result of this test is displayed in Fig. D.12. Part (a) shows the effect of PMD on the spectral components measured after transmission. The frequencies for sampling were chosen as 1/2, 1/4 and 1/8 of the bit rate (the bit rate for all experiments were 10 Gb/s, unless explicitly noted). As a guideline we also indicated the expected dependence for the worst case of $\gamma = 0.5$. Even though we attempted to adjust the polarization to this value, the ratio might have been slightly different, explaining the deviation of the measured data from the theoretical prediction. As is apparent in the graph, the dependence of the PSD components on the DGD is not monotonic, but rather periodic. For high probe frequencies the sensitivity is

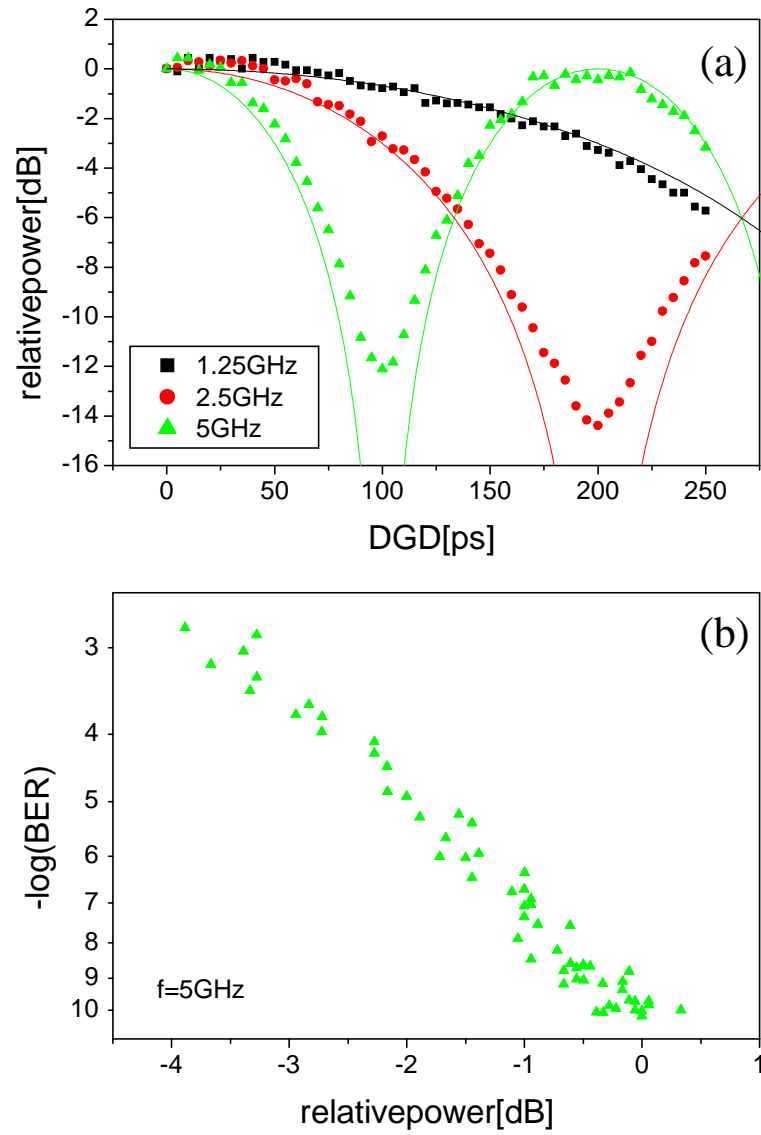


Figure D.12: Calibration of the spectral probe. Part (a) shows the effect of first order PMD on different parts of the spectrum and part (b) shows the correlation with the BER.

large for small values of the DGD. The trade-off is a shorter period. In our experiments we were generally limited to values of DGD that were smaller than the bit period. Therefore we chose the sampling point at half the bit rate ($f = 5$ GHz). If a larger DGD range is required, smaller frequency components can be considered as well. It is important to note that as a result of the positive slope of the error function for a DGD value exceeding half the period the maximization of this frequency component will drive the system to a larger value of DGD.

Again the correlation of the BER with the DGD was investigated. Part (b) of Fig. D.12 shows the BER versus the PSD component at 5 GHz, where τ was restricted to smaller than 60 ps. In this regime the dependence is monotonic resulting in a useful maximization signal. As mentioned above, for larger distortions (beyond the minimum point) the maximization will drive the system away from its optimum point.

Control elements

DGD Elements As elements introducing PMD (source) and compensating PMD (compensator) we used commercial first order PMD emulators (JDS Uniphase PE4). The operation principle of these devices was described in Sec. D.3.3. The compensator was set at a fixed delay during an experimental run. The DGD of the source was varied via remote control. A next step would be to use a concatenation of several first order sources to introduce higher order effects. Ultimately a long span of high-PMD fiber should be tested, preferably under field conditions.

Polarization controller The core of the compensator is the polarization controller. It has to be able to transform any static incoming state of polarization (SOP) to any desired outgoing SOP. In addition to this (static) requirement there are restrictions on the dynamics of this mapping, i.e., on how the mapping changes for dynamically changing input SOP. We will investigate the implications of these requirements in Sec. D.4.2.

The polarization controller we used is the Agere 2722C. It consists of sections of Lithium-Niobate crystals acting as 5 independently controlled quarter-wave plates. It is a packaged device that has a fiber input and output. Each “wave plate” is controlled by two voltages that determine the respective plate angle. All plates are endlessly rotatable.

To verify the operation of the polarization controller we placed it between the PMD

source and the compensator and systematically rotated two of the quarter-wave plates through a complete 2π rotation each. Both PMD emulators were set to a DGD of 50 ps ($\tau = \tau_c = 50$ ps). We then recorded the resulting DOP after passing through this arrangement. Figure D.13 shows the DOP as a function of the wave plate angles. As expected, the DOP

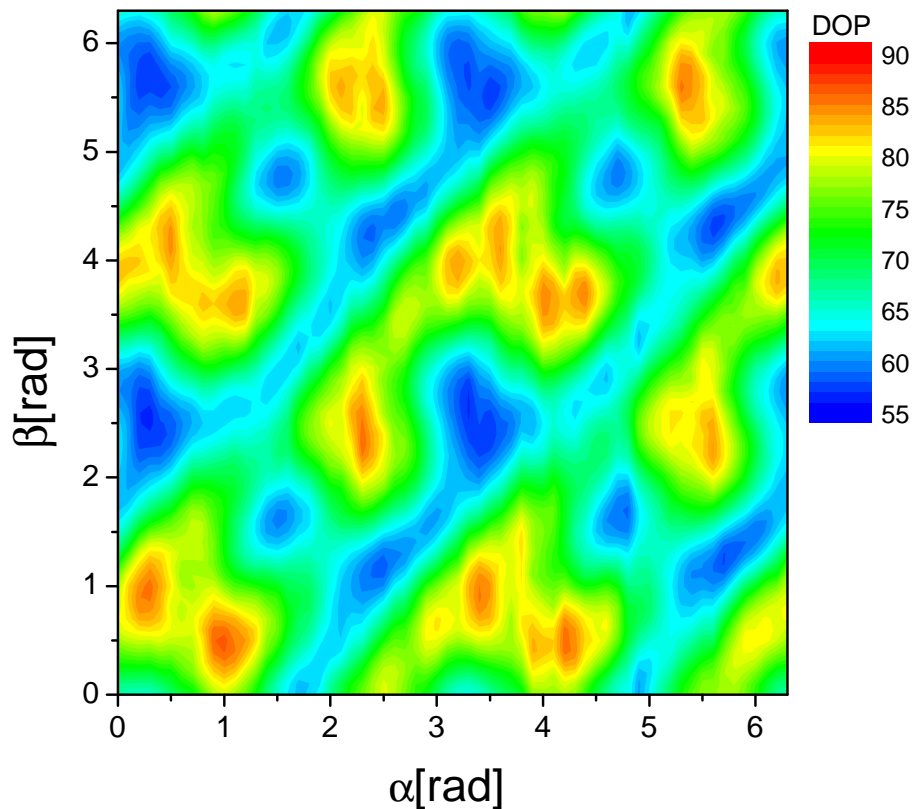


Figure D.13: Color coded plot of the DOP as a function of the angles of two of the polarization controller wave plates ($\tau = \tau_c = 50$ ps).

ranges from roughly 50% to 100%. When the slow PSP of the PMD source and the slow PSP of the PMD emulator are mapped onto each other by the polarization controller, the total DGD is the sum of the individual DGD's, leading to a DOP of 50%. If the slow PSP of one element is mapped onto the fast PSP of the other, the effect cancels and the DOP approaches 100%. A periodicity of π with respect to each of the wave plate angles is also apparent. It is interesting to note that within one unit cell we can observe several minima and maxima. There are several possible causes for this effect. Firstly, the mapping of the polarization rotation onto the DOP might not be injective (one-to-one), i.e., several

positions of the polarizations launched into the PMD compensator could result in the same DOP. Secondly, the mapping of the wave plate angles onto the polarization rotation might not be injective either. The existence of these local optima can lead to a degradation of the compensator performance.

Parameterization of SOP rotations The key element in our PMD compensator is the polarization controller. By rotating the light polarization between two DGD elements it controls the PMD properties of the link. However, there is not a unique way to rotate one Stokes vector onto another. Even though the available optical elements restrict the way a Stokes vector can be rotated, many different configurations of such elements can be used to achieve an arbitrary rotation of any input SOP to any output SOP. The investigation of some common configurations is described in this section.

The action of a controllable element depends on a set of parameters that can be actively actuated according to a predefined algorithm. To describe the parameterization of the transformation performed by the PC we use the formalism introduced in Sec. 2.2.1 and Appendix A. The PC insertion loss is not included in our description since it can be readily accounted for in the link loss budget. The transmission matrix of the PC is consequently entirely described by its birefringence matrix which is consistent with its functionality. The PC is in general built as the concatenation of discrete (at least conceptually) elementary birefringent elements. It can always be thought to be implemented in a “mechanical” way as the concatenation of rotatable plates made out of a birefringent material. This is why we will be representing the PC parameterization on the following illustrative figures as angles giving the positions of the fast eigenaxes of the concatenated plates relative to a fixed laboratory reference frame as shown on Fig. D.14.

The elementary birefringent plates we will be using are the quarter-wave plate (QWP) and half-wave plate (HWP). The Jones matrix of a QWP will be noted Q and that of a HWP will be noted H in the next paragraphs. The expression of those matrices as a function of their elementary control parameter is given hereafter:

$$Q(\alpha) = \frac{1}{\sqrt{2}} \begin{pmatrix} 1 - i \cos(\alpha) & -i \sin(\alpha) \\ -i \sin(\alpha) & 1 + i \cos(\alpha) \end{pmatrix} = \frac{1}{\sqrt{2}} I_2 - i \frac{1}{\sqrt{2}} \vec{n}(\alpha) \cdot \vec{\sigma} = e^{-i \frac{\pi}{2} \vec{n}(\alpha) \cdot \frac{\vec{\sigma}}{2}},$$

$$H(\gamma) = \begin{pmatrix} i \cos(\gamma) & -i \sin(\gamma) \\ -i \sin(\gamma) & i \cos(\gamma) \end{pmatrix} = -i \vec{n}(\gamma) \cdot \vec{\sigma} = e^{-i \pi \vec{n}(\gamma) \cdot \frac{\vec{\sigma}}{2}},$$

where in the previous expressions $\vec{n}(\cdot) = \begin{pmatrix} \cos(\cdot) \\ \sin(\cdot) \\ 0 \end{pmatrix}$.

The action of the QWP and HWP on the SOP's represented in Stokes space is clear from the exponential form of the corresponding Jones matrix as explained in Appendix A. The action on the Poincaré sphere of the QWP of Jones matrix $Q(\alpha)$ is that of a rotation of angle $\pi/2$ and axis $\vec{n}(\alpha)$. The action of the HWP of Jones matrix $H(\gamma)$ is that of rotation of π and axis $\vec{n}(\gamma)$ (i.e., of an orthogonal reflection relative to $\vec{n}(\gamma)$).

It is of interest now to derive the Jones matrix of sequences of such wave plates that will constitute our PC. A closed-form expression for such a matrix can make important properties apparent as well as natural combinations of the basic parameters for control purposes. It can also be used to perform efficient computations in a simulation platform bypassing the implementation of multiple matrices multiplications. As an example we give here the Jones matrix for the concatenation QWP/HWP/QWP (abbreviated as QHQ) shown in Fig. D.14. This configuration has been extensively studied in [Hei02]. We give here different ways of expressing the Jones matrix of such a system

$$\begin{aligned} T_\epsilon(\alpha, \gamma) &= Q(\alpha + \epsilon)H(\gamma)Q(\alpha) \\ &= -\cos(\tilde{\gamma}_\epsilon) \cos(\epsilon/2)I_2 - i \begin{pmatrix} -\sin(\tilde{\gamma}_\epsilon) \sin(\alpha + \epsilon/2) \\ \sin(\tilde{\gamma}_\epsilon) \cos(\alpha + \epsilon/2) \\ -\cos(\tilde{\gamma}_\epsilon) \sin(\epsilon/2) \end{pmatrix} \cdot \vec{\sigma} \end{aligned} \quad (\text{D.4})$$

where the parameter $\tilde{\gamma}_\epsilon = \gamma - \alpha - \epsilon/2$ appears naturally. A few special cases where the parameter ϵ is kept constant are of importance here:

- $\epsilon = 0$: $T_{\epsilon=0} = -(\cos(\tilde{\gamma}_0)I_2 + i \sin(\tilde{\gamma}_0)\vec{n}_\perp(\alpha) \cdot \vec{\sigma})$ where $\vec{n}_\perp(\alpha) = \vec{n}(\alpha + \pi/2)$. It is clear from the previous expression that the system actually emulates a generalized linearly birefringent element. The parameter α controls the position of its axis on the equator of the Poincaré sphere and the parameter $\tilde{\gamma}_0$ sets the Stokes space rotation angle.
- $\epsilon = \pi$: $T_{\epsilon=\pi} = i(\sin(\tilde{\gamma}_\pi)\vec{n}(\alpha) + \cos(\tilde{\gamma}_\pi)\vec{e}_3) \cdot \vec{\sigma}$ and this case emulates a generalized HWP: the rotation angle is fixed and equal to π but the position of the rotation axis is totally arbitrary on the Poincaré sphere and controlled through the parameters α and $\tilde{\gamma}_\pi$.

Any of those special cases allows the transformation of any arbitrary input SOP into any

arbitrary output SOP showing that in principle only two parameters are needed in order to perform the PC control. We will see later that increasing the number of control parameters (for instance by making ϵ variable in this case) can be beneficial in the implementation of a control algorithm.

It is finally interesting to point out that the general case where ϵ has an arbitrarily fixed value is related to one of the specific cases described above in a formal way. More precisely

$$T_\epsilon = e^{-i(\epsilon-\pi)\frac{\sigma_3}{2}} \tilde{T}_\epsilon,$$

where $\tilde{T}_\epsilon = i(\sin(\tilde{\gamma}_\epsilon)\vec{n}(\alpha) + \cos(\tilde{\gamma}_\epsilon)\vec{e}_3) \cdot \vec{\sigma}$ has exactly the same form as $T_{\epsilon=\pi}$ with $\tilde{\gamma}_\pi$ replaced by $\tilde{\gamma}_\epsilon$. This tells that when ϵ (the relative position of the two extremal QWP's) is kept constant the PC behaves fundamentally the same way as one of the special cases. The only difference being a fixed output SOP rotation.

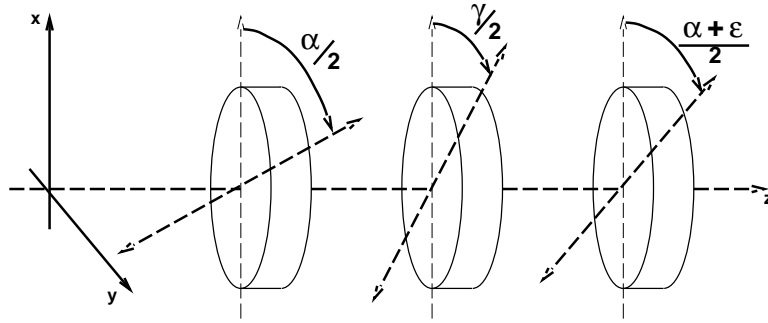


Figure D.14: QHQ configuration and parameterization for polarization control.

By concatenating basic elements such as QWP and HWP more elaborate PC behaviors can be implemented by increasing the dimensionality of the configuration space. By using the algebra applied to the example above it is possible to analyze and compare different implementations as well as perform numerical simulations for the complete system as we shall see later.

Parameterization critical points When the PC is operated by changing its control parameters several characteristics are of importance. Firstly, it is necessary that the PC should be able to map any input SOP onto any output SOP. Secondly since the system is operated in a feedback loop where the control parameters are updated according to a smooth cost

function computed from the PC output itself it is clear that the parameterization of the PC can have an effect on the ability of the system to identify and track the state it ideally needs to put itself into in order to compensate for the source PMD.

This can be explored through experiments and results were already presented in the previous paragraph. Yet some analysis can be performed to understand the limitations of the PC configuration being used. The operation of the QHQ configuration with fixed Q-Q offset is analyzed in great detail in [Hei02].

Even for PC configurations comprising a small number of plates the analysis can get cumbersome. One way to classify the different configurations regarding their static and dynamic operation inside a control feedback loop is to point out the critical points generated by the configuration. Ideally the PC parameterization itself does not create any critical point (parameter value such that the differential of the map is singular, i.e., non-invertible) and the only such points appearing in the cost (or performance) metric expressed as a function of control parameters are intrinsic to the cost (or performance) metric (DOP, component of the electrical signal spectrum, ...). If that metric is well behaved the only critical points correspond to global minima (or maxima). In the worst case it could be possible that a critical point related to the parameterization of the PC translates into a critical point of the performance function and possibly an unwanted local optimum. Milder cases could include critical points appearing as multidimensional saddle-points.

One way to differentiate the configurations is to consider the critical points of the input SOP to output SOP mapping rotation as a function of the control parameters $(\theta_1, \dots, \theta_n)$. This can be studied through the concept of *dynamic eigenstate* (DES) attached to each degree of freedom (each θ_i in our discussion) introduced in [SK01]. In that reference the example of the concatenation of three half-wave plates is given and it is shown that the three control parameters have the same DES. This means that for an input SOP equal to the DES the output is constant to first order in the variations of each scalar parameter. For this input SOP any function of the output SOP will show a critical point (“dead spot”) for all degrees of freedom, possibly impairing the convergence of the adaptive system to an intrinsic optimum of the performance measure function.

Feedback loop and control algorithm Another key element of the PMD compensator is the feedback algorithm. Due to its simplicity and computational ease we chose the steepest descent algorithm. As the name suggests, this method tries to find the maximum

of the DOP (if we choose the DOP as the error signal which we assume for these explanations) curve by locally investigating its surrounding and choosing the path that provides the steepest path “uphill” (to higher DOP). Let \vec{p}_n be the point in configuration space of the polarization controller for an iteration n . For a controller consisting of two quarter-wave plates (configuration QQ), the dimensionality of this vector would be two, for the configuration of quarter-half-quarter wave plates (QHQ) it would be three, etc⁶. The coordinates for the next iteration would then be calculated as

$$\vec{p}_{n+1} = \vec{p}_n + d \cdot \vec{\nabla}(\text{DOP}),$$

where ∇ is the gradient operator and d is a dimensionless scaling factor adjusting the magnitude of the step. For simplicity each partial derivative in the gradient is approximated by only nearest neighbors as in

$$\frac{\partial \text{DOP}}{\partial \varphi_i} \approx \frac{\text{DOP}^+ - \text{DOP}^-}{2\Delta},$$

with φ_i being the angle of the respective wave plate and Δ the step size to determine the derivative. DOP^+ and DOP^- are the measured DOP values at $\vec{p}_n \pm \Delta \hat{e}_i$. Both Δ and d have to be adjusted for optimum performance. If Δ is chosen too large, the derivative will not be approximated well, if it is too small the inevitable noise contribution will lead to large errors in the calculation of the gradient. If d is chosen too small the convergence is slower than necessary. If it is chosen too large the system might overshoot the maximum or leave the maximum too far if noise in the gradient calculation falsely indicates a slope. In a real application the iterative loop has to respond fast enough to track the changing PMD conditions of the link. Acoustic vibrations determine the fastest relevant time scale. In order to track those changes the loop iteration rate should be at least several tens of kHz.

An example series of iterations using the DOP as the signal to maximize set for the parameters $\tau = \tau_c = 50$ ps is shown in Fig. D.15. We can clearly see the convergence to a local maximum. Due to noise in the DOP acquisition the system does not track the maximum ideally for changes in the system condition but rather scatter in the vicinity of the local maximum.

⁶A half-wave plate is configured as two quarter-wave plates rotating synchronously

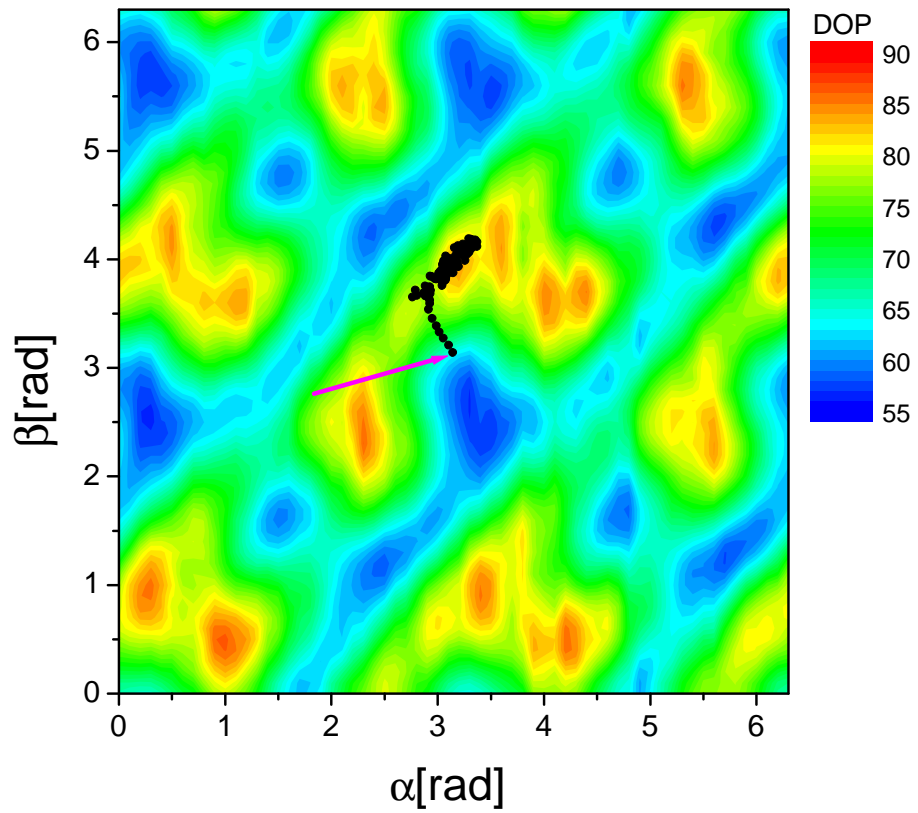


Figure D.15: Plot of a sample trace for the PMD compensator, showing the convergence of the feedback loop. The points are overlaid on the color coded DOP plot of Fig. D.13. The initial starting point is marked with an arrow.

D.4.3 Experimental setup

The entire experiment is computer-controlled. A block diagram of the setup is shown in Fig. D.16.

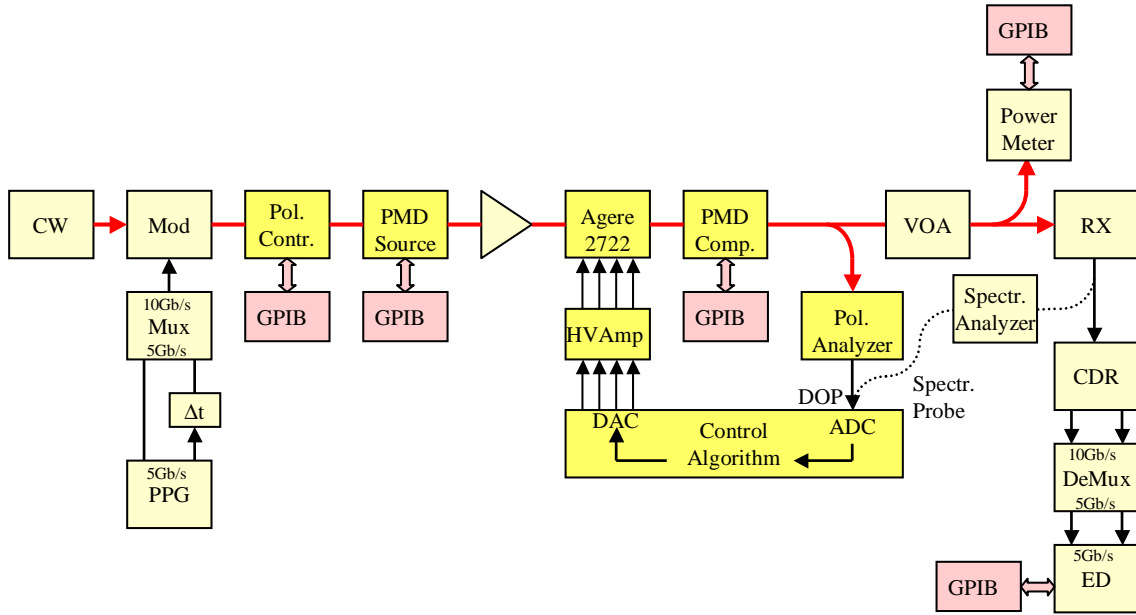


Figure D.16: Block diagram of the experimental setup.

The CW laser source is encoded with a 10 Gb/s data signal by a Mach-Zehnder (MZ) modulator. The PMD source and the polarization controller at its input are remotely controlled via GPIB interface to adjust the magnitude of the first order PMD effect. The core part of the feedback loop is the polarization controller and the PMD compensator. The Agere PC is controlled by up to 10 analog voltages (2 voltages per wave plate). Since the digital-to-analog converter board can only deliver ± 10 V, these voltages need to be amplified. Even though the DGD of the PMD compensator is adjustable remotely, its value during a compensation run is not dynamically varied since we are interested in a fixed-DGD compensation module. We use the adjustability only to set the compensator DGD to 0 ps to obtain the uncompensated case for comparison. We can choose the monitor signal to be used in the feedback loop. One possibility is to read the analog voltage proportional to the DOP generated by the Agilent polarization analyzer. The other option is to obtain the power spectral density of the received electrical signal from a spectrum analyzer (HP 8566B)

at a certain frequency. This is done by operating the spectrum analyzer in ‘zero span’ mode and tapping off part of the analog video signal. This way we can take advantage of the built-in logarithmic amplifier and the video filter. Even though the DOP as well as the power spectrum could be obtained digitally from the devices, the analog method (ADC as a computer board) operates faster. Synchronization issues limited the acquisition speed to about 30 ms for the DOP case and 1 ms for the spectral probe case. Assuming 7 acquisitions per iteration⁷ for the QWQ configuration (3 dimensions) this limits the loop speed to about 5 Hz and 100 Hz respectively. This limitation is imposed by the test equipment used and can easily be accelerated with proper components and synchronization. Finally we acquire the transmitted power and the resulting BER via GPIB.

D.4.4 Results

Preliminary results In this section we describe the performance of our PMD compensator. We also point out some limitations of the first order compensation system. The setup of the compensator was described in the previous section. As an illustration of our measurement procedure we display a typical experimental run in Fig. D.17.

This figure shows the measured BER for the compensated and uncompensated scenario. In the uncompensated case, the compensator DGD was set to 0 ps, in which case the setting of the polarization controller before the compensator was irrelevant. In the compensated case, the compensator DGD was set to the fixed value of $\tau_c = 50$ ps. In this figure the source DGD was scanned in the range from 0 to 100 ps in steps of 5 ps. The measurement time for each BER measurement was 1 minute. Since for low bit error rate during such a short measurement one does not encounter many bit errors, the accuracy of the results is limited by the acquired statistics. Before acquiring each data point the polarization controller was reset to a specific point in configuration space, i.e., a specific arrangement of wave plate angles.

Several interesting features of this compensator structure can be seen in Fig. D.17. Whereas for large values of the source DGD a clear improvement in the BER can be observed, the compensating action actually seems to degrade the system for small DGD values. This degradation is due to the fact that for a source DGD that is much smaller than the DGD of the fixed compensating element the polarization controller has to be precisely

⁷To get the derivative we need 2 points for each dimension. We also record one point at the center for data logging purpose.

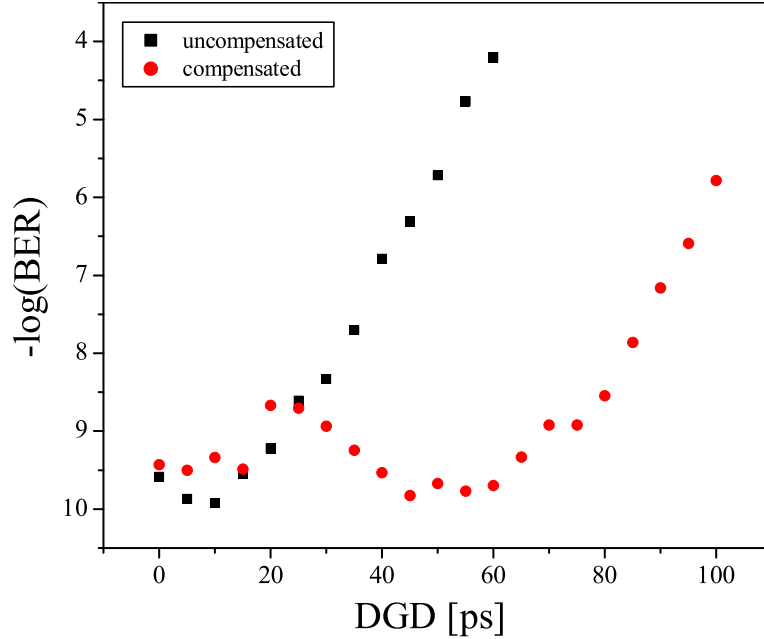


Figure D.17: Typical compensator performance for $\tau_c = 50$ ps.

aligned to avoid the generation of PMD effects in the compensator. Due to the nature of the feedback procedure a certain local environment of the optimum point needs to be sampled, leading to a degradation.

It is interesting to note that for source DGD values smaller than the compensator DGD value (50 ps in this case) the PMD effect can not seem to be compensated entirely. Only for a source DGD value equal to the compensator DGD does the BER reach the value of the case without impairment (uncompensated with zero source DGD). This seems to be in contrast with the arguments in Sec. D.3.3, where we noted that for $\tau_C \geq \tau_F$ there always exists a solution that eliminates first order PMD effects. Since we only use first order DGD elements, this treatment should apply. Even though correct, it is limited to only first order PMD effects. The degradation we see here is due to higher order PMD effects. The occurrence of these higher order effects can be illustrated by considering two concatenated birefringent sections where the two sections are physically rotated with respect to each other. The resulting combined DGD lies between $|\tau_1 - \tau_2|$ and $\tau_1 + \tau_2$, depending on the angle between the sections. However, even though the individual PSP's, the individual DGD's and the combined DGD are frequency-independent, the combined PSP's are not (except for

the special case of alignment of the individual PSP's). The frequency dependent combined PSP is a source for second-order PMD effects (rotation of the PSP's with frequency invariant DGD, i.e., without PCD).

Another illustration of this effect is given in Fig. D.18. Here we display false color pictures of the DOP. The coordinates on the graphs correspond to the angles of the wave plates in a polarization controller consisting of two successive quarter wave plates. This PC is located between source and compensator DGD elements. The source DGD was fixed to 50 ps for all pictures displayed, whereas the compensator DGD was adjusted from 0 to 100 ps from panel (a) through (e). The input polarization into the source DGD element was aligned for equal power in the PSP's. The scanning of the two quarter wave plates allows for an arbitrary (static) transformation of any SOP into any other. We can see that the DOP without compensation is degraded by the source DGD. For the case where $\tau_C = \tau_F$ (Panel (c)) the DOP does reach its maximum. For $\tau_C \neq \tau_F$, however, the DOP does not reach the same maximum value, even though in the displayed graphs all possible SOP transformations are sampled. This is an indication that it is an intrinsic property of the system and not its operation mode that prevents perfect mitigation of the PMD impairments for this case.

Despite the shortcomings for small source DGD's mentioned above the compensator increases the tolerable first order DGD for higher source DGD's (by up to the compensator DGD).

Polarization control In our experiments we used the Agere polarization controller 2722C. It consists of sections of Lithium-Niobate crystals that can be used as five independent quarter-wave plates. Two successive quarter-wave plates can be operated at identical rotation angles to form a half-wave plate.

The simplest configuration of the polarization controller which allows the rotation of any input SOP to any output SOP is a series of two quarter wave plates (QQ). Another configuration that is commonly used in experimental setups is a succession of a quarter, a half and another quarter wave plate (QHQ) as described in the previous section.

Figure D.19 compares the performance of the compensator for those two configurations. Part (a) shows the configuration QQ, whereas in part (b) configuration QHQ was used. For both graphs the DOP was used as a sensor signal and the measurement time for the BER was one minute. The compensator DGD was set to 25 ps for the compensated case. The performance of the feedback system critically depends on the initial condition of the

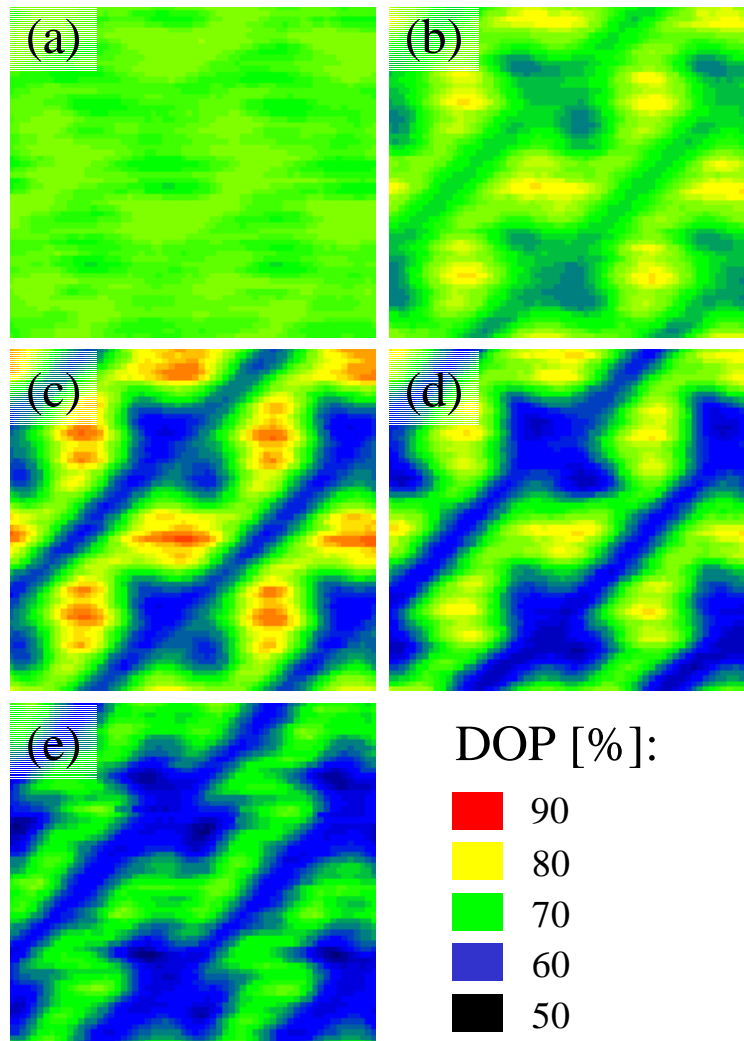


Figure D.18: DOP scans for various ratios of compensating to source DGD. The ratios are (a) 0, (b) 0.5, (c) 1, (d) 1.5 and (e) 2. The scans are over a full rotation over each of the two quarter-wave plates.

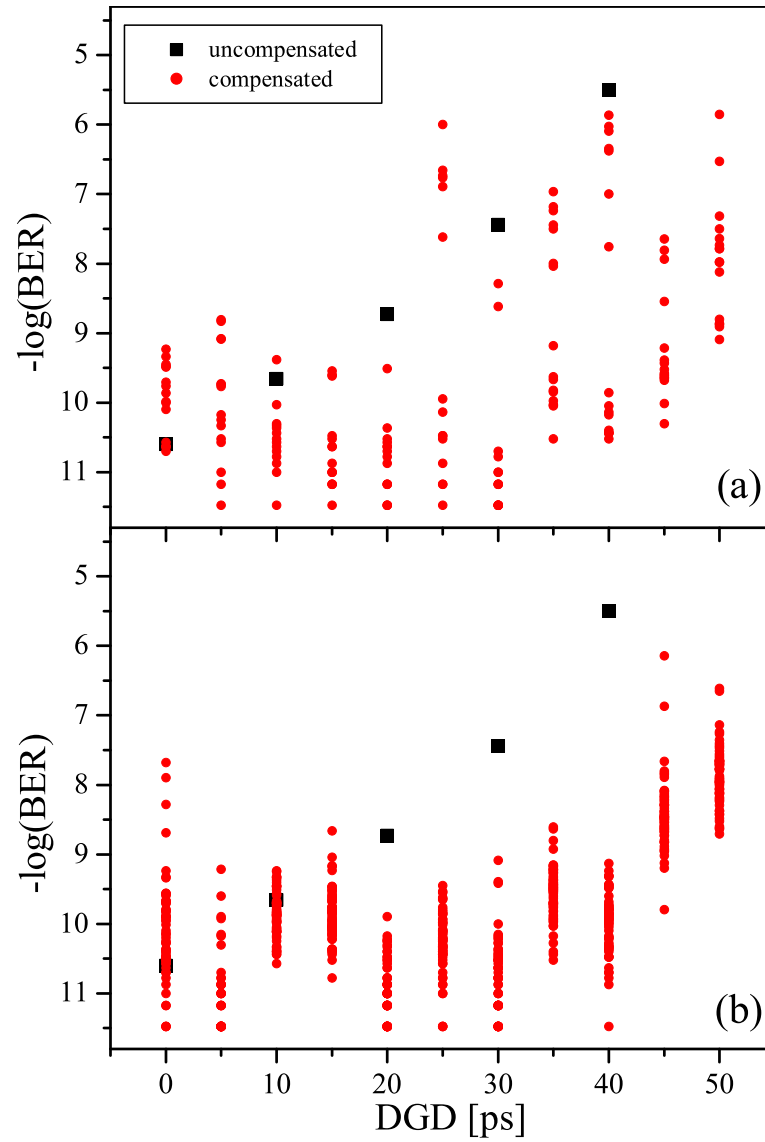


Figure D.19: Comparison between different polarization controller parameterizations. Part (a) shows the compensator performance with a quarter/quarter wave plate configuration. Part (b) uses a quarter/half/quarter wave plate configuration with independent rotation angles. Data for four initial conditions of each wave plate were acquired.

polarization controller at the time when the loop is activated. Therefore the experimental sequence for each value of the source DGD was repeated several times with different initial settings of the polarization controller. For each wave plate four different starting angles were chosen in Fig. D.19.

There is a clear difference in performance between those two operating modes. The configuration QQ in part (a) shows a much bigger scatter of the BER measurements for different initial conditions of the polarization controller. For many initial conditions the BER in the compensated case is close to or even exceeds the uncompensated value. This is especially apparent and important for large values of the source DGD. For the QHQ configuration in part (b) the compensation for larger source DGD's yields BER values that are consistently lower than the uncompensated value. The reason for this difference in performance lies in the way the polarization controller can dynamically adjust its rotation properties. This property depends on the PC configuration and its impact is described in more detail below.

Error signals In this section we compare the compensator performance using different error signals. The two signals described in Sec. D.4 are the degree of polarization (DOP) and components of the electrical spectrum.

Figures D.20 through D.22 compare the performance between the DOP and the spectral probe feedback method. Each run was repeated with each feedback signal and otherwise identical starting conditions. Again a large range of initial conditions were tested. Figure D.20 shows the results for the 3-parameter QHQ configuration with a compensator DGD of 25 ps. Figs. D.21 and D.22 show the case for 50 ps, where in the latter figure an even higher degree of redundancy (all 5 quarter wave plates in series) was used.

Several features of these results are confirming our previous observations. In accordance with these findings, the best performance is obtained if the source DGD is equal to the compensating DGD. Also it is evident that there is a degradation of the system as compared to the uncompensated case for small values of the source DGD. For the case of the 5-parameter configuration (QQQQQ) there is a slight improvement in the performance as compared to the 3-parameter (QHQ) configuration.

The most important information about these data, however, is the comparison of the feedback methods. It is apparent that the compensating performance using the electrical spectrum probe as an error signal is superior in most instances. In general the BER values

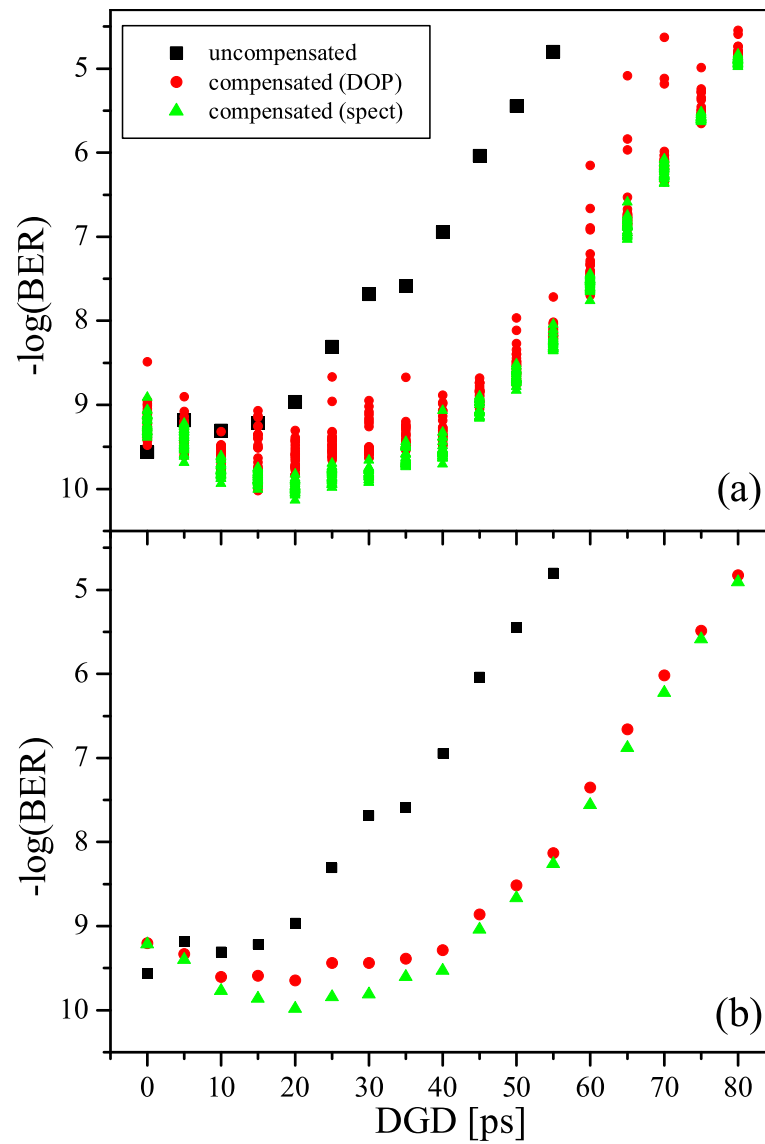


Figure D.20: Performance comparison for DOP and electrical spectrum feedback for a 3-parameter (QHQ) PC configuration and a compensator DGD of 25 ps. Part (a) shows the data for all initial conditions, part (b) shows the averaged result.

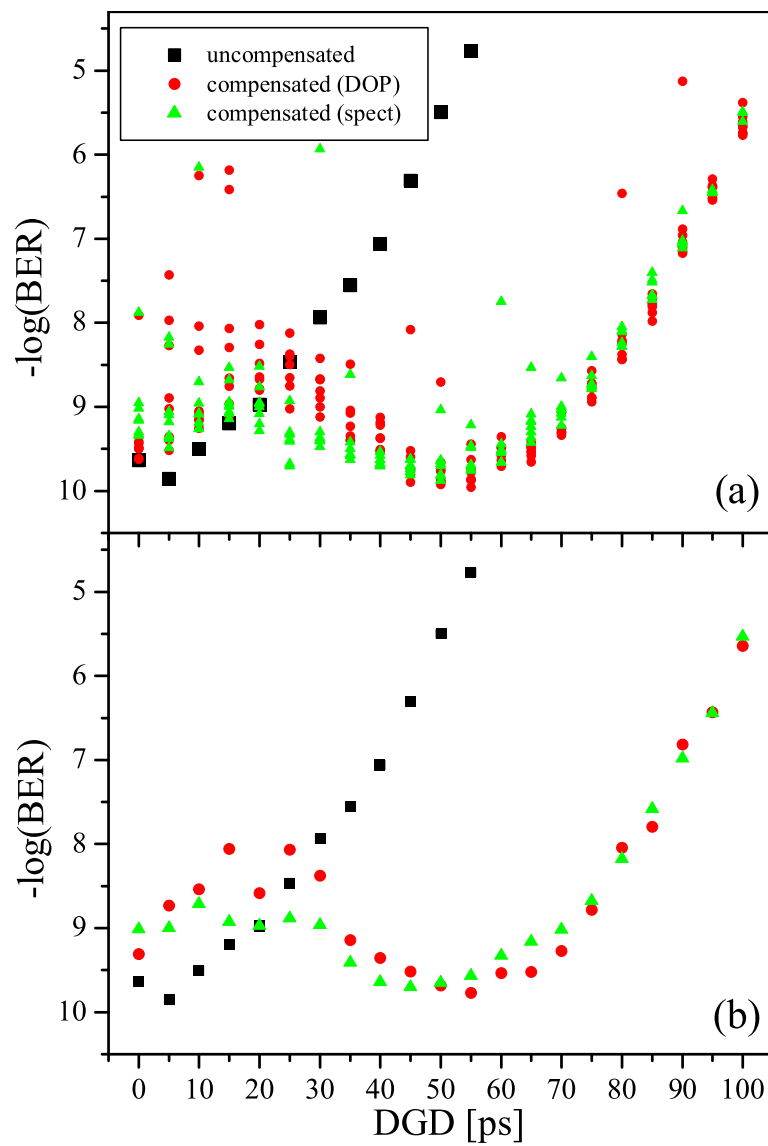


Figure D.21: Performance comparison for DOP and electrical spectrum feedback for a 3-parameter (QHQ) PC configuration and a compensator DGD of 50 ps. Part (a) shows the data for all initial conditions, part (b) shows the averaged result.

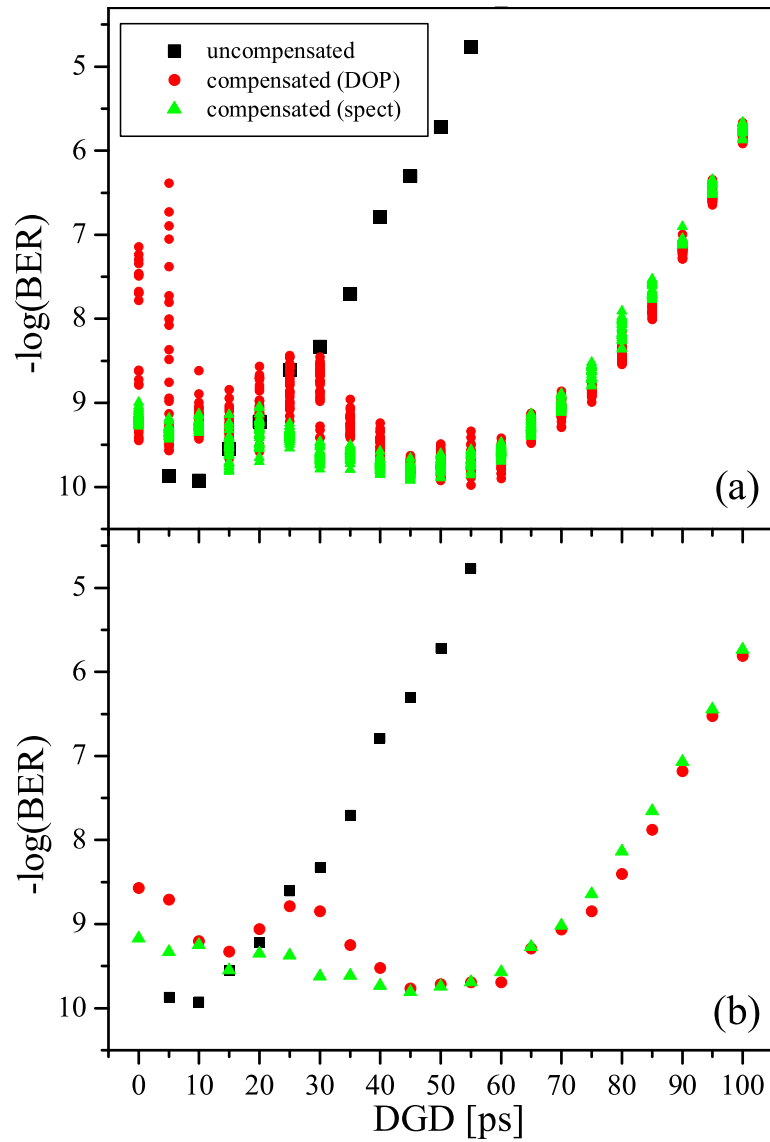


Figure D.22: Performance comparison for DOP and electrical spectrum feedback for a 5-parameter (QQQQQ) PC configuration and a compensator DGD of 50 ps. Part (a) shows the data for all initial conditions, part (b) shows the averaged result.

using this method are not only lower, but also their deviation from the mean is smaller. Please note that for averaging in part (b) of each figure the displayed logarithmic value was used. This performance difference is especially pronounced for source DGD's that are on the order or smaller than the compensator DGD.

D.4.5 Analysis and discussion

Error signals performance comparison

Simplified model investigation Modelling and numerical simulations can provide understanding of the underlying mechanisms at play in the compensator. From such an analysis new experiments can subsequently be devised in order to test previous interpretations and understanding.

The primary purpose of an adaptive system is to find the optimal value of an unknown parameter. In our case this parameter is the value of a vector of PC control parameters $\Theta^* = (\theta_1^*, \dots, \theta_n^*)$. The optimization is performed according to an observed quantity related to the performance of the overall system. Starting from a initial condition it is updated according to an adaptive algorithm referred to as a feedback method in the previous sections. As for every adaptive system a set of questions has to be answered in order to determine whether it is solving the problem it is being designed for.

- So the How well is the parameter, which is defined by a maximum of the quantity under observation (DOP or probed power spectrum components), tied to the system performance? Experimental elements of answer were provided in Sec. D.4.4. Yet the combination of first and second order PMD in the complete system does not allow us to state a clear *a priori* answer.
- Does the system necessarily converge to the target parameter in stationary conditions?
- Only when the answer to the previous question is known to be affirmative can one explore the real efficiency of the adaptive system by evaluating its rate of convergence in stationary conditions. The last thing that would need to be characterized is the ability of the system to track variations of the parameter when the PMD source changes with time and derive the best tuning strategy.

Several decisions were made regarding the structure of the compensator related to its complexity and feasibility with the current technology. Despite having chosen the simplest

compensator setup, manageable closed-form solutions that would allow us to definitely answer the first question above could not be found. Given these constraints we still have to choose the quantity to be used for optimization. Our primary purpose here is to determine in specific cases which of the two simply available quantities is the best one to use in order to get an adaptive system that improves the optical data transmission reliability.

Our basis for analysis assumes that the source PMD is purely first-order and the compensator provides a fixed amount of first order PMD. Without losing generality the configuration of the PC is chosen to be QHQ with ϵ fixed and equal to 0 (the extremal quarter-wave plates move together). This is one of the special cases for the QHQ operation as explained in Section D.4.2. Without loss of generality the PSP's of the source and the compensator are chosen to be aligned with the laboratory reference frame. Any relative rotation of the two PSP's can be lumped into the polarization controller. Finally the input state of polarization is assumed to be so that equal power appears in each PSP of the PMD source which corresponds to a worst case scenario for the transmission system if there is no PMD compensator. This defines an infinite number of SOP's (a great circle on the Poincaré sphere). So we will choose a specific one. If the PMD source PSP's define a direct orthonormal basis $(\vec{e}_1, \vec{e}_2, \vec{e}_3)$, the PSP's in Stokes space are \vec{e}_1 and $-\vec{e}_1$ and we fix the input SOP to \vec{e}_2 . Like every model the one used for the present analysis is a simplification of the real system operation but it is supposed to capture all relevant aspects.

In the subsequent numerical evaluations and simulations the bit rate D_b is equal to 40 Gb/s corresponding to a bit period of $T = 25$ ps, the source DGD, τ_f , is equal to $0.25T$ and the compensator DGD, τ_c , is equal to $0.5T$.

The following figures are organized in such a way that a sub-figure (a) shows a level plot of the quantity under discussion depending on the control parameters α and $\tilde{\gamma}_0 = \gamma - \alpha$. If we consider the set of all PC actions when those two parameters vary between 0 and π , firstly the mapping of $]0, \pi[\times]0, \pi[$ on this set is one-to-one and secondly for almost all given couple input SOP-output SOP there is a unique such action that maps the first one onto the other. If we now consider a fixed reference vector on the Poincaré sphere, \vec{e}_1 for instance, applying each action (rotation) on this vector will give another vector on the sphere and any vector of the sphere can be thus generated. We consequently see that the natural structure of such a set of rotations is that of a sphere. This property is intrinsic as opposed to the parameterization itself that is not. Any injective smooth function on $]0, \pi[\times]0, \pi[$ would generate a pair of parameters that could be also used as control parameters. We will call

intrinsic any property of the system that is true when using the spherical representation for the different values of the PC rotation. Sub-figures (b) and (c) will be showing two views of the sphere. Sub-figure (b) makes the unit vectors \vec{e}_1 , \vec{e}_3 and $-\vec{e}_2$ visible on the surface of the sphere. Whereas sub-figure (c) makes the unit vectors $-\vec{e}_1$, $-\vec{e}_2$ and \vec{e}_3 visible on the surface of the sphere.

In order to easily interpret the results summarized in the sphere representation we have to recall that we assumed that the fast PSP's of the source and the compensator are both equal to \vec{e}_1 . In this case, each point of the sphere is a unit vector \vec{p} that is the result of the action of the PC on the source fast PSP. The point indexed by the tip of \vec{p} is colored according to the values of the quantity being displayed and a predefined color map. In our case the relative position of \vec{p} , the source PSP after the action of the PC, and \vec{e}_1 which is also the compensator fast PSP is obviously central in describing the operation of the system. For instance when $\vec{p} = \vec{e}_1$ the DGD of the system is the sum of the source and compensator DGD and when $\vec{p} = -\vec{e}_1$ it is the difference. In any interpretation based on the sphere representation we also have to remember that in our model the input SOP is equal to \vec{e}_2 .

The BER is the measure of a communication system reliability. It can be evaluated experimentally with more or less ease and speed depending on operating conditions. A closed-form expression for the BER can only be derived in simple and basic cases and simulations for low BER values appear very unrealistic in terms of simulation time and computation power. Yet the partly heuristic formalism introduced earlier can be useful in this instance.

If we note $\vec{\tau}_f$ the PMD vector of the source, $\vec{\tau}_c$ the PMD vector of the compensator, $\vec{\tau}_0$ the value of the complete system first-order PMD vector at the optical carrier frequency we have

$$\vec{\tau}_0 = \vec{\tau}_c + R\vec{\tau}_f,$$

where R is the PC rotation in Stokes space. If we note $\vec{\tau}'_0$ the value of the second-order PMD vector at the optical carrier frequency we have

$$\vec{\tau}'_0 = \vec{\tau}_c \times R\vec{\tau}_f.$$

According to Sec. D.2 the system power penalty measure is given by

$$\mathcal{A}\frac{1}{4}|R^{-1}\vec{\tau}_0 \times \vec{S}_{\text{in}}|^2 D_b^2 + \mathcal{B}\frac{1}{4}|\vec{\tau}'_0|^2 D_b^4,$$

where D_b is the bit rate. \mathcal{A} and \mathcal{B} are constants depending on the data format and the receiver structure. Values for those constants are reported on page 188. We chose \mathcal{A} equal to 70 and \mathcal{B} equal to 85 here since the NRZ format is used.

In order to distinguish each contribution as a function of the system configuration defined by its control parameters we represented in Fig. D.23 the normalized first order PMD contribution to the system power penalty measure:

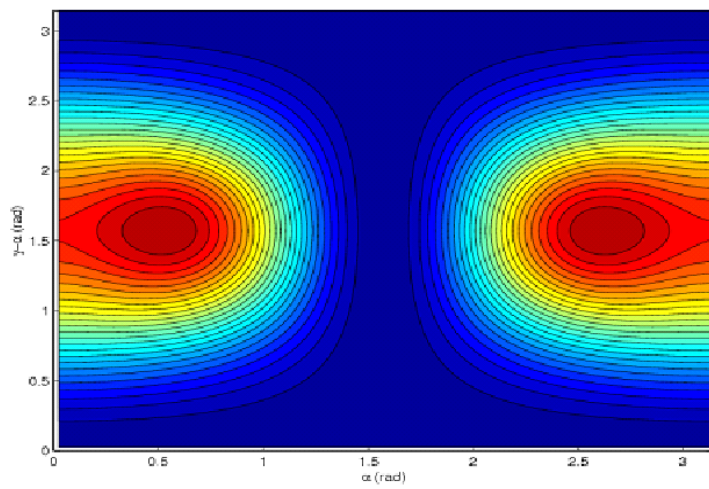
$$\frac{|R^{-1}\vec{\tau}_0 \times \vec{S}_{\text{in}}|^2}{(|\vec{\tau}_c| + |\vec{\tau}_f|)^2},$$

and in Fig. D.24 the normalized second-order PMD contribution to the system power penalty measure:

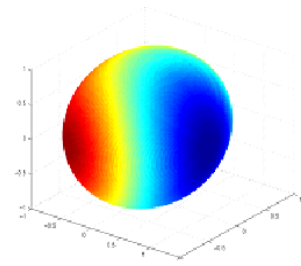
$$\frac{|\vec{\tau}'_0|^2}{(|\vec{\tau}_c| |\vec{\tau}_f|)^2}.$$

On the displayed figures a value of the plotted contribution close to 0 (low penalty, high performance) is represented in red and a value close to 1 (high penalty, low performance) is represented in blue with intermediate values associated with intermediate colors. This is so that in every figure relative to this paragraph a higher system performance is associated to a dark red color and a lower one with a dark blue color with obvious variations in between. Using the values $\mathcal{A} = 70$ and $\mathcal{B} = 85$ we plotted the system power penalty measure in Fig. D.25.

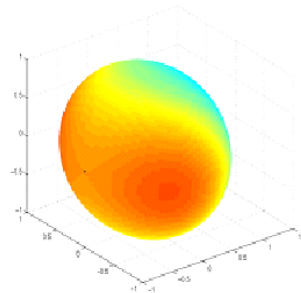
Figure D.23 illustrates something we already knew when the compensator DGD is bigger than the source DGD. The first-order PMD contribution is minimized when the sum of the source and compensator PMD vectors is aligned with the input SOP (equal to \vec{e}_2 here). That is to say when we make the input SOP equal to one of the PSP's of the complete system. We can note the existence of two ‘‘symmetrical’’ global optimal points with a saddle-point configuration in between when the source and compensator PMD vectors are pointing in opposite directions (which would be the optimal configuration if the source DGD were greater than the compensator DGD). Figure D.24 illustrates the fact that the concatenation of two first-order PMD systems can generate second-order PMD with detrimental effects on the system performance. The second-order PMD contribution to the system performance



(a)

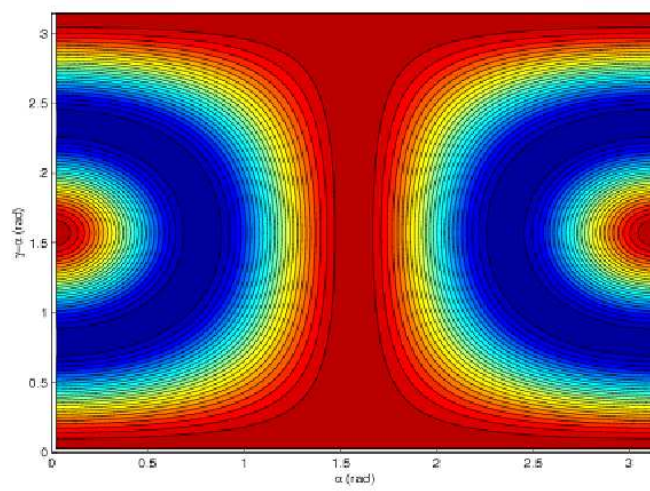


(b)

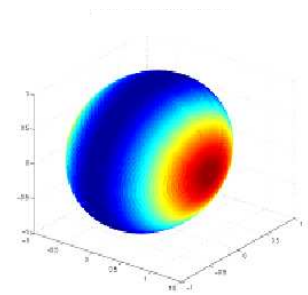


(c)

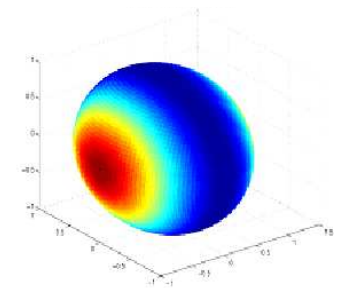
Figure D.23: Normalized contribution of 1st-order PMD to the system power penalty for $\tau_f/T = 0.25$ and $\tau_c/T = 0.5$. Dark red is associated with the value 0 and dark blue with the value 1.



(a)



(b)



(c)

Figure D.24: Normalized contribution of 2nd-order PMD to the system power penalty for $\tau_f/T = 0.25$ and $\tau_c/T = 0.5$. Dark red is associated with the value 0 and dark blue with the value 1.

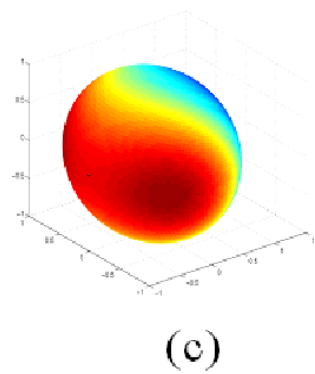
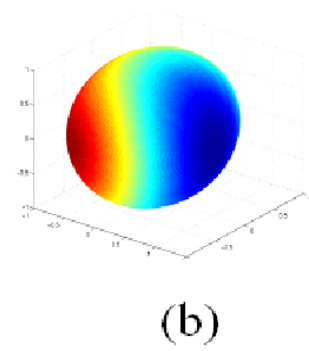
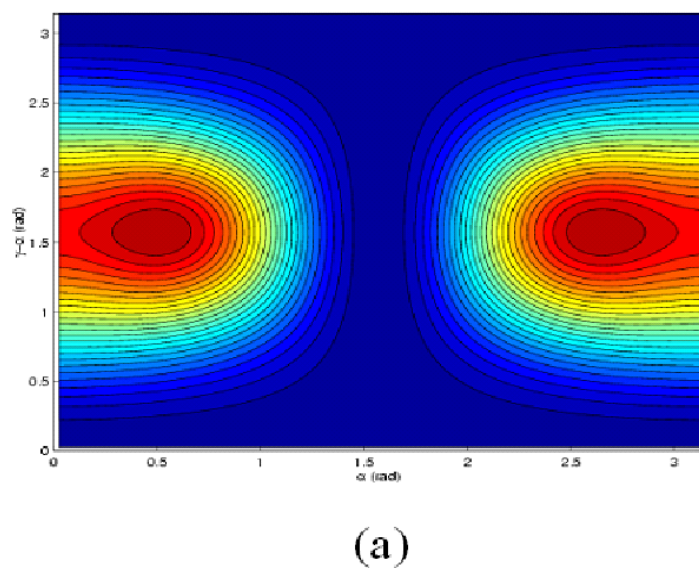


Figure D.25: System performance measure for $D_b = 1/T = 40$ Gb/s, $\mathcal{A} = 70$, $\mathcal{B} = 85$, and for $\tau_f/T = 0.25$ and $\tau_c/T = 0.5$

degradation is the highest when the source and compensator PMD vectors are orthogonal. Figure D.25 summarizes the fact that optimal points of operation are in our case slightly different from the ones defined by minimizing the first-order PMD contribution alone. The overall system performance measure depends on the coefficients \mathcal{A} and \mathcal{B} and the bit-rate D_b . The previous conclusion would become more obvious at higher bit-rates and possibly other OOK (on-off keying) formats such as RZ, whereas it should become negligible at lower bit rates given the relative weighting factor between the two effects scaling with D_b^2 .

A closed form expression of the DOP (not presented in this dissertation) can be found for our system model. Using this expression the DOP values can be computed in a very efficient way and displayed as shown in Fig. D.26. In general, values of the DOP can vary

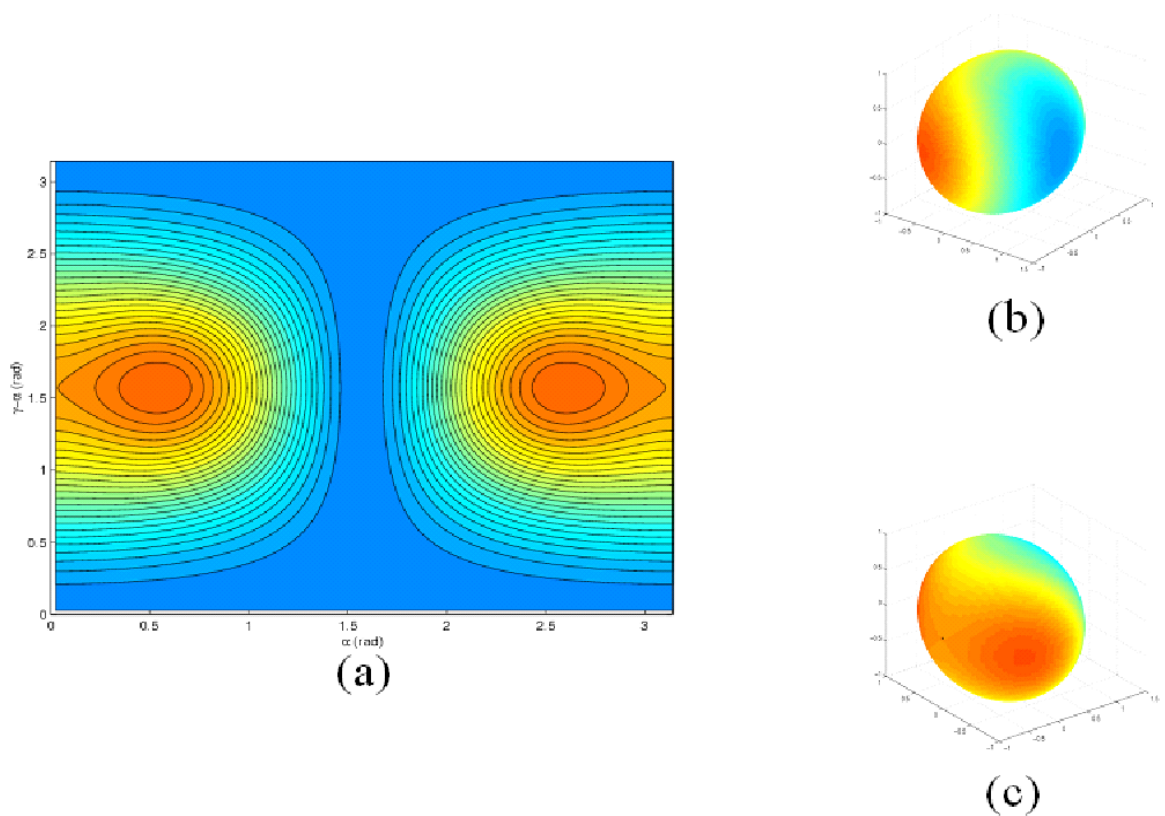


Figure D.26: Degree of polarization for different PC configurations for $\tau_f/T = 0.25$ and $\tau_c/T = 0.5$.

between 0.5 (fully depolarized optical pulse stream) and 1. Furthermore if the simple first-order PMD model for the system operation were fully valid the DOP should reach two global optima where its value is equal to 1 and located exactly where the optimal points relative to the first-order PMD contribution are. This is obviously not the case here as second-order PMD comes into play and partially depolarizes the bit stream when the source and compensator PMD vectors are not aligned. It can be noted that the DOP maxima are still close to the points minimizing the first-order PMD contribution. Observation of the eye diagram when the system has reached such an optimum should consequently bear almost no sign of first-order PMD. But effects of second-order PMD such as overshoots (filtered by the electrical receiver filter) should be apparent as described in Sec. D.4.2.

Instead of finding a closed-form expression of the value of the power spectrum of the received electrical bit stream signal at a specified frequency⁸ we used the models developed in Chapter 2 to build a simulation platform for the experimental setup using spectral probing where the frequency of interest is $D_b/2$, i.e., 20 GHz in our case. Results are shown in Fig. D.27 where the color map is defined from the minimum simulated value (dark blue) of the spectral component to its maximum simulated value (dark red) over the configuration space. One of the main observations here is the loss of the symmetry that was present in the case of the DOP. There is now a global maximum and local maximum each located near one of the optimal points determined by the system performance measure. The cause of such an observation is clearly the effects of second-order PMD generated by the system on the signal spectrum.

The question is now to compare the locations of the optimal points according to the two different criteria (DOP and electrical spectrum component) with the system performance measure (power penalty) serving as a reference. This is shown in Fig. D.28 where the system performance measure levels are represented over the control parameters configuration space. The symbol + indicates the position of the optima of the system performance measure, the symbol \star indicates the position of the DOP maxima and the symbol \circ indicates the position of the spectral component maxima.

Whichever observed quantity is used (DOP or probed spectrum) two main convergence domains can be delimited. One domain actually leads to the same optimal point for the DOP and probed spectrum cases. Yet the other domain would actually bring the system

⁸Second-order PMD is complicated to handle analytically since it appears as a non-linear phenomenon after conversion of the signal from the optical to the electrical domain.

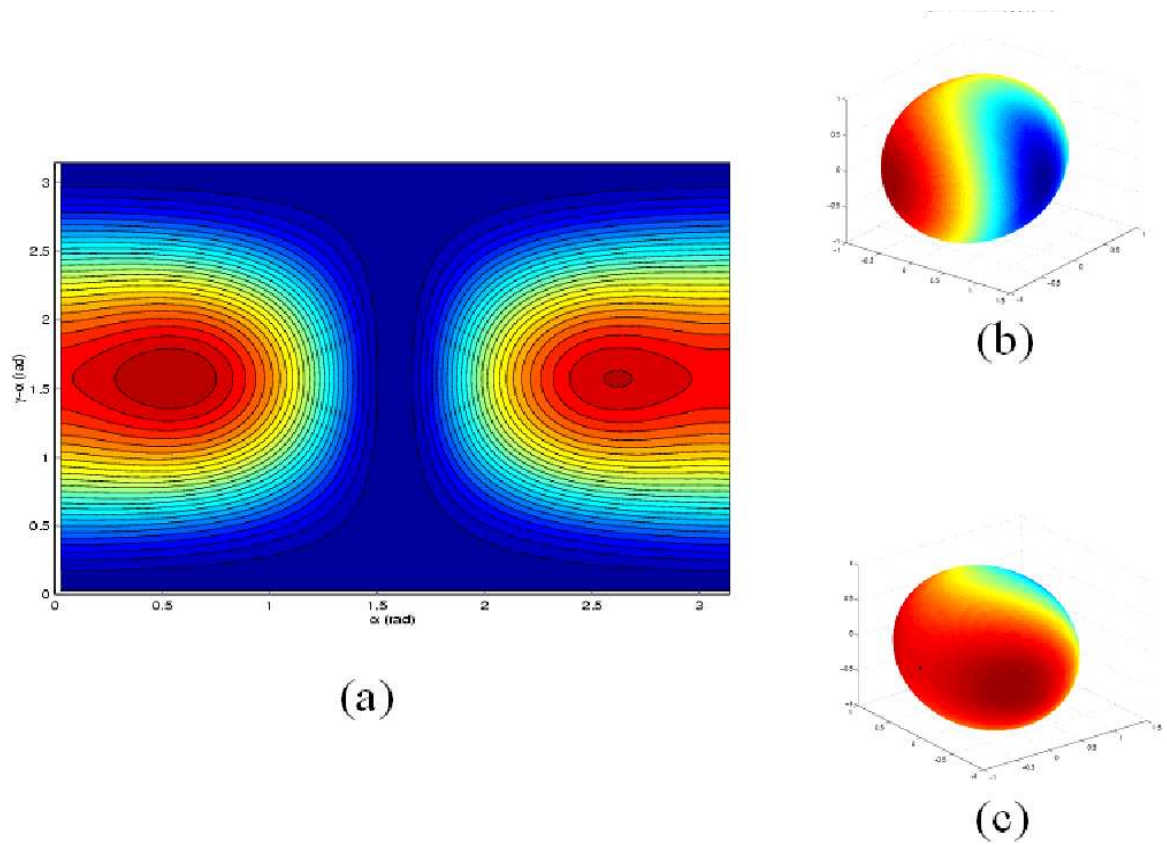


Figure D.27: Probed spectrum component at 20 GHz for different PC configurations for $D_b = 40$ Gb/s, $\tau_f/T = 0.25$ and $\tau_c/T = 0.5$.

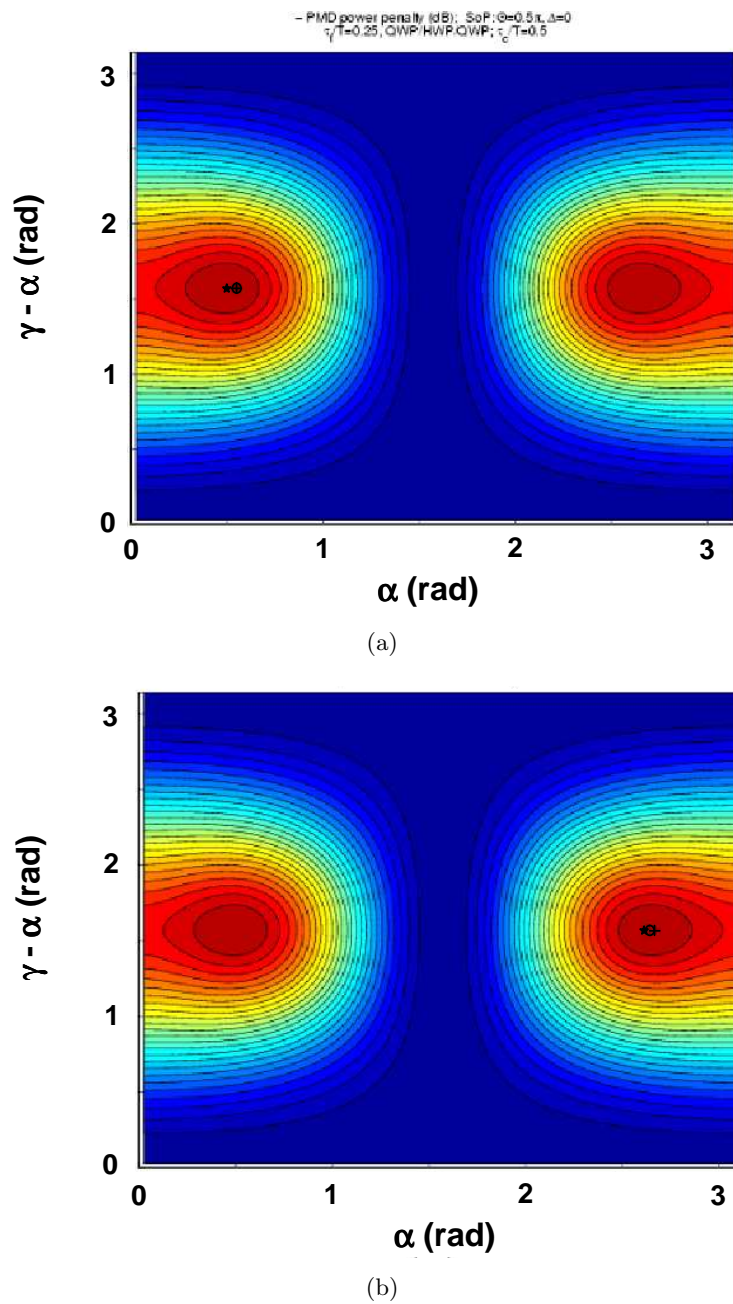
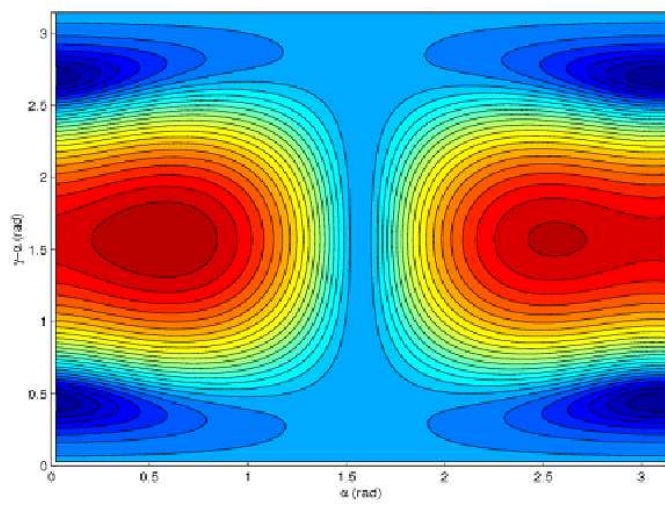


Figure D.28: Comparison of the optimal points defined by the system performance measure (+), the DOP (\star) and the probed spectral component (o) in the proximity of one optimum (a), and the other (b).

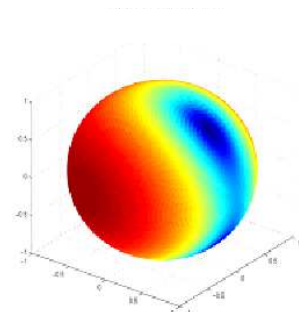
after convergence to different optima depending on whether the DOP or probed spectrum is used. As a matter of fact it appears that the probed spectrum strategy would perform better. These conclusions could be validated by considering second-order PMD effects in the eye diagrams after the system convergence using the DOP and the probed spectrum respectively. For the case considered here the analysis seems to show superiority of the probed spectrum strategy over the DOP. This is interesting since this is actually the solution that would be easier and cheaper to implement in an integrated way including electrical circuits for detection and control.

In accordance with previous observations in the literature it was noted in Sec. D.4.2 that when variable first-order PMD is introduced in the line, a system trying to maximize the power of a specific spectral component of the electrical signal can end up actually increasing the amount of DGD thus further degrading the transmission reliability. Fig. D.29 shows the power for the component of the received electrical signal at a frequency of 20 GHz for a NRZ bit stream running at 40 Gb/s with a source DGD of 10 ps ($\tau_f/T = 0.4$) and a compensator DGD of 20 ps ($\tau_c/T = 0.8$). As the total DGD of the link can vary between 0.4 and 1.2 times the bit period the problem should be apparent here. It actually is since an initial system configuration close to a minimum for the observed quantity could, in a worst case scenario, “see” a steepest ascent path leading it to \vec{e}_1 where the system performance is actually worse than anywhere else. But this point is not a local maximum and a path orthogonal to the previously followed direction will finally lead the system to one of the previously considered maxima close to a system performance measure maximum. This is an intrinsic property and is valid even if other fixed and continuous operations (fixed rotations, different parameterization of the QHQ, ...) are added to our simple model. Yet, as is apparent in Fig. D.29(a), the parameterization is such in this case that the system could end-up spending a lot of time finding its way in a “flat” region (the vicinity of a critical point) where the system performance is actually very poor.

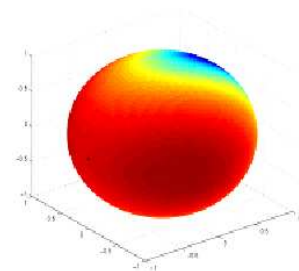
Second-order PMD contribution and eye diagrams at 40 Gb/s As described in Sec. D.4.4 we observed a better performance of the compensator when we used the electrical spectral component as a feedback signal. In Sec. D.4.5 we then argued that this superiority stems from an asymmetry of the spectral component over the system configuration space, which happens to come with a better match of its optimum with the optimum of the performance measure (power penalty minimum).



(a)



(b)



(c)

Figure D.29: Probed spectrum component at 20 GHz for different PC configurations for $D_b = 40$ Gb/s, $\tau_f/T = 0.4$ and $\tau_c/T = 0.8$.

In an attempt to validate this conclusion we investigated the second order contribution to the power penalty. As can be inferred from Figs. D.24 and D.25, this contribution is very sensitive in the region of the before-mentioned optima. Unfortunately we can not easily single out this second order contribution to the degradation in the experiment. However, one way to determine the relative importance of second order effects is to look at the electrical eye diagram after the receiver. As was pointed out in Sec. 2.3.5, rotation of the PMD vector with frequency leads to a characteristic overshoot in the rising and falling edges of the pulse. In order to maximize the visibility of the effect we performed this task at 40 Gb/s. The increased bandwidth at higher bit rates increases the relative contribution of higher order PMD to the power penalty and in this case the eye diagram degradation.

D.4.6 Validation

Figure D.30 shows three electrical eye diagrams at 40 Gb/s, where the source DGD was set to 10 ps and the compensator DGD to 20 ps. All eye diagrams were acquired during operation of the feedback loop. In part (a) the DOP was used to generate the feedback signal. During acquisition of the diagram the DOP was therefore at a local optimum. In part (b) and (c) the electrical spectrum component at 20 GHz was maximized. In these cases the feedback loop converged to two different maxima, distinguishable by the opposite shape of the overshoot feature. In addition to the different shape, the magnitude of the overshoot is slightly different for cases (b) and (c). This seems to validate the finding of the asymmetry of the spectral component resulting from higher order PMD effects. For the case of the DOP feedback signal (case (a)), no such asymmetry was apparent.

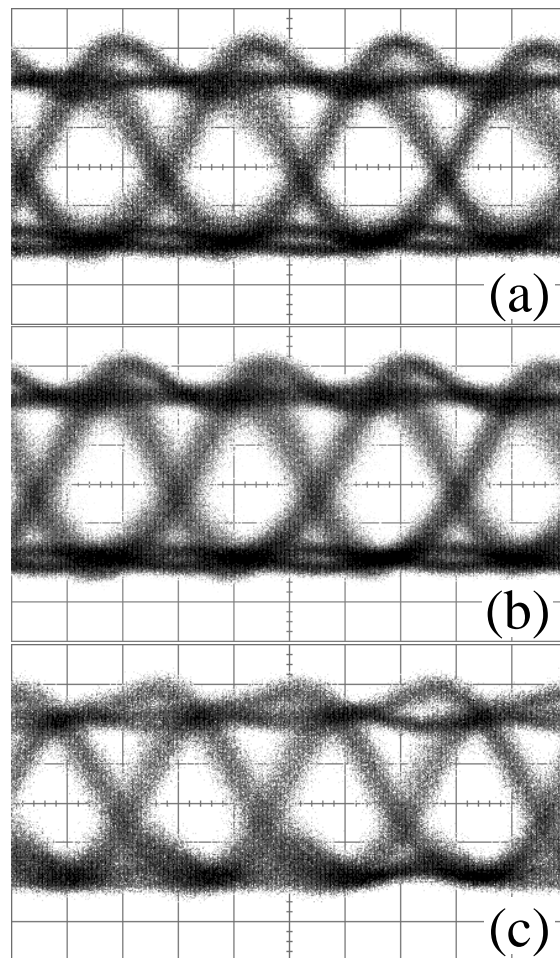


Figure D.30: Eye diagrams for maximized error signal for a 40 Gb/s NRZ signal. The source DGD was set to 10 ps and the compensator DGD was chosen to be 20 ps. Part (a) shows the case for a DOP error signal. Parts (b) and (c) show two different positions of the polarization controller leading to an asymmetric maximum.

Appendix E

Version française réduite

E.1 Introduction

De nombreuses applications telles que les communications sans fil et les communications sur la paire de cuivre ont bénéficié des avancées effectuées dans le domaines du traitement du signal numérique. Les communications optiques, quant à elles, utilisent principalement des modulations binaires rendant l'implémentation de solutions de traitement du signal et de l'information très difficiles à des vitesses de modulation dépassant les 10 Gb/s. Les travaux présentés s'intéressent à l'application de techniques de modulation et de traitement du signal numérique aux communications optiques. Ils se concentrent sur la conception d'un système de communication optique sur courte distance à 40Gb/s comme représenté à la figure E.1.

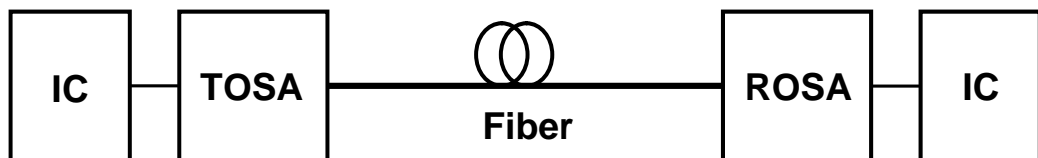


Figure E.1: Connection optique simple. IC: circuits intégrés; TOSA: module optoélectronique transmetteur; ROSA: module optoélectronique récepteur.

La section E.2 présente des modèles optiques simplifiés pour des fibre mono-modes utilisées dans des conditions d'optique linéaire. La section E.3 décrit une modulation combinant multiplexage de sous-porteuses et codage de symboles sur plusieurs niveaux afin d'obtenir une efficacité spectrale élevée requise par les composants et les technologies du système qui doit combiner haut débit et très bas coûts. La section E.4 définit complètement et modélise en détail la chaîne de transmission optoélectronique. Un modèle simplifié y est présenté permettant d'estimer la capacité du canal. La section E.5 rassemble modèles et concepts introduits pour la spécification d'un système basé sur des fonctions analogiques de modulation/démodulation implémentées en technologie CMOS. Une puce test et un prototype du système sont présentés.

E.2 Modélisation des fibres optiques

E.2.1 Introduction

Dans les communications optiques, un signal électrique porteur d'information est converti en signal optique qui se propage dans une fibre de silice pour être ensuite reconverti en signal électrique. Si la fibre utilisée est une fibre mono-mode, le signal optique peut subir un certain nombre de distorsions dues aux propriétés du matériau dont la fibre est constituée et à sa géométrie. Les effets sur le signal optique se répartissent en deux classes:

- Effets linéaires: atténuation, dispersion chromatique et dispersion des modes de polarisation (polarization-mode dispersion; PMD).
- Effets non-linéaires: diffusion de Brillouin, diffusion de Raman, fluctuations de l'indice de réfraction.

L'impact de tels effets sur le signal dépend essentiellement des conditions d'opération (longueur d'onde, puissance optique en entrée, longueur de fibre, conditions de fabrication et environnement de la fibre). Sous certaines conditions, certains de ces effets peuvent être négligés devant d'autres pour donner des modèles simplifiés permettant une compréhension des phénomènes importants et des calculs numériques rapides.

E.2.2 Modèle en régime linéaire

De façon générale, la propagation des signaux optiques dans une fibre se décrit à l'aide d'une équation aux dérivées partielles non-linéaire, l'équation de Shrödinger non-linéaire (non-linéar Shrödinger equation; NLS). Si les effets de polarisation doivent être pris en compte l'équation maîtresse devient l'équation de Shrödinger non-linéaire couplée (coupled non-linéar Shrödinger equation; CNLS).

Pour l'application qui nous intéresse, les effets non-linéaires peuvent être négligés devant les effets linéaires. Et dans ce cas, les effets de transmission dans la fibre peuvent être entièrement décrits par une relation entrée/sortie linéaire. Le champs électrique du signal optique guidé dans la fibre s'écrit

$$\mathbf{E}(\vec{r}, t) = \text{Re} \left(G(x, y) A(z, t) e^{-i\beta_0 z} e^{+i\omega_0 t} \right),$$

où $G(x, y)$ décrit la distribution spatiale de la puissance du mode dans le plan transverse

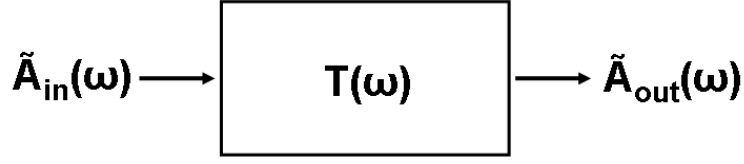


Figure E.2: Modélisation du comportement entrée/sortie linéaire d'une fibre par une matrice de transmission.

à la direction de propagation, et $A(z, t)$ décrit l'évolution de l'enveloppe du signal selon la direction de propagation et dans le temps. Lorsque G est normalisée, $|A(z_0, t_0)|^2$ représente alors la puissance optique traversant la section de fibre située à $z = z_0$ au temps $t = t_0$. $\tilde{A}(z, \omega) = \int A(z, t)e^{-i\omega t}dt$ désigne la transformation de Fourier temporelle du signal optique.

Le champ optique à la sortie de la fibre, $\tilde{A}_{\text{out}}(\omega) = \tilde{A}(L, \omega)$, est lié au champ optique en entrée, $\tilde{A}_{\text{in}}(\omega) = \tilde{A}(0, \omega)$, par la relation linéaire représentée sur la figure E.2

$$\tilde{A}_{\text{out}}(\omega) = T(\omega)\tilde{A}_{\text{in}}(\omega),$$

où T est la matrice de transmission. Elle se décompose en

$$T(\omega) = e^{-(\frac{\alpha}{2} + i\bar{\beta}(\omega))L}M(\omega),$$

où le premier terme, le terme de propagation commune, est une fonction complexe de ω et le second terme $M(\omega)$, la matrice de biréfringence ou de Jones, est une fonction de ω qui prend ses valeurs dans le groupe $SU(2)$. La matrice de transmission T agit séparément sur l'amplitude complexe commune des deux composantes du champ et son état de polarisation (state of polarization; SOP). Le terme de propagation commune rend compte du temps de propagation de groupe du signal optique sur la longueur de la fibre, de la dispersion chromatique et de l'atténuation (α). La matrice de biréfringence M lie l'état de polarisation du champ optique à la sortie à l'état de polarisation à l'entrée et rend compte de la variation du temps de propagation de groupe et de la dispersion chromatique en fonction de l'état de polarisation. Ce dernier point est représenté sur la figure E.3.

Une quantité de grande importance dans l'étude des effets sur les signaux optiques de

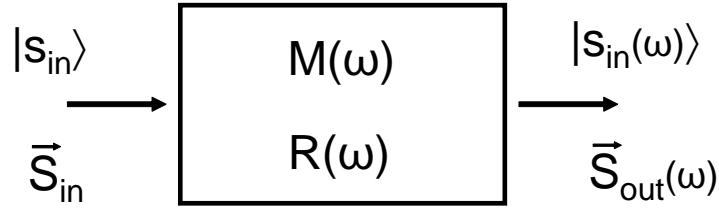


Figure E.3: Illustration de la dépendance fréquentielle du SOP en sortie due à la dépendance fréquentielle de la relation linéaire entrée/sortie.

la birefringence de fibre est le vecteur de PMD, $\vec{\tau}$, défini par

$$i \frac{\partial M}{\partial \omega} M^{-1} = \frac{1}{2} (\vec{\tau} \cdot \vec{\sigma}),$$

où $\vec{\sigma}$ est le “vecteur” colonne formé des matrices de Pauli $\sigma_1 = \begin{pmatrix} 1 & 0 \\ 0 & -1 \end{pmatrix}$, $\sigma_2 = \begin{pmatrix} 0 & 1 \\ 1 & 0 \end{pmatrix}$

et $\sigma_3 = \begin{pmatrix} 0 & -i \\ i & 0 \end{pmatrix}$, et où \cdot désigne un produit scalaire formel. Si $\vec{\tau}$ est non-nul, on définit alors un couple d'états de polarisation orthogonaux, les états principaux de polarisation (principal states of polarization; PSP), représentés par des points \vec{p} , état principal de polarisation lent, and $\vec{q} = -\vec{p}$, état principal de polarisation rapide, situés aux antipodes de la sphère de Poincaré où

$$\vec{p} = \frac{\vec{\tau}}{|\vec{\tau}|}.$$

La longueur du vecteur PMD, $\tau = |\vec{\tau}|$, est appelé temps de propagation de groupe différentiel (differential group delay; DGD).

Les propriétés importantes sont les suivantes. Si l'on imagine que l'on envoie une impulsion optique polarisée dans la fibre, tout d'abord avec un état de polarisation égal à l'état principal de polarisation rapide, puis avec un état de polarisation égal à l'état principal de polarisation lent, on constate une différence entre les temps de propagation moyens. Cette différence est égale au temps de propagation de groupe différentiel comme illustré en figure E.4.

Les effets de biréfringence des fibres sont essentiellement dus à des imperfections dans la géométrie circulaire ou à des contraintes mécaniques appliquées sur leur longueur. Le détail

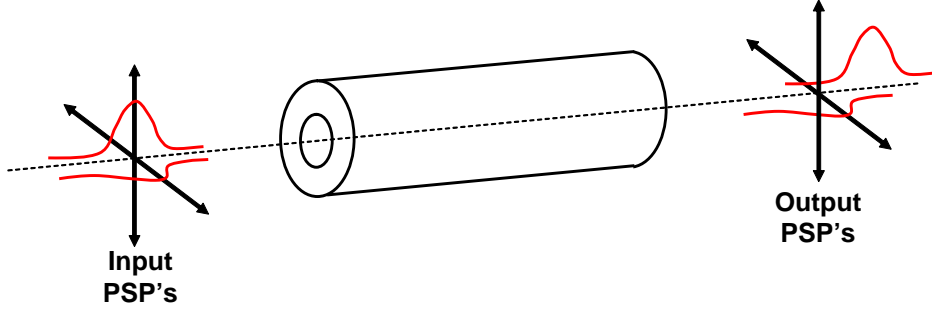


Figure E.4: Etats principaux de polarisation.

de ces effets dépendant de conditions non connues et variables, les effets de biréfringence sont modélisés par des processus aléatoires. Les propriétés aléatoires sont identiques pour une population de fibres homogène obtenues par les mêmes méthodes de fabrication et placées dans des conditions similaires. En particulier, le vecteur PMD et ses variations fréquentielles sont des variables aléatoires dont les lois ont été caractérisées de façon théorique et expérimentale [FP91, FJNK99, FNK00, NJKF00, JNK99]. La table E.1 résume les principaux résultats et permet de noter que toutes les lois sont dépendantes du même facteur d'échelle, $\bar{\tau} = E(\tau)$, le DGD moyen. Un résultat fondamental est la dépendance de la déviation standard (mais aussi de la valeur moyenne) du DGD qui est proportionnelle à la racine carrée de la longueur de fibre L ,

$$\sqrt{E(\bar{\tau}^2)} = D_{pmd}\sqrt{L}.$$

Le facteur de proportionnalité D_{pmd} dépend de la population de fibres considérée.

E.2.3 Modèles simplifiés et prédictions

Du point de vue de la transmission du signal, la modélisation de la dépendance en fréquence de la matrice de transmission T est importante. Pour l'amplitude complexe, cela revient à modéliser le coefficient de propagation $\bar{\beta}(\omega) \approx \beta_1\omega + \frac{1}{2}\beta_2\omega^2$ pour tenir compte de la dispersion chromatique. Pour les degrés de liberté de polarisation, il est naturel de déduire les variations fréquentielles de la matrice de biréfringence à partir du vecteur PMD par la relation

$$i\frac{\partial M}{\partial \omega}M^{-1} = \frac{1}{2}(\vec{\tau} \cdot \vec{\sigma}).$$

X	$p_X(x)$	$E(X)$	$E(X^2)$
τ_i	$\frac{2}{\pi\bar{\tau}} e^{-\frac{1}{\pi}(\frac{2x}{\bar{\tau}})^2}$, Gaussian	0	$\frac{\pi}{8}\bar{\tau}^2 = \sigma^2$
$\tau = \bar{\tau} $	$\frac{8}{\pi^2\bar{\tau}} (\frac{2x}{\bar{\tau}})^2 e^{-\frac{1}{\pi}(\frac{2x}{\bar{\tau}})^2} \mathbf{1}_{x \geq 0}$, Maxwellian	$\bar{\tau}$	$\frac{3\pi}{8}\bar{\tau}^2 = 3\sigma^2$
τ'_i	$\frac{4}{\pi\bar{\tau}^2} \operatorname{sech}(\frac{4x}{\bar{\tau}^2})$, soliton amplitude	0	$(\frac{\pi}{8})^2\bar{\tau}^4 = \sigma^4$
$ \bar{\tau}' $	$\frac{8}{\pi\bar{\tau}^2} \frac{4x}{\bar{\tau}^2} \tanh(\frac{4x}{\bar{\tau}^2}) \operatorname{sech}(\frac{4x}{\bar{\tau}^2}) \mathbf{1}_{x \geq 0}$	$\frac{2G\bar{\tau}^2}{\pi}$ $G \approx 0.915965$	$3(\frac{\pi}{8})^2\bar{\tau}^4 = 3\sigma^4$
$\tau' = \frac{d}{d\omega} \bar{\tau}' $	$\frac{2}{\bar{\tau}^2} \operatorname{sech}^2(\frac{4x}{\bar{\tau}^2})$, soliton intensity	0	$\frac{1}{3}(\frac{\pi}{8})^2\bar{\tau}^4 = \frac{\sigma^4}{3}$

Table E.1: Densité de probabilité de quantités liées à la PMD établies and validées par simulation et expérimentation [FP91, FJNK99, FNK00]

Cette équation différentielle ne se laisse pas intégrer à l'aide de fonctions élémentaires si les variations de $\vec{\tau}$ ne sont pas simples. Des hypothèses simplificatrices peuvent cependant être faites en tenant compte de la largeur spectrale du signal autour de la fréquence de la porteuse optique. C'est sur cette largeur que les variations des quantités ont une importance et peuvent être approchées. Ceci n'est possible que si la largeur considérée reste faible par rapport à l'échelle de fréquence sur laquelle les variations des quantités considérées s'effectuent.

A titre d'exemple, si l'on peut supposer que le vecteur PMD est constant sur la largeur spectrale du signal, $\vec{\tau}(\omega) = \vec{\tau}_0$, l'expression de la matrice de biréfringence se déduit immédiatement:

$$M(\omega) = e^{-i\omega\vec{\tau}_0 \cdot \frac{\vec{\sigma}}{2}} = P_1 \begin{pmatrix} e^{-i\frac{\tau_0}{2}\omega} & 0 \\ 0 & e^{+i\frac{\tau_0}{2}\omega} \end{pmatrix} P_2.$$

Dans cette expression, $\tau_0 = |\vec{\tau}_0|$ est le temps de propagation de groupe différentiel. P_1 et P_2 sont deux matrices de $SU(2)$ constantes reliant le référentiel du laboratoire à ceux définis par la base orthonormal d'états principaux de polarisation, à l'entrée et à la sortie de la fibre respectivement. Le temps de propagation différentiel, τ_0 , suit une loi maxwellienne comme indiqué dans la table E.1.

Ces modèles simplifiés permettent de déduire, qualitativement et quantitativement, la façon dont les impulsions lumineuses utilisées pour la transmission d'information binaire dans la plupart des systèmes de communication optique actuels sont modifiées par la propagation dans la fibre. Il est aussi possible d'évaluer de façon analytique l'impact des effets

de propagation sur la performance du système. Ils fournissent également la base de schémas numériques pour simuler la transmission de signaux dans les fibres optiques mono-modes en régime optique linéaire. Les étapes de calcul sont les suivantes:

- Calculer la transformée de Fourier rapide sur la version convenablement discrétisée du signal optique à l'entrée de la fibre, A_{in} ,
- Appliquer la valeur de matrice de transmission T à chaque fréquence discrète,
- Calculer la transformée de Fourier rapide inverse du résultat afin d'obtenir une version discrétisée du signal optique à la sortie de la fibre, A_{out} .

Le contrôle des paramètres de base des modèles simplifiés permet d'explorer les conditions les plus intéressantes (cas typique, pire cas, etc) et d'explorer les configurations aléatoires possibles de manière efficace.

E.2.4 Conclusions

La modélisation présentée, valable dans un régime optique linéaire, est applicable au système de transmission à courte distance au cœur de cette thèse. Elle fournit des outils très efficaces pour l'étude des systèmes utilisant des modulations de type "on-off keying" (optique binaire). Le présent système se propose d'utiliser d'autres types de modulations présentant des efficacités spectrales plus élevées. Les modèles et schémas numériques présentés forment la base des outils de simulation de ce système.

E.3 Modulations à haute efficacité spectrale

E.3.1 Multiplexage de sous-porteuses

Il sera vu en section E.4.4 qu'un modèle simplifié du canal qui nous intéresse prédit que des efficacités spectrales dépassant 6b/s/Hz peuvent être atteintes sur une bande de fréquence proche de 15 GHz. Les modulations de types "on-off keying" sont alors clairement sous-optimales du point de vue de la capacité du système. Dans les applications optiques à courte distance, l'efficacité spectrale peut être accrue en échange de la réduction de l'efficacité en puissance au travers d'un choix de modulation numérique approprié.

L'utilisation d'un codage de symboles sur plusieurs niveaux est une façon simple d'accroître le débit d'information pour une bande passante fixée. La combinaison d'un multiplexage de sous-porteuses (sub-carrier multiplexing; SCM) et d'un codage de symboles sur plusieurs niveaux permet une réduction supplémentaire de la fréquence de symboles en subdivisant la bande passante disponible en plusieurs sous-bandes radio-fréquence (RF).

La figure E.5 montre une comparaison de l'occupation spectrale du signal porteur d'information pour NRZ et SCM avec QAM-16 sur 16 porteuses RF et un débit binaire de 40 Gb/s. SCM combine à la fois une occupation spectrale réduite et une fréquence de symboles très basse.

Pour le système qui nous intéresse, la fréquence de symboles par canal RF est de 666 Mbaud et les canaux sont séparés par 833 MHz occupant ainsi une bande fréquentielle totale de moins de moins de 14GHz. Les paramètres de modulation choisis sont résumés dans la table E.2.

Espacement des porteuses	833 MHz
Constellation	QAM-16
Fréquence de symbole	666 Mbaud
Fréquence de porteuse maximale	13.32 GHz

Table E.2: Résumé des paramètres de modulation choisis.

Une des limitations de la modulation à multiplexage de sous-porteuses provient de l'espacement des canaux RF et des imperfections dans la réalisation des fonctions analogiques à haute fréquence en technologie de circuit CMOS (filtres de transmission et de réception, mixeurs, génération de porteuses). Ces imperfections se traduisent par une interférence entre canaux linéaire ayant un impact sur le taux d'erreur binaire du système si l'on tente

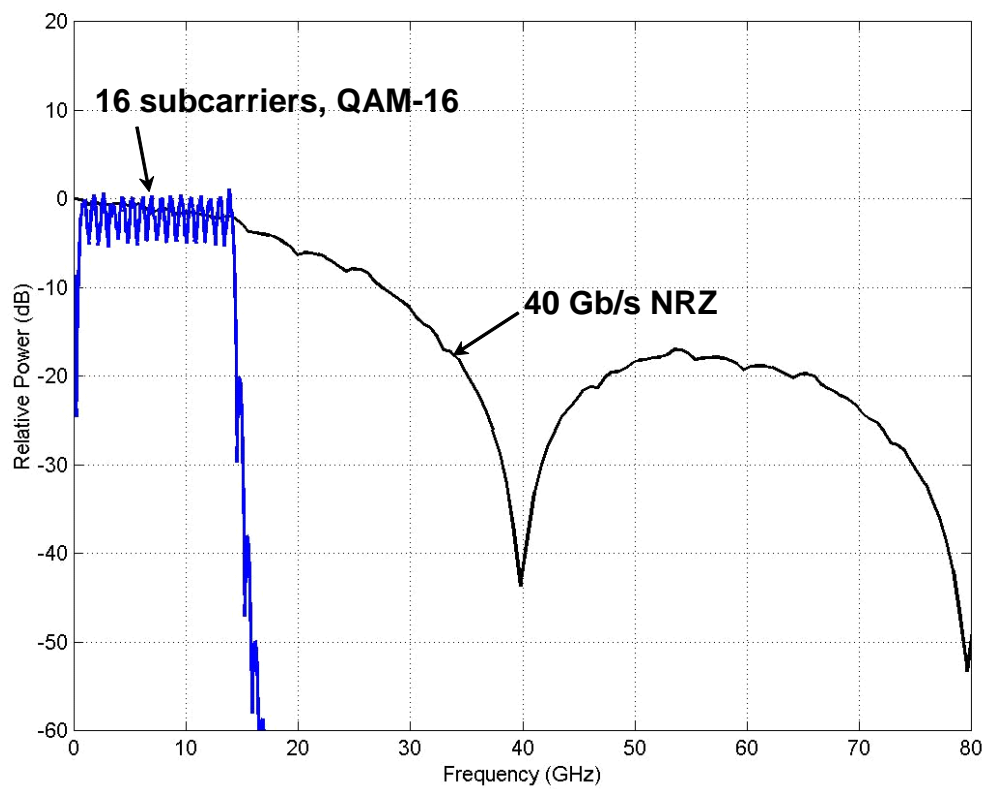


Figure E.5: Comparaison de la densité spectrale de puissance de signaux NRZ et QAM-16 sur 16 porteuses pour un débit binaire de 40 Gb/s.

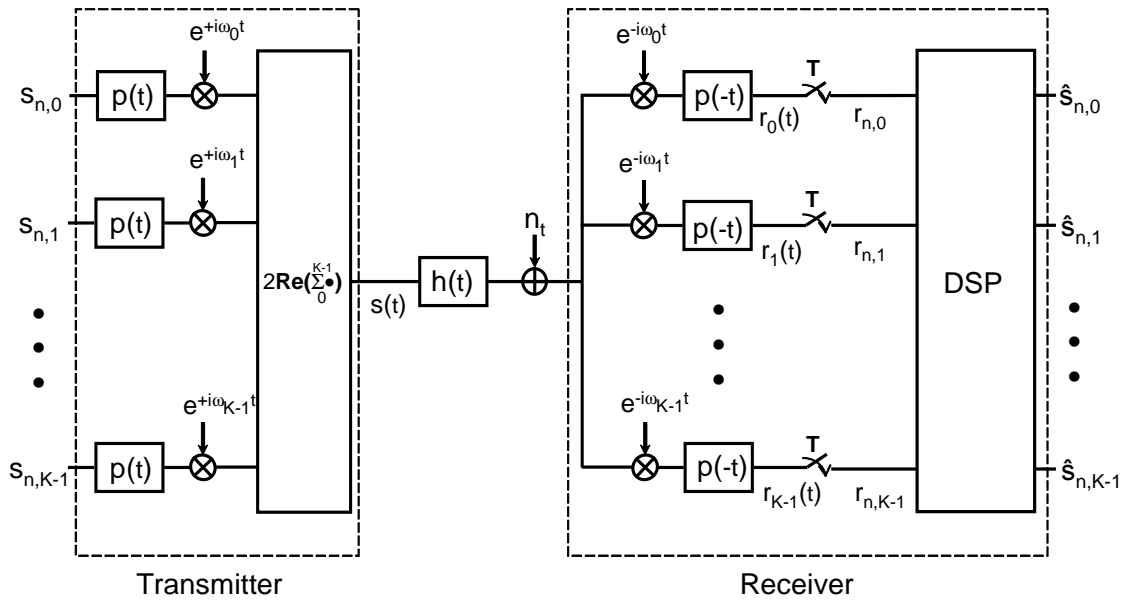


Figure E.6: Système de communication à sous-porteuses multiplexées incluant un bloc DSP en dernier étage du récepteur.

d'atteindre les hautes efficacités spectrales espérées. Ces problèmes peuvent être résolus en imposant des contraintes et spécifications strictes au système et à ses composants. Cependant, il en résulte une augmentation du coût global et des difficultés d'implémentation. La section suivante présente des architectures de traitement du signal numérique qui permettent de contourner ces contraintes tout en préservant simplicité de conception et économie.

E.3.2 Traitement du signal: égaliseur temps-fréquence

La figure E.6 montre une vue complète d'un système de transmission à sous-porteuses multiplexées dans le cas général de K canaux. Le système présenté inclus un étage de traitement du signal numérique intégré au récepteur. Le système est composé de K porteuses situées à des fréquences angulaires $0 < \omega_0 < \omega_1 < \dots < \omega_{K-1}$. L'entrée du transmetteur est formée de K flots de symboles porteurs d'information $(s_{n,0})_n, (s_{n,1})_n, \dots, (s_{n,K-1})_n$ de période commune T . Chaque symbole est pris parmi les points d'une constellation donnée. Pour chaque canal, la chaîne de transmission est composée du même filtre de transmission $p(t)$ and d'un mixeur effectuant l'opération de modulation du signal en bande de base avec la

porteuse correspondante. Les K signaux passe-bandes sont ajoutés pour former le signal $s(t)$ à la sortie du transmetteur. Ce signal est transmis au travers du canal physique, ici modélisé par un système linéaire avec bruit additif. Le signal à la sortie du canal passe à travers K chaînes de démodulation, dont chacune comprend un filtre de réception adapté au filtre de transmission, pour donner K signaux démodulés. La sortie de chacune de ces chaînes de démodulation est échantillonnée à la fréquence de symboles $1/T$ et numérisée pour produire K suites de d'échantillons reçus $(r_{n,0})_n, (r_{n,1})_n, \dots, (r_{n,K-1})_n$. Cette dernière opération est contrôlée par un sous-système de synchronisation (recupération de porteuse et de phase) non représenté ici. Comme indiqué sur la figure E.6, le récepteur peut inclure un bloc de traitement du signal numérique (digital signal processing; DSP) fonctionnant à la fréquence de symboles. Ce bloc traite la suite d'échantillons reçus dans l'ensemble des K canaux pour produire K suite de variables de décision $(\hat{s}_{n,0})_n, (\hat{s}_{n,1})_n, \dots, (\hat{s}_{n,K-1})_n$. Ces variables de décision forment les estimateurs ultimes des symboles transmis $s_{n,k}$ avant d'être présentées à l'étage de décision (comparateurs multi-niveaux pour les dimensions en phase et en quadrature de phase dans le cas d'une constellation QAM).

Les échantillons reçus dans chaque canal au temps discret nT peuvent être arrangés en un vecteur complexe, R_n , de dimensions $K \times 1$ relié à la suite de symboles à l'entrée par la relation

$$R_n = \theta_n^{-1} \sum_{q=0}^{N-1} (A_q \theta_{n-q} S_{n-q} + B_q (\theta_{n-q} S_{n-q})^*) + N_n,$$

où $(S_p)_p$ est la suite de vecteurs complexes de dimensions $K \times 1$ formés des symboles en entrée,

$$\theta_p = \begin{pmatrix} e^{i\omega_0 p T} & 0 & \dots & 0 \\ 0 & \ddots & \ddots & \vdots \\ \vdots & \ddots & \ddots & 0 \\ 0 & \dots & 0 & e^{i\omega_{K-1} p T} \end{pmatrix},$$

$(N_n)_n$ est la suite de vecteurs complexes de dimensions $K \times 1$ formés des échantillons de bruit et $*$ représente l'opérateur de conjugaison des composantes d'un vecteur complexe. Dans l'expression précédente, N désigne le nombre de symboles sur lesquels l'interférence entre symboles se produit. Les matrices complexes de dimensions $K \times K$ A_0, A_1, \dots, A_{N-1} modélisent l'interférence entre symboles et entre canaux. B_0, B_1, \dots, B_{N-1} modélisent

l'interférence due aux bandes-images et l'interférence entre dimensions réelles (déséquilibre I/Q, effets de canal). Si le système était un multiplexage de fréquences orthogonal (orthogonal frequency division multiplex; OFDM), ces matrices seraient toutes nulles, exceptée A_0 qui serait égale à la matrice identité. Ceci est le cas, par exemple, lorsque le filtre de transmission est de réponse impulsionnelle idéalement rectangulaire de durée T , le filtre de réception est un intégrateur idéal sur la durée T et les fréquences des porteuses sont précisément positionnées à des multiples pairs ou impairs de π/T . Cela est également le cas si le filtre de transmission et le filtre de réception ont chacun un spectre en racine carrée de cosinus surélevé et les spectres de chacun des canaux ne se recouvrent pas. Le premier exemple est très sensible à l'imprécision sur le placement des porteuses et aux erreurs faites lors de la récupération de la base de temps et de la phase d'échantillonnage. Ceci rend son implémentation très difficile pour le présent système où les fréquences considérées sont au moins un ordre de grandeur plus élevées que dans les applications de communications sans fil. Le second exemple requiert que les canaux RF soient suffisamment distants les uns des autres, l'espacement dépendant grandement de la qualité du filtre de transmission et en particulier de l'excès de bande passante (excess bandwidth). A nouveau, même si implémentée pour les applications sans fil par une combinaison appropriée de sur-échantillonnage et de filtrage numérique et analogique, cette solution se heurte à de grandes difficultés dans l'application présente si l'on souhaite préserver un excès de bande passante réduit. De façon générale, les conditions OFDM imposent des contraintes drastiques en termes de placement des porteuses et de filtrage qui rendent l'implémentation du système extrêmement difficile si l'on souhaite arriver à une efficacité spectrale proche des limites théoriques. Ces contraintes peuvent cependant être relâchées en permettant au système de n'être qu'approximativement OFDM à condition d'ajouter des opérations d'égalisation et de suppression d'interférences effectuées par un bloc DSP constituant le dernier étage du récepteur précédant l'étage de décision.

Afin de supprimer l'interférence entre symboles et l'interférence entre canaux dans le canal k une structure numérique "feedforward" linéaire comme celle représentée en figure E.7 peut être utilisée. Après être passés par un étage produisant dans le domaine temps discret un effet inverse de celui de l'étage de démodulation analogique à la réception, les échantillons reçus sont filtrés et combinés linéairement pour passer dans un étage inversant dans le domaine temps discret l'effet de l'étage de modulation à la transmission pour former la suite des symboles reçus dans le canal k , $(\hat{s}_{n,k})_n$. Le filtre de réponse impulsionnelle finie $\lambda_{k,k}(z)$

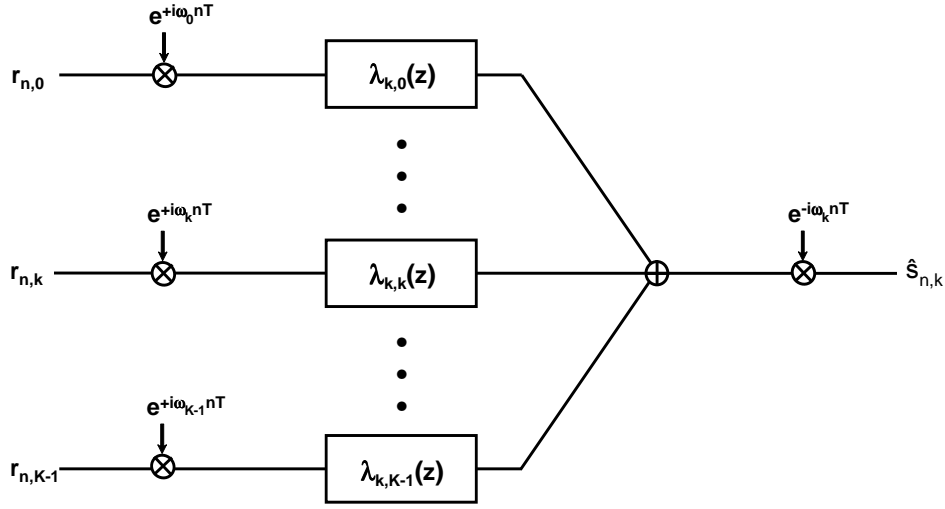


Figure E.7: Egalisation temps-fréquence et suppression d'interférence dans le canal k .

supprime l'interférence entre symboles dans le canal k tandis que les filtres $\lambda_{k,l}(z)$, $l \neq k$, effectuent la suppression de l'interférence provenant des autres canaux fréquentiels. Cette même structure se répète pour chacun des K canaux. La structure complète de traitement du signal numérique remplit les fonctions d'égalisation et de suppression d'interférences dans les dimensions de temps et de fréquence.

Si la longueur de chacun des filtres à réponse impulsionnelle finie est P , le vecteur des K symboles reçus au temps discret nT , \hat{S}_n , est donné par une combinaison linéaire des KP symboles reçus à P instants différents nT , $(n+1)T$, \dots , $(n-P+1)T$ dans les K canaux

$$\hat{S}_n = \theta_n^{-1} (\Lambda_0 \theta_n R_n + \Lambda_1 \theta_{n-1} R_{n-1} + \dots + \Lambda_{P-1} \theta_{n-P+1} R_{n-P+1}),$$

où les matrices de coefficients de filtres $\Lambda_0, \Lambda_1, \dots, \Lambda_{P-1}$ sont liées à la matrice d'égalisation et de suppression d'interférence entre symboles:

$$\Lambda(z) = \Lambda_0 + \Lambda_1 z^{-1} + \dots + \Lambda_{P-1} z^{-(P-1)}$$

La figure E.8 montre la structure complète en commençant par l'étage d'échantillonnage et en finissant par l'étage de décision dont la sortie fournit la suite de symboles estimés, $(\check{S}_n)_n$. La valeur des coefficients des filtres est contrôlable et est mise à jour selon un

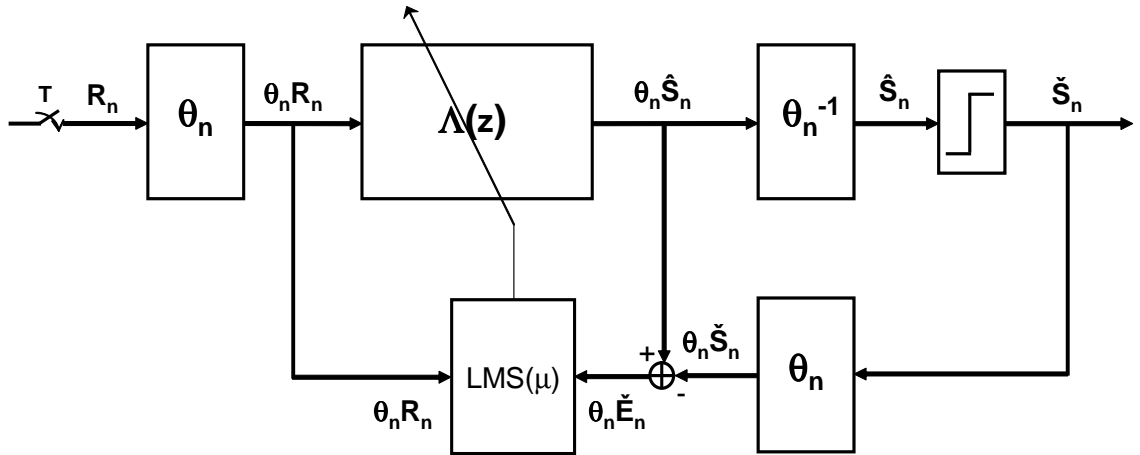


Figure E.8: Diagramme du bloc DSP supprimant l'interférence entre canaux et l'interférence entre symboles. (Bloc d'adaptation LMS de pas μ également représenté.)

algorithme tel que celui du gradient stochastique.

Cette architecture peut être améliorée afin d'effectuer des opérations linéaires similaires sur les conjugués des échantillons complexes reçus. Ceci a pour effet de supprimer l'interférence des bandes-images ainsi qu'entre les dimensions de signal réel en phase et en quadrature de phase dans chaque canal. Ce dernier type d'interférence peut être dû à l'imperfection inhérente à l'implémentation des étages de modulation et de démodulation. Cette architecture de traitement du signal numérique améliorée est représentée en figure E.9.

L'algorithme d'adaptation utilisé est celui des moindres carrés (ou du gradient stochastique) basé sur les symboles décidés. Lorsque le pas d'adaptation est désigné par μ les coefficients des filtres sont mis à jour de façon itérative selon les expressions

$$\begin{aligned}\mathbf{\Lambda}_{m+1} &= \mathbf{\Lambda}_m - \mu \theta_m \check{E}_m (\theta_m \mathbf{R}_m)^H \\ \mathbf{\Gamma}_{m+1} &= \mathbf{\Gamma}_m - \mu \theta_m \check{E}_m ((\theta_m \mathbf{R}_m)^*)^H\end{aligned}$$

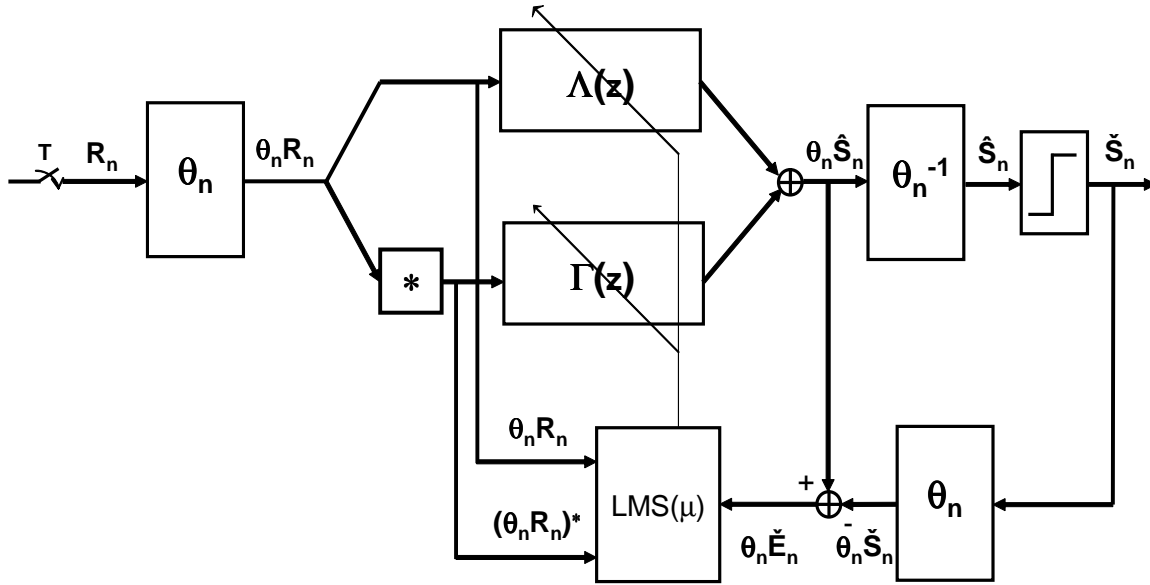


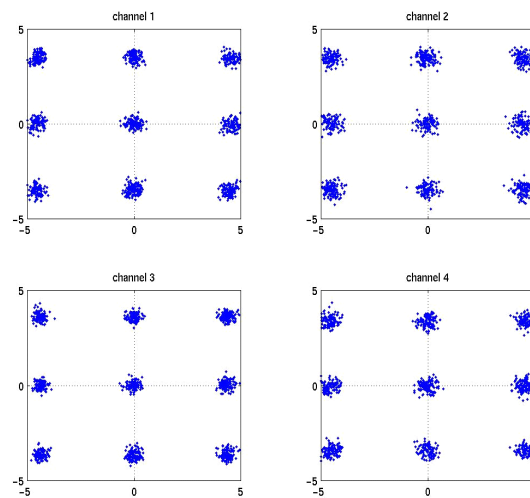
Figure E.9: Bloc DSP pour l'adaptation temps-fréquence adaptative.

où $\mathbf{\Lambda}$ et $\mathbf{\Gamma}$ sont des matrices complexes de dimensions $K \times KP$ réunissant l'ensemble des coefficients des filtres, $(\check{E}_n)_n$ est la suite de vecteurs d'erreur et $(R_n)_n$ est la suite des KP échantillons reçus dans les K canaux à P instants discrets différents.

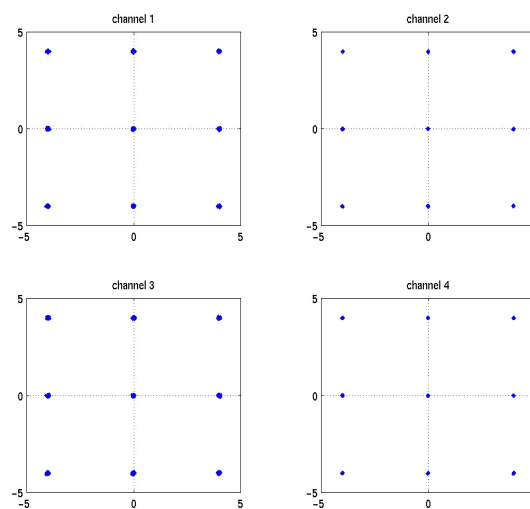
A titre de comparaison, les figures E.10(a) et E.10(b) montrent la juxtaposition des éléments d'une suite de symboles reçus après convergence de l'algorithme d'adaptation pour les architectures simple (figure E.8) et améliorée (figure E.9) respectivement. Dans cet exemple, des symboles QAM-9 sont transmis sur 4 porteuses avec des filtres de transmissions et de réception de type Butterworth rendant l'interférence entre symboles et l'interférence entre canaux non nulles. L'architecture améliorée permet un gain de 27 dB sur l'erreur quadratique moyenne. Dans le cas présent, cela est essentiellement dû à sa capacité à supprimer l'interférence des bandes-images.

E.3.3 Conclusion

Dans un système où l'efficacité en puissance peut être réduite afin d'obtenir un gain en efficacité spectrale, une modulation combinant multiplexage de sous-porteuses et codage



(a)



(b)

Figure E.10: Constellation QAM-9 sur 4 porteuses. Le filtre de transmission est Butterworth du 3^{ème} ordre avec $F_c = 1.2/T$. Le filtre de réception est Butterworth du 5^{ème} ordre avec $F_c = 0.9/T$. La conversion analogique/numérique est effectuée avec 10 bits de précision. Egalisation et suppression d'interférence entre canaux avec filtres numériques de longueur P égale à 8. (a) Structure DSP de la figure E.8. (b) Structure DSP de la figure E.9.

de symboles sur plusieurs niveaux peut être utilisée. Les avantages d'une telle modulation peuvent être exploités de façon pratique. Les difficultés d'implémentation peuvent être contournées par l'utilisation d'un traitement du signal numérique capable d'adaptation automatique. En fonction du système précis de multiplexage de sous-porteuses considéré, des compromis peuvent être faits entre les spécifications des blocs analogiques et la complexité de l'architecture numérique. Si les porteuses doivent être très proches les unes des autres parce que la bande passante est rare, et si les contraintes imposées dans la conception des filtres analogiques doivent être relâchées pour des raisons technologiques, l'interférence entre canaux est non négligeable, même entre canaux non-adjacents. Les structures de traitement du signal numérique doivent alors être implémentées dans leur intégralité. Dans le cas contraire, de nombreuses simplifications sont possibles. Les choix à effectuer dépendent de la nature du canal de transmission, c'est à dire de la chaîne de transmission optoélectronique dans notre cas.

E.4 Canal optique: caractéristiques et modèles

E.4.1 Système et définition du canal optique

La figure E.11 présente une vue d'ensemble la chaîne de transmission optique envisagée. Elle est composée d'un étage numérique et d'un étage analogique de transmission, d'un convertisseur électro-optique (EO), du milieu de transmission optique (fibre mono-mode), d'un convertisseur opto-électrique (OE), d'un étage analogique et d'un étage numérique de réception. Le canal optique est ici défini pour inclure:

- le milieu de transmission physique,
- les convertisseurs EO et OE,
- les étages analogiques comprenant les filtres analogiques et amplificateurs RF.



Figure E.11: Chaîne de transmission optoélectronique: vue d'ensemble.

Pour des raisons de simplicité et de coût, la méthode de transmission optique est l'intensité modulée avec détection directe représentée sur la figure E.12. Pour les mêmes raisons, un laser directement modulé de type DFB (distributed feedback) opérant à une longueur d'onde de 1310 nm est choisi comme convertisseur EO. Lorsque le courant d'opération fourni à la diode laser dépasse un niveau de seuil, un faisceau cohérent de lumière est émis. La diode laser est un système non-linéaire mais les conditions d'opération (courant d'opération, niveau de signal en entrée) peuvent être choisies de telle sorte que la conversion s'effectue de manière quasi-linéaire. Le taux de conversion est mesuré par l'efficacité externe, η_{ext} , exprimée en W/A, liant la puissance optique en sortie au courant au-dessus du seuil en entrée. Le rapport de la déviation standard du signal RF sur le courant d'opération au-dessus du seuil est appelé indice de modulation optique (optical modulation index; OMI)

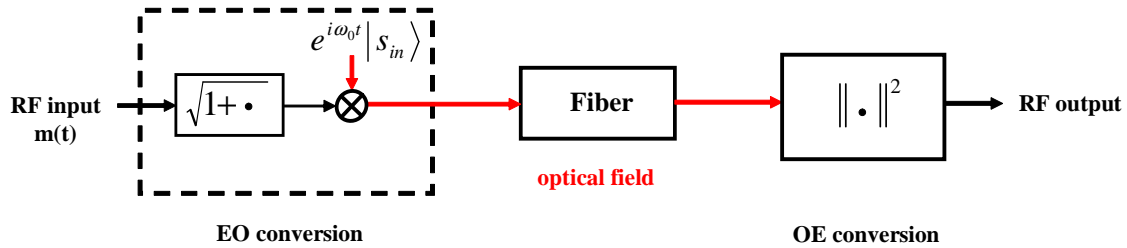


Figure E.12: Méthode de transmission en intensité modulée avec détection directe (IM/DD).

et mesure la profondeur de modulation. Le laser est également une source de bruit filtrée provenant essentiellement du phénomène d'émission spontanée. Les caractéristiques du bruit en intensité sont importantes à connaître. Le convertisseur OE est une photodiode qui convertit linéairement la puissance optique en entrée en courant en sortie. Le taux de conversion est mesuré par la responsivité, R_{resp} , exprimée en A/W. Etant donné que le gain de la chaîne EO/fibre/OE est en-dessous de l'unité, des étages d'amplification sont également nécessaires.

E.4.2 Distorsions et bruit de canal

Distorsions linéaires La linéarisation de la réponse de la chaîne optoélectronique formée par le laser directement modulé, une fibre optique mono-mode dispersive et la photodiode permet de déterminer les distorsions linéaires subies par le signal transmis. La longueur d'onde de lumière émise par le laser, dont la température est contrôlée, est spécifiée à ± 20 nm autour de 1310 nm. Une déviation par rapport à la valeur nominale a pour effet d'induire des effets de filtrage linéaire dus à une combinaison de la modulation en fréquence de la porteuse optique inhérente au fonctionnement des lasers directement modulés et de la dispersion dans la fibre comme illustré sur la figure E.13. Ceci a pour effet de modifier la distribution de puissance entre les porteuses, ainsi que le rapport signal sur bruit dans chaque canal lorsqu'une modulation de type SCM est utilisée pour transmettre l'information.

Distorsions non-linéaires Le signal SCM formé de plusieurs canaux RF est très sensible aux non-linéarités du canal de transmission avec des conséquences directes sur la performance du système de communication. Ces effets ont été étudiés de manière très

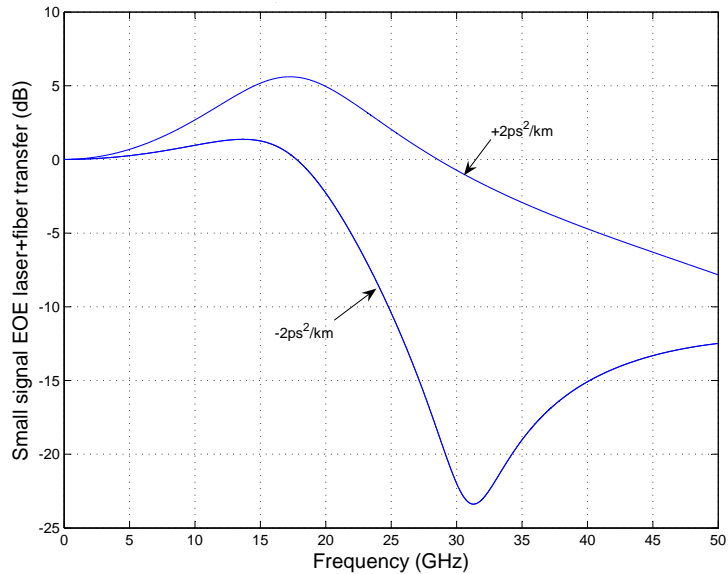


Figure E.13: Réponse linéarisée du laser et de la fibre (photodiode idéale) pour un courant d’opération laser fixé à 50 mA au-dessus du seuil et une fibre de 10 km pour des longueurs d’ondes telles que la dispersion chromatique soit de $+2 \text{ ps}^2/\text{km}$ et $-2 \text{ ps}^2/\text{km}$.

complète dans le cas des applications utilisant un hybride fibre-cable coaxial (HFC) et “common antenna television” (CATV) [PD97, PDMF91, PD93].

Deux mesures sont couramment utilisées afin de quantifier l’effet des différentes contributions non-linéaires sur le signal composite transmis: la distorsion composite de deuxième ordre (composite second-order distortion; CSO) et la distorsion composite de troisième ordre (composite triple beat distortion; CTB). Pour un canal donné k à la fréquence f_k , le CSO est le rapport de la somme des puissances de toutes les raies résultant du mixage de deux fréquences prises parmi les fréquences formant le signal composite d’entrée et tombant à la fréquence f_k , et de la puissance du signal à la fréquence f_k (signal utile). De la même manière, le CTB est le rapport de la somme des puissances de toutes les raies résultant du mixage de trois quelconques fréquences prises parmi les fréquences du signal composite d’entrée et tombant à la fréquence f_k , et de la puissance du signal à la fréquence f_k .

Les mesures de CSO et CTB peuvent être déterminées pour la plupart des distorsions non-linéaires:

- La combinaison de la modulation de fréquence de la porteuse optique produite par le laser directement modulé et de la dispersion chromatique dans la fibre mono-mode

produit des distorsions non-linéaires. La modulation de fréquence corrélée à la modulation de la puissance optique est convertie par la dispersion chromatique en nouvelle contribution aux variations de la puissance optique.

- La combinaison de dispersion chromatique et des fluctuations de l'indice de réfraction en régime optique non-linéaire produit également des distorsions non-linéaires. La modulation de fréquence optique dû au changement d'indice lié aux variations de la puissance optique est convertie en contribution aux variations de puissance optique par le même mécanisme impliquant la dispersion chromatique que dans le point précédent. Lorsque comparée aux autres contributions, celle-ci est négligeable dans les conditions d'opération pratiques. Ceci justifie en particulier l'utilisation de modèles de fibre linéaires tels que présentés dans la section E.2.
- Les fonctions des circuits analogiques (filtres, mixeurs, etc) opèrent en régime quasi-linéaire. Leur conception doit être régie par des spécifications de linéarité compatible avec le budget de distorsions acceptables par le système.
- L'écart de la réponse du laser par rapport à la réponse linéarisée autour du point d'opération est source de non-linéarité à prendre en compte dans le budget de distorsions.

En sus des distorsions précédentes qui sont similaires dans leur caractérisation, il faut également tenir compte des effets de pincement laser qui sont illustrés par la figure E.14. Lorsque la déviation du signal d'entrée est trop grande, il est possible que le signal total (incluant le courant d'opération) passe en-dessous du seuil créant ainsi un "écrasement" du signal composite.

Bruit Les contributions au bruit de canal sont les suivantes:

- La lumière produite par la diode laser est inévitablement bruitée du fait de la statistique des photons et des porteurs de charges dans le milieu à gain optique. La lumière laser peut être représentée par une onde monochromatique portant des fluctuations aléatoires d'amplitude et de phase. En particulier, le bruit d'intensité relatif (relative intensity noise; RIN) désigne les fluctuations de puissance à la sortie du laser. La caractérisation d'un tel bruit est fondamentale pour les systèmes optiques IM/DD n'incluant pas d'étage d'amplification optique. Les fluctuations de phase doivent

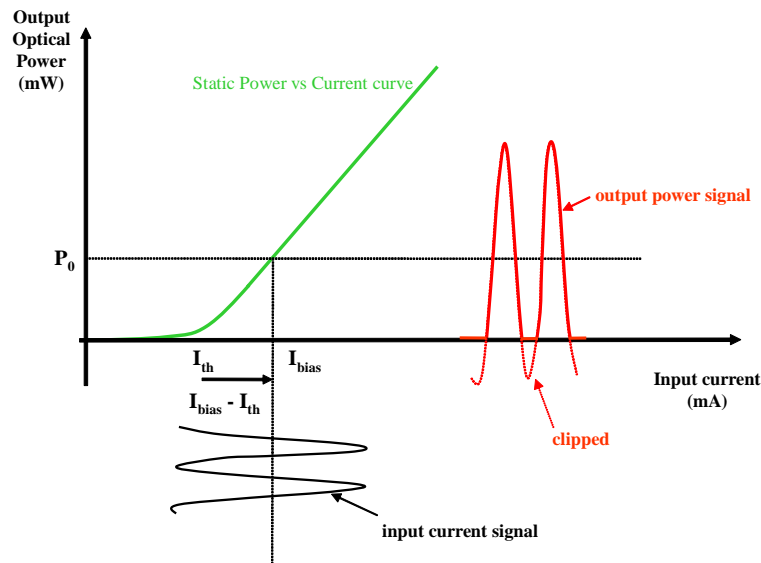


Figure E.14: Distorsion non-linéaire de pincement laser lorsque les valeurs extrêmes du courant d'entrée dépassent la valeur du courant d'opération au-dessus du seuil laser.

également être prises en compte si des phénomènes de conversion de modulation de fréquence en modulation d'intensité, tels que la dispersion chromatique, interviennent.

- Les réflexions au niveau des discontinuités telles que les connecteurs optiques peuvent créer du bruit d'intensité. Celui-ci est d'autant plus faible que la large spectrale du signal optique considéré est grande. Pour le système présent, cette contribution est négligeable devant le bruit d'intensité de la diode laser.
- Le bruit dans le photorécepteur et les étages d'amplification électronique doit être pris en compte. Cette contribution limite la portée du système compte tenu de l'atténuation dans la fibre.

Toutes les contributions importantes peuvent être décrites au niveau du récepteur optique et sont représentées sur la figure E.15. Il s'agit du bruit de photon (shot), du bruit thermique (therm) et du bruit d'intensité (RIN).

Le rapport signal sur bruit s'écrit alors

$$\text{SNR} = \frac{\text{OMI}^2 I_{\text{pin}}^2}{\text{BW}_N \left(4 \frac{k_B T_0}{R} F + 2q I_{\text{pin}} + \text{RIN} I_{\text{pin}}^2 \right)},$$

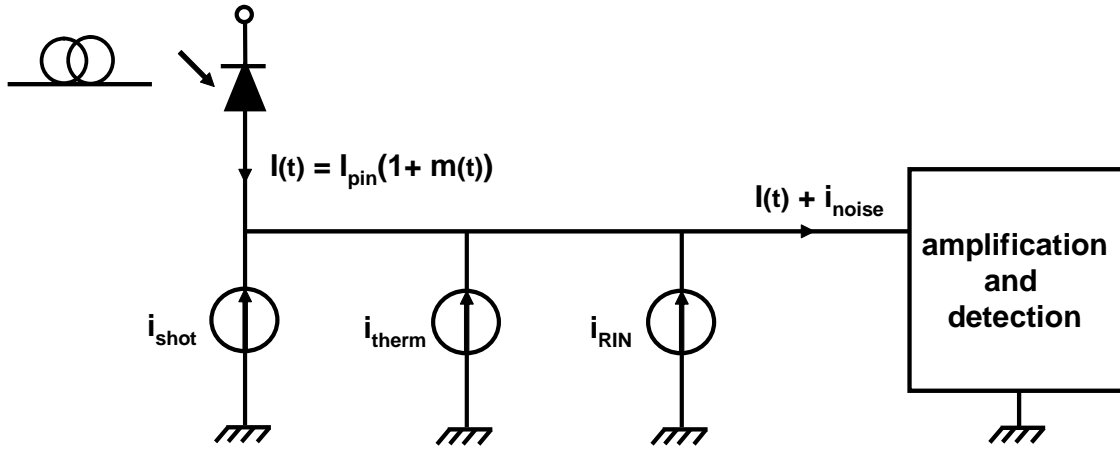


Figure E.15: Modèle de signal et bruit au niveau du récepteur optique.

où OMI est l'indice de modulation optique, R est la valeur de la résistance à la sortie de la photodiode, k_B est la constante de Boltzmann, T_0 est la température, F est le facteur de bruit caractérisant la contribution au bruit thermique ajoutée par les amplificateurs électriques, q est la charge de l'électron, RIN est la densité spectrale de puissance de bruit d'intensité relatif, BW_N est la bande passante de bruit équivalente. Le photocourant moyen, I_{pin} , au niveau de la photodiode est donné par

$$I_{\text{pin}} = R_{\text{resp}} e^{-\alpha_l L} \eta_{\text{ext}} (I_b - I_{\text{th}}),$$

où R_{resp} est la responsivité de la photodiode, α_l est l'atténuation dans la fibre, L est la longueur de fibre, η_{ext} est l'efficacité externe de la diode laser, I_b est le courant d'opération et I_{th} le courant de seuil du laser. Pour de courtes distances, le bruit d'intensité est la contribution dominante. Le rapport signal sur bruit d'intensité est primordial afin de déterminer si le système est capable de fonctionner avec un taux d'erreur suffisamment bas. Les autres sources de bruit, et le bruit thermique en particulier, limitent la distance maximale de fonctionnement du système (une fois admis qu'il fonctionne à très courtes distances).

E.4.3 Modèle et mesure d'un laser directement modulé

La diode laser est la source principale de distorsions et de bruit dans le système. Il convient donc d'en déterminer précisément les caractéristiques et la dynamique de manière théorique et expérimentale.

La dynamique et le bruit du laser sont décrits par l'évolution de trois variables d'état N , le nombre d'électrons, P , le nombre de photons et ϕ , la phase. Cette évolution est régie par les équations couplées du laser exprimées ici sous forme d'équations différentielles stochastiques pour inclure les sources de bruit et normalisées de façon commode:

$$\begin{cases} dN_t &= (i_L(t) - G(N_t, P_t)P_t - R_{rec}(N_t)) dt + dN_t^{sp} \\ dP_t &= ((G(N_t, P_t) - \alpha_L) P_t + R_{sp}(N_t)) dt + dP_t^{sp} \\ d\phi_t &= \frac{\alpha}{2} (G_0(N_t) - \alpha_L) dt + d\phi_t^{sp} \end{cases}$$

Dans ces équations, i_L est le courant en entrée, $G(N, P) = \frac{G_0}{1+\varepsilon P} \ln\left(\frac{N}{N_T}\right)$ est le gain laser, où ε est le coefficient de saturation, N_T est le nombre d'électron au seuil et G_0 est le coefficient de gain non-saturé. Le terme $R_{rec}(N) = AN + BN^2 + CN^3$ est le taux de "destruction" de porteurs de charge dû aux différents processus de recombinaison électron-trou, où A est le coefficient de recombinaison non-radiative, B est le coefficient de recombinaison radiative et C est le coefficient d'Auger. Le terme $R_{sp}(N) = \beta_{sp}N^2$ est le taux de création de photon dû à l'émission spontanée, où β_{sp} est le facteur d'émission spontanée. Le coefficient α est le facteur d'élargissement de raie spectrale et $G_0(N) = G_0 \ln(N/N_T)$ est le gain non-saturé. Les processus aléatoires N^{sp} , P^{sp} and ϕ^{sp} sont des mouvements browniens décrivant les sources de fluctuations du nombre d'électron, du nombre de photon et de la phase du champs optique dues aux recombinaisons de porteurs et à l'émission spontanée. Les coefficients de diffusion de ces processus sont donnés par

$$\begin{aligned} 2D_{PP} &= 2R_{sp}(N)P \\ 2D_{NN} &= 2(R_{sp}(N)P + R_{rec}(N)) \\ 2D_{PN} &= -2R_{sp}(N)P \\ 2D_{\phi\phi} &= \frac{R_{sp}(N)}{2P} \\ 2D_{\phi P} &= 0 \\ 2D_{\phi N} &= 0. \end{aligned}$$

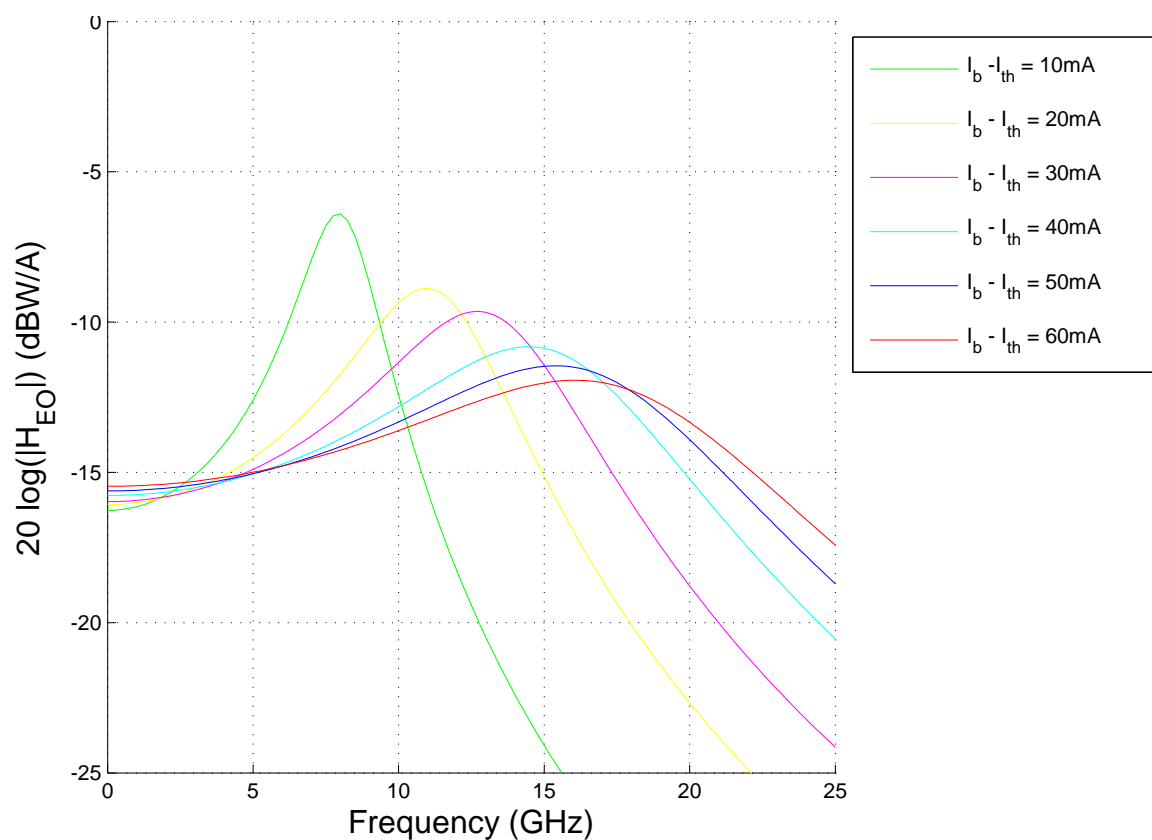


Figure E.16: Amplitude de la réponse en fréquence électro-optique linéarisée du laser pour un courant d'opération de 5, 10, 20, 30, 40, 50 and 60 mA au-dessus du seuil.

Les équations déterministes (sans les processus aléatoires) peuvent être linéarisées pour obtenir la réponse électro-optique linéarisée de la diode laser qui dépend du courant d'opération comme illustré sur la figure E.16.

La linéarisation des équations stochastiques lorsque le courant en entrée est constant (égal au courant d'opération) permet de déterminer théoriquement la densité spectrale de puissance de bruit en intensité relatif (RIN). La figure E.17 montre une comparaison des densités spectrales déduites de façon théorique et calculées par simulation (implémentation numérique des équations différentielles stochastiques complètes).

Afin de valider les modèles, une comparaison entre les densités spectrales de puissance de bruit en intensité théorique et expérimentale peut également être effectuée comme le montre la figure E.18.

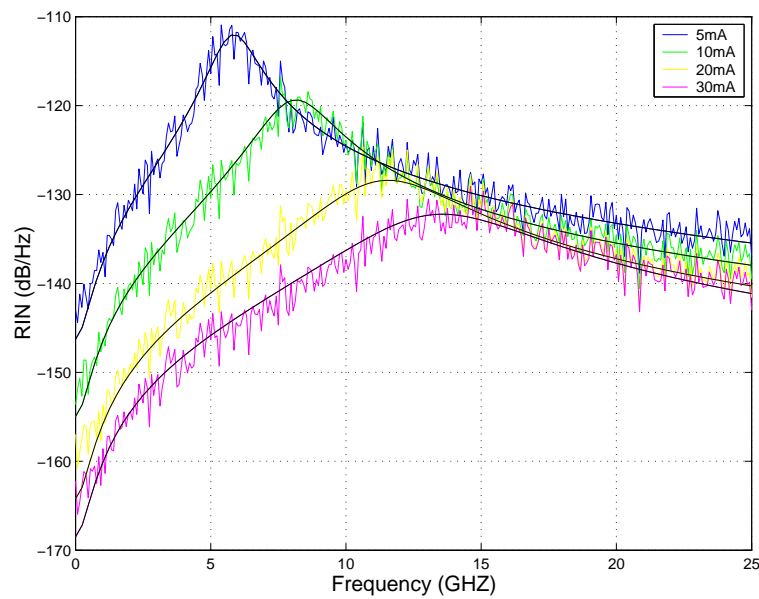


Figure E.17: Comparaison des densités spectrales de puissance de RIN données par la théorie (noir) et la simulation numérique (couleur) pour différentes valeurs du courant d'opération.

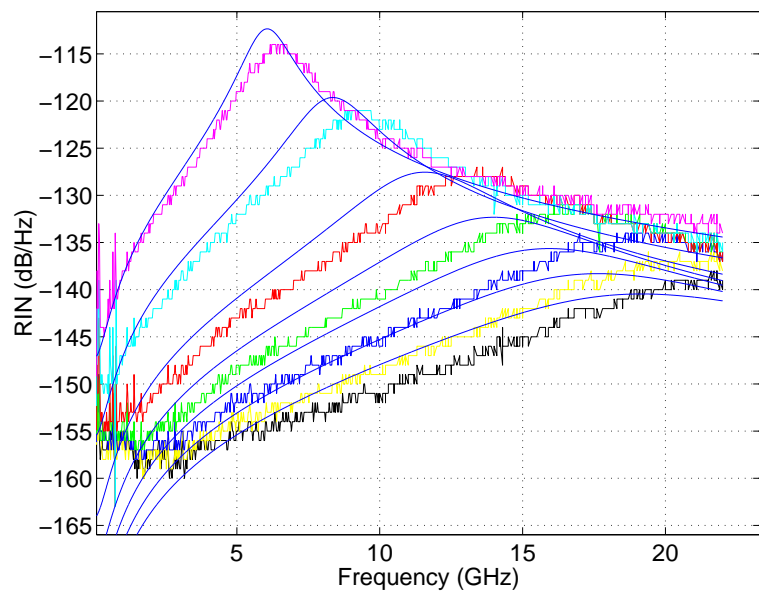


Figure E.18: Comparaison des densités spectrales de puissance de RIN théorique et mesurée pour un courant d'opération de 5, 10, 20, 30, 40, 50 and 60 mA au-dessus du seuil.

Les modèles peuvent également être validés dans le contexte de la transmission d'un signal composite formé de porteuses RF multiples. Cela est effectué à l'aide du montage représenté en figure E.19.

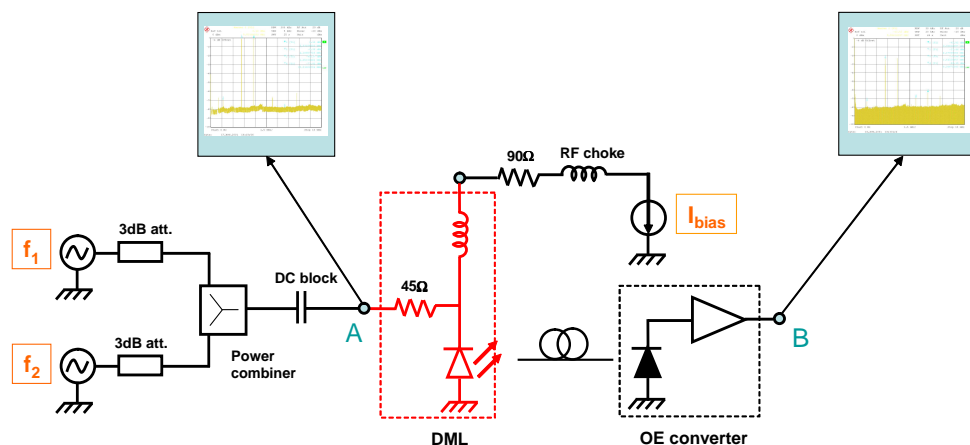


Figure E.19: Montage pour la mesure des distorsions d'intermodulation.

Expérimentation et simulation donnent des résultats concordants comme illustré par un résultat en figure E.20.

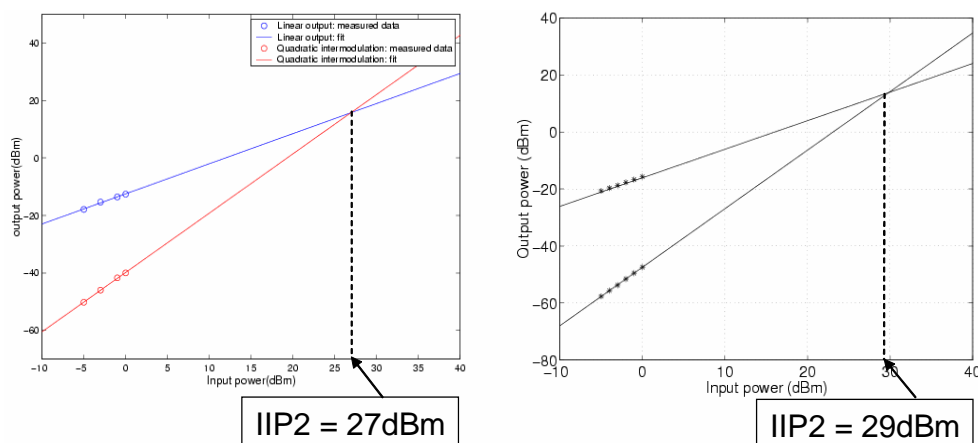


Figure E.20: Input-referred intercept point d'ordre 2 (IIP2) pour deux porteuses aux fréquences $f_5 = 4.17$ GHz et $f_7 = 5.83$ GHz et un courant d'opération laser de $I_b = 50$ mA au-dessus du seuil. Mesures (gauche) et simulations numériques (droite).

E.4.4 Modèle simplifié et capacité de canal

La théorie de l'information fournit un cadre théorique et des méthodes pour déterminer une borne supérieure du débit d'information pour la transmission sur un canal donné avec un taux d'erreur arbitrairement faible. Ainsi peuvent être définis des points de référence importants auxquels peuvent être comparés les objectifs désignés pour la conception du système de communication. L'étude du canal optique défini dans les sections précédentes est compliquée par l'existence de non-linéarités dues au processus de conversion électro-optique de la diode laser et à la fibre optique. Des modèles pour des canaux similaires au canal présent ont été cependant proposés [FH95].

Cette section présente un modèle simplifié permettant l'estimation de la capacité de canal et de ses variations en fonction de paramètres de système importants: courant d'opération du laser, indice de modulation optique (OMI noté μ) et longueur de fibre.

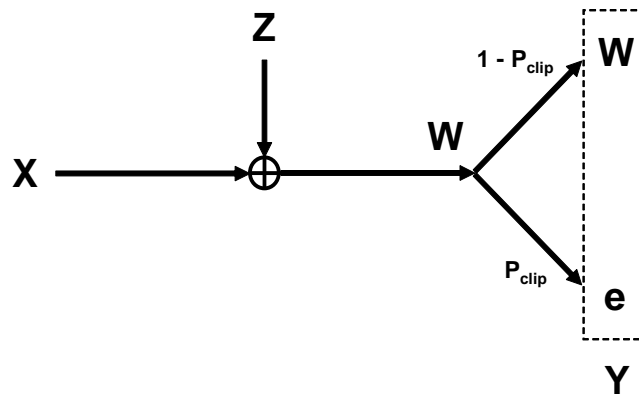


Figure E.21: Vue d'ensemble du modèle de canal simplifié.

La figure E.21 schématise le modèle défini de la manière suivante:

- Le signal X est un processus gaussien stationnaire modélisant le photocourant dans la photodiode correspondant au signal RF en entrée de la diode laser. La variance (puissance) de X est donnée par:

$$\sigma_X^2 = \mu^2 (I_{\text{pin}}(L))^2,$$

où μ désigne l'OMI. La valeur du photocourant moyen, I_{pin} , au niveau de la photodiode

dépend, en particulier, de la longueur de fibre L

$$I_{\text{pin}}(L) = R_{\text{resp}} e^{-\alpha_l L} \eta_{\text{ext}} (I_b - I_{\text{th}}),$$

où R_{resp} est la responsivité de la photodiode, α_l est l'atténuation dans la fibre, L est la longueur de fibre, η_{ext} est l'efficacité externe de la diode laser, I_b est le courant d'opération et I_{th} le courant de seuil du laser.

- Le bruit Z est un processus gaussien de moyenne nulle représentant les différentes contributions au bruit de canal telles que définies à la section E.4.2. Sa variance s'exprime

$$\sigma_Z^2 = B \left(\frac{4k_B T_0}{R} F + 2q I_{\text{pin}}(L) + \text{RIN} (I_{\text{pin}}(L))^2 \right).$$

Les termes de cette expression ont été définis à la section E.4.2 et la bande passante de bruit à été identifiée ici avec la bande passante du système pour simplifier.

- Il est fait l'hypothèse que la source principale de non-linéarités est la distorsion de pincement laser représentée à la figure E.14. Cette distorsion peut être modélisée par un bruit additif de type impulsif qui ramène le signal à zéro lors des excursions dans le domaine des valeurs négatives. Pour un signal d'entrée quasi-gaussien formé de la composition de K porteuses RF et d'indice de modulation μ , la probabilité d'avoir un événement de pincement pendant une période de symbole est donnée par

$$P_{\text{clip}} = 1 - e^{-\frac{K}{\sqrt{3}} e^{-\frac{1}{2\mu^2}}}.$$

Afin de prendre en compte les effets du bruit de pincement laser sur la transmission de l'information, il est supposé que dès qu'un événement de pincement se produit dans la période d'un symbole, il en résulte un effacement du symbole transmis. Cela est schématisé sur la figure E.21 et définit la variable aléatoire représentant le signal reçu Y :

$$Y = \begin{cases} W & \text{si } \theta = 0 \\ e & \text{si } \theta = 1 \end{cases}$$

où $W = X + Z$, e est le symbole d'effacement et θ est une variable aléatoire de Bernoulli

indépendante de X et Z telle que

$$\mathbb{P}(\theta = 1) = P_{\text{clip}}.$$

Ce modèle simple doit pouvoir servir de base pour le calcul de la capacité de canal et ses variations. Il ne tient cependant pas compte:

- Des non-linéarités du laser (hormis le pincement) qui ont pour effet de mixer les canaux RF,
- de la déviation de la longueur d'onde optique produite par le laser par rapport au point de dispersion zéro de la fibre et ses effets linéaires et non-linéaires sur le signal et le bruit d'intensité.

Dans le régime quasi-linéaire où le bruit de pincement peut être négligé $Y = W$ et la capacité de canal gaussien linéaire C est donnée par [CT91]

$$C = B \log_2 \left(1 + \frac{\sigma_X^2}{\sigma_Z^2} \right).$$

La variation de la capacité avec la longueur de fibre pour un courant laser d'opération (fixant la valeur moyenne du signal à l'entrée de la fibre et la valeur maximale de la densité spectrale de bruit d'intensité, RIN) de 50 mA au-dessus du seuil, un indice de modulation de 13% et une bande passante du système de 14 GHz est représentée sur la figure E.22. Les capacités prédites sont gigantesques et approchent 100 Gb/s à courte distance, soit une efficacité spectrale atteignable dépassant 6b/s/Hz! L'efficacité spectrale de SCM QAM-16 sur 16 canaux telle que définie à la section E.3.1 est proche de 3b/s/Hz à titre de comparaison.

Lorsque les distorsions de pincement ne peuvent pas être négligées, le modèle de canal gaussien avec effacement donne la capacité de canal c

$$\begin{aligned} c &= (1 - P_{\text{clip}})C \\ &= B e^{-\frac{\kappa}{\sqrt{3}}} e^{-\frac{1}{2\mu^2}} \log_2 \left(1 + \frac{\mu^2 I_{\text{pin}}^2}{\sigma_Z^2} \right). \end{aligned}$$

Les variations de la capacité de canal c et de la majoration donnée par la capacité du canal linéaire C en fonction de l'indice de modulation μ sont représentées sur la figure E.23. Alors que C croît arbitrairement avec μ , c est bornée. Il existe un indice de modulation

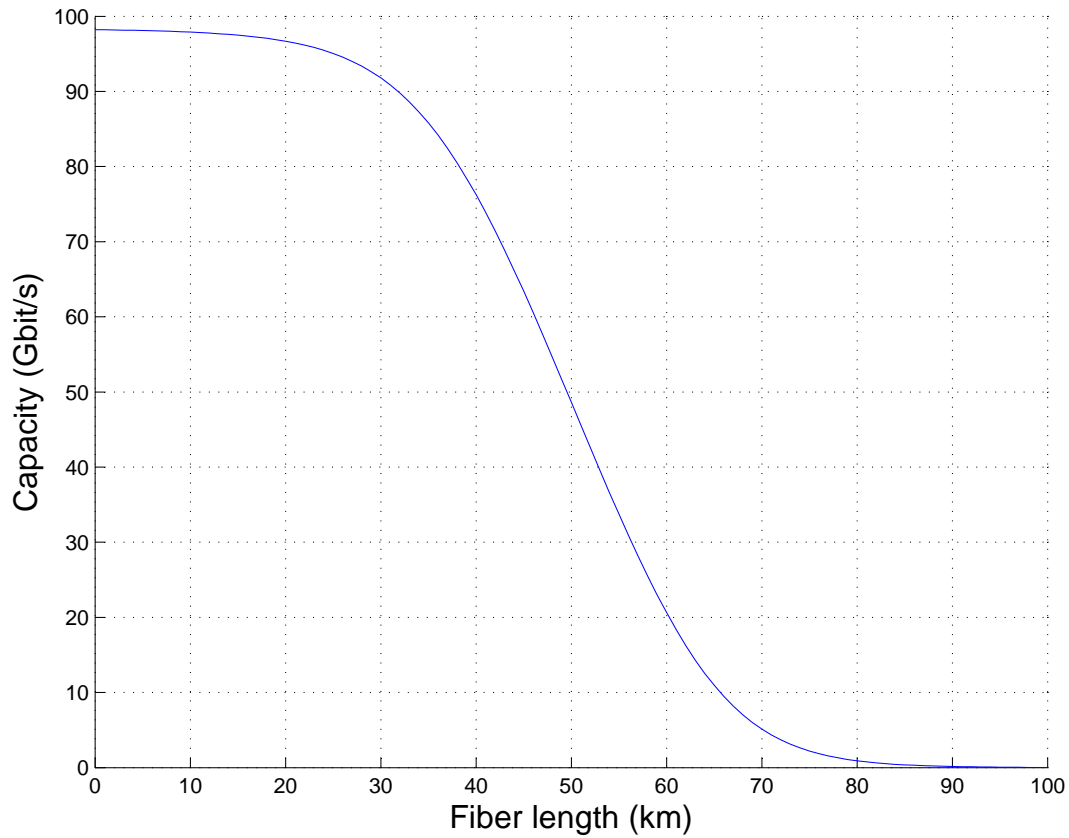


Figure E.22: Capacité de canal en fonction de la longueur de fibre pour un système opérant au point de dispersion zéro de la fibre avec RIN, bruit thermique et bruit de photons au niveau du récepteur. $\mu = 0.13$; B choisi égal à 14 GHz; $I_b - I_{th} = 50$ mA; $T_0 = 293$ K.

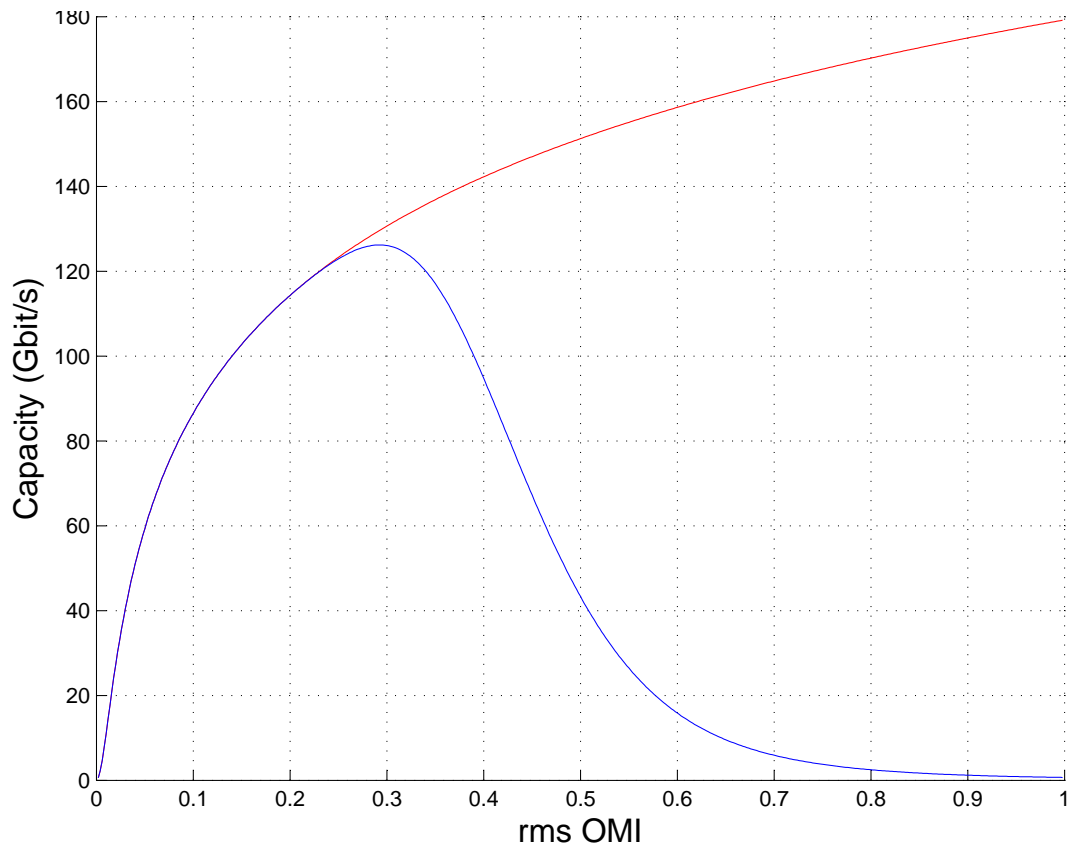


Figure E.23: Capacité de la diode laser en fonction de l'indice de modulation μ avec RIN et bruit de pincement laser (courbe bleue); majoration par la capacité du canal Gaussien linéaire (courbe rouge). $K = 16$; $B = 14$ GHz; $I_b - I_{th} = 50$ mA.

optimum comme illustré sur la figure E.23. Pour un indice de modulation de 13% l'hypothèse du régime quasi-linéaire est valable. Les modèles et résultats présentés peuvent servir de base à la conception de codes performants adaptés au canal considéré.

E.5 Application

E.5.1 Simulations numériques et performance

Cette section présente l'environnement de simulation numérique utilisant les modèles des sections précédentes conçu afin de prouver que le système de communication optique SCM à 40 Gb/s proposé fonctionne avec un taux d'erreur binaire en deçà de 10^{-15} . Cette environnement doit permettre de préciser la définition des paramètres du système déterminés au préalable par des estimations théoriques et par des simulations à faible niveau de détails. Il doit également permettre de spécifier les composants du système.

Après avoir pris en compte les contraintes de bande passante et de vitesse de traitement numérique, la modulation SCM telle que définie à la section E.3.1 est porteuse d'un débit de 40 Gb/s et est compatible avec les vitesses de traitement, les composants et les technologies utilisées. L'environnement de simulation inclus les modèles pour les fonctions analogiques (filtres, mixeurs, linéarité, bruit), le laser directement modulé (cf. section E.4.3), la fibre optique (cf. section E.2), le photorécepteur et les étages d'amplification (responsivité, bande passante, transimpédance, bruit), le bloc DSP et les fonctions de récupération d'horloge, de porteuses et de phase.

Les figures E.24 et E.25 montrent les résultats de simulation obtenus dans une configuration où la longueur de fibre est très faible. Sur chacune des figures est représenté le rapport signal sur bruit exprimé en décibels dans chacun des 16 canaux RF après convergence (récupération de porteuses et égalisation) suite à la transmission d'une séquence d'entraînement.

La figure E.24 est obtenue en faisant varier le courant d'opération du laser tout en fixant l'indice de modulation optique à 15%. Il apparaît que la performance du système s'améliore pour des courants croissants. Ceci s'explique par la réduction du bruit d'intensité laser et une amélioration de la linéarité. Du fait essentiellement de la structure de la densité spectrale de puissance de bruit d'intensité, le rapport signal sur bruit n'est pas constant d'un canal à l'autre et décroît en allant vers les canaux de fréquence plus élevée.

La figure E.25 montre les variations de la performance du système en fonction de l'indice de modulation pour un courant d'opération laser fixé à 80 mA au-dessus du seuil. Tous les canaux ne se comportent pas de la même façon dans le domaine considéré. Les canaux de fréquences les plus élevées, qui sont les plus affectés par le bruit d'intensité, sont aussi les plus sensibles aux non-linéarités grandissant avec l'indice de modulation.

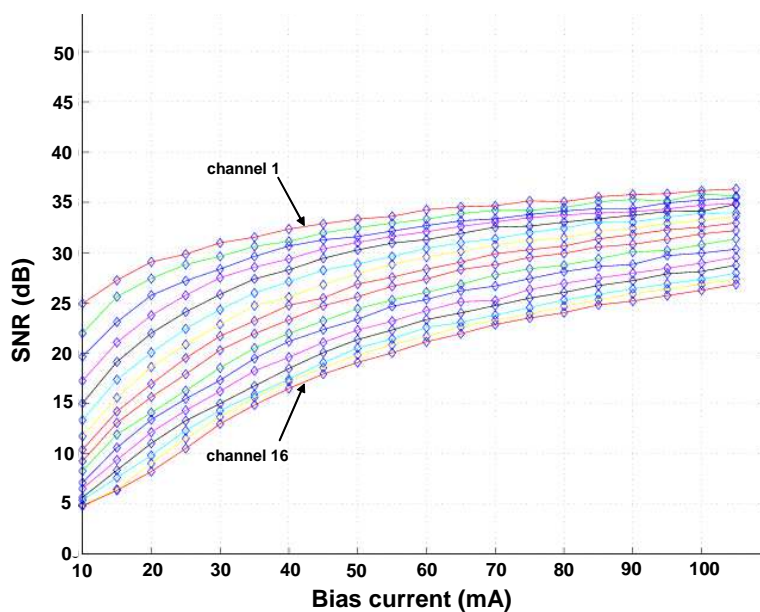


Figure E.24: Variations du rapport signal sur bruit pour chacun des 16 canaux en fonction du courant d'opération laser pour un indice de modulation fixé à 15%.

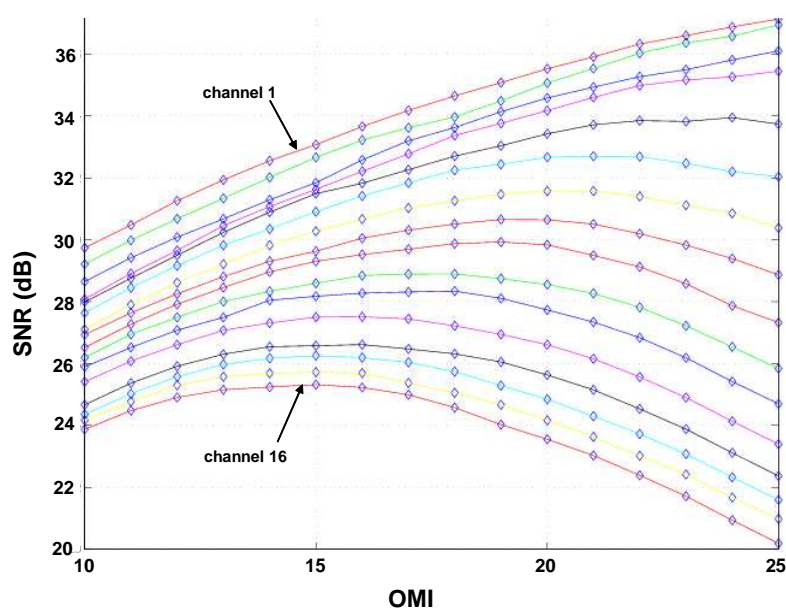


Figure E.25: Variations du rapport signal sur bruit pour chacun des 16 canaux en fonction de l'indice de modulation (exprimé en % de la puissance optique moyenne) pour un courant d'opération laser de 80 mA au-dessus du seuil.

Les résultats d'autres simulations ont été récoltés et analysés une fois le courant d'opération laser et l'indice de modulation fixés. Afin d'obtenir un taux d'erreur de moins de 10^{-15} dans le cas d'une modulation SCM utilisant QAM-16, le rapport signal sur bruit minimal doit être supérieur à 25 dB. Cette exigence peut être relâchée si des codes correcteurs d'erreur sont utilisés. Avec un code en bloc RS(255,239), il suffit alors d'obtenir un rapport signal sur bruit de 19 dB. Il a été fait l'hypothèse lors de la conception du système que RS(255,239) est utilisé, ce qui ajoute 7% au débit binaire brut qui passe de 40 Gb/s à 43 Gb/s. Les résultats tels que ceux illustrés par les figures E.24 et E.25 montrent que le système correctement spécifié par une combinaison de simulations et d'analyse permet d'atteindre les objectifs fixés.

E.5.2 Circuit test

Malgré la possibilité d'utiliser la technologie CMOS pour des débits dépassant 40 Gb/s ouverte par l'utilisation de la modulation et du traitement du signal prescrits, les défis présentés par l'implémentation des circuits RF sont réels. Afin de prouver que l'implémentation est possible, l'équipe High Speed Communications VLSI a réalisé une puce test pour la modulation et démodulation du 16^{ème} canal RF de plus haute fréquence à 13.32 GHz.

La figure E.26 montre un schéma de la puce CMOS comprenant:

- un transmetteur composé d'un block de génération de données pseudo-aléatoires rythmé par un signal d'horloge externe à 666 MHz, un étage de conversion numérique-analogique, un étage de modulation utilisant les versions en phase et quadrature de phase de la porteuse fournie par un oscillateur externe fonctionnant à 13.32 GHz, un étage d'amplification et d'adaptation d'impédance à 50Ω ,
- un récepteur composé d'un étage d'adaptation d'impédance, d'un étage de démodulation fournissant les composantes en phase et en quadrature de phase suivi de deux amplificateurs permettant l'observation à l'aide d'un oscilloscope.

Une photographie de la puce de modulation/démodulation QAM est présentée sur la figure E.26. Les caractéristiques de la puce sont résumées dans la table E.3.

Après la mesure expérimentale des qualités de la puce test, celle-ci a été utilisée pour la conception d'un prototype de la chaîne de transmission complète pour le canal RF de fréquence 13.32 GHz. Dans une expérience illustrative, le signal composé de la porteuse RF unique fourni par la sortie du transmetteur est appliqué à l'entrée du laser directement

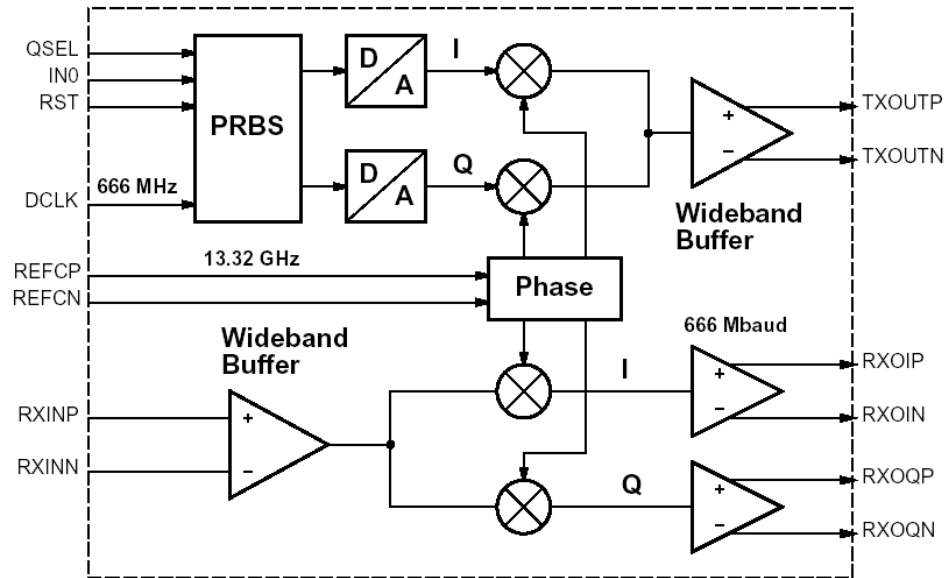


Figure E.26: Schéma de la puce test. PRBS: générateur de séquence de bits pseudo-aléatoire; D/A: conversion numérique/analogique.

Technology	0.14 μm , 1.5 V CMOS
Area	3.6 mm^2
Power	340 mW
Modulation	QAM-16 or QPSK
Carrier frequency	13.32 GHz
Bit rate	2.664 Gb/s (QAM16 mode)

Table E.3: Résumé des caractéristiques de la puce de modulation/démodulation QAM.

modulé avec un indice de modulation de 17.5% pour traverser une longueur de fibre allant jusqu'à 30 km, être amplifié et démodulé par le récepteur. La figure E.28 montre les constellations obtenues à la sortie du récepteur. L'estimation du taux d'erreur binaire à partir de ces observations est de 10^{-5} ce qui est compatible avec les résultats de simulation obtenus précédemment pour le système. Le taux d'erreur peut être amené en-dessous de 10^{-15} à l'aide de codes correcteurs d'erreur.

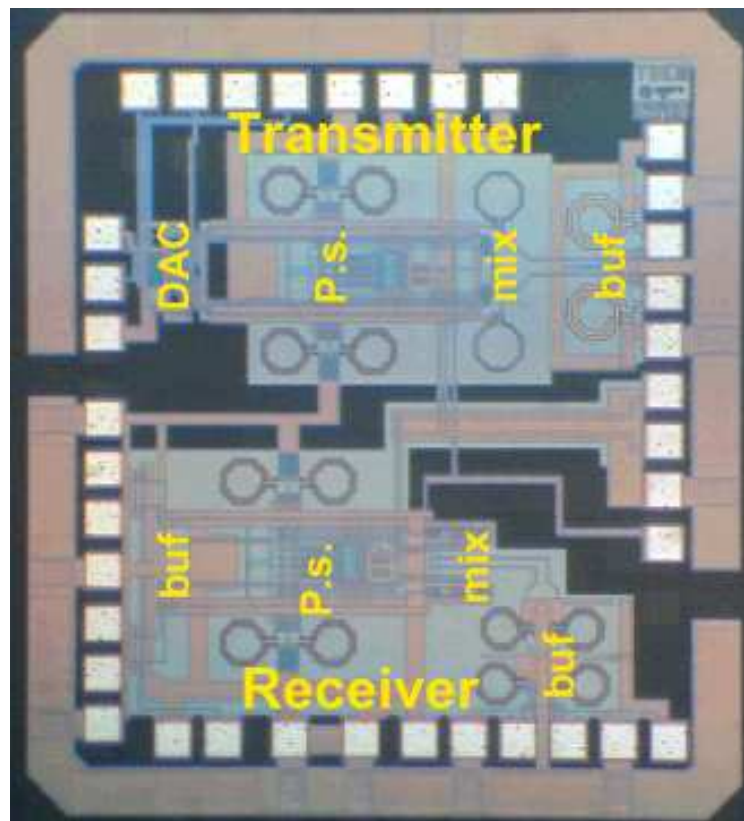
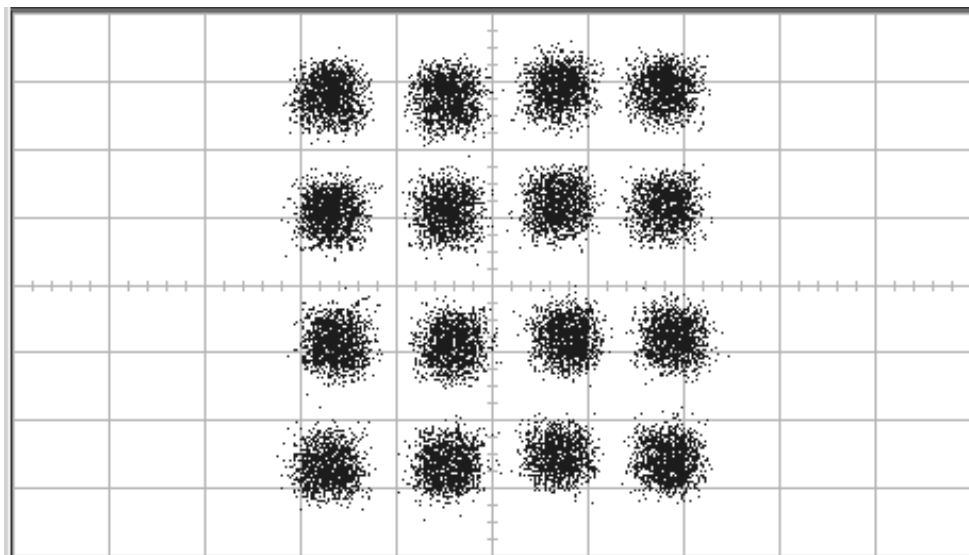
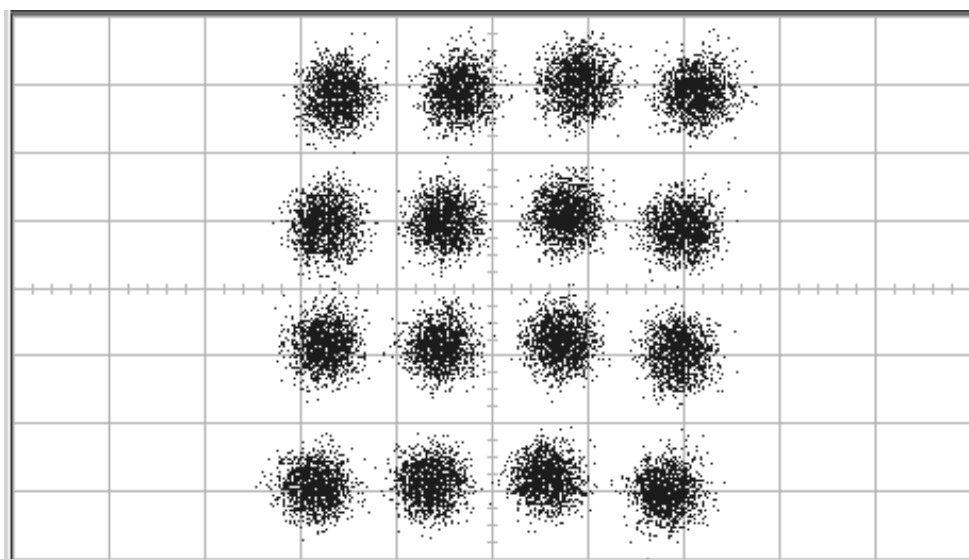


Figure E.27: Microphotographie de la puce test. DAC: convertisseur analogique-numérique; P.s.: déphaseur; mix: mixeur; buf: bloc de d'amplification et adaptation d'impédance.



(a)



(b)

Figure E.28: Constellation QAM-16 mesurée: (a) sans fibre, et (b) avec 30 km de fibre mono-mode.

E.6 Conclusions

Les travaux présentés proposent l'usage de modulations à haute efficacité spectrale du type sous-porteuses multiplexées avec codage de symboles sur plusieurs niveaux offrant une alternative, pour des systèmes à haut débit (dépassant 40 Gb/s) sur courtes distances (quelques dizaines de kilomètres), aux modulations optiques binaires couramment utilisées. Ces modulations permettent de réduire la bande passante nécessaire à la transmission de l'information, pour faire passer 40 Gb/s dans une bande de moins de 14 GHz. Le codage de symboles sur plusieurs niveaux permet de réduire la vitesse de traitement numérique. Les circuits peuvent ainsi être réalisés en technologie CMOS et des fonctions de traitement du signal élaborées peuvent être intégrées. Les structures de traitement du signal présentées permettent de relâcher les contraintes de conception du système multi-porteuses et, en particulier, celle de réalisation des fonctions analogiques. Les avantages en termes de coût et de flexibilité dans le cadre d'une production industrielle sont multiples: correction des variations des paramètres de production industrielle, correction des distorsions de canal linéaires, technologies utilisées avec une marge d'opération raisonnable. Des composants optiques habituellement utilisés pour la réalisation de systèmes de communication optiques à 10 Gb/s peuvent composer ce système transmettant 40 Gb/s. Les modèles et outils de simulation numérique développés permettent de montrer qu'un tel système est, théoriquement, opérationnel et satisfait les critères de performance exigés par le champs d'application. Une puce test formant le modulateur/démodulateur QAM le plus rapide connu jusqu'alors est utilisée pour la réalisation d'un prototype fonctionnel et se comportant comme prédit par la modélisation et l'étude du système. Un modèle de canal optique simplifié indique que le débit de 40 Gb/s n'est pas une limite et peut être dépassé à courtes distances tout en conservant des taux d'erreur binaires arbitrairement petits pour atteindre des efficacités spectrales dépassant 6b/s/Hz.

Les travaux futurs peuvent inclure:

- la réalisation d'un prototype complet comprenant les 16 canaux QAM,
- la conception de codes correcteurs adaptés au canal optique utilisé et ayant une performance améliorée,
- la conception de systèmes similaires pour d'autres canaux optiques (modulateurs externes, modulations optiques à bande unique) intégrant les technologies de multiplexage dense de longueurs d'onde (dense wavelength division multiplex; DWDM) pour

une application aux réseaux métropolitains à haut débit,

- la conception d'un modèle de canal optique plus élaboré pour aller au-delà des limitations indiquées à la section E.4.4.

Bibliography

- [AD93] Govind P. Agrawal and Niloy K. Dutta. *Semiconductor Lasers*. Kluwer Academic Publisher, second edition, 1993.
- [Agr95a] Govind P. Agrawal. *Fiber-Optic Communication Systems*, chapter 4, pages 170–172. Wiley Interscience, second edition, 1995.
- [Agr95b] Govind P. Agrawal. *Nonlinear Fiber Optics*. Academic Press, second edition, 1995.
- [AHS⁺02] Kamran Azadet, Eric F. Haratsch, Fadi Saibi, Jeffrey H. Saunders, Michael Shaffer, Leilei Song, and Meng-Lin Yu. Equalization and FEC Techniques for Optical Transceivers. *IEEE J. of Solid-State Circuits*, 37(3):317–327, March 2002.
- [BB99] Sergio Benedetto and Ezio Biglieri. *Principles of Digital Transmission with Wireless Applications*. Kluwer Academic/Plenum Publishers, 1999.
- [BBK00] H. Bülow, F. Buchali, and W. Keubart. Adaptation of an electronic PMD mitigator by maximization of the eye opening. In *ECOC*, pages 209–210, 2000.
- [BBT00] H. Bülow, F. Buchali, and G. Thielecke. Electronically enhanced optical PMD compensation. In *ECOC*, pages 39–40, 2000.
- [Bül02] H. Bülow. Electronic equalization of transmission impairments. In *OFC*, TuE4, 2002.
- [CT91] Thomas M. Cover and Joy A. Thomas. *Elements of Information Theory*. John Wiley & Sons, Inc., 1991.

- [CW97] Pi-Yang Chiang and Winston I. Way. Ultimate Capacity of a Laser Diode in Transporting Multichannel M-QAM Signals. *IEEE J. of Lightwave Tech.*, 15(10):1914–1924, October 1997.
- [DS91] Thomas E. Darcie and George E. Bodeep Adel A. Saleh. Fiber-Reflection-Induced Impairments in Lightwave AM-VSB CATV Systems. *IEEE J. of Lightwave Tech.*, 9(8):991–995, August 1991.
- [FBPC00] C. Francia, F. Bruyère, D. Pennickx, and M. Chbat. PMD Second-order Effects on Pulse Propagation in Single-Mode Optical Fibers. *IEEE Phot. Tech. Letters*, 10(12), December 2000.
- [FGL⁺00] G. L. Frazer, M. W. Goodwin, K. E. Leonard, J. P. Moffat, and F. Zhang. Static and dynamic performance of an adaptive receiver for 10 Gb/s optical transmission. In *ECOC*, pages 113–114, 2000.
- [FH95] G. J. Foschini and I. M. I. Habbab. Capacity of Broadcast Channels in the Near-Future CATV Architecture. *IEEE J. of Lightwave Tech.*, 13(3):507–515, March 1995.
- [FJNK99] G. J. Foschini, R. M. Jopson, L. E. Nelson, and H. Kogelnik. The Statistics of PMD-induced Chromatic Fiber Dispersion. *IEEE J. of Lightwave Tech.*, 17(9), September 1999.
- [FNK00] G. J. Foschini, L. E. Nelson, and H. Kogelnik. Probability Densities of Second-Order Polarization Mode Dispersion including Polarization Dependent Chromatic Fiber Dispersion. *IEEE Phot. Tech. Letters*, 12(3), March 2000.
- [FP91] G. J. Foschini and C. D. Poole. Statistical Theory of Polarization Mode Dispersion in Single Mode Fibers. *IEEE J. of Lightwave Tech.*, 9(11), November 1991.
- [Fra91] Pierre Luc François. Nonlinear Propagation of Ultrashort Pulses in Optical Fibers: Total Field Formulation in the Frequency Domain. *J. Opt. Soc. Am. B*, 8(2), February 1991.

- [FV01] E. Forestieri and L. Vincetti. Exact evaluation of the Jones matrix of a fiber in the presence of Polarization-Mode Dispersion of any Order. *IEEE J. of Lightwave Tech.*, 19(12), December 2001.
- [GK91] J. P. Gordon and H. Kogelnik. PMD Fundamentals: Polarization Mode Dispersion in Optical Fibers. *PNAS*, 97(9):4541–4550, April 1991.
- [Hei02] F. Heisman. Analysis of a Reset-Free Polarization Controller for Fast Automatic Polarization Stabilization in Fiber-optic Transmission Systems. *IEEE J. of Lightwave Tech.*, 12(4), April 2002.
- [Hen83] C. H. Henry. Theory of the Phase Noise and Power Spectrum of a Single Mode Injection Laser. *IEEE J. of Quantum Electronics*, 19(9):1391–1397, September 1983.
- [Hen86] C. H. Henry. Phase Noise in Semiconductor Lasers. *IEEE J. of Lightwave Tech.*, 14(3):298–311, March 1986.
- [HTLLAD94] Lofti Hassine, Zeno Toffano, Françoise Lamnabhi-Lagarrigue, and Christelle Birocheau Alain Destrez. Volterra Functional Series Expansions for Semiconductor Lasers under Modulation. *IEEE Journal of Quantum Electronics*, 30(4):918–928, April 1994.
- [JNK99] R. M. Jopson, L. E. Nelson, and H. Kogelnik. Measurement of Second-Order Polarization Mode Dispersion Vectors in Optical Fibers. *IEEE Phot. Tech. Letters*, 11(9), September 1999.
- [Jop99] R. Jopson. Polarization-Mode Dispersion in Return-to-Zero and Nonreturn-to-Zero Systems. In *OFC*, WE3, 1999.
- [Kar98] M. Karlsson. Polarization Mode Dispersion-induced Pulse Broadening in Optical Fibers. *Optics Letters*, 23(9), May 1998.
- [Kas82] B. L. Kasper. Equalization of multi-mode optical fiber systems. *Bell Syst. Tech. J.*, pages 1267–1388, December 1982.
- [KGP00] Nicole El Karoui, Emmanuel Gobet, and Etienne Pardoux. *Introduction au calcul stochastique*. Ecole Polytechnique, 2000.

- [KNGJ00] H. Kogelnik, L. E. Nelson, J. P. Gordon, and R. M. Jopson. Jones Matrix for Second-Order Polarization Mode Dispersion. *Optics Letters*, 25(1), January 2000.
- [KW91] Sanjay Kasturia and Jack H. Winters. Techniques for high-speed implementation of nonlinear cancellation. *IEEE J. on Selected Areas in Comm.*, 9(5), June 1991.
- [KWOY89] M. Kawai, H. Watanabe, T. Ohtsuka, and K. Yamaguchi. Smart Optical Receiver With Automatic Decision Threshold Setting and Retiming Phase Alignment. *IEEE J. of Lightwave Tech.*, 7(11):1634–1640, November 1989.
- [Lam00] Cedric F. Lam. A Simplified Model for Estimating the Capacity Limit of an Optical Link in Transporting Multichannel M-QAM signals. *IEEE Phot. Tech. Letters*, 12(11):1579–1581, November 2000.
- [Li01] M. J. Li. Recent progress in fiber dispersion compensators. In *ECOC*, pages 486–489, 2001.
- [Maz92] J. E. Mazo. Asymptotic Distortion Spectrum of Clipped dc-Biased, Gaussian noise. *IEEE Transactions on Communications*, 40(8):1339–1344, August 1992.
- [Men89] C. R. Menyuk. Pulse Propagation in an Elliptically Birefringent Kerr Medium. *IEEE J. Quantum Electron.*, 25:2674–2682, 1989.
- [MMW97] D. Marcuse, C. R. Menyuk, and P. K. Wai. Application of the Mankov-PMD equation to studies of signal propagation in optical fibers with randomly varying birefringence. *IEEE J. of Lightwave Tech.*, 15(9), September 1997.
- [MPY00] W. K. Marshall, J. Palaski, and A. Yariv. Reduction of Relative Intensity Noise of the output Field of a Semiconductor Laser due to Propagation in Dispersive Optical Fibers. *IEEE Phot. Tech. Letters*, 12(4):413–415, April 2000.
- [Nel01] L. Nelson. Optical Fiber Properties for Long-Haul Transmission. In *ECOC*, pages 346–349, 2001.

- [NJKF00] L. E. Nelson, R. M. Jopson, H. Kogelnik, and G. J. Foschini. Measurement of Depolarization and Scaling associated with Second-Order Polarization Mode Dispersion in Optical Fibers. *IEEE Phot. Tech. Letters*, 11(12), December 2000.
- [PD93] C. D Poole and T. E. Darcie. Distortion Related to Polarization-Mode Dispersion in Analog Lightwave Systems. *IEEE J. of Lightwave Tech.*, 11(11):1749–1759, November 1993.
- [PD97] Mary R. Phillips and Thomas E. Darcie. Lightwave analog video transmission. In Ivan P. Kaminow and Thomas L. Koch, editors, *Optical Fiber Telecommunications*, volume IIIA, chapter 14, pages 523–559. Wiley Interscience, 1997.
- [PDK97] J. Peters, A. Dori, and F. Kapron. Bellcore’s fiber measurement audit of existing cable plant for use with high bandwidth systems. In *NFOEC*, 1997.
- [PDMF91] M. R. Phillips, T. E. Darcie, D. Marcuse, and N. J. Frigo. Nonlinear Distortion Generated by Dispersive Transmission of Chirped Intensity-Modulated Signals. *IEEE Phot. Tech. Letters*, 3(5):481–483, May 1991.
- [PMY98] E. Peral, W. K. Marshall, and A. Yariv. Precise Measurement of Semiconductor Laser Chirp Using Effect of Propagation in Dispersive Fiber and Application to Simulation of Transmission through Fiber Gratings. *IEEE J. of Lightwave Tech.*, 16(10):1874–1880, October 1998.
- [PTCF91] C. D. Poole, R. W. Tkach, A. R. Chraplyvy, and D. A. Fishman. Fading in lightwave systems due to polarization-mode dispersion. *IEEE Phot. Tech. Letters*, 3(1), January 1991.
- [PW86] C. D. Poole and R. E. Wagner. Phenomenological Approach to Polarization Mode Dispersion in Long Single-Mode Fibres. *Elec. Letters*, 22(19), September 1986.
- [Ref99] James J. Refi. Optical Fibers for Optical Networking. *Bell Labs Technical Journal*, Jan.-March, 1999.

- [SD89] M. Sherif and P. A. Davis. Decision-point steering in optical fiber communication systems: theory. *IEE Proceedings*, 36(3):169–176, June 1989.
- [Shi99] W. Shieh. Principal States of Polarization for an Optical Pulse. *IEEE Phot. Tech. Letters*, 11(6), June 1999.
- [Shi00] W. Shieh. On the Second-Order Approximation of PMD. *IEEE Phot. Tech. Letters*, 12(3), March 2000.
- [SK01] W. Shieh and H. Kogelnik. Dynamic Eigenstates of Polarization. *IEEE Phot. Tech. Letters*, 13(1), January 2001.
- [SM00] M. Shtaif and A. Mecozzi. Study of the Frequency Autocorrelation of the Differential Group Delay in Fibers with Polarization Mode Dispersion. *Optics Letters*, 25(10), March 2000.
- [SO96] Henrique M. Salgado and John J. O'Reilly. Accurate Performance Modeling of Subcarrier Multiplexed Fiber/Radio Systems: Implications of Laser Non-linear Distortion and Wide Dynamic Range. *IEEE Transactions on Communications*, 44(8):988–996, August 1996.
- [SSC⁺03] Fadi Saibi, Edward Säckinger, Jinghong Chen, Joe Othmer, David Inglis, Meng-Lin Yu, Kuang-Hu Huang, TP Liu, and Kamran Azadet. A 40 Gb/s SCM Optical Communication System based on an Integrated CMOS Transceiver. In *ECOC*, Th1.5.6, 2003.
- [Sun02] H. Sunnerud. A Comparison Between Different PMD Compensation Techniques. *IEEE J. of Lightwave Tech.*, 20(3):368, 2002.
- [WCW00] Ming-Chia Wu, Pi-Yang Chiang, and Winston I. Way. On the Validity of Using CW tones to Test the Linearity of Multichannel M-QAM Subcarrier Multiplexed Lightwave Systems. *IEEE Phot. Tech. Letters*, 12(4):413–415, April 2000.
- [WE03] Peter J. Winzer and René-Jean Essiambre. Advanced optical modulation formats. In *ECOC*, Th2.6.1, 2003.

- [WK91] Jack H. Winters and Sanjay Kasturia. Constrained maximum-likelihood detection for high-speed fiber-optic systems. In *GLOBECOM*, pages 1574–1579, 1991.
- [WK92] Jack H. Winters and Sanjay Kasturia. Adaptive Nonlinear Cancellation for High-Speed Fiber-Optic Systems. *IEEE J. of Lightwave Tech.*, 10(7):971–977, July 1992.
- [WM96] P. K. Wai and C. R. Menyuk. Polarization Dispersion, Decorrelation and Diffusion in Optical Fibers with Randomly Varying Birefringence. *IEEE J. of Lightwave Tech.*, 14(2), February 1996.
- [WMZ97] P. K. Wai, C. R. Menyuk, and J. W. Zhang. Nonlinear Polarization-Mode Dispersion in Optical Fibers with Randomly Varying Birefringence. *J. Opt. Soc. Am. B*, 14(11), November 1997.
- [YK02] Roy You and Joseph M. Kahn. Upper-bounding the capacity of optical IM/DD channels with multiple-subcarrier modulation and fixed bias using trigonometric moment space method. *IEEE Transactions on Information Theory*, 38(2):514–523, February 2002.
- [YW02] Q. Yu and A. E. Willner. Performance Limits of First-Order PMD Compensators. *IEEE Phot. Tech. Letters*, 14(3):304, 2002.